Windowed integral equation methods for problems of scattering by defects and obstacles in layered media

Thesis by

Carlos A. Pérez Arancibia

In Partial Fulfillment of the Requirements

for the Degree of

Doctor of Philosophy

Caltech

California Institute of Technology

Pasadena, California

2017

(Defended August 15, 2016)

Acknowledgements

First of all I would like to express my deepest gratitude for my advisor and mentor, Prof. Oscar Bruno, under whose caring, patient and generous guidance I could accomplish this thesis. His passion for mathematics and his assiduous pursuit of excellence and originality will always inspire me.

My sincerest thanks to Profs. Catalin Turc (NJIT) and Mark Lyon (U. of New Hampshire) who contributed to the development of the Windowed Green Function method, and Prof. Yue Ying Lau and Dr. Peng Zhang of the University of Michigan who proposed to us the interesting physics problems that eventually inspired the subject of this thesis.

I would also like to thank my thesis committee; Profs. Dan Meiron, Houman Owhadi and Peter Schroeder, for the useful comments and suggestions.

Thanks to my fellow groupmates and friends; Agustín Fernandez-Lado, Eldar Akhmet-galiyev, Emmanuel Garza-Gonzales, Thomas Anderson, Martín Maas and Edwin Jimenez, for all the interesting discussions that took place over countless lunches and coffee breaks at Steele House. I would also like to thank Carmen Sirois and Sydney Garstang for their travel, scheduling and organizational support, and for making the office feel like home.

Special thanks to all the good friends I have made during my time at Caltech, specially Wael, Alex, Krishna, Cristián, Camila, George, Valentina, Soledad, Alejandro, Maricruz, Steven and Emma, with whom I shared so many great moments.

Last but not least, I would like to thank my family: my parents Osvaldo and Herminda, my brothers César and Néstor and my aunt Rita, for their unconditional support.

My greatest gratitude goes to my beloved wife Ruby, who has selflessly accompanied me throughout this intellectual journey over all these years. This would not have been possible without your constant love and support for which I will be forever grateful.

Abstract

This thesis concerns development of efficient high-order boundary integral equation methods for the numerical solution of problems of acoustic and electromagnetic scattering in the presence of planar layered media in two and three spatial dimensions. The interest in such problems arises from application areas that benefit from accurate numerical modeling of the layered media scattering phenomena, such as electronics, near-field optics, plasmonics and photonics as well as communications, radar and remote sensing.

A number of efficient algorithms applicable to various problems in these areas are presented in this thesis, including (i) A Sommerfeld integral based high-order integral equation method for problems of scattering by defects in presence of infinite ground and other layered media, (ii) Studies of resonances and near resonances and their impact on the absorptive properties of rough surfaces, and (iii) A novel *Window Green Function Method* (WGF) for problems of scattering by obstacles and defects in the presence of layered media. The WGF approach makes it possible to completely avoid use of expensive Sommerfeld integrals that are typically utilized in layer-media simulations. In fact, the methods and studies referred in points (i) and (ii) above motivated the development of the markedly more efficient WGF alternative.

Table of Contents

vi

Chapter 1

Introduction

Early history. The interest on the propagation of light in presence of materials has remained at the forefront of human inquiry for over two millennia: the study of the phenomena of reflection, refraction and diffraction of electromagnetic waves dates back at least to the ancient Greeks [18]. Indeed, Greek philosophers and mathematicians were already familiar with certain aspects of the nature of light now encompassed within the theory of geometrical optics—such as the notion of rectilinear propagation, the law of reflection and the phenomenon of refraction. Yet the precise law of refraction was only established (experimentally) by Willebrord Snell in 1621.

Although successful at providing a good description of the reflection and refraction of light across (locally) planar material interfaces, the geometrical optics paradigm encountered severe difficulties at explaining the significantly more complex phenomenon of diffraction— which arises, for instance, as light impinges upon structures containing sharp boundaries (such as e.g. slits and screens). In fact, the so-called wave theory of light was originally put forth in an attempt to account for the diffraction phenomenon [34, 62]. In its early stages, however, this theory could not explain the reflection, refraction and rectilinear propagation of light. The first two aforementioned difficulties were overcame by Christian Huygens, who, relying on the famous principle that now bears his name[1], was able to re-derive from wave-based principles the previously (experimentally) established laws of reflection and refraction.

---

[1]According to [18, p. xxvi], Huygens enunciated the principle according to which "Every point of the aether upon which the luminous disturbance falls may by regarded as the centre of a new disturbance propagated in the form of spherical waves".

It took several decades until Augustin Fresnel in his celebrated "Mémoire sur la loi des modifications que la réflexion imprime a la lumière polarisée", published in 1819, demonstrated that diffraction can indeed be explained by applying Huygens' principle and Young's principle of interference. Remarkably, in that same memoir Fresnel provided the presently well-known expressions for the amplitude of the reflected and transmitted waves that arise when a plane-wave impinges on the flat interface between two homogeneous media with different optical properties. Fresnel's memoire contains also the formula for the amplitudes of the multiple reflections that take place between the two parallel boundaries of a single homogeneous plate of finite-thickness and, furthermore, it describes how these results could be extended to account for more than one plate [124]. This formula has been re-derived independently by a number of authors, including George Stokes [120] and George Airy [2], the former of whom gave the complete solution to the problem of scattering of a plane-wave by a planar multilayered medium. Fresnel's analysis of diffraction was later put on a firm mathematical basis by Gustav Kirchhoff, who around 1882 established an integral representation formula which expresses a scalar-wave-field at an arbitrary point in terms of the field values and its normal derivative at an arbitrary closed surface. (This representation formula was derived earlier in acoustics for monochromatic time-harmonic waves by Helmholtz in 1859.) The corresponding integral representation formulae for (vectorial) electromagnetic fields were not available until 1939, when Stratton and Chu published their well known contribution [121].

In the meantime, the seemingly disconnected developments on electricity and magnetism were unified by James Clerk Maxwell. Maxwell's works published between 1861 and 1862, which convey his celebrated system of differential equations, led him subsequently to conjecture that light waves are in fact electromagnetic waves. Maxwell's conjecture regarding the nature of light was empirically verified by Heinrich Hertz in 1888 [116]. As is well-known, Maxwell's and Hertz's discoveries turned out to have enormous practical consequences. Applying Maxwell's ideas pioneers experimentalists such as Marconi and Braun, who received the Nobel prize in 1909, started the era of wireless radio communications [115].

The problem of radio wave propagation over the surface of the earth—which relates

closely to the present dissertation—attracted considerable attention at the beginning of the 20th century in connection with theoretical efforts seeking to explain long-distance transmission of radio signals. Indeed, using a two-layer model that regards the earth and the air as homogeneous conducting and dielectric half-spaces, respectively, Jonathan Zenneck [138] studied the possibility that the earth surface could support a surface wave (also known as lateral wave) with low attenuation. Using this two-layer model Zenneck showed that a surface wave with the aforementioned characteristics (which additionally decays exponentially away from the planar interface) could exist, yet his work did not consider an excitation mechanism [131].

The excitation problem was studied mathematically by Arnold Sommerfeld [117], who obtained expressions for the fields produced by electric and magnetic dipoles located over the earth's surface—under the assumptions inherent in Zenneck's air/earth model. Sommerfeld's solution is expressed in terms of certain Fourier-Bessel integrals known as *Sommerfeld integrals*, which, unfortunately, cannot be evaluated in closed form. (A detailed discussion concerning Sommerfeld integrals can be found in the recent review [90] by Michalsky and Mosig.) Deforming the integration path from real-axis into the complex plane Sommerfeld identified two contributions—stemming from the branch cuts of the integrand and from the residue of a pole (the Sommerfeld pole), respectively. Sommerfeld's 1909 paper [117] also contains an asymptotic analysis of the solution for large lateral distances which, famously, turned out to be erroneous. Sommerfeld's results were eventually corrected and largely improved in various subsequent contributions, including very recent ones (see [90] and references therein). Further extensions of these ideas include studies of surface-waves arising in multi-layer models of the earth.

Sommerfeld-like methods undoubtedly provided a general understanding of the layered-media scattering phenomena. They are, however, not suited to directly tackle problems of scattering involving obstacles and/or surface defects, the latter of which interested Marconi who experimentally studied the field attenuation when a hill was located between the transmitting and receiving antennas [131]. Separation-of-variables techniques, in turn, can only produce exact solutions to simple scattering problems involving perfect electric conducting

(PEC) scatterers. In 1907, for example, Lord Rayleigh [109] obtained a Fourier-Bessel series solution for the problem of scattering of a plane-electromagnetic wave by a single cylindrical bump with semi-circular cross-section on a PEC half-space. A year later, Mie [91] presented the exact solution for the problem of scattering of a plane-electromagnetic wave by a PEC sphere in free space. These ideas were later utilized to solve the closely related surface-defect problem for which of a PEC semi-spherical boss (or bump, in our nomenclature) is placed on a PEC half-space [126]. Unfortunately, however, separation-of-variables techniques could not effectively deal with penetrable layered media problems, as no series expansions are known to satisfy the suitable transmission conditions at the planar interfaces between two dielectric or finitely-conducting layers.

An alternative to separation-of-variables techniques was then considered by Maue in 1949 [85]. Resorting to use of Kirchhoff's integral representation formula—which he re-derived from Green's third identity utilizing the free-space Green function for the Helmholtz equation—Maue showed that problems of scattering by PEC bounded obstacles in free-space can be recast as a boundary integral equation (BIE). As was shown in subsequent years by a number of authors, general problems of scattering—not only arising in electromagnetism, but also in acoustic and linear elasticity—can often by recast in terms of boundary integral formulations, provided that a *suitable Green function* is available. When this is the case, the scattered field can be expressed in terms of an integral representation formula which contains an integral density function—which can itself be obtained as a solution of an associated BIE. BIE methods, such as boundary element methods [114] as well as high-order Nyström methods [23, 27, 29, 31, 75, 84], provide several advantages over methods based on volume discretization of the computational domain, such as finite difference and finite element methods. For example, BIE methods can easily handle unbounded domains and radiation conditions at infinity without recourse to approximate absorbing/transparent boundary conditions for truncation of the computational domain [58]. Additionally, BIE methods are based on discretization of the relevant physical boundaries, and they therefore give rise to linear systems of reduced dimensionality—which, although dense, can be efficiently solved by means of accelerated iterative linear algebra solvers [13, 17, 29, 59]. And,

finally, BIE methods do not suffer from dispersion errors, which is a highly desirable property in the context of wave propagation problems.

To highlight these issues we mention the contribution [40], one of whose authors is also the author of the renowned FDTD text [122] (finite-difference time-domain). In particular, the contribution [40] utilizes the FDTD scheme to solve the problem of scattering of a plane electromagnetic wave by a two-dimensional circular dielectric scatterer. The wavelength of the incident plane wave in this example is 500 nm and the diameter of the circles is 5 μm— which makes the circles 10 wavelengths in diameter. Using 100 points per wavelength the FDTD discretization required around 12 million grid points in the interior of each one of the circles to achieve errors of ±15 percent of the value of the exact solution. The total number of grid points needed to achieve such errors was, of course, much larger than 12 million, as the FDTD scheme also required a fine discretization of the exterior domain including the PML regions, that must be placed at a certain distance from the obstacles to suppress unwanted features such as frequency-dependent reflections [122]. Comparable errors are obtained in this thesis for similar problems on the basis of discretizations containing a total of the order of 100 points. Thus, as is well known, use of integral equation methods enable solution of a wide range of problems that lie well outside the range of applicability of volumetric methods.

In spite of these advantages, integral equation methods for problems of scattering in presence of layered media have remained inefficient—in view of the expense required for computation of the point values of the Green function suitable for layered media—which has typically rendered BIE treatment of large scale three-dimensional layered-media scattering problems essentially unfeasible. As discussed in what follows, this thesis provides an efficient integral-equation alternative for the solution of layered-media problems.

Content and Layout of the Thesis.   As discussed above, the classical BIE approach for layered-media problems is based on use of the layer Green function (LGF) in conjunction with an integral equation posed on the boundary of each bounded obstacle (Section 2.4). The LGF, which is in fact closely related to the aforementioned Sommerfeld's half-space excitation problem and which can be obtained by means of the corresponding Sommerfeld

integrals, equals the (total field) solution of the problem of scattering of a point source embedded in one of the layers. Thus, a scattering solution produced by means of the LGF automatically enforces the transmission conditions on the planar interfaces.

In the earlier stages of this thesis work an improved and extended high-order LGF-based integral equation method [104] was introduced which can be used to tackle general problems of scattering by defects in the presence of layered media in two-dimensional space (Chapter 3). The proposed method enjoys several advantages: a) it requires evaluation of a minimal number of integral operators (and, thus, a minimal number of Sommerfeld-integrals); b) it is based on a highly-efficient procedure we introduced (on the basis of windowing methods) for evaluation of Sommerfeld integrals; and c) it incorporates a novel algorithm for resolution of spurious resonances that arise in our minimal integral-equation formulation.

The interest in the problems of scattering by obstacles and defects in layered media arose from a collaboration with a group of applied physicists at The University of Michigan seeking to quantify electromagnetic power absorption that arises as electromagnetic fields illuminate rough conducting surfaces [105]. This collaboration led to the development and validation of the LGF approach described above. In particular, numerical studies based on our LGF algorithm revealed that a connection exists between enhanced power absorption and the existence of certain "pseudo-resonant" frequencies—that correspond to scattering poles near the real axis—at which large currents are induced near the boundary of the defect; see Section 3.5.1. As discussed in that section, further, the LGF algorithm was also utilized to study pseudo-resonance phenomenon in the context of surface plasmons scattering by micro-cavities in metals.

In view of the aforementioned work on the LGF method it is expected that complex three-dimensional problems cannot be reasonably treated by means of a method of LGF-type. In fact it was this very difficulty that led to our development of a novel BIE approach that outperforms the LGF method by completely bypassing the use of expensive Sommerfeld integrals. This new approach (Chapter 4 and [24]), which is referred to as the Windowed Green Function (WGF) method, is based on use of smooth windowing functions and integral kernels that can be expressed directly in terms of the free-space Green function. The WGF

method is fast, accurate, flexible and easy to implement. In particular straightforward modifications of existing (accelerated or unaccelerated) solvers suffice to incorporate the WGF capability. The mathematical basis of the method is simple: the approach relies on a certain integral equation that is smoothly windowed by means of a low-rise windowing function, and is thus supported on the union of the obstacle and a small flat section of the interface between the two penetrable media. Various numerical experiments presented in this thesis demonstrate that both the near- and far-field errors resulting from the proposed approach decrease faster than any negative power of the window size. In some of those examples the proposed method is up to thousands of times faster, for a given accuracy, than a corresponding LGF method (Figure 4.14). Analysis and generalizations of the WGF method to problems of scattering by obstacles in layered media composed by any finite number of layers in two (Chapter 5) and three spatial dimensions (Chapter 6) are also included in this dissertation.

This thesis is organized as follows. Chapter 2 presents both previously existing as well as new background materials concerning problems of scattering in the presence of layered media. These include the exact solution of the problem of scattering of a plane-wave by (planar) two- and multi-layer media, a detailed derivation and asymptotic analysis of the layer Green function in two and three spatial dimensions, a window-integration procedure for the efficient numerical evaluation of Sommerfeld integrals, and the description of a simple version of the aforementioned high-order Nyström-LGF method for problems of scattering by obstacles in the presence of layered media. Chapter 3 presents our full LGF method for problems of scattering by surface defects in the presence of layered media, and it includes sample applications to problems of electromagnetic power absorption and surface-plasmon-polariton scattering by metals. Chapter 4 introduces the WGF method for the problems of scattering by defects in a two-layer medium in two-dimensions, and presents a theoretical basis for the observed algorithmic traits. Chapters 5 and 6 then extend the approach to general multi-layer structures in two dimensions, and to three-dimensional scattering problems, respectively. Chapter 7, finally, presents our conclusions along with a description of ongoing and suggested future work.

Chapter 2

Scattering in planar layered media: Basic elements

The present chapter concerns three classical problems of scattering by layered media, namely, 1) scattering of a plane-wave by a planar layered medium, 2) scattering of a point-source field by a planar layered medium and evaluation of associated Sommerfeld integrals, and 3) scattering of a plane-wave by an bounded obstacle embedded in a planar layered medium, under the simplifying assumption (that is eliminated in Chapter 3) that the obstacle boundary does not intersect any of the planar interfaces between the layers. In particular, this chapter summarizes certain well-known aspects of the aforementioned problems as well as novel results concerning the numerical evaluation of Sommerfeld integrals and their asymptotics (Sections 2.3.4 and 2.3.5, respectively).

The structure of this chapter is as follows: Section 2.1 describes the geometry of the planar layered media considered throughout this thesis and it presents the relevant partial differential equations and boundary/transmission conditions at material interfaces that arise in problems of electromagnetic scattering in the frequency domain. Section 2.2, in turn, presents closed-form expressions for the solution of the problem of scattering of a plane electromagnetic wave by a layered medium. Subsequently, Section 2.3 deals with the problem of scattering of a point-source field by planar layered media, whose solution equals the so-called layer Green function. Finally, Section 2.4 describes the aforementioned LGF boundary integral equation methods for the numerical solution of problems of scattering by obstacles embedded in a layered medium, and it illustrates the presentation by means of a

few representative numerical examples.

2.1 Preliminary considerations

Throughout this thesis we consider planar layered media composed by N $(N > 1)$ layers $D_j = \{-d_j < y < -d_{j-1}\}$ of homogeneous dielectric/conducting materials. We let $\Pi_j = \{y = -d_j\}$ denote the plane at the interface between the layers D_j and D_{j+1}, $j = 1, \ldots, N-1$, (see Figure 2.1), where $d_{j+1} > d_j$ and $d_0 = -\infty$ and $d_N = \infty$.
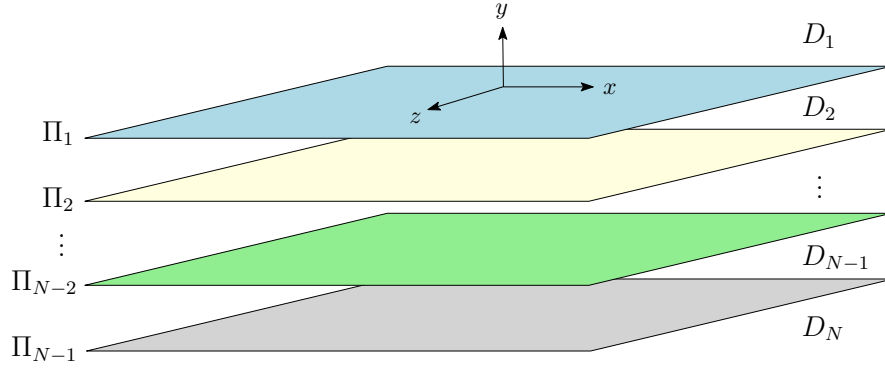
Figure 2.1: Planar layered medium.

Under the assumption that the electromagnetic field is driven by a time-harmonic source with time dependence given by $\mathrm{e}^{-i\omega t}$ (where $\omega > 0$ denotes the angular frequency), it follows that the total electric and total magnetic fields $\mathbf{E}$ and $\mathbf{H}$ satisfy Maxwell's equations [18, 64]

$$\operatorname{curl}\mathbf{E} - i\omega\mu_j\mathbf{H} = \mathbf{0}, \tag{2.1a}$$

$$\operatorname{curl}\mathbf{H} + i\omega\varepsilon_j\mathbf{E} = \mathbf{0}, \tag{2.1b}$$

within the layer D_j, $j = 1, \ldots, N$, with material constants μ_j and $\varepsilon_j = \varepsilon'_j + \frac{i\sigma_j}{\omega}$. Here ε'_j, $\sigma_j \geq 0$ and $\mu_j > 0$ denote the electrical permittivity, the electrical conductivity, and the magnetic permeability of the medium D_j, respectively.

The transmission conditions satisfied at the interface between two dielectric or conducting media [18, 64] enforce the continuity of the tangential components of the electric and magnetic fields across Π_j for $j = 1, \ldots, N-1$. Letting $\mathbf{E}_j$ (resp. $\mathbf{H}_j$) denote the limit

value of the electric (resp. magnetic) field at Π_j from the subdomain D_j, these continuity conditions can be expressed in the forms

$$\mathbf{n} \times [\mathbf{E}_j - \mathbf{E}_{j+1}] \;=\; \mathbf{0}, \tag{2.2a}$$

$$\mathbf{n} \times [\mathbf{H}_j - \mathbf{H}_{j+1}] \;=\; \mathbf{0}, \tag{2.2b}$$

on Π_j, where $\boldsymbol{n}$ denotes the unit normal vector which points from the dielectric medium D_{j+1} to the dielectric medium D_j.

The transmission conditions (2.2) become boundary conditions when one of the media, say D_{j+1}, is made of a infinitely conducting material. In fact, modeling D_{j+1} as a perfect electric conductor (PEC), that is, setting $\sigma_{j+1} = \infty$, the transmission conditions (2.2a) and (2.2b) reduce to the boundary condition

$$\mathbf{n} \times \mathbf{E}_j = \mathbf{0} \tag{2.3}$$

at the PEC boundary.

2.2 Plane-wave scattering

2.2.1 Maxwell's equations in TE and TM polarizations

The present section describes how, under certain symmetry assumptions, the Maxwell's system (2.1) in three-dimensional space can be equivalently expressed as a decoupled system of Helmholtz equations in a (two-dimensional) plane.

Consider an electromagnetic field $(\mathbf{E}, \mathbf{H})$, solution of (2.1), which remains constant along the z-axis:

$$\mathbf{E}(\boldsymbol{r}) = E_x(x, y)\mathbf{e}_x + E_y(x, y)\mathbf{e}_y + E_z(x, y)\mathbf{e}_z,$$

$$\mathbf{H}(\boldsymbol{r}) = H_x(x, y)\mathbf{e}_x + H_y(x, y)\mathbf{e}_y + H_z(x, y)\mathbf{e}_z,$$

where $\mathbf{e}_x = (1, 0, 0)$, $\mathbf{e}_y = (0, 1, 0)$ and $\mathbf{e}_z = (0, 0, 1)$ denote the canonical basis vectors. It is

easy to check that the field $(\mathbf{E}, \mathbf{H})$ is a solution of Maxwell's equations (2.1) if and only if the equations

$$\frac{\partial E_z}{\partial y} - i\omega\mu_j H_x = 0, \tag{2.4a}$$

$$-\frac{\partial E_z}{\partial x} - i\omega\mu_j H_y = 0, \tag{2.4b}$$

$$\left(\frac{\partial E_y}{\partial x} - \frac{\partial E_x}{\partial y}\right) - i\omega\mu_j H_z = 0, \tag{2.4c}$$

and

$$\frac{\partial H_z}{\partial y} + i\omega\varepsilon_j E_x = 0, \tag{2.5a}$$

$$-\frac{\partial H_z}{\partial x} + i\omega\varepsilon_j E_y = 0, \tag{2.5b}$$

$$\left(\frac{\partial H_y}{\partial x} - \frac{\partial H_x}{\partial y}\right) + i\omega\varepsilon_j E_z = 0, \tag{2.5c}$$

are satisfied. It follows from (2.4) and (2.5) that the electromagnetic field is completely determined by E_z and H_z:

$$\mathbf{E} = \frac{i}{\omega\varepsilon}\frac{\partial H_z}{\partial y}\mathbf{e}_x - \frac{i}{\omega\varepsilon}\frac{\partial H_z}{\partial x}\mathbf{e}_y + E_z\mathbf{e}_z, \tag{2.6a}$$

$$\mathbf{H} = -\frac{i}{\omega\mu}\frac{\partial E_z}{\partial y}\mathbf{e}_x + \frac{i}{\omega\mu}\frac{\partial E_z}{\partial x}\mathbf{e}_y + H_z\mathbf{e}_z. \tag{2.6b}$$

Substituting these expressions into (2.4c) and (2.5c), and defining the wavenumber k_j by

$$k_j^2 = \omega^2\varepsilon_j\mu_j = \omega^2\left(\varepsilon_j' + \frac{i\sigma_j}{\omega}\right)\mu_j, \tag{2.7}$$

we obtain the Helmholtz equations

$$\frac{\partial^2 E_z}{\partial x^2} + \frac{\partial^2 E_z}{\partial y^2} + k_j^2 E_z = 0, \tag{2.8a}$$

$$\frac{\partial^2 H_z}{\partial x^2} + \frac{\partial^2 H_z}{\partial y^2} + k_j^2 H_z = 0, \tag{2.8b}$$

for the z components E_z and H_z. It is easy to check that equations (2.6) and (2.8) are equivalent to (2.4) and (2.5).

The electromagnetic field $(\mathbf{E}, \mathbf{H})$ obtained by solving (2.8a) for E_z, assuming $H_z = 0$, is known as the *transverse electric (TE) field*, while the solution obtained by solving (2.8b) for H_z, assuming $E_z = 0$, is known as the *transverse magnetic (TM) field*.

Noting, on the other hand, that at the interface Π_j the z-coordinates of the tangential components of the fields are given by

$$(\boldsymbol{n} \times \mathbf{E}_j) \cdot \mathbf{e}_z = -\frac{i}{\omega \varepsilon_j} \nabla H_{jz} \cdot \mathbf{n} = -\frac{i}{\omega \varepsilon_j} \frac{\partial H_{jz}}{\partial n},$$

$$(\boldsymbol{n} \times \mathbf{H}_j) \cdot \mathbf{e}_z = \frac{i}{\omega \mu_j} \nabla E_{jz} \cdot \mathbf{n} = \frac{i}{\omega \mu_j} \frac{\partial E_{jz}}{\partial n},$$

it follows that the transmission conditions (2.2) can be expressed (in terms of E_z and H_z only) as

$$E_{jz} = E_{j+1,z}, \qquad \frac{\partial E_{jz}}{\partial n} = \nu_j^E \frac{\partial E_{j+1,z}}{\partial n}, \tag{2.9a}$$

$$H_{jz} = H_{j+1,z}, \qquad \frac{\partial H_{jz}}{\partial n} = \nu_j^H \frac{\partial H_{j+1,z}}{\partial n}, \tag{2.9b}$$

at the interface Π_j, where

$$\nu_j^E = \frac{\mu_j}{\mu_{j+1}} \quad \text{and} \quad \nu_j^H = \frac{\varepsilon_j}{\varepsilon_{j+1}}. \tag{2.10}$$

Similarly, the boundary condition (2.3) at the boundary of a PEC leads to the following boundary conditions for the transverse components of the electric and magnetic fields:

$$E_z = 0, \tag{2.11a}$$

$$\frac{\partial H_z}{\partial n} = 0. \tag{2.11b}$$

2.2.2 Two-layer medium

Consider a layered medium composed of two half-spaces $D_1 = \{y > 0\}$ and $D_2 = \{y < 0\}$ characterized by their respective wavenumbers, k_1 and k_2, and let $\Pi_1 = \{y = 0\}$ be the interface between the half-spaces. Further, let an incident electromagnetic plane-wave $(\mathbf{E}^{\text{inc}}, \mathbf{H}^{\text{inc}})$ of the form

$$\mathbf{E}^{\text{inc}} = (\mathbf{p} \times \mathbf{k}) \, e^{i\mathbf{k}\cdot\mathbf{r}} \quad \text{and} \quad \mathbf{H}^{\text{inc}} = \frac{1}{\omega\mu_1} \mathbf{k} \times \mathbf{E}^{\text{inc}}, \tag{2.12}$$

be given, where $\mathbf{p} = (p_x, p_y, p_z)$ is a constant vector parallel to $\mathbf{H}$, and where, without loss of generality, a wavevector of the form $\mathbf{k} = (k_{1x}, -k_{1y}, 0)$, $k_{1y} \geq 0$, with $|\boldsymbol{k}| = \sqrt{k_{1x}^2 + k_{1y}^2} = k_1$ is assumed. Clearly, the z-independent plane-wave (2.12), which is determined by its transverse components $E_z^{\text{inc}} = E_0 \, e^{i(k_{1x}x - k_{1y}y)}$ $(E_0 = -p_y k_{1x} - p_x k_{1y})$ and $H_z^{\text{inc}} = H_0 \, e^{i(k_{1x}x - k_{1y}y)}$ $(H_0 = k_1 p_z)$, is a solution of (2.1) in D_1.

Similarly, the total electromagnetic field $(\mathbf{E}_j, \mathbf{H}_j)$ in D_j, which equals the incident plus the reflected field in D_1, and equals the transmitted field in D_2, is completely determined by E_{jz} and H_{jz}, which satisfy homogeneous Helmholtz equations (2.8a) and (2.8b) in D_j with $k = k_j$ and transmission conditions (2.9a) and (2.9b) with $j = 1$.

Applying the method of separations of variables and using the continuity of total transverse fields across Π_1, we get that the physically meaningful solutions E_z and H_z of (2.8a) and (2.8b) respectively, are given by

$$E_z(x, y) = E_0 \, e^{ik_{1x}x} \begin{cases} e^{-ik_{1y}y} + R_{12}^{\text{TE}} \, e^{ik_{1y}y} & \text{in} \quad D_1, \\ T_{12}^{\text{TE}} \, e^{-ik_{2y}y} & \text{in} \quad D_2, \end{cases} \tag{2.13a}$$

and

$$H_z(x, y) = H_0 \, e^{ik_{1x}x} \begin{cases} e^{-ik_{1y}y} + R_{12}^{\text{TM}} \, e^{ik_{1y}y} & \text{in} \quad D_1, \\ T_{12}^{\text{TM}} \, e^{-ik_{2y}y} & \text{in} \quad D_2, \end{cases} \tag{2.13b}$$

where $k_{2y} = \sqrt{k_2^2 - k_{1x}^2}$ with the complex square root defined such that $\text{Im}\, k_{2y} \geq 0$ and $\text{Re}\, k_{2y} > 0$. Note, in particular, that k_{2y} equals $\sqrt{k_2^2 - k_{1x}^2}$ if $k_2^2 \geq k_{1x}^2$, and it equals $i\sqrt{k_{1x}^2 - k_2^2}$ if $k_2^2 < k_{1x}^2$ in the case $\text{Im}\, k_2 = 0$. Thus, enforcing the transmission condi-

tions (2.9a) and (2.9b), we obtain the following systems of equations:

$$1 + R_{12}^{\mathrm{TE}} = T_{12}^{\mathrm{TE}}, \qquad k_{1y}(1 - R_{12}^{\mathrm{TE}}) = k_{2y}\nu_1^E T_{12}^{\mathrm{TE}},$$

$$1 + R_{12}^{\mathrm{TM}} = T_{12}^{\mathrm{TM}}, \qquad k_{1y}(1 - R_{12}^{\mathrm{TM}}) = k_{2y}\nu_1^H T_{12}^{\mathrm{TM}},$$

whose solutions are the Fresnel coefficients [18]:

$$R_{j,j+1}^{\mathrm{TE}} = \frac{k_{jy} - \nu_j^E k_{j+1,y}}{k_{jy} + \nu_j^E k_{j+1,y}}, \qquad T_{j,j+1}^{\mathrm{TE}} = \frac{2k_{jy}}{k_{jy} + \nu_j^E k_{j+1,y}}, \tag{2.14a}$$

$$R_{j,j+1}^{\mathrm{TM}} = \frac{k_{jy} - \nu_j^H k_{j+1,y}}{k_{jy} + \nu_j^H k_{j+1,y}}, \qquad T_{j,j+1}^{\mathrm{TM}} = \frac{2k_{jy}}{k_{jy} + \nu_j^H k_{j+1,y}}. \tag{2.14b}$$

The fields $E_0 R_{12}^{\mathrm{TE}}\, \mathrm{e}^{ik_{1x}x + ik_{1y}y}$ and $H_0 R_{12}^{\mathrm{TM}}\, \mathrm{e}^{ik_{1x}x + ik_{1y}y}$ in (2.13) are referred to as reflected fields, while the fields $E_0 T_{12}^{\mathrm{TE}}\, \mathrm{e}^{ik_{1x}x - ik_{2y}y}$ and $H_0 T_{12}^{\mathrm{TM}}\, \mathrm{e}^{ik_{1x}x - ik_{2y}y}$ are referred to as transmitted fields. The physical interpretation of the reflected fields and the transmitted fields in the case $\mathrm{Im}\, k_2 = 0$, $k_2^2 \geq k_{1x}^2$, corresponds to plane-waves that propagate upwards and downwards, respectively, whose directions of propagation are determined by Snells's law [18]. The transmitted fields corresponding to wavenumbers $k_2^2 < k_{1x}^2$ or $\mathrm{Im}\, k_2 > 0$, in turn, correspond to evanescent waves that decay exponentially towards the lower half-plane, and thus they do not propagate.

Finally, we note that in the presence of a PEC half-plane D_2, the total transverse electric and magnetic fields are given by

$$E_z(x,y) = E_0\, \mathrm{e}^{ik_{1x}x} \begin{cases} \mathrm{e}^{-ik_{1y}y} - \mathrm{e}^{ik_{1y}y} & \text{in } D_1, \\ 0 & \text{in } D_2, \end{cases} \tag{2.15a}$$

and

$$H_z(x,y) = H_0\, \mathrm{e}^{ik_{1x}x} \begin{cases} \mathrm{e}^{-ik_{1y}y} + \mathrm{e}^{ik_{1y}y} & \text{in } D_1, \\ 0 & \text{in } D_2, \end{cases} \tag{2.15b}$$

in TE and TM polarizations respectively.

The final expression for the electromagnetic field $(\mathbf{E}, \mathbf{H})$ solution of (2.1) is obtained by replacing (2.13) or (2.15) in (2.6), depending on whether a penetrable or PEC layer D_2 is

considered.

2.2.3 Multi-layer medium

Utilizing the physical nomenclature considered in Section 2.2.2 we now derive the solution of the problem of scattering of a plane electromagnetic wave by a layered medium composed by N layers, with planar interfaces Π_j determined by positive numbers d_j, $j = 1, \ldots, N-1$. The derivations presented in this subsection are based on the waves-tracing arguments presented in [41], which date back to the seminal work of G. G. Stokes [120]. Similar derivations can also be found [20, 124].

For the sake of brevity in the exposition only the TE-polarization case in presented in this section. The TM-polarization case is completely analogous. Letting $k_{jy} = \sqrt{k_j^2 - k_{1y}^2}$, $j = 2, \ldots, N$, where once again the complex square root is defined such that $\operatorname{Im} k_{jz} \geq 0$ and $\operatorname{Re} k_{jy} > 0$, the total transverse electric field is expressed as

$$E_z(x,y) = E_0\, e^{ik_{1x}x} \begin{cases} e^{-ik_{1y}y} + \widetilde{R}_{12}^{\mathrm{TE}}\, e^{ik_{1y}(y+2d_1)} & \text{in} \quad D_1, \\ A_j^{\mathrm{TE}} \left\{ e^{-ik_{jy}y} + \widetilde{R}_{j,j+1}^{\mathrm{TE}}\, e^{ik_{jy}(y+2d_j)} \right\} & \text{in} \quad D_j,\ 2 \leq j \leq N, \end{cases} \tag{2.16}$$

in terms of the generalized reflection coefficients $\widetilde{R}_{j,j+1}^{\mathrm{TE}}$ and amplitudes A_j^{TE}. Clearly E_z in (2.16) satisfies the Helmholtz equation with wavenumber k_j in each one of the layers D_j, $j = 1, \ldots, N$.

In order to determine the unknown coefficients $\widetilde{R}_{j,j+1}^{\mathrm{TE}}$ and A_j^{TE}, we observe that the down-going wave within D_j, which equals $A_j^{\mathrm{TE}}\, e^{ik_{jy}d_{j-1}}$ at Π_{j-1}, is given by the transmitted wave from the layer above, which equals $T_{j-1,j}^{\mathrm{TE}} A_{j-1}^{\mathrm{TE}}\, e^{ik_{j-1,y}d_{j-1}}$ at Π_{j-1}, plus the reflected wave by the layer below that is reflected by the layer above, which equals $R_{j,j-1}^{\mathrm{TE}} A_j^{\mathrm{TE}} \widetilde{R}_{j,j+1}^{\mathrm{TE}}\, e^{ik_{jy}(2d_j-d_{j-1})}$ at Π_{j-1}. Therefore, it follows from (2.16) that the down-going wave at Π_{j-1} satisfies

$$A_j^{\mathrm{TE}}\, e^{ik_{jy}d_{j-1}} = T_{j-1,j}^{\mathrm{TE}} A_{j-1}^{\mathrm{TE}}\, e^{ik_{j-1,y}d_{j-1}} + R_{j,j-1}^{\mathrm{TE}} A_j^{\mathrm{TE}} \widetilde{R}_{j,j+1}^{\mathrm{TE}}\, e^{ik_{jy}(2d_j-d_{j-1})}. \tag{2.17}$$

On the other hand, the up-going wave within D_{j-1}, which equals $A_{j-1}^{\mathrm{TE}} \widetilde{R}_{j-1,j}^{\mathrm{TE}}\, e^{ik_{j-1,y}d_{j-1}}$ at Π_{j-1}, is caused by the reflection of the down-going wave reflected by the layer below,

which equals $A_{j-1}^{\text{TE}} R_{j-1,j}^{\text{TE}}\, \mathrm{e}^{ik_{j-1,y}d_{j-1}}$ at Π_{j-1}, plus the transmission of the up-going wave in layer below, which equals $T_{j,j-1}^{\text{TE}} A_j^{\text{TE}} \widetilde{R}_{j,j+1}^{\text{TE}}\, \mathrm{e}^{ik_{jy}(2d_j-d_{j-1})}$ at Π_{j-1}. Thus, from (2.16) we obtain that the up-going wave at Π_{j-1} satisfies

$$A_{j-1}^{\text{TE}} \widetilde{R}_{j-1,j}^{\text{TE}}\, \mathrm{e}^{ik_{j-1,y}d_{j-1}} = A_{j-1}^{\text{TE}} R_{j-1,j}^{\text{TE}}\, \mathrm{e}^{ik_{j-1,y}d_{j-1}} + T_{j,j-1}^{\text{TE}} A_j^{\text{TE}} \widetilde{R}_{j,j+1}^{\text{TE}}\, \mathrm{e}^{ik_{jy}(2d_j-d_{j-1})}\,. \qquad (2.18)$$

From Equations (2.17) and (2.18) we then obtain the following recursive relations for the amplitudes and generalized reflection coefficients:

$$A_j^{\text{TE}} = \frac{T_{j-1,j}^{\text{TE}} A_{j-1}^{\text{TE}}\, \mathrm{e}^{i(k_{j-1,y}-k_{jy})d_{j-1}}}{1 - R_{j,j-1}^{\text{TE}} \widetilde{R}_{j,j+1}^{\text{TE}}\, \mathrm{e}^{2ik_{jy}(d_j-d_{j-1})}}, \qquad (2.19a)$$

$$\widetilde{R}_{j-1,j}^{\text{TE}} = R_{j-1,j}^{\text{TE}} + \frac{T_{j,j-1}^{\text{TE}} \widetilde{R}_{j,j+1}^{\text{TE}} T_{j-1,j}^{\text{TE}}\, \mathrm{e}^{2ik_{jy}(d_j-d_{j-1})}}{1 - R_{j,j-1}^{\text{TE}} \widetilde{R}_{j,j+1}^{\text{TE}}\, \mathrm{e}^{2ik_{jy}(d_j-d_{j-1})}}, \qquad (2.19b)$$

where R_j^{TE} and T_j^{TE} are defined in (2.14a).

The condition that there is no up-going wave in the lowermost layer, i.e., $\widetilde{R}_{N,N+1}^{\text{TE}} = 0$, allows us to find the generalized reflection coefficients $\widetilde{R}_{j,j+1}^{\text{TE}}$, $j = 1, \ldots N - 1$, recursively. Having obtained the generalized reflection coefficients, the amplitude coefficients A_j^{TE}, $j = 2, \ldots, N$ are determined from (2.19a) using the condition that $A_1^{\text{TE}} = 1$.

2.3 The Layer Green function

2.3.1 Line source in a two-layer medium

In this section we consider the problem of evaluation of the electromagnetic field produced by a line source along a straight line parallel to the planar interface contained in a two-layer medium. In view of the discussion in Section 2.2.1 above, this is a two-dimensional problem. Thus, it can be equivalently formulated as the problem of computing the Green function for the Helmholtz equation in a layered medium composed by the half-planes $D_1 = \{y > 0\} = \mathbb{R}_+^2$ and $D_2 = \{y < 0\} = \mathbb{R}_-^2$, with wavenumbers k_1 and k_2, respectively, whose common boundary is $\Pi_1 = \{y = 0\}$.

The desired Green function, $G(\cdot, \boldsymbol{r}') : \mathbb{R}^2 \to \mathbb{C}$, satisfies

$$
\begin{aligned}
\Delta_{\boldsymbol{r}} G(\boldsymbol{r}, \boldsymbol{r}') + k_j^2 G(\boldsymbol{r}, \boldsymbol{r}') &= -\delta_{\boldsymbol{r}'} && \text{in} \quad D_j, \ j = 1, 2, \\
G(\boldsymbol{r}, \boldsymbol{r}')\big|_{y=0^+} &= G(\boldsymbol{r}, \boldsymbol{r}')\big|_{y=0^-} && \text{on} \quad \Pi_1, \\
\frac{\partial G}{\partial y}(\boldsymbol{r}, \boldsymbol{r}')\bigg|_{y=0^+} &= \nu \frac{\partial G}{\partial y}(\boldsymbol{r}, \boldsymbol{r}')\bigg|_{y=0^-} && \text{on} \quad \Pi_1,
\end{aligned}
\tag{2.20a}
$$

and the Sommerfeld radiation condition [45] at infinity:

$$
\lim_{|\boldsymbol{r}| \to \infty} \sqrt{|\boldsymbol{r}|} \left\{ \frac{\partial G}{\partial |\boldsymbol{r}|}(\boldsymbol{r}, \boldsymbol{r}') - ik_j G(\boldsymbol{r}, \boldsymbol{r}') \right\} = 0 \quad \text{uniformly in all directions} \quad \frac{\boldsymbol{r}}{|\boldsymbol{r}|} \in D_j,
\tag{2.20b}
$$

where the constant ν equals ν_1^E in TE-polarization and ν_1^H in TM-polarization (see definition (2.10)), and where $\delta_{\boldsymbol{r}'} \in \mathcal{S}'(\mathbb{R}^2)$ denotes the Dirac delta distribution supported at the point $\boldsymbol{r}' \in \mathbb{R}^2$. Throughout this section, we refer to $\boldsymbol{r}' = (x', y')$ as the "source point", and to $\boldsymbol{r} = (x, y)$ as the "observation point".

As is known, G can be computed explicitly in terms of Fourier integrals [20], sometimes called Sommerfeld integrals. To obtain such explicit expressions, given a fixed point $\boldsymbol{r}' \in D_i$, $i = 1, 2$, we define the functions $g_j^{(i)}(\boldsymbol{r}) = G(\boldsymbol{r}, \boldsymbol{r}')$, $\boldsymbol{r} \in D_j$, $j = 1, 2$. Expressing $g_j^{(i)}$ as inverse Fourier transforms

$$
g_j^{(i)}(x, y) = \frac{1}{2\pi} \int_{-\infty}^{\infty} \widehat{g}_j^{(i)}(\xi, y)\, e^{i\xi(x-x')} \, d\xi
\tag{2.21}
$$

and replacing (2.21) in (2.20a), a system of ordinary differential equations (ODE) for the unknown functions $\widehat{g}_j^{(i)}$ is obtained which can be solved analytically. Two cases arise. For

$r' \in D_1$, the ODE system is given by

$$
\begin{cases}
\dfrac{\partial^2 \widehat{g}_1^{(1)}}{\partial y^2} - \gamma_1^2 \widehat{g}_1^{(1)} &= -\delta_{y'} \qquad && \text{if } \quad y > 0, \\[2mm]
\dfrac{\partial^2 \widehat{g}_2^{(1)}}{\partial y^2} - \gamma_2^2 \widehat{g}_2^{(1)} &= 0 \qquad && \text{if } \quad y < 0, \\[2mm]
\widehat{g}_1^{(1)}(\xi, 0) &= \widehat{g}_2^{(1)}(\xi, 0), \\[2mm]
\dfrac{\partial \widehat{g}_1^{(1)}}{\partial y}(\xi, 0) &= \nu \dfrac{\partial \widehat{g}_2^{(1)}}{\partial y}(\xi, 0),
\end{cases}
$$

whose unique physically admissible solution is

$$
\begin{aligned}
\widehat{g}_1^{(1)}(\xi, y) &= \frac{e^{-\gamma_1 |y - y'|}}{2\gamma_1} + R_{12} \frac{e^{-\gamma_1 |y + y'|}}{2\gamma_1} \qquad (y > 0), \\[2mm]
\widehat{g}_2^{(1)}(\xi, y) &= T_{12} \frac{e^{\gamma_2 y - \gamma_1 y'}}{2\gamma_1} \qquad\qquad\quad (y < 0),
\end{aligned}
\tag{2.22}
$$

where

$$
R_{12} = \frac{\gamma_1 - \nu \gamma_2}{\gamma_1 + \nu \gamma_2}, \qquad T_{12} = \frac{2\gamma_1}{\gamma_1 + \nu \gamma_2},
\tag{2.23}
$$

and $\gamma_j = \gamma_j(\xi) = \sqrt{\xi^2 - k_j^2}$. The determination of physically admissible branches of the functions $\gamma_j(\xi) = \sqrt{\xi - k_j}\sqrt{\xi + k_j}$ require selection of branch cuts for each one of the two associated square root functions. The relevant branches, which are determined by consideration of Sommerfeld's radiation condition, are $-3\pi/2 \le \arg(\xi - k_j) < \pi/2$ for $\sqrt{\xi - k_j}$ and $-\pi/2 \le \arg(\xi + k_j) < 3\pi/2$ for $\sqrt{\xi + k_j}$. In particular, for real values of ξ and a positive real wavenumber k_j, we have that $\gamma_j(\xi) = \sqrt{\xi^2 - k_j^2} \ge 0$ if $|\xi| \ge k_j$ and $\gamma_j(\xi) = -i\sqrt{k_j^2 - \xi^2}$ if $|\xi| < k_j$ with $\sqrt{k_j^2 - \xi^2} > 0$. The domain of definition of the function γ_j is depicted in Figure 2.2.
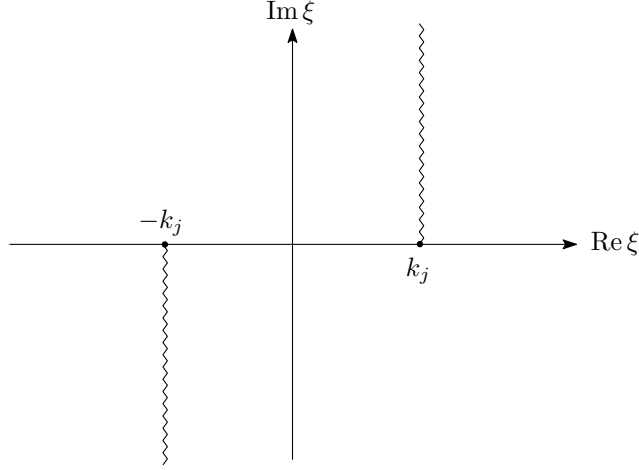
Figure 2.2: Branch-cuts and domain of definition for the function $\gamma_j = \sqrt{\xi^2 - k_j^2}$.

Similarly, the ODE system for $\boldsymbol{r}' \in D_2$ is given by

$$\begin{cases} \dfrac{\partial^2 \widehat{g}_1^{(2)}}{\partial y^2} - \gamma_1^2 \widehat{g}_1^{(2)} = 0 & \text{if} \quad y > 0, \\[2mm] \dfrac{\partial^2 \widehat{g}_2^{(2)}}{\partial y^2} - \gamma_2^2 \widehat{g}_2^{(2)} = -\delta_{y'} & \text{if} \quad y < 0, \\[2mm] \widehat{g}_1^{(2)}(\xi, 0) = \widehat{g}_2^{(2)}(\xi, 0), \\[2mm] \dfrac{\partial \widehat{g}_1^{(2)}}{\partial y}(\xi, 0) = \nu \dfrac{\partial \widehat{g}_2^{(2)}}{\partial y}(\xi, 0), \end{cases}$$

whose solution can be expressed as

$$\begin{aligned} \widehat{g}_1^{(2)}(\xi, y) &= T_{21} \frac{e^{-\gamma_1 y + \gamma_2 y'}}{2\gamma_2} & (y > 0), \\[2mm] \widehat{g}_2^{(2)}(\xi, y) &= \frac{e^{-\gamma_2 |y - y'|}}{2\gamma_2} + R_{21} \frac{e^{-\gamma_2 |y + y'|}}{2\gamma_2} & (y < 0), \end{aligned} \tag{2.24}$$

where

$$R_{21} = \frac{\nu \gamma_2 - \gamma_1}{\nu \gamma_2 + \gamma_1}, \qquad T_{21} = \frac{2\nu \gamma_2}{\nu \gamma_2 + \gamma_1}. \tag{2.25}$$

Taking the inverse Fourier transform (2.21) of $\widehat{g}_j^{(1)}$ in (2.22) and $\widehat{g}_j^{(2)}$ in (2.24), and utilizing

the well-known expression of the free-space Green function [41, 134]

$$\frac{i}{4}H_0^{(1)}(k_j|\boldsymbol{r}-\boldsymbol{r}'|) = \frac{1}{4\pi}\int_{-\infty}^{\infty}\frac{\mathrm{e}^{-\gamma_j|y-y'|}}{\gamma_j}\,\mathrm{e}^{i\xi(x-x')}\,\mathrm{d}\xi, \tag{2.26}$$

we obtain the following form of the Green function

$$G(\boldsymbol{r},\boldsymbol{r}') = \begin{cases} \dfrac{i}{4}H_0^{(1)}(k_1|\boldsymbol{r}-\boldsymbol{r}'|) + \dfrac{1}{4\pi}\displaystyle\int_{-\infty}^{\infty}R_{12}\dfrac{\mathrm{e}^{-\gamma_1|y+y'|}}{\gamma_1}\,\mathrm{e}^{i\xi(x-x')}\,\mathrm{d}\xi, & y',y > 0, \\[3mm] \dfrac{1}{4\pi}\displaystyle\int_{-\infty}^{\infty}T_{12}\dfrac{\mathrm{e}^{\gamma_2 y-\gamma_1 y'}}{\gamma_1}\,\mathrm{e}^{i\xi(x-x')}\,\mathrm{d}\xi, & y' > 0, y < 0, \\[3mm] \dfrac{1}{4\pi}\displaystyle\int_{-\infty}^{\infty}T_{21}\dfrac{\mathrm{e}^{-\gamma_1 y+\gamma_2 y'}}{\gamma_2}\,\mathrm{e}^{i\xi(x-x')}\,\mathrm{d}\xi, & y' < 0, y > 0, \\[3mm] \dfrac{i}{4}H_0^{(1)}(k_2|\boldsymbol{r}-\boldsymbol{r}'|) + \dfrac{1}{4\pi}\displaystyle\int_{-\infty}^{\infty}R_{21}\dfrac{\mathrm{e}^{-\gamma_2|y+y'|}}{\gamma_2}\,\mathrm{e}^{i\xi(x-x')}\,\mathrm{d}\xi, & y',y < 0, \end{cases} \tag{2.27}$$

where $R_{12} = R_{12}(\xi)$ and $T_{12} = T_{12}(\xi)$ (resp. $R_{21} = R_{21}(\xi)$ and $T_{21} = T_{21}(\xi)$) are defined in (2.23) (resp. (2.25)).

The fact that the expression in (2.27) satisfies the Sommerfeld radiation condition (2.20b) is shown in Section 2.3.4 below.

Remark 2.3.1. *It is easy to see from (2.27) and the definition of R_{12}, T_{12}, R_{21} and T_{21} that the layer-Green function $G(\cdot,\boldsymbol{r}')$, solution of (2.20), satisfies*

$$G(\boldsymbol{r},\boldsymbol{r}') = \begin{cases} G(\boldsymbol{r}',\boldsymbol{r}), & y,y' > 0, \\[2mm] \nu G(\boldsymbol{r}',\boldsymbol{r}), & y > 0, y' < 0, \\[2mm] \dfrac{1}{\nu}G(\boldsymbol{r}',\boldsymbol{r}), & y < 0, y' > 0, \\[2mm] G(\boldsymbol{r}',\boldsymbol{r}), & y,y' < 0. \end{cases} \tag{2.28}$$

Thus, taking the limits as $y' \to 0^{\pm}$ in (2.28) we obtain

$$\begin{aligned} G(\boldsymbol{r},\boldsymbol{r}')\big|_{y'=0^+} &= G(\boldsymbol{r}',\boldsymbol{r})\big|_{y'=0^+} = G(\boldsymbol{r}',\boldsymbol{r})\big|_{y'=0^-} = \frac{1}{\nu}G(\boldsymbol{r},\boldsymbol{r}')\big|_{y'=0^-}, \\ \frac{\partial G}{\partial y'}(\boldsymbol{r},\boldsymbol{r}')\bigg|_{y'=0^+} &= \frac{\partial G}{\partial y'}(\boldsymbol{r}',\boldsymbol{r})\bigg|_{y'=0^+} = \nu\frac{\partial G}{\partial y'}(\boldsymbol{r}',\boldsymbol{r})\bigg|_{y'=0^-} = \frac{\partial G}{\partial y'}(\boldsymbol{r},\boldsymbol{r}')\bigg|_{y'=0^-}, \end{aligned} \tag{2.29}$$

for an observation point $\boldsymbol{r} = (x, y) \in D_1$ *($y > 0$), where the identities* $G(\boldsymbol{r}', \boldsymbol{r})\big|_{y'=0+} = G(\boldsymbol{r}', \boldsymbol{r})\big|_{y'=0-}$ *and* $\frac{\partial G}{\partial y'}(\boldsymbol{r}', \boldsymbol{r})\big|_{y'=0+} = \nu \frac{\partial G}{\partial y'}(\boldsymbol{r}', \boldsymbol{r})\big|_{y'=0-}$ *follow from the transmission conditions in (2.20a). Similarly, for an observation point* $\boldsymbol{r} = (x, y) \in D_2$ *($y < 0$) we obtain*

$$
\begin{aligned}
G(\boldsymbol{r}, \boldsymbol{r}')\big|_{y'=0+} &= \frac{1}{\nu} G(\boldsymbol{r}', \boldsymbol{r})\big|_{y'=0+} = \frac{1}{\nu} G(\boldsymbol{r}', \boldsymbol{r})\big|_{y'=0-} = \frac{1}{\nu} G(\boldsymbol{r}, \boldsymbol{r}')\big|_{y'=0-}, \\
\frac{\partial G}{\partial y'}(\boldsymbol{r}, \boldsymbol{r}')\bigg|_{y'=0+} &= \frac{1}{\nu} \frac{\partial G}{\partial y'}(\boldsymbol{r}', \boldsymbol{r})\bigg|_{y'=0+} = \frac{\partial G}{\partial y'}(\boldsymbol{r}', \boldsymbol{r})\bigg|_{y'=0-} = \frac{\partial G}{\partial y'}(\boldsymbol{r}, \boldsymbol{r}')\bigg|_{y'=0-}.
\end{aligned}
\tag{2.30}
$$

Therefore we conclude that the function $G(\boldsymbol{r}, \cdot) : \mathbb{R}^2 \to \mathbb{C}$ *satisfies*

$$
\begin{aligned}
\Delta_{\boldsymbol{r}'} G(\boldsymbol{r}, \boldsymbol{r}') + k_j^2 G(\boldsymbol{r}, \boldsymbol{r}') &= -\delta_{\boldsymbol{r}} && in \quad D_j, \ j = 1, 2, \\
\nu G(\boldsymbol{r}, \boldsymbol{r}')\big|_{y'=0+} &= G(\boldsymbol{r}, \boldsymbol{r}')\big|_{y'=0-} && on \quad \Pi_1, \\
\frac{\partial G}{\partial y'}(\boldsymbol{r}, \boldsymbol{r}')\bigg|_{y'=0+} &= \frac{\partial G}{\partial y'}(\boldsymbol{r}, \boldsymbol{r}')\bigg|_{y'=0-} && on \quad \Pi_1,
\end{aligned}
$$

and the radiation condition

$$
\lim_{|\boldsymbol{r}| \to \infty} \sqrt{|\boldsymbol{r}'|} \left\{ \frac{\partial G}{\partial |\boldsymbol{r}'|}(\boldsymbol{r}, \boldsymbol{r}') - ik_j G(\boldsymbol{r}, \boldsymbol{r}') \right\} = 0 \quad uniformly \ in \ all \ directions \quad \frac{\boldsymbol{r}'}{|\boldsymbol{r}'|} \in D_j.
\tag{2.31}
$$

In order to improve the rate of decay as $|\xi| \to \infty$ of the functions that define $\widehat{g}_j^{(i)}(\xi, y)$, so that the spatial derivatives of G can be computed differentiating under the integral sign of the inverse Fourier transform even in the case $y = y' = 0$, we express (2.22) and (2.24) as

$$
\begin{aligned}
\widehat{g}_1^{(1)}(\xi, y) &= \frac{e^{-\gamma_1 |y - y'|}}{2\gamma_1} + \left(\frac{1 - \nu}{1 + \nu}\right) \frac{e^{-\gamma_1 |y + y'|}}{2\gamma_1} + \frac{\nu(k_2^2 - k_1^2) e^{-\gamma_1(y + y')}}{(1 + \nu)(\gamma_1 + \nu\gamma_2)(\gamma_1 + \gamma_2)\gamma_1} && (y > 0), \\
\widehat{g}_2^{(1)}(\xi, y) &= \left(\frac{1}{1 + \nu}\right) \frac{e^{-\gamma_1(y' - y)}}{\gamma_1} + \left\{ \frac{e^{\gamma_2 y - \gamma_1 y'}}{\gamma_1 + \nu\gamma_2} - \left(\frac{1}{1 + \nu}\right) \frac{e^{-\gamma_1(y' - y)}}{\gamma_1} \right\} && (y < 0),
\end{aligned}
\tag{2.32a}
$$

for $\boldsymbol{r}' \in D_1$, and

$$
\widehat{g}_1^{(2)}(\xi, y) = \left(\frac{\nu}{1+\nu}\right) \frac{\mathrm{e}^{-\gamma_2|y-y'|}}{\gamma_2} + \left\{ \frac{\nu\,\mathrm{e}^{-\gamma_1 y + \gamma_2 y'}}{\gamma_1 + \nu\gamma_2} - \frac{\nu}{1+\nu} \frac{\mathrm{e}^{-\gamma_2(y-y')}}{\gamma_2} \right\} \quad (y > 0),
$$

$$
\widehat{g}_2^{(2)}(\xi, y) = \frac{\mathrm{e}^{-\gamma_2|y-y'|}}{2\gamma_2} + \left(\frac{\nu-1}{\nu+1}\right) \frac{\mathrm{e}^{-\gamma_2|y+y'|}}{2\gamma_2} + \frac{\nu(k_1^2 - k_2^2)\,\mathrm{e}^{\gamma_2(y+y')}}{(1+\nu)(\gamma_1 + \nu\gamma_2)(\gamma_2 + \gamma_1)\gamma_2} \quad (y < 0),
$$

$$
(2.32\mathrm{b})
$$

for $\boldsymbol{r}' \in D_2$.

Note that the following asymptotic estimates hold for the last term in each of the formulae (2.32) above:

$$
\left| \frac{\mathrm{e}^{-\gamma_1(y+y')}}{(\gamma_1 + \nu\gamma_2)(\gamma_1 + \gamma_2)\gamma_1} \right| = \mathcal{O}(\mathrm{e}^{-|\xi|(y+y')}\,|\xi|^{-3}), \quad (y, y' > 0),
$$

$$
\left| \frac{\mathrm{e}^{\gamma_2 y - \gamma_1 y'}}{\gamma_1 + \nu\gamma_2} - \frac{1}{1+\nu} \frac{\mathrm{e}^{-\gamma_1(y'-y)}}{\gamma_1} \right| = \mathcal{O}(\mathrm{e}^{-|\xi|(y'-y)}\,|\xi|^{-3}), \quad (y < 0, y' > 0),
$$

$$
\left| \frac{\nu\,\mathrm{e}^{-\gamma_1 y + \gamma_2 y'}}{\gamma_1 + \nu\gamma_2} - \frac{\nu}{1+\nu} \frac{\mathrm{e}^{-\gamma_2(y-y')}}{\gamma_2} \right| = \mathcal{O}(\mathrm{e}^{-|\xi|(y-y')}\,|\xi|^{-3}), \quad (y > 0, y' < 0),
$$

$$
\left| \frac{\nu(k_1^2 - k_2^2)\,\mathrm{e}^{\gamma_2(y+y')}}{(1+\nu)(\gamma_1 + \nu\gamma_2)(\gamma_2 + \gamma_1)\gamma_2} \right| = \mathcal{O}(\mathrm{e}^{-|\xi||y'+y|}\,|\xi|^{-3}), \quad (y, y' < 0),
$$

$$
(2.33)
$$

as $|\xi| \to \infty$. Thus, taking the inverse Fourier transform (2.21) of $\widehat{g}_j^{(i)}$ in (2.32) using the identity in (2.26) we arrive to

$$
G(\boldsymbol{r}, \boldsymbol{r}') = \begin{cases} \dfrac{i}{4}H_0^{(1)}(k_1|\boldsymbol{r} - \boldsymbol{r}'|) + \dfrac{i}{4}\left(\dfrac{1-\nu}{1+\nu}\right) H_0^{(1)}(k_1|\boldsymbol{r} - \overline{\boldsymbol{r}}'|) + \Phi_R^{(1)}(\boldsymbol{r}, \boldsymbol{r}'), & y, y' > 0, \\[3mm] \dfrac{i}{2}\left(\dfrac{1}{1+\nu}\right) H_0^{(1)}(k_1|\boldsymbol{r} - \boldsymbol{r}'|) + \Phi_T^{(1)}(\boldsymbol{r}, \boldsymbol{r}'), & y < 0, y' > 0, \\[3mm] \dfrac{i}{2}\left(\dfrac{\nu}{1+\nu}\right) H_0^{(1)}(k_2|\boldsymbol{r} - \boldsymbol{r}'|) + \Phi_T^{(2)}(\boldsymbol{r}, \boldsymbol{r}'), & y > 0, y' < 0, \\[3mm] \dfrac{i}{4}H_0^{(1)}(k_2|\boldsymbol{r} - \boldsymbol{r}'|) + \dfrac{i}{4}\left(\dfrac{\nu-1}{\nu+1}\right) H_0^{(1)}(k_2|\boldsymbol{r} - \overline{\boldsymbol{r}}'|) + \Phi_R^{(2)}(\boldsymbol{r}, \boldsymbol{r}'), & y, y' < 0, \end{cases}
$$

$$
(2.34\mathrm{a})
$$

where $\overline{\boldsymbol{r}}' = (x', -y')$ denotes the image of the source point $\boldsymbol{r}' = (x', y')$ with respect to the plane $\Pi_1 = \{y = 0\}$ and where, taking advantage of the parity of γ_j, the functions $\Phi_R^{(i)}$ and

$\Phi_T^{(i)}$, $i = 1, 2$, are explicitly given by

$$
\begin{aligned}
\Phi_R^{(1)}(\boldsymbol{r}, \boldsymbol{r}') &= \frac{\nu(k_2^2 - k_1^2)}{\pi(1 + \nu)} \int_0^\infty \frac{\mathrm{e}^{-\gamma_1(y+y')} \cos(\xi(x - x'))}{\gamma_1(\gamma_1 + \gamma_2)(\gamma_1 + \nu\gamma_2)} \, \mathrm{d}\xi, \\[2mm]
\Phi_T^{(1)}(\boldsymbol{r}, \boldsymbol{r}') &= \frac{1}{\pi} \int_0^\infty \left\{ \frac{\mathrm{e}^{\gamma_2 y - \gamma_1 y'}}{\gamma_1 + \nu\gamma_2} - \frac{\mathrm{e}^{\gamma_1(y - y')}}{(1 + \nu)\gamma_1} \right\} \cos(\xi(x - x')) \, \mathrm{d}\xi, \\[2mm]
\Phi_T^{(2)}(\boldsymbol{r}, \boldsymbol{r}') &= \frac{\nu}{\pi} \int_0^\infty \left\{ \frac{\mathrm{e}^{-\gamma_1 y + \gamma_2 y'}}{\gamma_1 + \nu\gamma_2} - \frac{\mathrm{e}^{-\gamma_2(y - y')}}{(\nu + 1)\gamma_2} \right\} \cos(\xi(x - x')) \, \mathrm{d}\xi, \\[2mm]
\Phi_R^{(2)}(\boldsymbol{r}, \boldsymbol{r}') &= \frac{\nu(k_1^2 - k_2^2)}{\pi(\nu + 1)} \int_0^\infty \frac{\mathrm{e}^{\gamma_2(y+y')} \cos(\xi(x - x'))}{\gamma_2(\gamma_2 + \gamma_1)(\gamma_1 + \nu\gamma_2)} \, \mathrm{d}\xi.
\end{aligned}
\tag{2.34b}
$$

The expressions in (2.34) are utilized in Section 2.3.5 to numerically evaluate the layer Green function.

In view of the enhanced decay (2.33) of each one of the integrands in (2.34b) together with the Lebesgue's dominated convergence theorem, the gradient of the Green function (2.34a) can be evaluated from the expressions above by differentiation under the integral sign.

2.3.2 Point source in a two-layer medium

In this section we consider the full three-dimensional problem of finding the layer Green function for the Helmholtz equation in a two-layer medium. Letting $\delta_{\boldsymbol{r}'} \in \mathcal{S}'(\mathbb{R}^3)$ denote the Dirac delta function supported at the source point $\boldsymbol{r}' = (x', y', z') \in \mathbb{R}^3$, we have that the sought Green function, $G(\cdot, \boldsymbol{r}') : \mathbb{R}^3 \to \mathbb{C}$, satisfies

$$
\begin{aligned}
\Delta_{\boldsymbol{r}} G(\boldsymbol{r}, \boldsymbol{r}') + k_j^2 G(\boldsymbol{r}, \boldsymbol{r}') &= -\delta_{\boldsymbol{r}'} && \text{in} \quad D_j, \quad j = 1, 2, \\[2mm]
G(\boldsymbol{r}, \boldsymbol{r}')|_{y=0^+} &= G(\boldsymbol{r}, \boldsymbol{r}')|_{y=0^-} && \text{on} \quad \Pi_1, \\[2mm]
\frac{\partial G}{\partial z}(\boldsymbol{r}, \boldsymbol{r}')\bigg|_{y=0^+} &= \nu \frac{\partial G}{\partial z}(\boldsymbol{r}, \boldsymbol{r}')\bigg|_{y=0^-} && \text{on} \quad \Pi_1,
\end{aligned}
\tag{2.35a}
$$

as well as the Sommerfeld radiation condition [45] at infinity

$$\lim_{|\boldsymbol{r}|\to\infty} |\boldsymbol{r}| \left\{ \frac{\partial G}{\partial |\boldsymbol{r}|}(\boldsymbol{r}, \boldsymbol{r}') - ik_j G(\boldsymbol{r}, \boldsymbol{r}') \right\} = 0 \quad \text{uniformly in all directions} \quad \frac{\boldsymbol{r}}{|\boldsymbol{r}|} \in D_j \subset \mathbb{R}^3. \tag{2.35b}$$

As in the two-dimensional case, G can be computed explicitly by means of the Fourier transform. To obtain such explicit expression, given a fixed point source point $\boldsymbol{r}' \in D_i$ we define the function $g_j^{(i)}(\boldsymbol{r}) = G(\boldsymbol{r}, \boldsymbol{r}')$ for an observation point $\boldsymbol{r} \in D_j$, and we express it as the inverse two-dimensional Fourier transform

$$g_j^{(i)}(x, y, z) = \frac{1}{(2\pi)^2} \int_{-\infty}^{\infty} \int_{-\infty}^{\infty} \widehat{g}_j^{(i)}(\xi_1, \xi_2, y) \, e^{i(\xi_1(x-x') + \xi_2(z-z'))} \, d\xi_1 \, d\xi_2. \tag{2.36}$$

Taking advantage of the cylindrical symmetry of the problem, we make the following change of variables:

$$x - x' = \rho \cos\alpha, \quad z - z' = \rho \sin\alpha,$$

for the spatial variables, where $\rho = \sqrt{(x-x')^2 + (y-y')^2}$ and $0 \le \alpha \le 2\pi$, and

$$\xi_1 = \xi \cos\beta, \quad \xi_2 = \xi \sin\beta, \tag{2.37}$$

for the spectral variables, where $\xi = \sqrt{\xi_1^2 + \xi_2^2}$ and $0 \le \beta \le 2\pi$.

Note that since $g_j^{(i)}(x, y, z)$ is axisymmetric, i.e., does not depend on the angle θ, its Fourier transform $\widehat{g}_j^{(i)}(\xi_1, \xi_2, y)$ does not depend on α. Therefore, we can simply write $\widehat{g}_j^{(i)}(\xi_1, \xi_2, y) = \widehat{g}_j^{(i)}(\xi, y)$. Then, using the change of variables (2.37) and the integral representation of the Bessel function [134]

$$J_0(t) = \frac{1}{2\pi} \int_0^{2\pi} e^{it\cos\beta} \, d\beta,$$

we obtain that (2.36) can be equivalently expressed as a Hankel transform

$$g_j^{(i)}(x, y, z) = \frac{1}{2\pi} \int_0^{\infty} \widehat{g}_j^{(i)}(\xi, y) J_0(\xi\rho) \xi \, d\xi. \tag{2.38}$$

Replacing (2.38) in the partial differential equation (2.35a), we obtain the same system of ODEs for $\widehat{g}_j^{(i)}(\xi, y)$ obtained in the previous section, whose solution is given in (2.22) for $\boldsymbol{r}' \in D_1$, and in (2.24) for $\boldsymbol{r}' \in D_2$.

Subsequently, taking the inverse Hankel transform as defined in (2.38), of $\widehat{g}_j^{(i)}(\xi, y)$ and using the identity

$$\frac{e^{ik_j|\boldsymbol{r}-\boldsymbol{r}'|}}{4\pi|\boldsymbol{r}-\boldsymbol{r}'|} = \frac{1}{4\pi}\int_0^\infty \frac{e^{-\gamma_j|y-y'|}}{\gamma_j} J_0(\xi\rho)\xi \,\mathrm{d}\xi, \tag{2.39}$$

we obtain that the Green function is given by

$$G(\boldsymbol{r},\boldsymbol{r}') = \begin{cases} \dfrac{e^{ik_1|\boldsymbol{r}-\boldsymbol{r}'|}}{4\pi|\boldsymbol{r}-\boldsymbol{r}'|} + \dfrac{1}{4\pi}\displaystyle\int_0^\infty R_{12}\dfrac{e^{-\gamma_1|y+y'|}}{\gamma_1} J_0(\xi\rho)\xi \,\mathrm{d}\xi, & y, y' > 0, \\[4mm] \dfrac{1}{4\pi}\displaystyle\int_0^\infty T_{12}\dfrac{e^{\gamma_2 y - \gamma_1 y'}}{\gamma_1} J_0(\xi\rho)\xi \,\mathrm{d}\xi, & y < 0, y' > 0, \\[4mm] \dfrac{1}{4\pi}\displaystyle\int_0^\infty T_{21}\dfrac{e^{-\gamma_1 y + \gamma_2 y'}}{\gamma_2} J_0(\xi\rho)\xi \,\mathrm{d}\xi, & y > 0, y' < 0, \\[4mm] \dfrac{e^{ik_2|\boldsymbol{r}-\boldsymbol{r}'|}}{4\pi|\boldsymbol{r}-\boldsymbol{r}'|} + \dfrac{1}{4\pi}\displaystyle\int_0^\infty R_{21}\dfrac{e^{-\gamma_2|y+y'|}}{\gamma_2} J_0(\xi\rho)\xi \,\mathrm{d}\xi, & y, y' < 0, \end{cases} \tag{2.40}$$

where $R_{12} = R_{12}(\xi)$ and $T_{12} = T_{12}(\xi)$ (resp. $R_{21} = R_{21}(\xi)$ and $T_{21} = T_{21}(\xi)$) are defined in (2.23) (resp. (2.25)).

As in the two-dimensional case, the Green function can be equivalently expressed as

$$G(\boldsymbol{r},\boldsymbol{r}') = \begin{cases} \dfrac{e^{ik_1|\boldsymbol{r}-\boldsymbol{r}'|}}{4\pi|\boldsymbol{r}-\boldsymbol{r}'|} + \left(\dfrac{1-\nu}{1+\nu}\right)\dfrac{e^{ik_1|\boldsymbol{r}-\overline{\boldsymbol{r}}'|}}{4\pi|\boldsymbol{r}-\overline{\boldsymbol{r}}'|} + \Phi_R^{(1)}(\boldsymbol{r},\boldsymbol{r}'), & y, y' > 0, \\[4mm] \left(\dfrac{1}{1+\nu}\right)\dfrac{e^{ik_1|\boldsymbol{r}-\boldsymbol{r}'|}}{2\pi|\boldsymbol{r}-\boldsymbol{r}'|} + \Phi_T^{(1)}(\boldsymbol{r},\boldsymbol{r}'), & y < 0, y' > 0, \\[4mm] \left(\dfrac{\nu}{1+\nu}\right)\dfrac{e^{ik_2|\boldsymbol{r}-\boldsymbol{r}'|}}{2\pi|\boldsymbol{r}-\boldsymbol{r}'|} + \Phi_T^{(2)}(\boldsymbol{r},\boldsymbol{r}'), & y > 0, y' < 0, \\[4mm] \dfrac{e^{ik_2|\boldsymbol{r}-\boldsymbol{r}'|}}{4\pi|\boldsymbol{r}-\boldsymbol{r}'|} + \left(\dfrac{\nu-1}{\nu+1}\right)\dfrac{e^{ik_1|\boldsymbol{r}-\overline{\boldsymbol{r}}'|}}{4\pi|\boldsymbol{r}-\overline{\boldsymbol{r}}'|} + \Phi_R^{(2)}(\boldsymbol{r},\boldsymbol{r}'), & y, y' < 0, \end{cases} \tag{2.41a}$$

in terms of improper integrals that can be differentiated for all observation and source points, where $\overline{\boldsymbol{r}}' = (x', -y', z')$ denotes the image of the source point $\boldsymbol{r}' = (x', y', z')$ with respect to

the plane $\Pi_1 = \{y = 0\}$ and where the functions $\Phi_R^{(i)}$ and $\Phi_T^{(i)}$, $i = 1, 2$, are given by

$$
\Phi_R^{(1)}(\boldsymbol{r}, \boldsymbol{r}') = \frac{\nu(k_2^2 - k_1^2)}{2\pi(1 + \nu)} \int_0^\infty \frac{e^{-\gamma_1(y+y')}}{\gamma_1(\gamma_1 + \gamma_2)(\gamma_1 + \nu\gamma_2)} J_0(\xi\rho)\xi \, d\xi,
$$

$$
\Phi_T^{(1)}(\boldsymbol{r}, \boldsymbol{r}') = \frac{1}{2\pi} \int_0^\infty \left\{ \frac{e^{\gamma_2 y - \gamma_1 y'}}{\gamma_1 + \nu\gamma_2} - \frac{e^{\gamma_1(y-y')}}{(1+\nu)\gamma_1} \right\} J_0(\xi\rho)\xi \, d\xi,
$$

$$
\Phi_T^{(2)}(\boldsymbol{r}, \boldsymbol{r}') = \frac{\nu}{2\pi} \int_0^\infty \left\{ \frac{e^{-\gamma_1 y + \gamma_2 y'}}{\gamma_1 + \nu\gamma_2} - \frac{e^{-\gamma_2(y-y')}}{(\nu+1)\gamma_2} \right\} J_0(\xi\rho)\xi \, d\xi,
$$

$$
\Phi_R^{(2)}(\boldsymbol{r}, \boldsymbol{r}') = \frac{\nu(k_1^2 - k_2^2)}{2\pi(\nu + 1)} \int_0^\infty \frac{e^{\gamma_2(y+y')}}{\gamma_2(\gamma_2 + \gamma_1)(\gamma_1 + \nu\gamma_2)} J_0(\xi\rho)\xi \, d\xi.
$$

(2.41b)

In view of the asymptotic expansion for the Bessel function $J_0(z)$ as $|z| \to \infty$ [76, 134], the integrands in (2.41b) above decay more slowly than their two-dimensional counterparts (2.33) as $|\xi| \to \infty$. However, they and their gradients with respect to $\boldsymbol{r}$ and $\boldsymbol{r}'$ are still absolutely integrable for all source and observation points.

2.3.3   Line and point sources in a three-layer medium

This section deals with the problem of computation of the Green function for a three-layer medium in two and three dimensional spaces. Both Green functions are given by the solution of the transmission problem:

$$
\begin{aligned}
\Delta_{\boldsymbol{r}} G(\boldsymbol{r}, \boldsymbol{r}') + k_j^2 G(\boldsymbol{r}, \boldsymbol{r}') &= -\delta_{\boldsymbol{r}'} && \text{in} \quad D_j, \; j = 1, 2, \\
G(\boldsymbol{r}, \boldsymbol{r}')\big|_{y=-d_1^+} &= G(\boldsymbol{r}, \boldsymbol{r}')\big|_{y=-d_1^-} && \text{on} \quad \Pi_1, \\
G(\boldsymbol{r}, \boldsymbol{r}')\big|_{y=-d_2^+} &= G(\boldsymbol{r}, \boldsymbol{r}')\big|_{y=-d_2^-} && \text{on} \quad \Pi_2, \\
\frac{\partial G}{\partial y}(\boldsymbol{r}, \boldsymbol{r}')\bigg|_{y=-d_1^+} &= \nu_1 \frac{\partial G}{\partial y}(\boldsymbol{r}, \boldsymbol{r}')\bigg|_{y=-d_1^-} && \text{on} \quad \Pi_1, \\
\frac{\partial G}{\partial y}(\boldsymbol{r}, \boldsymbol{r}')\bigg|_{y=-d_2^+} &= \nu_2 \frac{\partial G}{\partial y}(\boldsymbol{r}, \boldsymbol{r}')\bigg|_{y=-d_2^-} && \text{on} \quad \Pi_2,
\end{aligned}
$$

(2.42)

where $\delta_{\boldsymbol{r}'}$ denotes a line source $\delta_{\boldsymbol{r}'} = \delta_{x'}\delta_y$, in the two dimensional case, and it denotes a points source $\delta_{\boldsymbol{r}'} = \delta_{x'}\delta_{z'}\delta_{z'}$ in the three-dimensional case. The suitable radiation condition

at infinity follows from the far-field form of the physically correct solution G obtained by Fourier transformations techniques.

As in the previous sections, we start by expressing G as an inverse Fourier transform (2.21) in the two-dimensional case, and as an inverse Hankel transform (2.38) in the three-dimensional case. Replacing the resulting expressions for G in (2.42) and applying the corresponding inverse transform we then obtain a system of ODEs for $G = G(\boldsymbol{r}, \boldsymbol{r}')$ in the spectral form, which is denoted by $\widehat{g}_j^{(i)}(\xi, y)$ for observation and source points $\boldsymbol{r} \in D_j$ and $\boldsymbol{r}' \in D_i$, respectively. Solving the ODE system, eliminating all the exponentially growing solutions (as $|\xi| \to \infty$) and enforcing the transmission conditions at the planar interfaces Π_1 and Π_2, the functions $\widehat{g}_j^{(i)}(\xi, y)$, $i, j = 1, 2, 3$ are obtained in closed form. In detail, we obtain that for a source point $\boldsymbol{r}' \in D_1$, the solution of the ODE system is given by

$$
\begin{aligned}
\widehat{g}_1^{(1)}(\xi, y) &= \frac{1}{2\gamma_1} \left\{ e^{-\gamma_1|y-y'|} + \frac{R_{12} + R_{23}\, e^{2\gamma_2(d_1-d_2)}}{1 + R_{12}R_{23}\, e^{2\gamma_2(d_1-d_2)}}\, e^{-\gamma_1(y+y'+2d_1)} \right\}, \\
\widehat{g}_2^{(1)}(\xi, y) &= \frac{1}{2\gamma_1} \frac{T_{12}\, e^{d_1(\gamma_2-\gamma_1)}}{[1 + R_{12}R_{23}\, e^{2\gamma_2(d_1-d_2)}]} \left\{ e^{\gamma_2 y - \gamma_1 y'} + R_{23}\, e^{-\gamma_2(y+2d_2)-\gamma_1 y'} \right\}, \qquad \text{(2.43a)} \\
\widehat{g}_3^{(1)}(\xi, y) &= \frac{1}{2\gamma_1} \frac{T_{23}T_{12}\, e^{d_1(\gamma_2-\gamma_1)+d_2(\gamma_3-\gamma_2)}}{[1 + R_{12}R_{23}\, e^{2\gamma_2(d_1-d_2)}]}\, e^{\gamma_3 y - \gamma_1 y'},
\end{aligned}
$$

where

$$
R_{ij} = \begin{cases} \dfrac{\gamma_i - \nu_i\gamma_j}{\gamma_i + \nu_i\gamma_j} & \text{if } j > i, \\[2ex] \dfrac{\nu_i\gamma_j - \gamma_i}{\nu_i\gamma_j + \gamma_i} & \text{if } i > j, \end{cases} \qquad \text{and} \quad T_{ij} = 1 + R_{ij}.
$$

The square root branches in the definition of $\gamma_3 = \sqrt{\xi^2 - k_3^2} = \sqrt{\xi - k_3}\sqrt{\xi + k_3}$ are the same that were previously utilized in the definition of the functions γ_j, $j = 1, 2$. For a point source in the middle layer $\boldsymbol{r}' \in D_2$, on the other hand, we obtain

$$
\begin{aligned}
\widehat{g}_1^{(2)}(\xi, y) &= \frac{1}{2\gamma_2} \frac{T_{21}\left[1 + R_{23}\, e^{-2\gamma_2(d_2+y')}\right] e^{\gamma_2 y'}}{[1 - R_{21}R_{23}\, e^{2\gamma_2(d_1-d_2)}]}\, e^{-d_1(\gamma_1-\gamma_2)}\, e^{-\gamma_1 y}, \\
\widehat{g}_2^{(2)}(\xi, y) &= \frac{1}{2\gamma_2} \left\{ e^{-\gamma_2|y-y'|} + A\, e^{\gamma_2(y-y')} + B\, e^{-\gamma_2(y-y')} \right\}, \qquad \text{(2.43b)} \\
\widehat{g}_3^{(2)}(\xi, y) &= \frac{1}{2\gamma_2} \frac{T_{23}\left[1 + R_{21}\, e^{2\gamma_2(d_1+y')}\right]}{[1 - R_{21}R_{23}\, e^{2\gamma_2(d_1-d_2)}]}\, e^{d_2(\gamma_3-\gamma_2)}\, e^{\gamma_3 y - \gamma_2 y'},
\end{aligned}
$$

where

$$A = \frac{R_{21}[1 + R_{23}\,\mathrm{e}^{-2\gamma_2(d_2+y')}]\,\mathrm{e}^{2\gamma_2(d_1+y')}}{1 - R_{21}R_{23}\,\mathrm{e}^{2\gamma_2(d_1-d_2)}} \quad \text{and } B = \frac{R_{23}[1 + R_{21}\,\mathrm{e}^{2\gamma_2(d_1+y')}]\,\mathrm{e}^{-2\gamma_2(d_2+y')}}{1 - R_{21}R_{23}\,\mathrm{e}^{2\gamma_2(d_1-d_2)}}.$$

Finally, for a point source $\boldsymbol{r}' \in D_3$, we have

$$\begin{aligned}
\widehat{g}_1^{(3)}(y;\xi) &= \frac{1}{2\gamma_3}\frac{T_{21}T_{32}\,\mathrm{e}^{d_1(\gamma_2-\gamma_1)+d_2(\gamma_3-\gamma_2)}}{[1 + R_{32}R_{21}\,\mathrm{e}^{2\gamma_2(d_1-d_2)}]}\,\mathrm{e}^{\gamma_3 y'-\gamma_1 y}, \\
\widehat{g}_2^{(3)}(y;\xi) &= \frac{1}{2\gamma_3}\frac{T_{32}\,\mathrm{e}^{d_2(\gamma_3-\gamma_2)}}{[1 + R_{32}R_{21}\,\mathrm{e}^{2\gamma_2(d_1-d_2)}]}\left\{\mathrm{e}^{-\gamma_2 y+\gamma_3 y'} + R_{21}\,\mathrm{e}^{\gamma_2(y+2d_1)+\gamma_3 y'}\right\}, \qquad (2.43\mathrm{c}) \\
\widehat{g}_3^{(3)}(y;\xi) &= \frac{1}{2\gamma_3}\left\{\mathrm{e}^{-\gamma_3|y-y'|} + \frac{R_{32} + R_{21}\,\mathrm{e}^{2\gamma_2(d_1-d_2)}}{1 + R_{32}R_{21}\,\mathrm{e}^{2\gamma_2(d_1-d_2)}}\,\mathrm{e}^{\gamma_3(y+y'+2d_2)}\right\}.
\end{aligned}$$

The layer Green function G is then obtained by evaluating the corresponding inverse integral transform ((2.21) in the two-dimensional case and (2.38) in the three-dimensional case) of the expressions in (2.43). Note that the point source term is explicitly obtained in both cases utilizing the identities (2.26) and (2.39) in the two- and three-dimensional cases respectively.

In order to improve the decay of the integrands in the resulting integral representation of G, the functions $\widehat{g}_j^{(i)}$, $i,j = 1,2,3$, are expressed as $\left[\widehat{g}_j^{(i)} - \widetilde{g}_j^{(i)}\right] + \widetilde{g}_j^{(i)}$, where $\widetilde{g}_j^{(i)}$ denotes the leading order asymptotic expansion of $\widehat{g}_j^{(i)}$ as $|\xi| \to \infty$, which is obtained utilizing the relations

$$\begin{aligned}
R_{ij} &= \frac{1-\nu_i}{1+\nu_i} + \frac{2\nu_i(k_j^2-k_i^2)}{(1+\nu_i)(\gamma_i+\nu_i\gamma_j)(\gamma_i+\gamma_j)} = \frac{1-\nu_i}{1+\nu_i} + \mathcal{O}(|\xi|^{-2}) \quad (j > i), \\
T_{ij} &= \frac{2}{1+\nu_i} + \frac{2\nu_i(k_j^2-k_i^2)}{(1+\nu_i)(\gamma_i+\nu_i\gamma_j)(\gamma_i+\gamma_j)} = \frac{2}{1+\nu_i} + \mathcal{O}(|\xi|^{-2}) \quad (j > i), \qquad (2.44) \\
\mathrm{e}^{-\gamma_j y} &= \mathrm{e}^{-\gamma_i y}\left\{1 + \mathcal{O}(|\xi|^{-1})\right\}
\end{aligned}$$

as $|\xi| \to \infty$. In view of (2.26) and (2.39) the inverse transform of $\widetilde{g}_j^{(i)}$ admits an explicit expression. Clearly, $\widehat{g}_j^{(i)} - \widetilde{g}_j^{(i)}$ decays faster than $\widehat{g}_j^{(i)}$ as $|\xi| \to \infty$. Thus, the improved integral representation of G, which can be numerically evaluated for all source and observation points,

follows by taking inverse transform of $\left[\widehat{g}_j^{(i)} - \widetilde{g}_j^{(i)}\right] + \widetilde{g}_j^{(i)}$ for $i, j = 1, 2, 3$.

2.3.4 Far-field pattern

The present section is devoted to the asymptotic analysis of the two- and three-dimensional two-layer Green function (which were obtained in Sections 2.3.1 and 2.3.2), as $|\boldsymbol{r}| \to \infty$, for a given point source $\boldsymbol{r}'$ in space and fixed wavenumbers k_1 and k_2 ($k_1 > 0$ and $\operatorname{Im} k_2 \geq 0$). The analysis presented here is based on the method of steepest descent for which we refer to [15, 20, 21, 41, 51]. The relevant steepest-descents formulae are summarized in Appendix A. Some of the results obtained in this subsection follow directly from the analysis provided by Bleistein [15, Section 8.1] for the asymptotic approximation of layer Green function in the limit when $k_1 \to \infty$ for fixed spatial variables and a fixed index of refraction $n = k_2/k_1$.

In detail, this section provides the leading order asymptotic expansion of the reflected and transmitted wave fields produced by point sources at $\boldsymbol{r}' \in D_j$, $j = 1, 2$, respectively, at an observation point $\boldsymbol{r} \in D_1$ ($y > 0$) where $|\boldsymbol{r}| \gg 1$. The leading order asymptotic expansions for the transmitted and reflected fields produced by point sources at $\boldsymbol{r}' \in D_j$, $j = 1, 2$, respectively, at an observation point $\boldsymbol{r} \in D_2$ ($y < 0$), $|\boldsymbol{r}| \gg 1$, can be obtained following a completely analogous procedure.

Polar coordinates. Expressing both the observation and source points in polar coordinates ($\boldsymbol{r} = |\boldsymbol{r}|(\cos\theta, \sin\theta)$, $\theta \in [0, \pi]$, $\boldsymbol{r}' = |\boldsymbol{r}'|(\cos\theta', \sin\theta')$ for $\theta' \in [0, 2\pi]$), the relevant reflected and transmitted fields in (2.27) for the present $y > 0$ case become

$$G_R(\boldsymbol{r}, \boldsymbol{r}') = \frac{1}{4\pi} \int_{-\infty}^{\infty} R_{12} \frac{\mathrm{e}^{-|\boldsymbol{r}'|(i\xi\cos\theta' + \gamma_1\sin\theta')}}{\gamma_1} \, \mathrm{e}^{|\boldsymbol{r}|(i\xi\cos\theta - \gamma_1\sin\theta)} \, \mathrm{d}\xi \quad \left(\boldsymbol{r}' \in D_1 = \mathbb{R}_+^2\right), \quad (2.45\mathrm{a})$$

and

$$G_T(\boldsymbol{r}, \boldsymbol{r}') = \frac{1}{4\pi} \int_{-\infty}^{\infty} T_{21} \frac{\mathrm{e}^{-|\boldsymbol{r}'|(i\xi\cos\theta' - \gamma_2\sin\theta')}}{\gamma_2} \, \mathrm{e}^{|\boldsymbol{r}|(i\xi\cos\theta - \gamma_1\sin\theta)} \, \mathrm{d}\xi \quad \left(\boldsymbol{r}' \in D_2 = \mathbb{R}_-^2\right), \quad (2.45\mathrm{b})$$

respectively. For notational simplicity we introduce the change of variables $\xi = k_1\zeta$; we thus obtain

$$G_R(\boldsymbol{r}, \boldsymbol{r}') = \frac{1}{4\pi} \int_{-\infty}^{\infty} g_R(\zeta) \, e^{|\boldsymbol{r}|\phi(\zeta)} \, d\zeta, \tag{2.46a}$$

$$G_T(\boldsymbol{r}, \boldsymbol{r}') = \frac{\nu}{2\pi} \int_{-\infty}^{\infty} g_T(\zeta) \, e^{|\boldsymbol{r}|\phi(\zeta)} \, d\zeta, \tag{2.46b}$$

where

$$g_R(\zeta) = \frac{\sqrt{\zeta^2 - 1} - \nu\sqrt{\zeta^2 - n^2}}{\sqrt{\zeta^2 - 1} + \nu\sqrt{\zeta^2 - n^2}} \frac{e^{-i|\boldsymbol{r}'|k_1(\zeta\cos\theta' - i\sqrt{\zeta^2-1}\sin\theta')}}{\sqrt{\zeta^2 - 1}}, \tag{2.47a}$$

$$g_T(\zeta) = \frac{e^{-ik_1|\boldsymbol{r}'|(\zeta\cos\theta' + i\sqrt{\zeta^2-n^2}\sin\theta')}}{\sqrt{\zeta^2 - 1} + \nu\sqrt{\zeta^2 - n^2}}, \tag{2.47b}$$

$$\phi(\zeta) = ik_1(\zeta\cos\theta + i\sqrt{\zeta^2 - 1}\sin\theta), \tag{2.47c}$$

and $\sqrt{\zeta^2 - 1} = \gamma_1(\zeta k_1)/k_1$ and $\sqrt{\zeta^2 - n^2} = \gamma_2(\zeta k_1)/k_1$.

Saddle points. In view of (2.47c) it follows that the first two derivatives of the phase function ϕ are given by

$$\phi'(\zeta) = ik_1\left(\cos\theta + i\frac{\zeta\sin\theta}{\sqrt{\zeta^2 - 1}}\right) \quad \text{and} \quad \phi''(\zeta) = \frac{k_1\sin\theta}{(\zeta^2 - 1)\sqrt{\zeta^2 - 1}}.$$

From the saddle-point condition $\phi'(\zeta_0) = 0$ we see that there is only one saddle point, given by $\zeta_0 = \cos\theta \in \mathbb{R}$, at which

$$\phi(\zeta_0) = ik_1 \quad \text{and} \quad \phi''(\zeta_0) = -\frac{ik_1}{\sin^2\theta}.$$

With reference to equation (A.2) it therefore follows that the directions of steepest descent at the saddle point are given by $\alpha_p = -\alpha/2 + (2p+1)\pi/2$, $p = 0, 1$, where $\alpha = \arg\phi''(\zeta_0) = -\pi/2$ (here we select $\arg z \in (-\pi, \pi]$). Clearly, $\alpha_0 = 3\pi/4$ and $\alpha_1 = -\pi/4$.

In oder to asymptotically determine the path of steepest descent passing through ζ_0 we observe that for large values of $|\zeta|$ with ζ in the first or fourth quadrants we have $\sqrt{\zeta^2 - 1} \sim \zeta$.

Consequently, the phase function satisfies

$$\phi(\zeta) = k_1 \zeta \left(-\sin\theta + i\cos\theta\right) + \mathcal{O}(|\zeta|^{-1})$$

$$= -k_1 \left\{\sin\theta \operatorname{Re}\zeta + \cos\theta \operatorname{Im}\zeta\right\} + ik_1 \left\{\cos\theta \operatorname{Re}\zeta - \sin\theta \operatorname{Im}\zeta\right\} + \mathcal{O}(|\zeta|^{-1}).$$

Since on the path of steepest descent, which is denoted by D, the imaginary part of ϕ remains constant and equal to k_1, we conclude that D approaches the line

$$\operatorname{Im}\zeta = \frac{\cos\theta}{\sin\theta}\operatorname{Re}\zeta - \frac{1}{\sin\theta} \quad \text{as} \quad |\zeta| \to \infty,$$

for $\operatorname{Re}\zeta > 0$. For large values of $|\zeta|$, with ζ in the second or third quadrants, on the other hand, we have $\sqrt{\zeta^2 - 1} \sim -\zeta$. Thus, in this case we obtain that the steepest descent path approaches the line

$$\operatorname{Im}\zeta = -\frac{\cos\theta}{\sin\theta}\operatorname{Re}\zeta + \frac{1}{\sin\theta} \quad \text{as} \quad |\zeta| \to \infty,$$

for $\operatorname{Re}\zeta < 0$.

This analysis implies that D intersects the real axis at two points; at the saddle point $\zeta = \cos\theta$, of course, and at $\zeta = 1/\cos\theta$, where the latter was obtained by noting that

$$\phi\left(\frac{1}{\cos\theta}\right) = -k_1\frac{\sin^2\theta}{|\cos\theta|} + ik_1.$$

The paths of steepest descent for the cases $x > 0$ and $x < 0$, are depicted in Figure 2.3.

From (A.2) it follows directly that, provided g_T and g_R are continuous and do not vanish at the point $\zeta = \zeta_0$, the saddle point contribution to the asymptotic expansion of (2.46a) as $|\boldsymbol{r}| \to \infty$ is given by

$$G_R^{(1)}(\boldsymbol{r}, \boldsymbol{r}') = \frac{i}{4\pi}\frac{\sin\theta - i\nu\sqrt{\cos^2\theta - n^2}}{\sin\theta + i\nu\sqrt{\cos^2\theta - n^2}}\sqrt{\frac{2\pi}{k_1|\boldsymbol{r}|}}\, \mathrm{e}^{-i|\boldsymbol{r}'|k_1\cos(\theta+\theta')}\, \mathrm{e}^{ik_1|\boldsymbol{r}|-i\pi/4}, \qquad (2.48a)$$

while the saddle point contribution to the asymptotic expansion of (2.46b) as $|\boldsymbol{r}| \to \infty$ is

given by

$$G_T^{(1)}(\boldsymbol{r}, \boldsymbol{r}') = \frac{i\nu}{2\pi} \frac{\sin\theta \, e^{-ik_1|\boldsymbol{r}'|(\cos\theta\cos\theta' + i\sqrt{\cos^2\theta - n^2}\sin\theta')}}{\sin\theta + i\nu\sqrt{\cos^2\theta - n^2}} \sqrt{\frac{2\pi}{k_1|\boldsymbol{r}|}} \, e^{ik_1|\boldsymbol{r}| - i\pi/4}. \tag{2.48b}$$

There are, however, four potential saddle points which are concurrently branch points at which this assumption is certainly not true. These are $\zeta_0 = \pm n$ and $\zeta_0 = \pm 1$.

In the case of a saddle point given by $\zeta_0 = \pm n$ it can be shown that the integrands g_R and g_T can be expressed as $p(\zeta) + q(\zeta)(\zeta - \zeta_0)^{1/2}$, where p and q are analytic functions in a neighborhood of ζ_0. Thus, from (A.3) we readily check that formulae (2.48) still remain valid in this case.

A saddle point given by $\zeta_0 = \cos\theta = \pm 1$, on the other hand, presents an additional difficulty, as the phase function ceases to be analytic at those points. Nevertheless, formulae (2.48) remain valid for $\theta = 0, \pi$ for as a long as $\theta' \neq 0, \pi$. This can be proved by applying the steepest descents method to obtain the leading order terms of the expansions of G_R as $|\boldsymbol{r} - \overline{\boldsymbol{r}}'| \to \infty$ and G_T as $|\boldsymbol{r} - \boldsymbol{r}'| \to \infty$ first, and subsequently using the fact that $|\boldsymbol{r} - \boldsymbol{p}| = |\boldsymbol{r}| - \frac{\boldsymbol{r} \cdot \boldsymbol{p}}{|\boldsymbol{r}|} + \mathcal{O}\left(\frac{1}{|\boldsymbol{r}|}\right)$ as $|\boldsymbol{r}| \to \infty$, where $\boldsymbol{p} = \overline{\boldsymbol{r}}'$ in the case of G_R and $\boldsymbol{p} = \boldsymbol{r}'$ in the case of G_T.

Polar singularities. We next consider the possibility of contributions to the asymptotic expansions of G_R and G_T due to poles of the functions g_R and g_T, respectively, which could arise when such poles happen to lie inside the region bounded by the ζ-real-axis to the path of steepest descent D. From (2.47) it follows that the possible poles of g_T and g_R must be given by the solutions of the algebraic equation

$$(\zeta^2 - 1) - \nu^2(\zeta^2 - n^2) = 0. \tag{2.49}$$

Clearly, solutions to this equation exist only when $\nu \neq \pm 1$ and are given by

$$\zeta = \pm\sqrt{\frac{n^2\nu^2 - 1}{\nu^2 - 1}}. \tag{2.50}$$

Thus, in view of (2.50), in the case of a real wavenumber k_2 the solutions of (2.49) are either real or imaginary.

Assume for the time being that both poles are real. In order for the denominator $\sqrt{\zeta^2 - 1} + \nu\sqrt{\zeta^2 - n^2} = [\gamma_1(\zeta k_1) + \nu\gamma_2(\zeta k_1)]/k_1$ to vanish, both $\gamma_1(\zeta k_1)$ and $\gamma_2(\zeta k_1)$ have to be either purely real or purely imaginary. If both are real, we have, by the definition of the functions γ_j, $j = 1, 2$, that $\gamma_j(\zeta k_1) \geq 0$. Therefore, they can not cancel each other. If both are imaginary, in turn, we have that $\operatorname{Im}\gamma_j(\zeta k_1) \leq 0$, and thus, again, they can not cancel each other. Therefore, the functions g_T and g_R do not have poles on the real axis.

Let us now consider the possibility of imaginary poles. By the definition of γ_j, $j = 1, 2$, we can easily check that $-3\pi/4 \leq \arg\gamma_j(\pm itk_1) \leq -\pi/4$, $t > 0$, which means that both complex numbers $\gamma_j(\pm itk_1)$, $j = 1, 2$, lie on the same half-plane in the complex plane. Therefore, we conclude that g_R and g_T do not have pole singularities in the complex plane when $k_2 \in \mathbb{R}$.

We now consider the possibility of pole singularities of g_R and g_T for a complex wavenumber $k_2 \in \mathbb{C}$, $\operatorname{Im}k_2 > 0$ in TM polarization in the case of a non-magnetic medium, i.e., $\mu_1 = \mu_2 = \mu_0$. (Since $\nu = 1$ in TE polarization, there are no poles of g_T and g_R in this case). Note that we are allowing the permittivity of the lower half-plane to be such that $\operatorname{Re}\varepsilon_2 < 0$, which, as matter of fact, corresponds to feasible physical values for highly conducting metals at low frequency [83].

Under the aforementioned assumptions we have that $\nu = \varepsilon_1/\varepsilon_2 = 1/\varepsilon_r$ and $n^2 = k_2^2/k_1^2 = \varepsilon_2/\varepsilon_1 = 1/\nu = \varepsilon_r$, where $\varepsilon_r = \varepsilon_2/\varepsilon_1 = |\varepsilon_r|\,e^{i\alpha}$, $\alpha \in (0, \pi)$. Replacing these identities in (2.50) we obtain that the solutions of (2.49) are given by $\zeta = \pm\zeta_p$, where

$$\zeta_p = \sqrt{\frac{1}{\nu + 1}} = \sqrt{\frac{\varepsilon_2}{\varepsilon_1 + \varepsilon_2}} = \sqrt{\frac{\varepsilon_r}{\varepsilon_r + 1}}.$$

Since $1 + \varepsilon_r = |1 + \varepsilon_r|\,e^{i\beta}$, $\beta \in (0, \alpha)$, we obtain

$$\zeta_p = \sqrt{\frac{\varepsilon_r}{1 + \varepsilon_r}} = \sqrt{\frac{|\varepsilon_r|}{|1 + \varepsilon_r|}}\,e^{i(\alpha - \beta)/2},$$

which implies that $\zeta = \zeta_p$ and $\zeta = -\zeta_p$ lie in the first and third quadrants respectively. In

order for ζ_p to be a pole of g_R and g_T then, we need the condition $\gamma_1(\zeta_p k_1) + \nu\gamma_2(\zeta_p k_2) = 0$ to be satisfied. Under the present definition of the functions γ_j, $j = 1, 2$ we have

$$\gamma_1(\zeta_p k_1) = k_1\sqrt{\zeta_p^2 - 1} = \begin{cases} ik_1\dfrac{\zeta_p}{\sqrt{\varepsilon_r}} & \text{if } \varepsilon_r \in R_1^+, \\[2ex] -ik_1\dfrac{\zeta_p}{\sqrt{\varepsilon_r}} & \text{if } \varepsilon_r \in R_1^-, \end{cases} \tag{2.51}$$

and

$$\gamma_2(\zeta_p k_1) = k_1\sqrt{\zeta_p^2 - \varepsilon_r} = \begin{cases} ik_1\zeta_p\sqrt{\varepsilon_r} & \text{if } \varepsilon_r \in R_2^+, \\[2ex] -ik_1\zeta_p\sqrt{\varepsilon_r} & \text{if } \varepsilon_r \in R_2^-, \end{cases} \tag{2.52}$$

where the connected regions $R_j^\pm$ are such that $R_j^+ \cap R_j^- = \emptyset$, $R_j^+ \cup R_j^- = \{z \in \mathbb{C} : \operatorname{Im} z > 0\}$, $j = 1, 2$.

Thus, in order for ζ_p to be a pole of g_R and g_T, it is necessary that $\zeta_p \in R_1^+ \cap R_2^-$ or $\zeta_p \in R_1^- \cap R_2^+$. Clearly, such conditions lead to

$$\gamma_1(\zeta_p k_1) + \nu\gamma_2(\zeta_p k_1) = ik_1\frac{\zeta_p}{\sqrt{\varepsilon_r}} - \frac{ik_1}{\varepsilon_r}\zeta_p\sqrt{\varepsilon_r} = 0.$$

As is well-documented [90, 131], the poles $\pm\zeta_p$ of the layer Green function in spectral form, which are known in the literature as Sommerfeld poles, depend on definition of γ_j, $j = 1, 2$. When present, a Sommerfeld pole may give rise to a surface-wave of the form $u_{\zeta_p}(\boldsymbol{r}) = c\,e^{ik_1\zeta_p|x| - ik_1\zeta_p/\sqrt{\varepsilon_r}y}$ in the asymptotic expansion of G_R and G_T. In order for this surface-wave to be physically meaningful, it is necessary that $\zeta_p \in R_1^+$; otherwise u_{ζ_p} does not satisfy the radiation condition. This surface-wave has historically received various names (Zeneck wave, surface plasmon polariton, Brewster mode, or Fano mode) depending on the values of the real and imaginary parts of ε_r [90]. In any case, it is clear that u_{ζ_p} decays exponentially fast as $|\boldsymbol{r}| = \sqrt{x^2 + y^2} \to \infty$, in virtue of the fact that $\operatorname{Im}\zeta_p > 0$ and $\operatorname{Im}(\zeta_p/\sqrt{\varepsilon_r}) < 0$. Therefore, these poles do not give to rise to contributions to the leading order asymptotic expansion of the layer Green function as $|\boldsymbol{r}| \to \infty$.

Branch points. In order to assess the asymptotic contribution of the branch points to the overall value of the integrals in (2.46), we distinguish three cases: Case (a): $|\cos\theta| < \operatorname{Re} n < |\cos\theta|^{-1}$, Case (b): $\operatorname{Re} n < |\cos\theta|$, and Case (c): $\operatorname{Re} n > |\cos\theta|^{-1}$. The integration paths for each of these case are shown in Figure 2.3.

It is clear that Case (a) leads to no additional contributions from the branch points, as the path of steepest descent D does not cross the branch cuts stemming from the branch points at $\zeta = \pm n$.

In Cases (b) and (c), in turn, the steepest descent path may or may not cross the branch cut starting at the branch point $\zeta = n$ (resp. $\zeta = -n$) when $\cos\theta > 0$ (resp. $\cos\theta < 0$), depending on how large $\operatorname{Im} n$ is. When it does, D has to be locally deformed around the branch cut, as it is shown in Figure 2.3b and 2.3c. The new path encompasses two new critical points, A and B, and an additional finite-length path around the branch cut. Since A and B lie in the valley of the phase function, it is easy to show that their contributions to integrals over the paths to left of A and to the right of B result in exponentially decaying terms as $|\boldsymbol{r}| \to \infty$. As is pointed out by Bleistein [15, Section 8.1, page 249], on the other hand, it can be shown that the paths from the branch point $\zeta = n$, which are parallel to the branch cut, are paths of descent. Therefore, the path integrals around the branch cut can be analyzed by considering the branch point as an additional critical point (since paths of descent and paths of steepest descent are asymptotically equivalent).

In order to evaluate the integrals around the branch cut from $\zeta = n$, we need to first determine the jumps of g_R and g_T across the branch cut stemming from $\zeta = n$. Letting $\zeta^+ = n + it + 0^+$ and $\zeta^- = n + it + 0^-$, $t > 0$, denote points on the right and on the left of the branch cut respectively, it follows from the definition of γ_2 (cf. Figure 2.2) that

$$\sqrt{(\zeta^+)^2 - n^2} = -\sqrt{(\zeta^-)^2 - n^2},$$

thus, setting $\zeta = n + 0^+ + it$, $t > 0$, the jumps of g_R and g_T at the branch cut are given by

$$[g_R](\zeta) = g_R(\zeta^+) - g_R(\zeta^-) = \frac{4\nu i \sqrt{\zeta^2 - n^2}\, e^{-i|\boldsymbol{r}'|k_1(\zeta\cos\theta' - i\sqrt{\zeta^2-1}\sin\theta')}}{\zeta^2(1-\nu^2) + \nu^2 n^2 - 1}$$
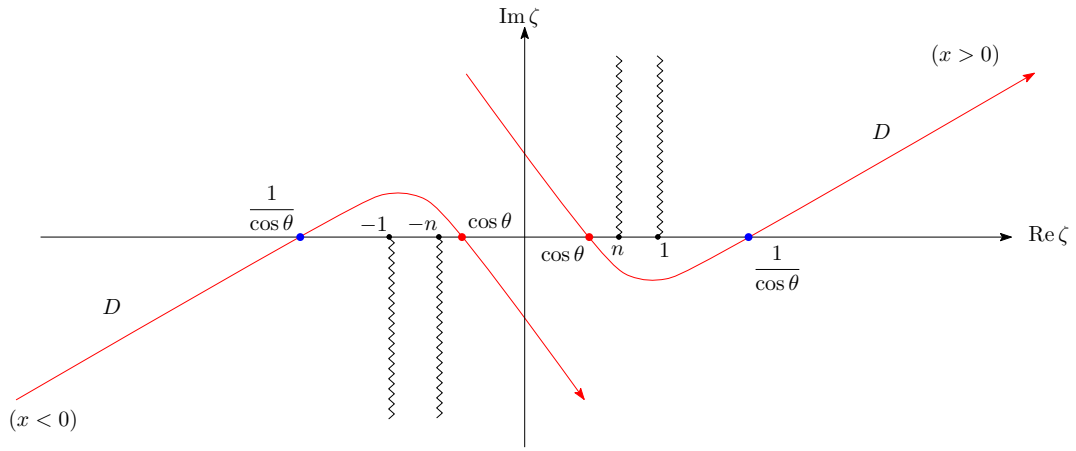
(a) $|\cos\theta| < n < |\cos\theta|^{-1}$.
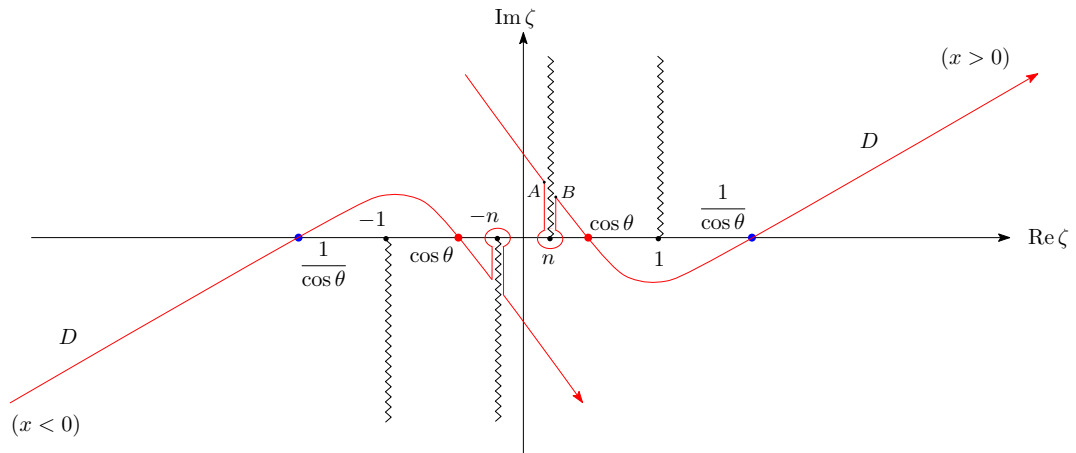
(b) $n < |\cos\theta|$.
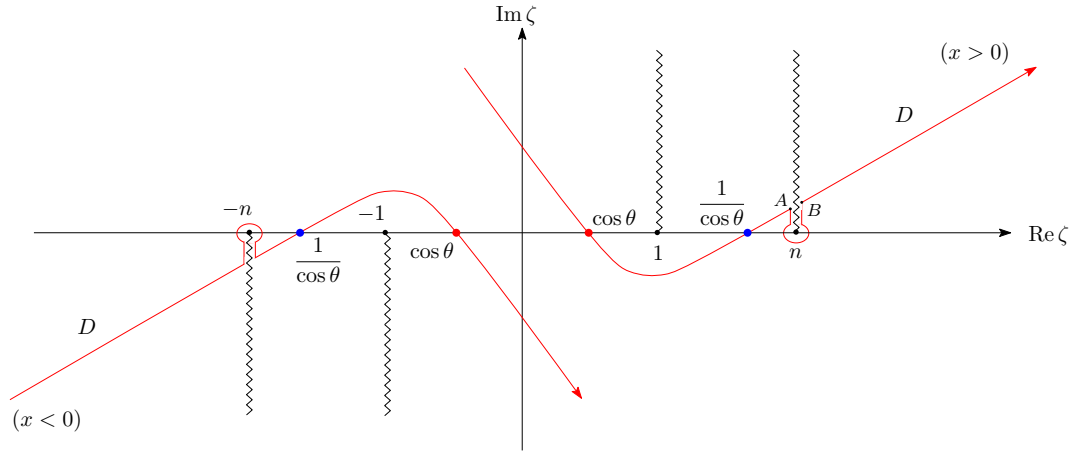
(c) $n > |\cos\theta|^{-1}$.

Figure 2.3: Paths of descent for the integrals (2.46). The saddle points are marked by red dots.

and

$$[g_T](\zeta) = g_T(\zeta^+) - g_T(\zeta^-)$$

$$= \left[\frac{e^{-ik_1|\boldsymbol{r}'|i\sqrt{\zeta^2-n^2}\sin\theta'}}{i\sqrt{\zeta^2-1}+\nu i\sqrt{\zeta^2-n^2}} - \frac{e^{ik_1|\boldsymbol{r}'|i\sqrt{\zeta^2-n^2}\sin\theta'}}{i\sqrt{\zeta^2-1}-\nu i\sqrt{\zeta^2-n^2}} \right] e^{-ik_1|\boldsymbol{y}|\zeta\cos\theta'}$$

respectively. Clearly the jumps satisfy

$$[g_R](\zeta) \sim \frac{4\nu i\sqrt{2n}\,e^{-i|\boldsymbol{y}|k_1(n\cos\theta'-i\sqrt{n^2-1}\sin\theta')}}{n^2-1}(\zeta-n)^{1/2} \quad \text{and}$$

$$[g_T](\zeta) \sim \frac{2\nu i\sqrt{2n}}{n^2-1}e^{-ik_1|\boldsymbol{y}|n\cos\theta'}(\zeta-n)^{1/2} \quad \text{as} \quad \zeta \to n, \tag{2.53}$$

Thus, the contribution of the branch point can be evaluated using formula (A.4) with

$$\alpha = \frac{\pi}{2}, \quad \beta = \frac{3}{2}, \quad n = \cos\theta_c, \quad \phi(n) = ik_1\cos(\theta_c-\theta), \quad \phi'(n) = ik_1\frac{\sin(\theta_c-\theta)}{\sin\theta_c},$$

which yields

$$G_R^{(2)}(\boldsymbol{r},\boldsymbol{r}') = \frac{i\nu\sqrt{\cot\theta_c}}{\sqrt{2\pi}\,[k_1|\boldsymbol{r}||\sin(\theta_c-\theta)|]^{3/2}}\,e^{-i|\boldsymbol{r}'|k_1\cos(\theta_c+\theta')}\,e^{ik_1|\boldsymbol{r}|\cos(\theta_c-\theta)-i\pi/4} \tag{2.54a}$$

and

$$G_T^{(2)}(\boldsymbol{r},\boldsymbol{r}') = \frac{i\nu^2\sqrt{\cot\theta_c}\,e^{-ik_1|\boldsymbol{r}'|\cos\theta_c\cos\theta'}}{\sqrt{2\pi}\,[k_1|\boldsymbol{r}||\sin(\theta_c-\theta)|]^{3/2}}\,e^{ik_1|\boldsymbol{r}|\cos(\theta_c-\theta)+i\pi/4}. \tag{2.54b}$$

Similarly, it can be shown that formulae in (2.54) remain valid when $\cos\theta < 0$, except that in this case θ_c is such that $\cos\theta_c = -n$.

Source and observation points at the interface. There is only one case left to be considered, which corresponds to the situation for which the observation and source points lie at the interface between the two half-planes. In this case the integrals (2.46) with $\boldsymbol{r} = (x,0)$

and $\boldsymbol{r}' = (x', 0)$ coincide with the Fourier integrals

$$
\begin{aligned}
G_R(\boldsymbol{r}, \boldsymbol{r}') &= \frac{1}{4\pi} \int_{-\infty}^{\infty} \frac{\sqrt{\zeta^2 - 1} - \nu\sqrt{\zeta^2 - n^2}}{\sqrt{\zeta^2 - 1} + \nu\sqrt{\zeta^2 - n^2}} \frac{e^{ik_1\zeta(x-x')}}{\sqrt{\zeta^2 - 1}} \, d\zeta, \\
G_T(\boldsymbol{r}, \boldsymbol{r}') &= \frac{\nu}{2\pi} \int_{-\infty}^{\infty} \frac{e^{ik_1\zeta(x-x')}}{\sqrt{\zeta^2 - 1} + \nu\sqrt{\zeta^2 - n^2}} \, d\zeta.
\end{aligned}
\tag{2.55}
$$

A direct application of Jordan's lemma yields that the integration contour (the real axis) can be deformed into the paths depicted in Figure 2.4, depending of the sign of $x - x'$, without changing the value of the integral. By doing so we obtain

$$
\begin{aligned}
G_R(\boldsymbol{r}, \boldsymbol{r}') &= -\frac{\nu}{\pi} e^{ik_2|x-x'|} \int_0^{\infty} \frac{\sqrt{t - 2in}\sqrt{t}}{(\nu^2 - 1)(t - in)^2 + n^2\nu^2 - 1} e^{-k_1 t|x-x'|} \, dt \\
&\quad + \frac{i}{2\pi} e^{ik_1|x-x'|} \int_0^{\infty} \frac{(1 + \nu^2)(t - i)^2 + 1 + n^2\nu^2}{(1 - \nu^2)(t - i)^2 + 1 - n^2\nu^2} \frac{e^{-k_1 t|x-x'|}}{\sqrt{2i - t}\sqrt{t}} \, dt, \\
G_T(\boldsymbol{r}, \boldsymbol{r}') &= -\frac{\nu^2}{\pi} e^{ik_2|x-x'|} \int_0^{\infty} \frac{\sqrt{t - 2in}\sqrt{t}}{(\nu^2 - 1)(t - in)^2 + n^2\nu^2 - 1} e^{-k_1 t|x-x'|} \, dt \\
&\quad - \frac{\nu}{\pi} e^{ik_1|x-x'|} \int_0^{\infty} \frac{\sqrt{t - 2i}\sqrt{t}}{(1 - \nu^2)(t - i)^2 + 1 - n^2\nu^2} e^{-k_1 t|x-x'|} \, dt.
\end{aligned}
$$
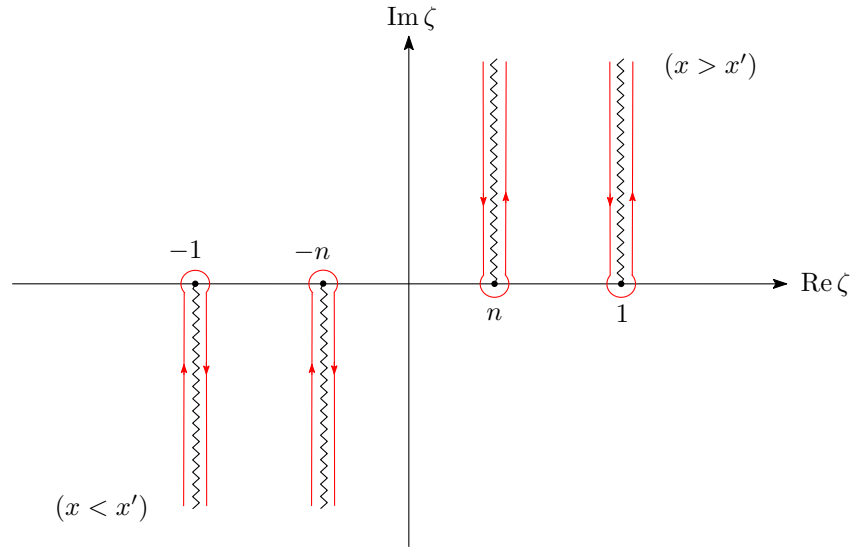
Figure 2.4: Integration paths used in the evaluation of the integrals (2.55).

Each one of these Laplace integrals can be analyzed in the light of Watson's lemma [15],

which yields

$$
G_R(\boldsymbol{r}, \boldsymbol{r}') = e^{ik_2|x-x'|} \sum_{n=0}^{\infty} \frac{a_n \Gamma(n+3/2)}{(k_1|x-x'|)^{n+3/2}} + e^{ik_1|x-x'|} \sum_{n=0}^{\infty} \frac{b_n \Gamma(n+1/2)}{(k_1|x-x'|)^{n+1/2}},
$$

$$
G_T(\boldsymbol{r}, \boldsymbol{r}') = e^{ik_2|x-x'|} \sum_{n=0}^{\infty} \frac{c_n \Gamma(n+3/2)}{(k_1|x-x'|)^{n+3/2}} + e^{ik_1|x-x'|} \sum_{n=0}^{\infty} \frac{d_n \Gamma(n+3/2)}{(k_1|x-x'|)^{n+3/2}}
$$

as $|x - x'| \to \infty$. In particular, the leading order asymptotic expansions of the integrals in (2.55) are given by

$$
G_R(\boldsymbol{r}, \boldsymbol{r}') \sim \frac{i\nu\sqrt{n}}{\sqrt{2\pi}(1-n^2)} \frac{e^{ik_2|x-x'|+i\pi/4}}{(k_1|x-x'|)^{3/2}} - \frac{i}{\sqrt{8\pi k_1|x-x'|}} e^{ik_1|x-x'|-i\pi/4}, \quad (2.56\text{a})
$$

$$
G_T(\boldsymbol{r}, \boldsymbol{r}') \sim \frac{i\nu^2\sqrt{n}}{\sqrt{2\pi}(1-n^2)} \frac{e^{ik_2|x-x'|+i\pi/4}}{(k_1|x-x'|)^{3/2}} - \frac{i}{\nu\sqrt{2\pi}(n^2-1)} \frac{e^{ik_1|x-x'|+i\pi/4}}{(k_1|x-x'|)^{3/2}}, \quad (2.56\text{b})
$$

as $|x - x'| \to \infty$.

Far-field form of the layer Green function in two-dimensions. The analysis carried out above in this section demonstrates that whenever either the source point or the observation point is away from the interface, the leading order asymptotic expansions of G_R and G_T are given by the sole contribution of the saddle point at $\xi = k_1\zeta = k_1\cos\theta$—since all contributions arising from the deformation of the steepest descent path around the branch cuts decay faster than $|\boldsymbol{r}|^{-1/2}$ as $|\boldsymbol{r}| \to \infty$. (In view of (2.54) the contribution of the branch point decays as $|\boldsymbol{r}|^{-3/2}$ for $n > 0$ and it decays exponentially fast for $n \in \mathbb{C}$, $\operatorname{Im} n > 0$.) Additionally, it is easy to check that for $\boldsymbol{r} = (x, 0)$ and $\boldsymbol{r}' = (x', 0)$, the expressions $G_R^{(1)}(\boldsymbol{r}, \boldsymbol{r}')$ and $G_T^{(1)}(\boldsymbol{r}, \boldsymbol{r}')$ in (2.48) coincide to leading order with the expressions (2.56). We thus conclude that

$$
G_R(\boldsymbol{r}, \boldsymbol{r}') \sim \frac{\sin\theta - i\nu\sqrt{\cos^2\theta - n^2}}{\sin\theta + i\nu\sqrt{\cos^2\theta - n^2}} \sqrt{\frac{1}{8\pi k_1|\boldsymbol{r}|}} e^{ik_1(|\boldsymbol{r}| - \widehat{\boldsymbol{r}} \cdot \overline{\boldsymbol{r}}') + i\pi/4}
$$

$$
\times \left\{ 1 + \mathcal{O}\left(\frac{1}{|\boldsymbol{r}|}\right) \right\}, \quad \boldsymbol{r}, \boldsymbol{r}' \in D_1, \tag{2.57a}
$$

and

$$G_T(\boldsymbol{r}, \boldsymbol{r}') \sim \frac{\nu \sin\theta \, \mathrm{e}^{ik_1(\sin\theta - i\sqrt{\cos^2\theta - n^2})y'}}{\sin\theta + i\nu\sqrt{\cos^2\theta - n^2}} \sqrt{\frac{1}{2\pi k_1|\boldsymbol{r}|}} \, \mathrm{e}^{ik_1(|\boldsymbol{r}| - \hat{\boldsymbol{r}} \cdot \boldsymbol{r}') + i\pi/4}$$
$$\times \left\{ 1 + \mathcal{O}\left(\frac{1}{|\boldsymbol{r}|}\right) \right\}, \quad \boldsymbol{r} \in D_1, \boldsymbol{r}' \in D_2, \tag{2.57b}$$

as $|\boldsymbol{r}| \to \infty$, where $\boldsymbol{r} = |\boldsymbol{r}|(\cos\theta, \sin\theta) = |\boldsymbol{r}|\hat{\boldsymbol{r}}$, $\theta \in [0, \pi]$, $\boldsymbol{r}' = (x', y')$, $\overline{\boldsymbol{r}}' = (x', -y')$ and $n = k_2/k_1$.

Applying a similar analysis to each of the derivatives of G_R and G_T, we obtain

$$\nabla_{\boldsymbol{r}'} G_R(\boldsymbol{r}, \boldsymbol{r}') \sim \frac{\sin\theta - i\nu\sqrt{\cos^2\theta - n^2}}{\sin\theta + i\nu\sqrt{\cos^2\theta - n^2}} \sqrt{\frac{k_1}{8\pi|\boldsymbol{r}|}} \, \mathrm{e}^{ik_1(|\boldsymbol{r}| - \hat{\boldsymbol{r}} \cdot \overline{\boldsymbol{r}}') - i\pi/4} \begin{bmatrix} \cos\theta \\ -\sin\theta \end{bmatrix} \left\{ 1 + \mathcal{O}\left(\frac{1}{|\boldsymbol{r}|}\right) \right\}, \tag{2.58a}$$

for $\boldsymbol{r}, \boldsymbol{r}' \in D_1$, and

$$\nabla_{\boldsymbol{r}'} G_T(\boldsymbol{r}, \boldsymbol{r}') \sim \frac{\nu \sin\theta \, \mathrm{e}^{ik_1(\sin\theta - i\sqrt{\cos^2\theta - n^2})y'}}{\sin\theta + i\nu\sqrt{\cos^2\theta - n^2}} \sqrt{\frac{k_1}{2\pi|\boldsymbol{r}|}} \, \mathrm{e}^{ik_1(|\boldsymbol{r}| - \hat{\boldsymbol{r}} \cdot \boldsymbol{r}') - i\pi/4}$$
$$\times \begin{bmatrix} \cos\theta \\ i\sqrt{\cos^2\theta - n^2} \end{bmatrix} \left\{ 1 + \mathcal{O}\left(\frac{1}{|\boldsymbol{r}|}\right) \right\}, \tag{2.58b}$$

for $\boldsymbol{r} \in D_1$ and $\boldsymbol{r}' \in D_2$, as $|\boldsymbol{r}| \to \infty$.

Therefore, the far field of the layer Green function and its gradient in the direction $\hat{\boldsymbol{r}} = (\cos\theta, \sin\theta)$, $\theta \in (0, \pi)$ are given by the expressions

$$G_\infty(\hat{\boldsymbol{r}}, \boldsymbol{r}') = \frac{\mathrm{e}^{i\pi/4}}{\sqrt{8\pi k_1}} \begin{cases} \mathrm{e}^{-ik_1\hat{\boldsymbol{r}} \cdot \boldsymbol{r}'} + \dfrac{\sin\theta - i\nu\sqrt{\cos^2\theta - n^2}}{\sin\theta + i\nu\sqrt{\cos^2\theta - n^2}} \mathrm{e}^{-ik_1\hat{\boldsymbol{r}} \cdot \overline{\boldsymbol{r}}'}, & \boldsymbol{r}' \in D_1, \\[4mm] \dfrac{2\nu \sin\theta \, \mathrm{e}^{ik_1(\sin\theta - i\sqrt{\cos^2\theta - n^2})y'}}{\sin\theta + i\nu\sqrt{\cos^2\theta - n^2}} \mathrm{e}^{-ik_1\hat{\boldsymbol{r}} \cdot \boldsymbol{r}'}, & \boldsymbol{r}' \in D_2, \end{cases} \tag{2.59}$$

and

$$\boldsymbol{H}_\infty(\hat{\boldsymbol{r}}, \boldsymbol{r}') = \sqrt{\frac{k_1}{8\pi}}\, \mathrm{e}^{-i\pi/4} \begin{cases} \mathrm{e}^{-ik_1\hat{\boldsymbol{r}}\cdot\boldsymbol{r}'}\,\hat{\boldsymbol{r}} + \dfrac{\sin\theta - i\nu\sqrt{\cos^2\theta - n^2}}{\sin\theta + i\nu\sqrt{\cos^2\theta - n^2}}\,\mathrm{e}^{-ik_1\hat{\boldsymbol{r}}\cdot\bar{\boldsymbol{r}}'} \\ \qquad\qquad \times \begin{bmatrix} \cos\theta \\ -\sin\theta \end{bmatrix}, & \boldsymbol{r}' \in D_1, \\[2em] \dfrac{2\nu\sin\theta\,\mathrm{e}^{ik_1(\sin\theta - i\sqrt{\cos^2\theta - n^2})y'}}{\sin\theta + i\nu\sqrt{\cos^2\theta - n^2}}\,\mathrm{e}^{-ik_1\hat{\boldsymbol{r}}\cdot\boldsymbol{r}'} \\ \qquad\qquad \times \begin{bmatrix} \cos\theta \\ i\sqrt{\cos^2\theta - n^2} \end{bmatrix}, & \boldsymbol{r}' \in D_2, \end{cases} \tag{2.60}$$

respectively.

The corresponding far-field patterns of the layer Green function and its gradient in a direction $\hat{\boldsymbol{r}} = (\cos\theta, \sin\theta)$, $\theta \in (-\pi, 0)$ can be easily obtained from (2.59) and (2.60) utilizing the identity in (2.28).

Remark 2.3.2. *Note that in view of formulae (2.57) and (2.58), both terms G_R and G_T satisfy the Sommerfeld radiation condition at infinity (2.20b) for observation points $\boldsymbol{r} \in D_1$ in the upper half-plane. Since the free-space Green function satisfies the radiation condition, it follows from (2.27) that the layer Green function G satisfies the radiation condition at infinity for observation points $\boldsymbol{r} \in D_1$. Similarly, it can shown that the layer Green function satisfies the radiation condition for observation points $\boldsymbol{r} \in D_2$ in the lower half-plane.*

Far-field form of the layer Green function in three-dimensions. We now extend the asymptotic analysis presented above in this section to derive the leading order asymptotic expansion of the layer Green function in three-dimensional space. With the exception of of a few details, the asymptotic analysis carried out above for the two-dimensional case is re-utilized here; once again, and without loss of generality, we provide explicit formulae for the reflected and transmitted fields in the upper-half space.

In view of the identity $J_0(z) = \frac{1}{2}\left(H_0^{(1)}(z) + H_0^{(1)}(-z)\right)$, $-\pi < \arg z \le \pi$ [76], the Hankel

transform of an even function $\widehat{g}$ can be expressed as

$$\int_0^\infty \widehat{g}(\xi)J_0(\xi\rho)\xi\,\mathrm{d}\xi = \frac{1}{2}\int_C \widehat{g}(\xi)H_0^{(1)}(\xi\rho)\xi\,\mathrm{d}\xi, \tag{2.61}$$

where the integration path C is depicted in Figure 2.5.

Therefore, from the uniform asymptotic expansion of the Hankel function [76],

$$H_0^{(1)}(z) = \left(\frac{2}{\pi z}\right)^{1/2} \mathrm{e}^{i(z-\pi/4)}\left[\sum_{k=0}^n \frac{\Gamma^2(k+1/2)}{\pi k!(2zi)^k} + \mathcal{O}(|z|^{-n-1})\right] \quad \text{as} \quad |z| \to \infty,$$

it follows that the Hankel transform (2.61) satisfies

$$\int_0^\infty \widehat{g}(\xi)J_0(\xi\rho)\xi\,\mathrm{d}\xi = \frac{1}{2}\int_{-\infty}^\infty \widehat{g}(\xi)\sqrt{\frac{2}{\pi\xi\rho}}\,\mathrm{e}^{i(\xi\rho-\pi/4)}\,\xi\,\mathrm{d}\xi\,\{1 + \mathcal{O}(\rho^{-1})\} \quad \text{as} \quad \rho \to \infty. \tag{2.62}$$

Note that the branch cut in the domain of definition of the square root is selected as the negative real axis in the ξ-plane.

Subsequently, letting

$$x - x' = R\cos\beta\cos\alpha, \quad y + |y'| = R\sin\beta, \quad z - z' = R\cos\beta\sin\alpha \tag{2.63}$$

with $\rho = R\cos\beta$ and $\alpha \in [0, 2\pi]$, $\beta \in [0, \pi/2)$, and using (2.62) we obtain that the reflected and transmitted fields in the upper half-plane satisfy

$$G_R(\boldsymbol{r}, \boldsymbol{r}') \sim \frac{1}{8\pi}\sqrt{\frac{2}{\pi R\cos\beta}}\,\mathrm{e}^{-i\pi/4}\int_{-\infty}^\infty \frac{\gamma_1 - \nu\gamma_2}{\gamma_1 + \nu\gamma_2}\frac{\sqrt{\xi}}{\gamma_1}\,\mathrm{e}^{R(i\xi\cos\beta-\gamma_1\sin\beta)}\,\mathrm{d}\xi \tag{2.64a}$$

and

$$G_T(\boldsymbol{r}, \boldsymbol{r}') \sim \frac{\nu}{4\pi}\sqrt{\frac{2}{\pi R\cos\beta}}\,\mathrm{e}^{-i\pi/4}\int_{-\infty}^\infty \frac{\mathrm{e}^{(\gamma_2-\gamma_1)y'}}{\gamma_1 + \nu\gamma_2}\sqrt{\xi}\,\mathrm{e}^{R(i\xi\cos\beta-\gamma_1\sin\beta)}\,\mathrm{d}\xi \tag{2.64b}$$

as $R \to \infty$. Note that $R = |\boldsymbol{r} - \overline{\boldsymbol{r}}'|$ for $\boldsymbol{r}' \in D_1$ and $\overline{\boldsymbol{r}}' = (x', -y', z')$ in the case of the reflected field, and $R = |\boldsymbol{r} - \boldsymbol{r}'|$ for $\boldsymbol{r}' \in D_2$ in the case of the transmitted field. Note also that $\beta \neq \pi/2$ in the definition above, so that $\rho = R\cos\beta > 0$ and thus $\rho \to \infty$ as $R \to \infty$.

Making the change of variable $\xi = k_1\zeta$, the integrals in (2.64) can be expressed as

$$G_R(\boldsymbol{r}, \boldsymbol{r}') \sim \frac{1}{8\pi} \sqrt{\frac{2k_1}{\pi R \cos\beta}} \, \mathrm{e}^{-i\pi/4} \, f_R(R) \quad \text{and} \quad G_T(\boldsymbol{r}, \boldsymbol{r}') \sim \frac{\nu}{4\pi} \sqrt{\frac{2k_1}{\pi R \cos\beta}} \, \mathrm{e}^{-i\pi/4} \, f_T(R),$$

$$(2.65)$$

where, letting

$$g_R(\zeta) = \frac{\sqrt{\zeta^2 - 1} - \nu\sqrt{\zeta^2 - n^2}}{\sqrt{\zeta^2 - 1} + \nu\sqrt{\zeta^2 - n^2}} \frac{\sqrt{\zeta}}{\sqrt{\zeta^2 - 1}}, \quad g_T(\zeta) = \frac{\sqrt{\zeta} \, \mathrm{e}^{-k_1\left(\sqrt{\zeta^2-1} - \sqrt{\zeta^2 - n^2}\right)y'}}{\sqrt{\zeta^2 - 1} + \nu\sqrt{\zeta^2 - n^2}}, \qquad (2.66)$$

and

$$\phi(\zeta) = ik_1(\zeta\cos\beta + i\sqrt{\zeta^2 - 1}\sin\beta),$$

the functions f_R and f_T are given by

$$f_R(R) = \int_C g_R(\zeta) \, \mathrm{e}^{R\phi(\zeta)} \, \mathrm{d}\zeta \quad \text{and} \quad f_T(R) = \int_C g_T(\zeta) \, \mathrm{e}^{R\phi(\zeta)} \, \mathrm{d}\zeta. \qquad (2.67)$$

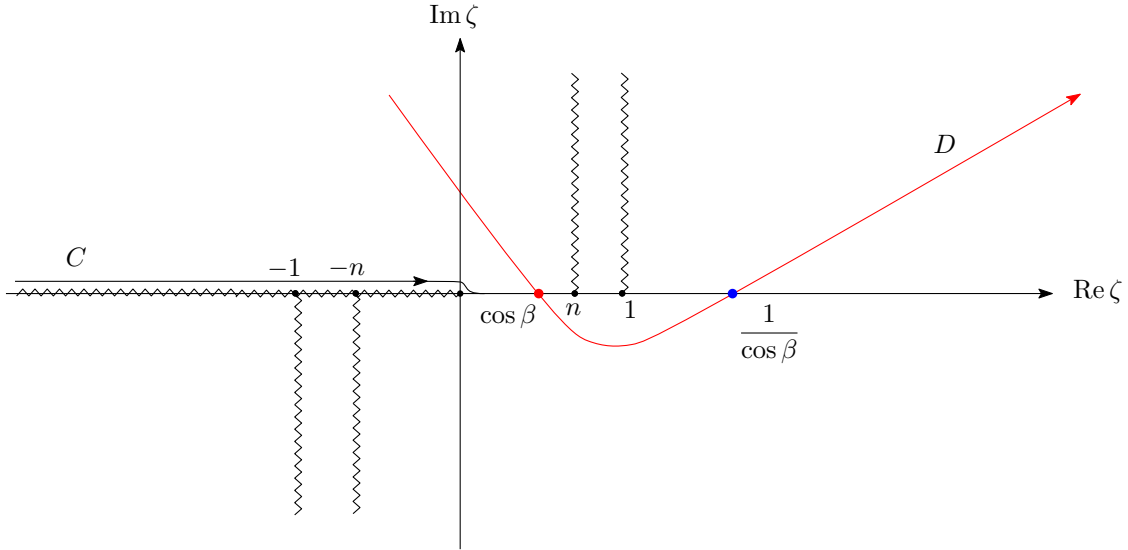Figure 2.5: Integration path C used in the evaluation of the Hankel transform (2.61) and steepest descent path through the saddle point $\zeta = \cos\beta$ utilized in the asymptotic approximation of the integrals (2.67).

In order to find the leading order asymptotic expansion of the integrals in (2.67) as $R \to \infty$, we apply the method of steepest descent summarized in Appendix A. Since, with

the substitution $\theta = \beta$, $\phi = \phi(\beta)$ coincides with the phase function in equation (2.47c), we find that, as in the two-dimensional case considered above in this section, we have 1) The only saddle point occurs at $\zeta = \cos\beta$, and 2) The steepest descent path D that passes through the saddle point is the one depicted in Figure 2.5. The additional branch cut along the negative real axis in the ζ-plane that arises in the present case on account of the $\sqrt{\zeta}$ term in (2.66) presents no difficulties—since, as $\cos\beta > 0$, the steepest descent path does not intersect the negative real axis. Thus, the leading order asymptotic expansions of f_R and f_T are determined by the saddle point contribution that can be evaluated utilizing formula (A.2); the results are

$$
\begin{aligned}
f_R(R) &= \frac{\sin\beta - i\nu\sqrt{\cos^2\beta - n^2}}{\sin\beta + i\nu\sqrt{\cos^2\beta - n^2}}\sqrt{\frac{2\pi\cos\beta}{k_1 R}}\, e^{ik_1 R - i\pi/4}\left\{1 + \mathcal{O}\left(\frac{1}{R}\right)\right\}, \\
f_T(R) &= \frac{\sin\beta\, e^{ik_1(\sin\beta - i\sqrt{\cos^2\beta - n^2})y'}}{\sin\beta + i\nu\sqrt{\cos^2\beta - n^2}}\sqrt{\frac{2\pi\cos\beta}{k_1 R}}\, e^{ik_1 R - i\pi/4}\left\{1 + \mathcal{O}\left(\frac{1}{R}\right)\right\},
\end{aligned}
\tag{2.68}
$$

as $R \to \infty$.

In order to obtain the final form of the leading order asymptotics of the G_R and G_T as $|\boldsymbol{r}| \to \infty$, we note that for a fixed vector $\boldsymbol{p} \in \mathbb{R}^3$ (which will be taken to equal either $\overline{\boldsymbol{r}}'$ or $\boldsymbol{r}'$ in what follows) we have

$$
R = |\boldsymbol{r} - \boldsymbol{p}| = |\boldsymbol{r}|\sqrt{1 - 2\frac{\widehat{\boldsymbol{r}}\cdot\boldsymbol{p}}{|\boldsymbol{r}|} + \frac{|\boldsymbol{p}|^2}{|\boldsymbol{r}|^2}} = |\boldsymbol{r}|\left\{1 - \frac{\widehat{\boldsymbol{r}}\cdot\boldsymbol{p}}{|\boldsymbol{r}|} + \mathcal{O}\left(\frac{1}{|\boldsymbol{r}|^2}\right)\right\} \quad \text{as} \quad |\boldsymbol{r}| \to \infty,
\tag{2.69a}
$$

where $\widehat{\boldsymbol{r}} = \boldsymbol{r}/|\boldsymbol{r}|$. But, letting $\boldsymbol{r} = |\boldsymbol{r}|(\cos\varphi\cos\theta, \sin\theta, \sin\varphi\cos\theta)$ ($\theta \in [0, \pi/2)$, $\varphi \in [0, 2\pi]$), and using (2.69a) with $\boldsymbol{p} = \boldsymbol{r}'$, the second equation in (2.63) yields

$$
\begin{aligned}
\sin\beta &= \left(\sin\theta + \frac{|y'|}{|\boldsymbol{r}|}\right)\left(1 - 2\frac{\widehat{\boldsymbol{r}}\cdot\boldsymbol{r}'}{|\boldsymbol{r}|} + \frac{|\boldsymbol{r}'|^2}{|\boldsymbol{r}|^2}\right)^{-1/2} = \sin\theta + \mathcal{O}\left(\frac{1}{|\boldsymbol{r}|}\right), \\
\cos\beta &= \sqrt{1 - \sin^2\beta} = \cos\theta + \mathcal{O}\left(\frac{1}{|\boldsymbol{r}|}\right) \quad \text{as} \quad |\boldsymbol{r}| \to \infty.
\end{aligned}
\tag{2.69b}
$$

Therefore, replacing the asymptotic expansions (2.69) in (2.68) and subsequently replacing

the resulting expressions for f_R and f_T in (2.65), we obtain

$$
G_R(\boldsymbol{r}, \boldsymbol{r}') \sim \frac{1}{4\pi} \frac{\sin\theta - i\nu\sqrt{\cos^2\theta - n^2}}{\sin\theta + i\nu\sqrt{\cos^2\theta - n^2}} \, \mathrm{e}^{-ik_1\widehat{\boldsymbol{r}}\cdot\overline{\boldsymbol{r}}'} \, \frac{\mathrm{e}^{ik_1|\boldsymbol{r}|}}{|\boldsymbol{r}|} \left\{ 1 + \mathcal{O}\left(\frac{1}{|\boldsymbol{r}|}\right) \right\}, \quad \boldsymbol{r}, \boldsymbol{r}' \in D_1,
$$

(2.70a)

and

$$
G_T(\boldsymbol{r}, \boldsymbol{r}') \sim \frac{\nu}{2\pi} \frac{\sin\theta \, \mathrm{e}^{ik_1(\sin\theta - i\sqrt{\cos^2\theta - n^2})y'}}{\sin\theta + i\nu\sqrt{\cos^2\theta - n^2}} \, \mathrm{e}^{-ik_1\widehat{\boldsymbol{r}}\cdot\boldsymbol{r}'} \, \frac{\mathrm{e}^{ik_1|\boldsymbol{r}|}}{|\boldsymbol{r}|}
$$
$$
\times \left\{ 1 + \mathcal{O}\left(\frac{1}{|\boldsymbol{r}|}\right) \right\}, \quad \boldsymbol{r} \in D_1, \boldsymbol{r}' \in D_2,
$$

(2.70b)

where $\boldsymbol{r}' = (x', y', z')$, $\overline{\boldsymbol{r}}' = (x', -y', z')$ and $\boldsymbol{r} = |\boldsymbol{r}|(\cos\theta\cos\varphi, \sin\theta, \cos\theta\sin\varphi)$.

A similar procedure yields the far-field form of the gradients of G_R and G_T with respect to $\boldsymbol{r}'$ and $\boldsymbol{r}$; the results are

$$
\nabla_{\boldsymbol{r}'} G_R(\boldsymbol{r}, \boldsymbol{r}') \sim \frac{ik_1}{4\pi} \frac{\sin\theta - i\nu\sqrt{\cos^2\theta - n^2}}{\sin\theta + i\nu\sqrt{\cos^2\theta - n^2}} \frac{\mathrm{e}^{ik_1(|\boldsymbol{r}| - \widehat{\boldsymbol{r}}\cdot\overline{\boldsymbol{r}}')}}{|\boldsymbol{r}|} \begin{bmatrix} -\cos\theta\cos\varphi \\ \sin\theta \\ -\cos\theta\sin\varphi \end{bmatrix} \left\{ 1 + \mathcal{O}\left(\frac{1}{|\boldsymbol{r}|}\right) \right\},
$$

(2.71)

for $\boldsymbol{r}, \boldsymbol{r}' \in D_1$, and

$$
\nabla_{\boldsymbol{r}'} G_T(\boldsymbol{r}, \boldsymbol{r}') \sim \frac{ik_1\nu}{2\pi} \frac{\sin\theta \, \mathrm{e}^{ik_1(\sin\theta - i\sqrt{\cos^2\theta - n^2})y'}}{\sin\theta + i\nu\sqrt{\cos^2\theta - n^2}} \frac{\mathrm{e}^{ik_1(|\boldsymbol{r}| - \widehat{\boldsymbol{r}}\cdot\boldsymbol{r}')}}{|\boldsymbol{r}|} \begin{bmatrix} -\cos\theta\cos\varphi \\ -i\sqrt{\cos^2\theta - n^2} \\ -\cos\theta\sin\varphi \end{bmatrix} \left\{ 1 + \mathcal{O}\left(\frac{1}{|\boldsymbol{r}|}\right) \right\},
$$

(2.72)

for $\boldsymbol{r} \in D_1$ and $\boldsymbol{r}' \in D_2$, as $|\boldsymbol{r}| \to \infty$.

The far-field pattern of the layer Green function and its gradient with respect to $\boldsymbol{r}'$ in

the direction $\hat{r} \in \mathbb{S}_+^2 = \{r \in \mathbb{R}^3 : |r| = 1, \ y \geq 0\}$ are then given by

$$
G_\infty(\hat{r}, r') = \begin{cases} \dfrac{1}{4\pi}\left\{e^{-ik_1\hat{r}\cdot r'} + \dfrac{\sin\theta - i\nu\sqrt{\cos^2\theta - n^2}}{\sin\theta + i\nu\sqrt{\cos^2\theta - n^2}} e^{-ik_1\widehat{r}\cdot\overline{r}'}\right\}, & r' \in D_1, \\[4mm] \dfrac{\nu}{2\pi}\dfrac{\sin\theta\, e^{ik_1(\sin\theta - i\sqrt{\cos^2\theta - n^2})y'}}{\sin\theta + i\nu\sqrt{\cos^2\theta - n^2}} e^{-ik_1\widehat{r}\cdot r'}, & r' \in D_2, \end{cases}
$$

(2.73)

and

$$
\boldsymbol{H}_\infty(\hat{r}, r') = \begin{cases} -\dfrac{ik_1}{4\pi}\left\{e^{-ik_1\hat{r}\cdot r'}\,\hat{r} + \dfrac{\sin\theta - i\nu\sqrt{\cos^2\theta - n^2}}{\sin\theta + i\nu\sqrt{\cos^2\theta - n^2}} e^{-ik_1\widehat{r}\cdot r'} \begin{bmatrix} \cos\theta\cos\varphi \\ -\sin\theta \\ \cos\theta\sin\varphi \end{bmatrix}\right\}, & r' \in D_1, \\[8mm] \dfrac{ik_1\nu}{2\pi}\dfrac{\sin\theta\, e^{ik_1(\sin\theta - i\sqrt{\cos^2\theta - n^2})y'}}{\sin\theta + i\nu\sqrt{\cos^2\theta - n^2}} e^{-ik_1\widehat{r}\cdot r'} \begin{bmatrix} -\cos\theta\cos\varphi \\ -i\sqrt{\cos^2\theta - n^2} \\ -\cos\theta\sin\varphi \end{bmatrix}, & r' \in D_2, \end{cases}
$$

(2.74)

where $\hat{r} = (\cos\varphi\cos\theta, \sin\theta, \sin\varphi\cos\theta)$, $\theta \in [0, \pi/2]$ and $\theta \in [0, 2\pi]$.

2.3.5 Numerical evaluation of the layer Green function

In this section we present a algorithm for the numerical evaluation of the Sommerfeld integrals $\Phi_R^{(i)}$ and $\Phi_T^{(i)}$, $i = 1, 2$ (equations (2.34b) and (2.41b)) and their derivatives, in both two and three dimensions. This approach, which results as a combination of the contour integration method described in [103] together with the smooth-windowing approach put forth in [25, 93] for evaluation of oscillatory integrals, can in fact be utilized to approximate Green functions for an arbitrary number of layers in two and three dimensional space. A survey on other methods available for the numerical evaluation of layer Green functions and related Sommerfeld integral can be found in the recent review paper [89].

This section presents details of the proposed numerical method for the evaluation of $\Phi_R^{(1)}$ (equation (2.34b)) with real wavenumbers k_1 and k_2; the remaining integrals in (2.34b) and (2.41b) and the case of complex k_2 can be treated by means of a completely analogous procedure.

The evaluation of $\Phi_R^{(1)}$ requires integration of the function

$$f(z) = \frac{\mathrm{e}^{-\sqrt{z^2-1}(\tilde{y}+\tilde{y}')}\cos(z(\tilde{x}-\tilde{x}'))}{\sqrt{z^2-1}[\sqrt{z^2-1}+\sqrt{z^2-n^2}][\sqrt{z^2-1}+\nu\sqrt{z^2-n^2}]},$$

on the positive real z-axis. The function f is expressed in terms of dimensionless variables $\widetilde{\boldsymbol{r}}$ and $\widetilde{\boldsymbol{r}}'$ which are defined by $k_1\boldsymbol{r} = \widetilde{\boldsymbol{r}} = (\tilde{x},\tilde{y})$, $k_1\boldsymbol{r}' = \widetilde{\boldsymbol{r}}' = (\tilde{x}',\tilde{y}')$. Clearly, f is highly oscillatory for wide ranges of values of the spatial variables $\widetilde{\boldsymbol{r}}$ and $\widetilde{\boldsymbol{r}}'$, and it is additionally singular at $z = 1$ and $z = n$. Note that $f, \partial f/\partial \tilde{y}$ and $\partial f/\partial \tilde{y}'$ decay exponentially fast as $z \to \infty$ when $\tilde{y} + \tilde{y}' > 0$. However, f decays as $|z|^{-3}$ and $\partial f/\partial \tilde{y}$ and $\partial f/\partial \tilde{y}'$ decay as $|z|^{-2}$ as $|z| \to \infty$ when $\tilde{y} = \tilde{y}' = 0$.
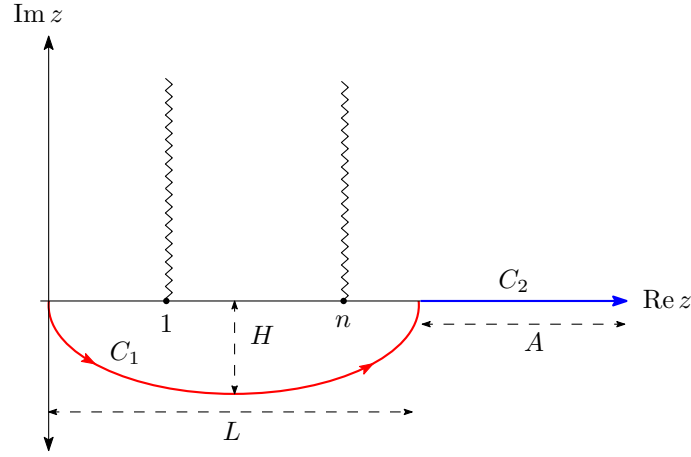
Figure 2.6: Integration path in the complex z-plane for the numerical evaluation of Sommerfeld integrals.

To proceed with the numerical evaluation of the needed integral of f we write

$$\int_0^\infty f(z)\,\mathrm{d}z = I_1 + I_2,$$

where $I_1 = \int_0^L f(z)\,\mathrm{d}z$ and $I_2 = \int_L^\infty f(z)\,\mathrm{d}z$, and where $L = 1 + n$.

Note that the singularities of f pose a difficulty to the direct numerical evaluation of I_1, which arises as a result of the presence of branch point singularities on the interval $[0, L]$. In the presence of a layered medium composed by more than two-layers, further, the integrands possess polar singularities for which Cauchy principal value integrals result. Both the present

integral as well as those arising in the multilayer case can be evaluated numerically by first using contour integration to express I_1 in the form

$$I_1 = \int_{C_1} f(z)\,dz = \int_0^\pi f(\zeta(t))|\zeta'(t)|\,dt, \tag{2.75}$$

where C_1 is a simple curve in the fourth quadrant which is parametrized by $\zeta : [0,\pi] \mapsto \mathbb{C}$ satisfying $\zeta(0) = 0$ and $\zeta(\pi) = L$ (see Figure 2.6). Throughout this thesis the curve C_1 is the ellipse

$$\zeta(t) = \left\{ \frac{L(1 + \cos(t + \pi))}{2} + iH\sin(t + \pi) : t \in [0,\pi] \right\}.$$

Note that on C_1 the function f grows exponentially as t increases from 0 to $\pi/2$. To estimate the largest value attained by $|f(\zeta(t))|$ for $t \in [0, \pi/2]$ we note that by the definition of the square root $\sqrt{\zeta^2 - 1}$, we have that

$$\frac{\theta_0 + \pi}{2} \le -\arg\sqrt{\zeta^2 - 1} \le \pi, \quad \zeta \in C_1,$$

where $\theta_0 = -\arctan(H/(1 + L/2)) \le 0$. Therefore we obtain

$$\left| e^{-|\tilde{y}+\tilde{y}'|\sqrt{\zeta^2-1}} \right| \le e^{|\tilde{y}+\tilde{y}'||\sqrt{\zeta^2-1}|\cos(\theta_0+\pi/2)} \le e^{-|\tilde{y}+\tilde{y}'|\sqrt{|\zeta_0|^2+1}\sin\theta_0} \le e^{|\tilde{y}+\tilde{y}'|H}, \quad \zeta \in C_1, \tag{2.76a}$$

where $\zeta_0 = \zeta(\pi/2) = L/2 - iH$. On the other hand, we have

$$|\cos(\tilde{x} - \tilde{x}')\zeta| \le \frac{e^{|\tilde{x}-\tilde{x}'|\operatorname{Im}\zeta} + e^{-|\tilde{x}-\tilde{x}'|\operatorname{Im}\zeta}}{2} \le e^{|\tilde{x}-\tilde{x}'|H}. \tag{2.76b}$$

Thus, in order to control the exponential growth towards the negative imaginary axis, we select $H = \{\max\{10, |\tilde{x} - \tilde{x}'| + |\tilde{y} + \tilde{y}'|\}\}^{-1}$. With this simple procedure, certain versions of which have often been used in the literature [89], we ensure that the exponents on the right-hand sides of (2.76) are smaller than one.

In our approach the resulting expression for the integral I_1 is then approximated by means of the Clenshaw-Curtis quadrature rule [106]—which, for the smooth integrand under consideration, yields rapid convergence. In view of the oscillatory behavior of the integrand,

on the other hand, and in order to maintain the same accuracy for all $\widetilde{r}$ and $\widetilde{r}'$, the number of quadrature points is chosen to grow linearly with $|\tilde{x} - \tilde{x}'|$ (see Table 2.1).

D	H	N	Relative error
10	0.20	98	4.31×10^{-08}
20	0.10	192	2.44×10^{-08}
40	0.05	382	3.28×10^{-08}
80	0.025	762	6.34×10^{-08}
160	0.0125	1523	4.49×10^{-08}

Table 2.1: Approximation of I_1 for $\widetilde{r} = (D, 10)$, $\widetilde{r}' = (0, 1)$, $n = 2$ and $L = 3$, using N Clenshaw-Curtis quadrature points.

In order to evaluate the oscillatory integral I_2, on the other hand, we utilize the windowing method put forth in [25]. Hence I_2 is approximated as

$$I_2 \approx \int_0^A f(t + L)w_A(t)\,\mathrm{d}t = \int_L^{A+L} f(t)w_A(t - L)\,\mathrm{d}t, \tag{2.77}$$

where the window function w_A is defined as follows.

Definition 2.3.3 (Window function)**.** *Let $0 < c < 1$ and $\eta \in C_0^\infty(\mathbb{R})$ be given by*

$$\eta(t; t_0, t_1) = \begin{cases} 1, & |t| \leq t_0, \\ \exp\left(\dfrac{2\,\mathrm{e}^{-1/u}}{u - 1}\right), & t_0 < |t| < t_1, u = \dfrac{|t| - t_0}{t_1 - t_0}, \\ 0, & |t| > t_1. \end{cases} \tag{2.78}$$

Then the window function is defined as

$$w_A(t) = \eta(t; cA, A).$$

As in the case of I_1, the integral in (2.77) is approximated by using Clenshaw-Curtis quadrature. In virtue of the oscillatory behavior of the integrand when $|\tilde{x} - \tilde{x}'| \neq 0$, and

exponential decay of the integrand when $\tilde{y} + \tilde{y}' \neq 0$, the integral in (2.77) converges to I_2 faster than any negative power $\sqrt{(\tilde{x} - \tilde{x}')^2 + (\tilde{y} + \tilde{y}')^2} A$ as A goes to infinity—as established in the following

Lemma 2.3.4 (Superalgebraic accuracy of windowed integration). *Let* $g : [L, \infty) \to \mathbb{C}$, $g \in C^\infty([L, \infty))$ *satisfy*

$$\left| \frac{\mathrm{d}^n g(t)}{\mathrm{d} t^n} \right| \leq \frac{C_n}{t^{n+\mu}} \quad \text{for all} \quad t > L, \quad n \geq 0, \tag{2.79}$$

for some positive constants C_n *and* μ, *and consider the improper integral*

$$I = \int_L^\infty e^{-\sqrt{t^2 - 1}\alpha + i\beta x} g(t) \, \mathrm{d}t,$$

where $\alpha \geq 0$, $\beta \in \mathbb{R}$ *and* $\sqrt{\alpha^2 + \beta^2} \neq 0$. *Then, for any* $n \geq 0$ *there exists a constant* $M_n > 0$, *independent of* A, *such that*

$$|I - I_A| \leq \frac{M_n}{(\alpha^2 + \beta^2)^{(n+1)/2} A^n} e^{-\alpha\sqrt{(Ac+L)^2 - 1}} \quad \text{for all} \quad A > A_0 > \frac{1}{c},$$

where

$$I_A = \int_L^\infty e^{-\sqrt{t^2 - 1}\alpha + i\beta t} g(t) w_A(t - L) \, \mathrm{d}t,$$

where w_A *denotes the window function introduced in Definition 2.3.3.*

Proof. Let $E = I - I_A$. From Definition 2.3.3 and utilizing the change of variables $t = As$ we obtain

$$E = \int_{cA+L}^\infty e^{-\sqrt{t^2 - 1}\alpha + i\beta t} g(t)[1 - w_A(t - L)] \, \mathrm{d}t$$

$$= A \int_{c+\ell}^\infty e^{-\sqrt{s^2 - 1/A^2}A\alpha + iA\beta t} g(As)[1 - w_A(A(s - \ell))] \, \mathrm{d}s,$$

where $\ell = L/A$. Note that by construction, the window function satisfies $w_A(As) = \eta(As; cA, A) = \eta(s; c, 1) = w_1(s)$. Thus, letting $\tilde{w}_1(s - \ell) = 1 - w_1(s - \ell)$ we express E

as

$$E = A \int_{c+\ell}^{\infty} e^{\kappa As\phi(s)} \, g(As)\widetilde{w}_1(s - \ell) \, ds,$$

where $\phi(s) = (-\sqrt{1 - (As)^{-2}}\,\alpha + i\beta)/(-\alpha + i\beta)$ and $\kappa = -\alpha + i\beta$. Integrating by parts we obtain

$$E = \left(\frac{e^{\kappa At\phi(s)}}{\kappa[s\phi(s)]'} g(As)\widetilde{w}_1(s) \right)\Bigg|_{c+\ell}^{\infty} - \frac{1}{\kappa} \int_{c+\ell}^{\infty} e^{\kappa As\phi(s)} \, D_\phi \left[g(As)\widetilde{w}_1(s - \ell) \right] \, ds,$$

where we have introduced the operator

$$D_\phi = \frac{d}{ds} \frac{1}{[s\phi(s)]'}.$$

Clearly the boundary term vanishes in virtue of the fact that $\widetilde{w}_1(c) = 1 - w_1(c) = 0$ and because of the decay of g as $t = As \to \infty$. Similarly, integrating by parts $(n + 1)$-times we obtain

$$E = \frac{(-1)^{n+1}}{\kappa^{n+1} A^n} \int_{c+\ell}^{\infty} e^{\kappa As\phi(s)} \, D_\phi^{n+1} \left[g(As)\widetilde{w}_1(s - \ell) \right] \, ds,$$

(since all the boundary contributions vanish), and we consequently obtain

$$|E| \leq \frac{1}{|\kappa|^{n+1} A^n} \int_{c+\ell}^{\infty} e^{-\alpha\sqrt{(As)^2 - 1}} \left| D_\phi^{n+1} \left[g(As)\widetilde{w}_1(s - L) \right] \right| \, ds$$

$$\leq \frac{e^{-\alpha\sqrt{(Ac+L)^2 - 1}}}{|\kappa|^{n+1} A^n} \int_{c+\ell}^{\infty} \left| D_\phi^{n+1} \left[g(As)\widetilde{w}_1(s - \ell) \right] \right| \, ds.$$

In order to complete the proof we need to show that $\| D_\phi^{n+1} \left[g(As)\widetilde{w}_1(s - \ell) \right] \|_{L^1([c+\ell, \infty))} \leq M_n$ for some constant M_n independent of A. Expanding the derivatives in $D_\phi^{n+1} \left[g(As)\widetilde{w}_1(s - \ell) \right]$ we obtain a linear combination of terms given by products of functions of the form

$$\left(\frac{d}{ds}[s\phi(s)] \right)^{-a} \left(\frac{d^{p+1}}{ds^{p+1}}[s\phi(s)] \right)^{b-1} \frac{d^q}{ds^q}[g(As)\widetilde{w}_1(s - \ell)] \text{ with integers } a, b, p, q \geq 1. \quad (2.80)$$

Thus, in order to prove the existence of the constant M_n it suffices to show that any function of this form belongs to $L^1([c + \ell, \infty)) \cap L^\infty([c + \ell, \infty))$ and has L^1- and L^∞-norms which are independent of A. (The L^∞ requirement ensures that the aforementioned *products* of these

L^1-norm-bounded functions are also in L^1-norm-bounded.) To achieve this we rely on the easily-checked lower bound

$$\left| \frac{\mathrm{d}}{\mathrm{d}s}[s\phi(s)] \right| = \left| \frac{-\alpha + i\beta\sqrt{1 - (As)^{-2}}}{(-\alpha + i\beta)\sqrt{1 - (As)^{-2}}} \right| = \left[\frac{\alpha^2 + \beta^2(1 - (As)^{-2})}{(\alpha^2 + \beta^2)(1 - (As)^{-2})} \right]^{1/2} \geq 1,$$

and upper bound

$$\left| \frac{\mathrm{d}^{p+1}}{\mathrm{d}s^{p+1}}[s\phi(s)] \right| \leq \frac{Q_p}{A_0^2 s^{p+2}[1 - (A_0 c + L)^{-2}]^{(2p+1)/2}}, \quad p \geq 1, \ s > c + \ell, \ A > A_0,$$

(Q_p positive constants). Therefore,

$$\left| \left(\frac{\mathrm{d}}{\mathrm{d}s}[s\phi(s)] \right)^{-a} \left(\frac{\mathrm{d}^{p+1}}{\mathrm{d}s^{p+1}}[s\phi(s)] \right)^{b-1} \right| \leq \left(\frac{Q_p}{A_0^2 s^{p+2}[1 - (A_0 c + L)^{-2}]^{(2p+1)/2}} \right)^{b-1}, \quad (2.81)$$

and

$$
\begin{aligned}
\left| \frac{\mathrm{d}^q}{\mathrm{d}s^q}[g(As)\widetilde{w}_1(s - \ell)] \right| &\leq \sum_{m=0}^{q} \binom{q}{m} \left| \frac{\mathrm{d}^{q-m}}{\mathrm{d}s^{q-m}} g(As) \right| \left| \frac{\mathrm{d}^m}{\mathrm{d}s^m} \widetilde{w}_1(s - \ell) \right| \\
&= \left| \frac{\mathrm{d}^q}{\mathrm{d}s^q} g(As) \right| \widetilde{w}_1(s) + \sum_{m=1}^{q} \binom{q}{m} \left| \frac{\mathrm{d}^{q-m}}{\mathrm{d}t^{q-m}} g(As) \right| \left| \frac{\mathrm{d}^m}{\mathrm{d}t^m} w_1(s - \ell) \right| \\
&\leq \frac{C_q}{A_0^\mu s^{q+\mu}} + \|w_1\|_{C^q(\mathbb{R})} \mathbf{1}_{[c,1]}\left(s - \frac{L}{A_0} \right) \sum_{m=1}^{q} \binom{q}{m} \frac{C_{q-m}}{A_0^\mu s^{\mu+q-m}}, (2.82)
\end{aligned}
$$

where the last inequality follows from the boundedness of the q-th derivative of the window function w_1 (which itself follows directly from Definition 2.3.3 and the bound (2.79)). Finally, from (2.81) and (2.82) we conclude that the functions in (2.80) belong to $L^1([c + \ell, \infty)) \cap L^\infty([c + \ell, \infty))$ with norms which are independent of A, and thus, the lemma follows. $\square$

Proposition 2.3.4 demonstrates the fast convergence of the windowed integral in (2.77) to I_2 as $A \to \infty$ for source and observation points satisfying the condition $\sqrt{\alpha^2 + \beta^2} = \sqrt{(\tilde{x} - \tilde{x}')^2 + (\tilde{y} + \tilde{y}')^2} \neq 0$—a dimensionless relation which is only violated for $\boldsymbol{r} = \boldsymbol{r}' \in \Pi_1$. In the special case $\boldsymbol{r} = \boldsymbol{r}' \in \Pi_1$, however, the integrand f is slowly decaying and does not oscillate, thus, it leads to slow convergence of the windowed-integral approximation (2.77)

to the integral I_2 as $A \to \infty$. In fact, utilizing the notation introduced in Proposition 2.3.4, we have

$$|I - I_A| = \mathcal{O}((cA)^{-\mu+1}),$$

for $\alpha = \beta = 0$ for a function g that decays as $|x|^{-\mu}$ as $x \to \infty$.

The super-algebraic/exponential convergence of the windowed integral allows I_2 to be approximated with a fix accuracy and a fixed computational cost by choosing A inversely proportional to $\sqrt{(\tilde{x} - \tilde{x}')^2 + (\tilde{y} + \tilde{y}')^2}$. The example in Table 2.2 illustrates this property. Throughout this thesis the value $c = 0.1$ is utilized in the numerical computation of Sommerfeld integrals. But some other important uses are made of the windowing function (2.78) (see e.g. Chapters 4, 5 and 6) for which a different values of c, which was found more advantageous, is used.

D	A	Relative error with windowing
10	100	2.89×10^{-12}
20	50	2.13×10^{-10}
40	25	1.60×10^{-10}
80	12.5	6.58×10^{-10}
160	6.25	2.50×10^{-10}

Table 2.2: Approximation of I_2 for $\tilde{r} = (D, 0)$, $\tilde{r}' = (0, 0)$, $n = 2$ and $L = 3$, using a fixed number of Clenshaw-Curtis quadrature points.

Figures 2.7 and 2.8 display the real part and the absolute value of the two-layer Green function (for a source point in the upper half-plane) that was evaluated by means of the numerical algorithm introduced in this section.

2.4 Scattering by obstacles in a layered medium

To illustrate the utility of the layer Green function methods introduced in Section 2.3.5 we now present and demonstrate an associated boundary integral equation algorithm for problems of scattering by PEC obstacles embedded in a layered medium. The integral equation

(a) Re G for $k_1 = 20$ and $k_2 = 40$.

(b) $|G|$ for $k_1 = 20$ and $k_2 = 40$.

(c) Re G for $k_1 = 40$ and $k_2 = 20$.

(d) $|G|$ for $k_1 = 40$ and $k_2 = 20$.
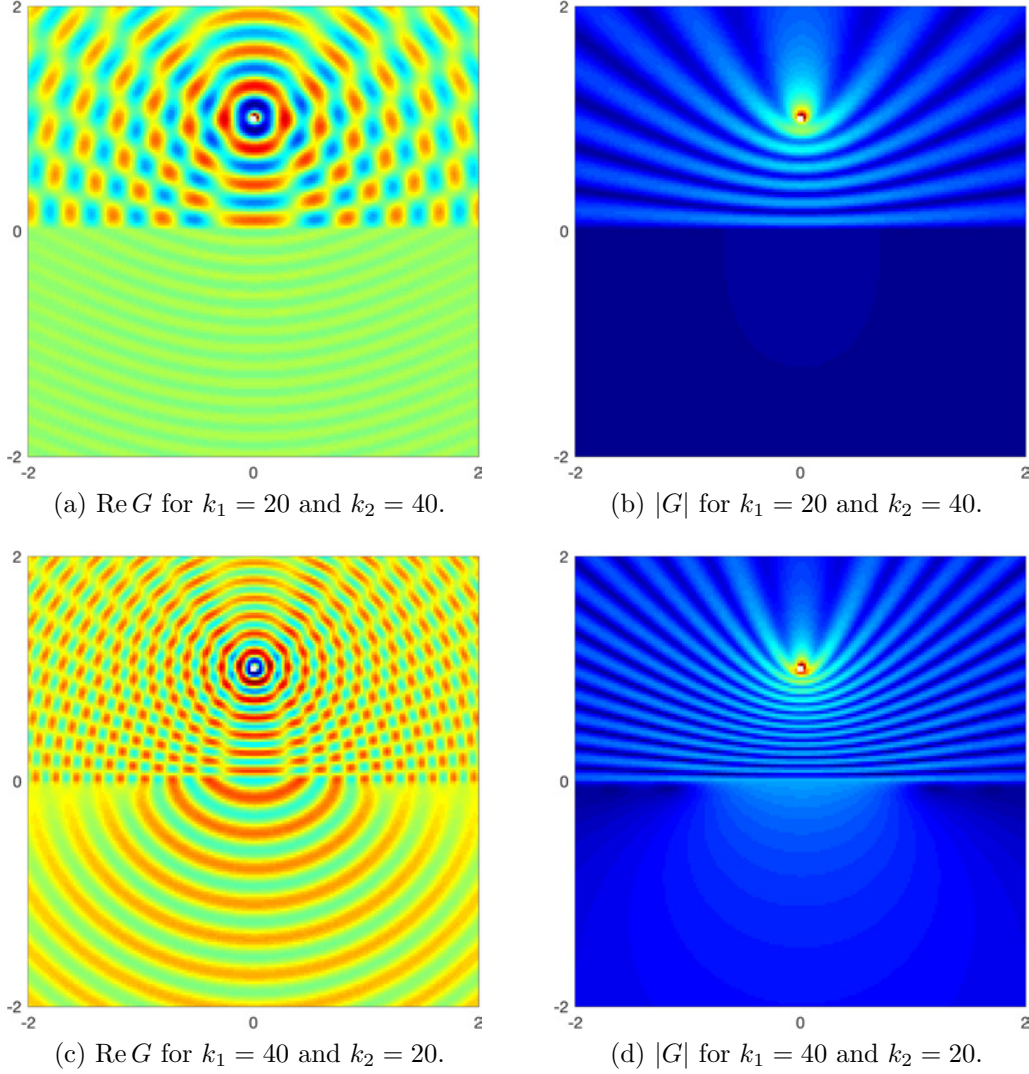
Figure 2.7: Plots of the two dimensional layer Green function $G(\boldsymbol{r}, \boldsymbol{r}')$ as a function of $\boldsymbol{r}$ with source point $\boldsymbol{r}' = (0, 1)$, $\Pi_1 = \{y = 0\}$, $\nu = (k_1/k_2)^2$ and under TM-polarization.

method described in this section, that we refer to as the Layer Green Function (LGF) method, is further extended in Chapter 3 to a much larger class of problems of scattering in layered media—including problems for which defects intersect the planar interface Π_1. In the discussion provided below in this section we focus primarily on the two-dimensional electromagnetic problem, but problems of acoustic scattering by sound-soft and sound-hard obstacles in two- and three-dimensional space can be treated in a similar fashion. The results presented herein for PEC obstacles (boundary conditions (2.11)) in TM- and TE-polarizations in the electro-

(a) $\operatorname{Re} G$ for $k_1 = 20$ and $k_2 = 40$.

(b) $|G|$ for $k_1 = 20$ and $k_2 = 40$.

(c) $\operatorname{Re} G$ for $k_1 = 40$ and $k_2 = 20$.

(d) $|G|$ for $k_1 = 40$ and $k_2 = 20$.
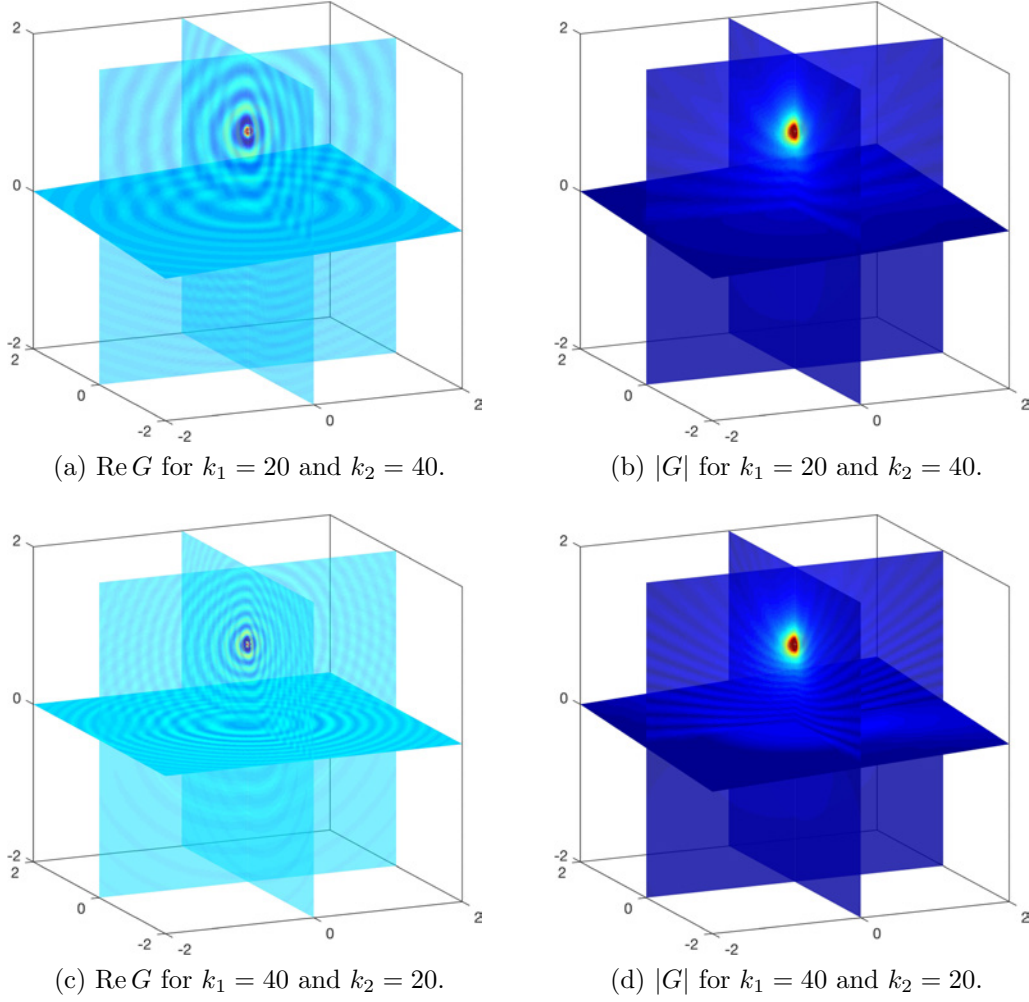
Figure 2.8: Plots of the three dimensional layer Green function $G(\boldsymbol{r}, \boldsymbol{r}')$ as a function of $\boldsymbol{r}$ with source point $\boldsymbol{r}' = (0, 1, 0)$, $\Pi_1 = \{y = 0\}$ and with $\nu = 1$.

magnetic case correspond to sound-hard and sound-soft boundary conditions in the acoustic case, respectively.

Let us thus consider a domain $\Omega \subset \mathbb{R}^2$ occupied by a smooth bounded PEC obstacle placed upon the dielectric half-plane D_2, and assume the structure is illuminated by an electromagnetic plane wave $(\mathbf{E}^{\mathrm{inc}}, \mathbf{H}^{\mathrm{inc}})$ as defined in (2.12). We assume the obstacle Ω lies entirely within one of the half-planes D_1 or D_2 and has a smooth boundary $\partial\Omega = \Gamma$. As shown in Section 2.2.1, the transverse component of the resulting total electric and magnetic fields, $u = E_z$ in TE-polarization, and $u = H_z$ in TM-polarization, satisfy the Helmholtz equation $\Delta u + k_j^2 u = 0$ in $D_j \setminus \overline{\Omega}$, $j = 1, 2$, and, furthermore, they satisfy PEC boundary

conditions: $u = 0$, in TE-polarization, and $\partial u / \partial n = 0$, in TM-polarization, on the boundary of the obstacle Γ. In oder to formulate the problem of scattering, we thus express the total field as

$$u = u^f + u^s \quad \text{in} \quad \mathbb{R}^2 \setminus \overline{\Omega}, \tag{2.83}$$

where u^f denotes the total field that corresponds to the solution of the problem of scattering of the plane-wave by the layered medium in absence of the PEC obstacle, which is given in (2.13) for both polarizations, and where u^s denotes the scattered field produced by the interaction of u^f with the PEC obstacle in presence of the layered medium. The scattered field thus satisfies:

$$
\begin{cases}
\Delta u^s + k_j^2 u^s = 0 & \text{in} \quad D_j \setminus \overline{\Omega}, \; j = 1, 2, \\[2mm]
u^s\big|_{y=0^+} = u^s\big|_{y=0^-} & \text{on} \quad \Pi_1, \\[2mm]
\dfrac{\partial u^s}{\partial y}\bigg|_{y=0^+} = \nu \dfrac{\partial u^s}{\partial y}\bigg|_{y=0^-} & \text{on} \quad \Pi_1, \\[2mm]
u^s = -u^f & \text{on} \quad \Gamma, \quad \text{(in TE-polarization)} \\[2mm]
\dfrac{\partial u^s}{\partial n} = -\dfrac{\partial u^f}{\partial n} & \text{on} \quad \Gamma, \quad \text{(in TM-polarization)} \\[2mm]
\displaystyle\lim_{|\boldsymbol{r}| \to \infty} \sqrt{|\boldsymbol{r}|} \left\{ \dfrac{\partial u^s}{\partial |\boldsymbol{r}|} - i k_j u^s \right\} = 0 & \text{in} \quad D_j, \; j = 1, 2.
\end{cases}
\tag{2.84}
$$

As it was shown by Kristensson [74], the boundary value problem (2.84) admits at most one solution $u^s : \mathbb{R}^2 \setminus \overline{\Omega} \to \mathbb{C}$.

In order to solve (2.84) we seek a scattered field given by the single-layer potential $u^s(\boldsymbol{r}) = \mathcal{S}[\psi](\boldsymbol{r})$ where, letting G denote the layer Green function (2.27), $\mathcal{S} : C(\Gamma) \to C^2(\mathbb{R}^2 \setminus \{\Gamma \cup \Pi_1\}) \cap C(\mathbb{R}^2)$ is given by

$$\mathcal{S}[\psi](\boldsymbol{r}) = \int_\Gamma G(\boldsymbol{r}, \boldsymbol{r}') \psi(\boldsymbol{r}') \, \mathrm{d}s_{\boldsymbol{r}'}, \quad \boldsymbol{r} \in \mathbb{R}^2 \setminus \Gamma, \tag{2.85}$$

where $\psi : \Gamma \to \mathbb{C}$ is an unknown density function. In view of the transmission problem (2.20) satisfied by the layer Green function, it can be easily shown that, for a continuous density

$\psi \in C(\Gamma)$ the single-layer potential (2.85) is a smooth function in $\mathbb{R}^2 \setminus \{\Gamma \cup \Pi_1\}$ that satisfies the Helmholtz equation with wavenumbers k_j in $D_j \setminus \overline{\Omega}$, $j = 1, 2$ as well as the appropriate transmission conditions (2.9) on Π_1 and the radiation condition at infinity. Enforcing the remaining PEC boundary condition on Γ we thus obtain the integral equations

$$
\begin{align}
S[\psi] &= -u^f \quad \text{(TE-polarization)} \tag{2.86a}\\
-\frac{\psi}{2} + K[\psi] &= -\frac{\partial u^f}{\partial n} \quad \text{(TM-polarization)} \tag{2.86b}
\end{align}
$$

on Γ. The single-layer and the adjoint double-layer integral operators $S : C(\Gamma) \to C(\Gamma)$ and $K : C(\Gamma) \to C(\Gamma)$ in (2.86) are given by

$$
S[\psi](\boldsymbol{r}) = \int_\Gamma G(\boldsymbol{r}, \boldsymbol{r}')\psi(\boldsymbol{r}')\, \mathrm{d}s_{\boldsymbol{r}'} \quad \text{and} \quad K[\psi](\boldsymbol{r}) = \int_\Gamma \frac{\partial G}{\partial n_{\boldsymbol{r}}}(\boldsymbol{r}, \boldsymbol{r}')\psi(\boldsymbol{r}')\, \mathrm{d}s_{\boldsymbol{r}'}, \quad \boldsymbol{r} \in \Gamma \quad (2.87)
$$

respectively.

The mapping properties of the single-layer potential and associated integral operators are well-known for problems of scattering by obstacles in free-space [45, 97]. Similar results can be obtained for the present layer-media scattering problem as it can be shown that the single-layer potential (2.85) is a smooth perturbation of the free-space single-layer potential, and that the operators S and K (2.87) are compact perturbations of the corresponding integral operators associated with the free-space problem (since the layer Green function in the layer D_j that contains the obstacle is given by $G(\boldsymbol{r}, \boldsymbol{r}') = G_{k_j}(\boldsymbol{r}, \boldsymbol{r}') + \Phi_j(\boldsymbol{r}, \boldsymbol{r}')$, where the Sommerfeld integral $\Phi_j : D_j \times D_j \to \mathbb{C}$ is a smooth function $\Phi \in C^\infty(D_j \times D_j)$). It thus follows that the integral equations (2.86) are of Fredholm type.

It can shown, on the other hand, that the integral equations (2.86) admit unique continuous solutions except for a countable (real) set of wavenumbers known as spurious resonances; which correspond to Dirichlet or Neumann eigenvalues (depending on the polarization) of the Laplace operator $-\Delta$ in the interior of Ω, cf. [45, 97]. For a wavenumber k_j that is not a spurious resonance, the single-layer potential (2.85) provides the unique solution of the exterior boundary value problem (2.84) where the density ψ is obtained by solving the relevant integral equation (2.86a) or (2.86b) in TE- or TM-polarization, respectively.

(a) Re u.

(b) $|u|$.

(c) $|u_\infty(\hat{\boldsymbol{r}})|$ where $\hat{\boldsymbol{r}} = (\cos\theta, \sin\theta)$, $\theta \in (0,\pi)$.

(d) Relative errors in semi-log scale.
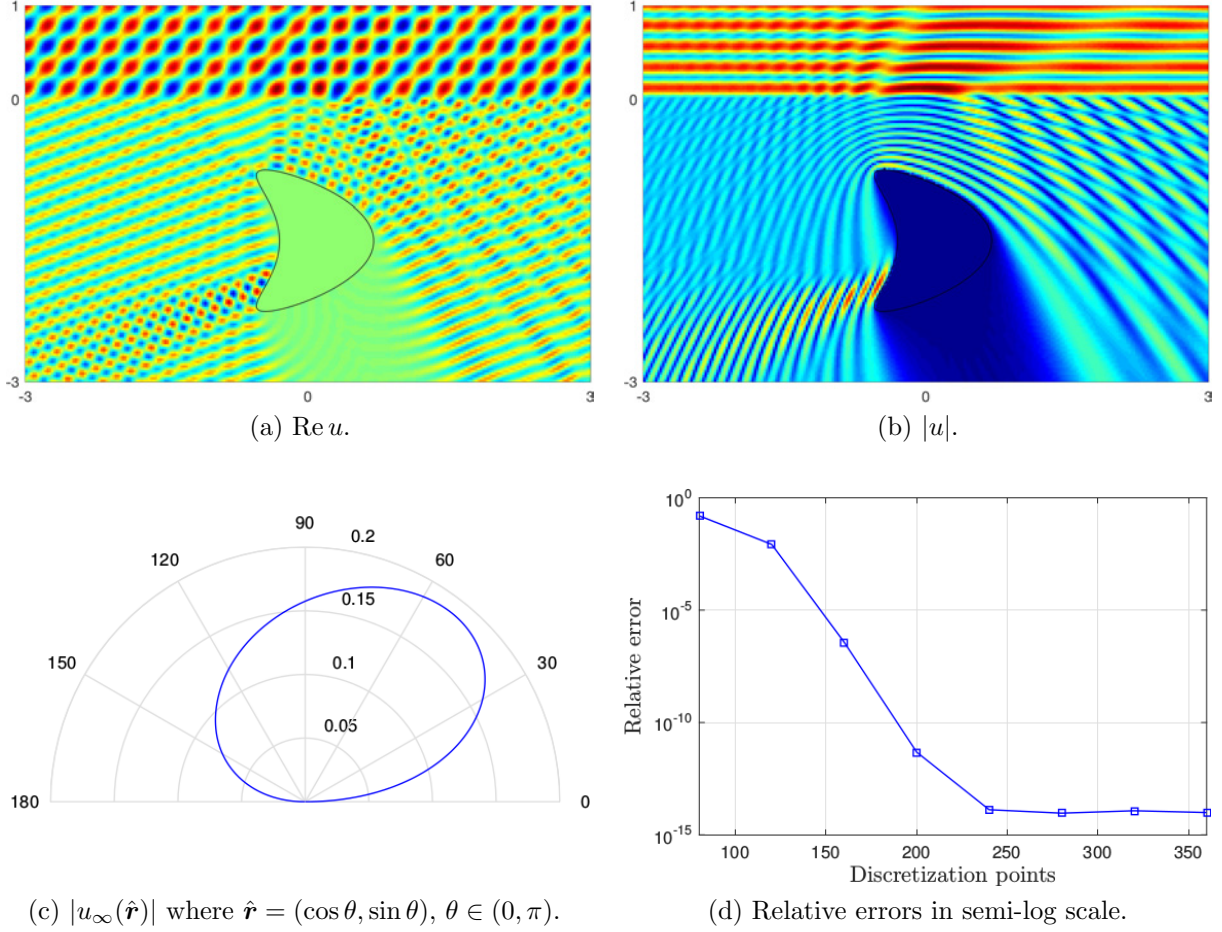
Figure 2.9: Solution of the problem of scattering of a TE-polarized plane-electromagnetic wave $u^{\mathrm{inc}}(\boldsymbol{r}) = \mathrm{e}^{ik_1(x\cos(\pi/4)-\sin(\pi/4)y)}$ by a PEC kite-like obstacle buried in a dielectric half-plane, for wavenumbers $k_1 = 20$, $k_2 = 40$. (a) Real part of the total field. (b) Absolute value of the total field. (c) Absolute value of the far-field pattern in the upper half-plane for all observation angles in the upper half-plane. (d) Relative errors in the far-field $u_\infty(\hat{\boldsymbol{r}})$ in maximum-norm for various discretizations the integral equation (2.86a).

There are various approaches to tackle the spurious resonance problem. Perhaps the most popular one is the so-called combined field integral equation (CFIE) [19, 78, 99], which relies on a certain field representation that involves a linear combination of single- and double-layer potentials. Such representation leads to an integral equation that is uniquely solvable for all (physically meaningful) wavenumbers. Although effective, this approach requires to duplicate the number of boundary integral operators that must be discretized. A CFIE based on use of the layer Green function entails a significantly larger computational cost than the

simple single-layer formulation (2.85), as the CFIE approach requires to at least duplicate the number of Sommerfeld integral evaluations necessary to form the associated linear system, even when k_j is far from a spurious resonances. In Section 3.3.2 we present a methodology which, at the expense of a reduced number of additional evaluations near spurious resonances, overcomes the spurious resonance problem without requiring duplication of the number of Sommerfeld integral evaluations.

In order to numerically approximate the unknown density ψ we utilize the Nyström method put forth independently by Martensen [84] and Kussmaul [75] which, for a smooth obstacle with boundary Γ of class $\mathcal{C}^\infty$, yields super-algebraic convergence: the maximum error in ψ decreases faster than any negative power of the number of discretization points used. To illustrate the excellent convergence properties of the overall Nyström approach we first consider the problem of scattering of a kite-shaped PEC obstacle buried in a dielectric plane. Figures 2.9a and 2.9b display the real part and the absolute value of total field $u = u^f + u^s$, respectively, which is obtained by solving the corresponding integral equation in TE-polarization (2.86a) by application of the Nyström method and by evaluating of the field through the representation formula (2.85). Figure 2.9d, in turn, displays the relative errors (in semi-log scale) in the far-field pattern:

$$u_\infty(\hat{\boldsymbol{r}}) = \int_\Gamma G_\infty(\hat{\boldsymbol{r}}, \boldsymbol{r}')\psi(\boldsymbol{r}')\, \mathrm{d}s_{\boldsymbol{r}'}, \qquad (2.88)$$

for $\hat{\boldsymbol{r}} = (\cos\theta, \sin\theta)$, $\theta \in [0, \pi]$, where G_∞ is given in (2.59). The far-field pattern is displayed in Figure 2.9c.

We now consider the problem of scattering of a plane-wave acoustic wave by a three-dimensional sound-hard bounded obstacle $\Omega \subset \mathbb{R}^3$ with smooth boundary $\Gamma = \partial\Omega$. The discussion presented above for the two-dimensional electromagnetic problem carries over directly to the three-dimensional acoustic scattering problem by letting the scattered field
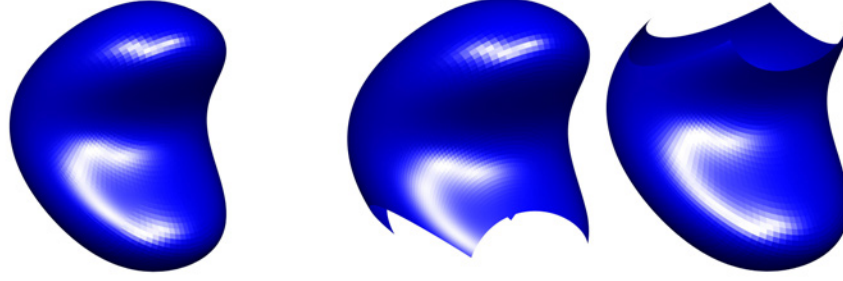
(a) Bean-shaped obstacle.   (b) Overlapping surface patches.

Figure 2.10: Bean-shaped obstacle [29, Section 6.4] and overlapping surface patches utilized for its parametrization.

be given by the solution of:

$$
\begin{cases}
\Delta u^s + k_j^2 u^s = 0 & \text{in} \quad D_j \setminus \overline{\Omega}, \ j = 1, 2, \\[2mm]
u^s\big|_{y=0^+} = u^s\big|_{y=0^-} & \text{on} \quad \Pi_1, \\[2mm]
\dfrac{\partial u^s}{\partial y}\bigg|_{y=0^+} = \nu \dfrac{\partial u^s}{\partial y}\bigg|_{y=0^-} & \text{on} \quad \Pi_1, \\[2mm]
u^s = -u^f & \text{on} \quad \Gamma, \quad \text{(sound-soft)} \\[2mm]
\dfrac{\partial u^s}{\partial n} = -\dfrac{\partial u^f}{\partial n} & \text{on} \quad \Gamma, \quad \text{(sound-hard)} \\[2mm]
\displaystyle\lim_{|\boldsymbol{r}|\to\infty} |\boldsymbol{r}| \left\{ \dfrac{\partial u^s}{\partial |\boldsymbol{r}|} - ik_j u^s \right\} = 0 & \text{in} \quad D_j, \ j = 1, 2,
\end{cases}
$$

and by letting the single-layer potential be given by

$$
\mathcal{S}[\psi](\boldsymbol{r}) = \int_\Gamma G(\boldsymbol{r}, \boldsymbol{r}') \psi(\boldsymbol{r}') \, \mathrm{d}s_{\boldsymbol{r}'}, \quad \boldsymbol{r} \in \mathbb{R}^3 \setminus \Gamma, \tag{2.89}
$$

in terms of the three-dimensional layer Green function (2.40). (A more detailed description of the three-dimensional acoustic scattering problem is presented in Section 6.1.)

The single-layer representation (2.89) of the scattered field u^s leads to the second-kind integral in (2.86b). In order to numerically solve (2.86b) in the present three-dimensional context we utilize the high-order Nyström method put forth in [27, 29]. To illustrate this solution

procedure, we consider the smooth bean-like scatterer shown in Figure 2.10. Figures 2.11a and 2.11b (resp. Figures 2.11d and 2.11e) display the total field $u^s + u^f$ solution of the problem of scattering of the plane-acoustic wave $u^{\text{inc}}(\boldsymbol{r}) = e^{ik_1(\cos(\pi/4)x - \sin(\pi/4)y)}$ by the bean scatterer embedded in the upper half-space D_1 (resp. lower half-space D_2), while Figure 2.11c (resp. Figure 2.11f) displays the far-filed pattern (2.88) for $\hat{\boldsymbol{r}} = (\cos\varphi\cos\theta, \sin\theta, \sin\varphi\cos\theta)$, $\theta \in [0, \pi/2]$ and $\theta \in [0, 2\pi]$, obtained using the far-field form the layer Green function (2.73).
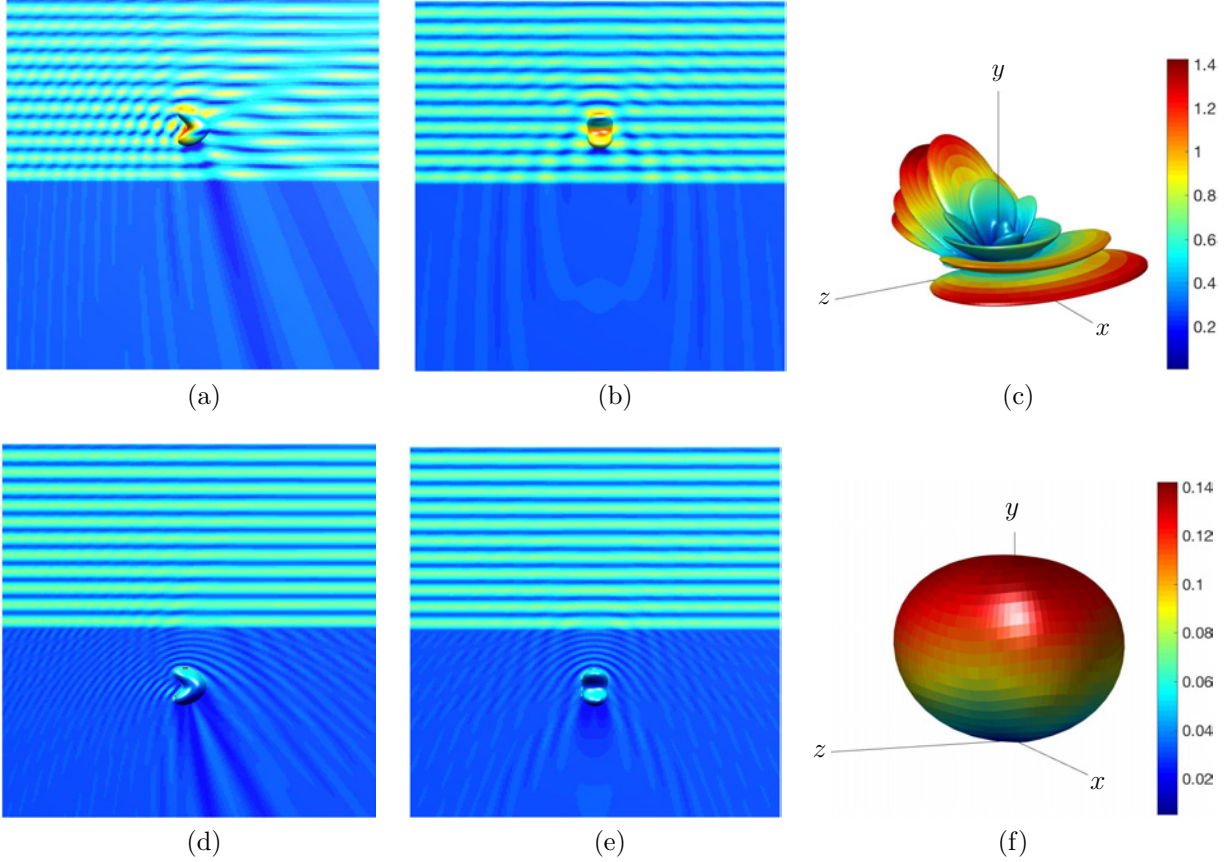
Figure 2.11: Solution of the problem of scattering of the acoustic incident plane-wave $u^{\text{inc}}(\boldsymbol{r}) = e^{ik_1(x\cos(\pi/4) - \sin(\pi/4)y)}$ by a sound-hard bean-shaped obstacle lying above (first row) and below (second row) the plane $\Pi_1 = \{y = 0\}$, in a two-layer medium with wavenumbers $k_1 = 5$ and $k_2 = 10$. First and second columns: absolute value of the total field. Third column: absolute value of the far-field pattern.

Chapter 3

Layer Green function Method for problems of scattering by defects in layered media

This chapter extends the LGF high-order integral equation methods developed in Section 2.4 so as to enable solution of problems of scattering of a plane electromagnetic wave by cylindrical dielectric defects that lie *at the interface* between two half-planes. Eight such classical problems are tackled in this chapter: scattering by a dielectric bump on 1) a perfectly electrically conducting (PEC) or 2) a dielectric half-plane (Figure 3.1a), scattering by a dielectric-filled cavity on 3) a perfectly-conducting or 4) a dielectric half-plane (Figure 3.1b), scattering by a dielectric-overfilled cavity on 5) a perfectly-conducting or 6) a dielectric half-plane (Figure 3.1c), and scattering by a void cavity on 7) a perfectly-conducting or 8) a dielectric half-plane (Figure 3.1d). From a mathematical perspective these eight different physical problems reduce to just three problem types for which this chapter provides numerical solutions on the basis of highly accurate and efficient boundary integral equation methods.

In all cases the proposed methods utilize field representations based on single-layer potentials for appropriately chosen Green functions, including the layer Green function obtained in Section 2.3.1. As is known, such single-layer formulations lead to non-invertible integral equations at certain spurious resonances—that is, for wavenumbers that coincide with interior Dirichlet eigenvalues for a certain differential operator—either the Laplace operator or an elliptic differential operator with piecewise constant coefficients (see Section 3.3.2 for

details). We nevertheless show that solutions *for all wavenumbers* can be obtained from such non-invertible formulations—including wavenumbers at which non-invertible integral equations result. Our method in these regards relies on the analyticity of the PDE solution as a function of the wavenumber together with a certain approach based on use of Chebyshev approximation.

(The use of field representations which give rise to non-invertible operators is advantageous in two main ways: on one hand this strategy allows one to bypass the need to utilize hypersingular operators, whose evaluation is computationally expensive and, otherwise, highly challenging near corner points; and, on the other hand, it leads to systems of integral equations containing fewer integral operators—with associated reduced computational cost.)

The problems considered in this chapter draw considerable interest in a wide range of settings. For example, the problem of scattering by bumps and cavities on a (perfect or imperfect) conducting half-plane is important in the study of the radio-frequency absorption and electric and magnetic field enhancement that arises from surface roughness [111, 140]. The problem of scattering by open groove cavities on a conducting plane, in turn, impacts on a variety of technologies, with applicability to design of cavity-backed antennas, non-destructive evaluation of material surfaces, and more recently, modeling of extraordinary transmission of light and plasmonics resonance, amongst many others (e.g. [8] and references therein).

There is vast literature concerning the types of problems considered in this chapter. For a circular bump a separation-of-variables analytical Fourier-Bessel expansion exists [109]. Related semi-analytical separation-of-variables solutions are available for other simple configurations, such as semi-circular cavities and rectangular bumps and cavities (e.g. [36, 37, 55, 77, 100, 101, 102, 127, 128, 137] and references therein), while solutions based on Fourier-type integral representations, mode matching techniques and staircase approximation of the geometry are available for more general domains (e.g. [12] and references therein). Even for simple configurations, such as a circular cavity or bump on a perfectly conduction plane, the semi-analytical separation-of-variables method requires solution of an infinite dimensional linear system of equations that must be truncated to an $n \times n$ system and solved numer-

ically [60, 101, 102, 112, 127, 128]. As it happens, the resulting (full) matrix is extremely ill-conditioned for large values of n. In practice only limited accuracy results from use of such algorithms: use of small values of n naturally produces limited accuracy, while for large values of n matrix ill-conditioning arises as an accuracy limiting element.

Finite element and finite difference methods of low order of accuracy have been used extensively over the last decade [7, 8, 11, 54, 79, 129, 133, 135]. As is well known, finite element and finite difference methods lead to sparse linear systems. However, in order to satisfy the Sommerfeld radiation condition at infinity, a relatively large computational domain containing the scatterer must be utilized (unless a non-local boundary condition is used, with a consequent loss of sparsity). In view of the large required computational domains (or large coupled systems of equations for methods that use non-local domain truncation) and their low-order convergence (especially around corners where fields are singular and currents are infinite), these methods yield very slow convergence, and, therefore, for adequately accurate solutions, they require use of large numbers of unknowns and a high computational cost.

Boundary integral equation methods, on the other hand, lead to linear systems of reduced dimensionality, the associated solutions automatically satisfy the condition of radiation at infinity, and, unlike finite element methods, they do not suffer from dispersion errors. Integral equation methods have been used previously for the solution of the problem of scattering by an empty and dielectric-filled cavity on a perfectly conducting half-plane; see e.g. [61, 132, 136]. However, previous integral approaches for these problems are based on use of low-order numerical algorithms and, most importantly, they do not accurately account for singular field behavior at corners—and, thus, they may not be sufficiently accurate for evaluation of important physical mechanisms that arise from singular electrical currents and local fields at and around corners.

The present chapter is organized as follows. Section 3.1 presents a brief description of the various problems at hand and Section 3.2 introduces a new set of integral equations for their treatment. Section 3.3 then describes the high-order solvers we have developed for the numerical solution of these integral equations, which include full resolution of singular fields at corners. The excellent convergence properties of the equations and algorithms

introduced in this text are demonstrated in Section 3.4. In particular, the high accuracy of the new methods in presence of corner singularities can be used to evaluate the effects of corner singularities on currents and local fields on and around bumps and cavities, and thus on important physical observables such as absorption, extraordinary transmission, cavity resonance, etc.

(a) Dielectric bump on a half-plane.

(b) Dielectric-filled cavity on a half-plane.

(c) Dielectric-overfilled cavity on a half-plane.

(d) Void cavity on a half-plane.
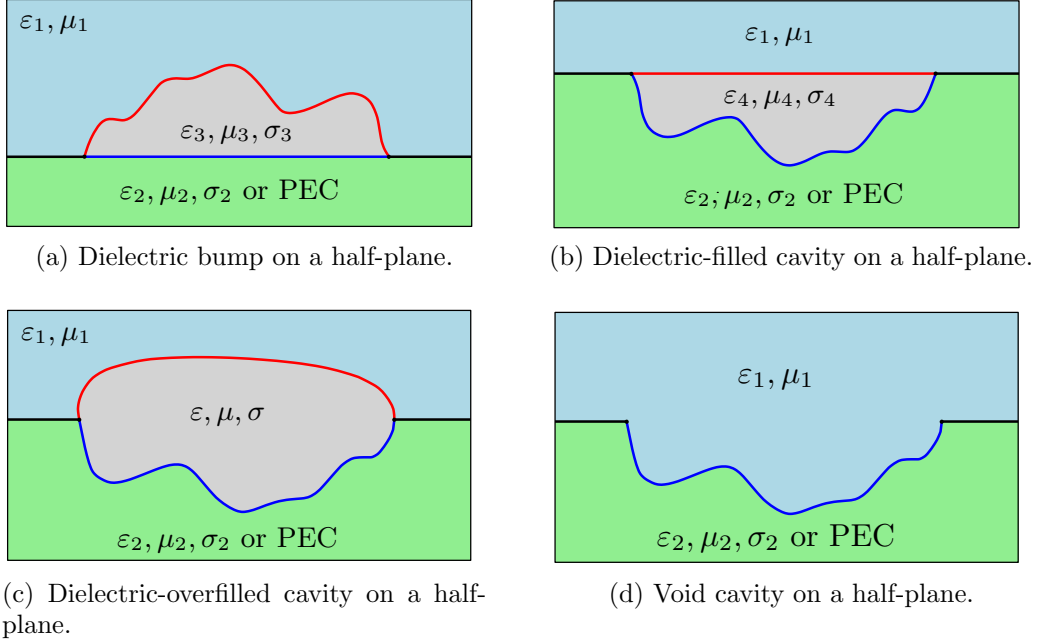
Figure 3.1: Schematics of the eight physical problems considered in this chapter.

3.1   Problem of scattering

All the problems considered in this chapter can be described mathematically following the compact depiction presented in Figure 3.2. Thus, a plane electromagnetic wave $(\mathbf{E}^{\text{inc}}, \mathbf{H}^{\text{inc}})$, which is defined in (2.12), impinges on a defect formed by the subdomains Ω_3 and Ω_4, which lies on the boundary of an otherwise planar horizontal interface between the infinite subdomains Ω_1 and Ω_2. As we showed in Section 2.2.1, the z components $u = E_z$ and $u = H_z$ of the total electric and magnetic field satisfy the Helmholtz equation

$$\Delta u + k_j^2 u = 0 \quad \text{in} \quad \Omega_j, \tag{3.1}$$

where, letting ω, ε_j and μ_j denote the angular frequency, the complex electric permittivity and the magnetic permeability of the medium Ω_j, the wavenumber k_j, defined in (2.7), is given by $k_j^2 = \omega^2 \varepsilon_j \mu_j$, $1 \leq j \leq 4$. Throughout this chapter it is assumed that Ω_1 is a lossless medium ($\sigma_1 = 0$).

In order to formulate transmission problems for the transverse components of the electromagnetic field, u is expressed as

$$u = \begin{cases} u_j & \text{in } \Omega_j, \ j = 3, 4, \\ u_j + u^f & \text{in } \Omega_j, \ j = 1, 2, \end{cases} \tag{3.2}$$

where u^f is the solution of the problem of scattering by the lower half-plane *in absence of the dielectric defect*. Note that, in particular, u^f satisfies appropriate transmission/boundary conditions at the flat interface Γ_{12} between Ω_1 and Ω_2. The solution u^f can be computed explicitly for each one of the problems considered in this chapter. For the problems in which Ω_2 is a perfectly flat PEC half-plane, u^f is given in (2.15), while for the problems in which Ω_2 is a flat dielectric or conducting half-plane, u^f is given in (2.13).
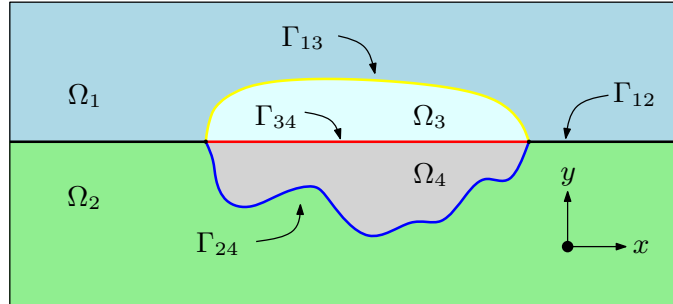
Figure 3.2: Compact mathematical description of the problems considered in this section.

Additionally, u satisfies the transmission conditions (2.9) which can be expressed as

$$u_i = u_j + g, \quad \text{and} \quad \nu_{ij} \frac{\partial u_i}{\partial n} = \frac{\partial u_j}{\partial n} + \frac{\partial g}{\partial n}, \tag{3.3}$$

at the interface Γ_{ij} between Ω_i and Ω_j, where $\nu_{ij} = \mu_j/\mu_i$ in TE-polarization and $\nu_{ij} = \varepsilon_j/\varepsilon_i$ in TM-polarization. For each one of the problems considered in this chapter, transmission conditions (3.3) are satisfied on Γ_{13} with $g = u^f$. In the case in which Ω_2 is filled by a

dielectric material the transmission conditions (3.3) are also satisfied with boundary data $g = u^f$ on Γ_{24}, and they are satisfied with boundary data $g = 0$ on Γ_{34}. On the other hand, from (2.11) we have that for the problem in which Ω_2 is a PEC half-plane, $u_2 = 0$ and, thus, the boundary conditions

$$u_j = 0 \quad \text{and} \quad \frac{\partial u_j}{\partial n} = 0, \quad j = 2, 3 \tag{3.4}$$

are satisfied on Γ_{2j} in TE- and TM-polarization, respectively. Additionally, we require that the scattering fields, which in this formulation correspond to u_j, $j = 1, 2$ in (3.2), satisfy the Sommerfeld radiation condition [45] at infinity:

$$\lim_{|\boldsymbol{r}| \to \infty} \sqrt{|\boldsymbol{r}|} \left\{ \frac{\partial u_j}{\partial |\boldsymbol{r}|}(\boldsymbol{r}) - ik_j u_j(\boldsymbol{r}) \right\} = 0 \quad \text{uniformly in all directions} \quad \frac{\boldsymbol{r}}{|\boldsymbol{r}|} \in \Omega_j, \ j = 1, 2. \tag{3.5}$$

Uniqueness results for the problems of scattering considered in this chapter can be found in [74, 110] for the cases in which Ω_2 is occupied by a dielectric or conducting material, and in [9, 139] for the cases in which Ω_2 is occupied by a PEC. In what follows of this chapter we assume that there exist unique, sufficiently regular, solutions to all of the problems of scattering considered.

3.2   Integral equation formulations

Three main problem types can be identified in connection with Figure 3.2, namely *Problem Type I*, where transmission conditions (3.3) are imposed on Γ_{13} and Γ_{24} (which, in our context, characterize the problem of scattering by a dielectric bump on a dielectric half-plane as well as the problems of scattering by a filled, overfilled or empty cavity on a dielectric half-plane); *Problem Type II*, where transmission conditions (3.3) are imposed on Γ_{13} and the PEC boundary condition (3.4) is imposed on Γ_{24}, which applies to the problem of scattering by a (filled, overfilled or empty) cavity on a PEC half-plane; and *Problem Type III*, where transmission conditions (3.3) are only imposed on Γ_{13}, with application to the problem of scattering by a dielectric bump on a perfectly conducting half-plane. In the following three

sections we derive systems of boundary integral equations for each one of these problem types.

3.2.1 Problem Type I

In Problem Type I the domains Ω_j $(1 \leq j \leq 4)$ contain dielectric media of finite or zero conductivity; we denote by k_j the (real or complex) wavenumber in the domain Ω_j. Note that

- For the problem of scattering by a *dielectric-filled cavity on dielectric half-plane* we have $k_1 = k_3, k_3 \neq k_4, k_4 \neq k_2, k_1 \neq k_2$;

- For the problem of scattering by an *overfilled cavity on dielectric half-plane* we have $k_1 \neq k_3, k_3 = k_4, k_4 \neq k_2, k_1 \neq k_2$; and

- For the problem of scattering by a *void cavity on a dielectric half-plane* we have $k_1 = k_3, k_3 = k_4, k_4 \neq k_2, k_1 \neq k_2$.

To tackle the Type I problem we express the total field u in (3.2) by means the single-layer-potential representation

$$
u = \begin{cases} \mathcal{S}_{\text{int}}[\psi_{\text{int}}] & \text{in} \quad \Omega_3 \cup \Omega_4, \\ \mathcal{S}_{\text{ext}}[\psi_{\text{ext}}] + u^f & \text{in} \quad \Omega_1 \cup \Omega_2, \end{cases} \tag{3.6}
$$

in terms of the unknown density functions ψ_{int} and ψ_{ext} where, letting $G_{k_j}^{k_i} = G$ denote the layer Green function (2.27) of the Helmholtz equation for the two-layer medium with wavenumbers k_i and k_j in the upper and lower half-planes respectively (see Section 2.3.1 for details), we have set

$$
\mathcal{S}_{\text{int}}[\psi](\boldsymbol{r}) = \int_{\Gamma_{13} \cup \Gamma_{24}} G_{k_4}^{k_3}(\boldsymbol{r}, \boldsymbol{r}')\psi(\boldsymbol{r}') \, \mathrm{d}s_{\boldsymbol{r}'}, \tag{3.7a}
$$

$$
\mathcal{S}_{\text{ext}}[\psi](\boldsymbol{r}) = \int_{\Gamma_{13} \cup \Gamma_{24}} G_{k_2}^{k_1}(\boldsymbol{r}, \boldsymbol{r}')\psi(\boldsymbol{r}') \, \mathrm{d}s_{\boldsymbol{r}'}. \tag{3.7b}
$$

The Green functions $G_{k_j}^{k_i}$ satisfy the transmission conditions (3.3) on Γ_{ij} (with (ij) equal to either (12) or (34)) and, therefore, they depend on the polarization (through the parameter ν_{ij}). Note, further, that for $k_i = k_j = k$ the Green function $G_{k_j}^{k_i}$ equals the free space Green function with wavenumber k.

It is easy to check that the representation (3.6) for the solution u satisfies the Helmholtz equation with wavenumber k_j in the domain Ω_j $(1 \leq j \leq 4)$ as well as the radiation conditions (3.5) at infinity (see Section 2.3.4 for details). Since the two-layer Green functions satisfy the relevant transmission conditions on Γ_{12} and Γ_{34}, there remain only two boundary conditions to be satisfied, namely, the transmission conditions (3.3) on the boundary of the defect $\Omega_3 \cup \Omega_4$. Using classical jump relations [45] for various layer potentials, these conditions lead to the system

$$
\begin{aligned}
S_{\text{int}}^{\Gamma_{13}}[\psi_{\text{int}}] - S_{\text{ext}}^{\Gamma_{13}}[\psi_{\text{ext}}] &= u^f, \\
\nu_{13} \left\{ \frac{\psi_{\text{int}}}{2} + K_{\text{int}}^{\Gamma_{13}}[\psi_{\text{int}}] \right\} + \frac{\psi_{\text{ext}}}{2} - K_{\text{ext}}^{\Gamma_{13}}[\psi_{\text{ext}}] &= \frac{\partial u^f}{\partial n}, \\
S_{\text{int}}^{\Gamma_{24}}[\psi_{\text{int}}] - S_{\text{ext}}^{\Gamma_{24}}[\psi_{\text{ext}}] &= u^f, \\
\nu_{24} \left\{ \frac{\psi_{\text{int}}}{2} + K_{\text{int}}^{\Gamma_{24}}[\psi_{\text{int}}] \right\} + \frac{\psi_{\text{ext}}}{2} - K_{\text{ext}}^{\Gamma_{24}}[\psi_{\text{ext}}] &= \frac{\partial u^f}{\partial n}
\end{aligned}
\tag{3.8}
$$

of boundary integral equations on the open curves Γ_{13} and Γ_{24} for the unknowns ψ_{int} and ψ_{ext}. The boundary integral operators in (3.8) for $(ij) = (13)$ and $(ij) = (24)$ are given by

$$
\begin{aligned}
S_{\text{int}}^{\Gamma_{ij}}[\psi](\boldsymbol{r}) &= \int_{\Gamma_{13} \cup \Gamma_{24}} G_{k_4}^{k_3}(\boldsymbol{r}, \boldsymbol{r}') \psi(\boldsymbol{r}') \, ds_{\boldsymbol{r}'}, \ \boldsymbol{r} \in \Gamma_{ij}, \\
S_{\text{ext}}^{\Gamma_{ij}}[\psi](\boldsymbol{r}) &= \int_{\Gamma_{13} \cup \Gamma_{24}} G_{k_2}^{k_1}(\boldsymbol{r}, \boldsymbol{r}') \psi(\boldsymbol{r}') \, ds_{\boldsymbol{r}'}, \ \boldsymbol{r} \in \Gamma_{ij}, \\
K_{\text{int}}^{\Gamma_{ij}}[\psi](\boldsymbol{r}) &= \int_{\Gamma_{13} \cup \Gamma_{24}} \frac{\partial G_{k_4}^{k_3}}{\partial n_{\boldsymbol{r}}}(\boldsymbol{r}, \boldsymbol{r}') \psi(\boldsymbol{r}') \, ds_{\boldsymbol{r}'}, \ \boldsymbol{r} \in \Gamma_{ij}, \\
K_{\text{ext}}^{\Gamma_{ij}}[\psi](\boldsymbol{r}) &= \int_{\Gamma_{13} \cup \Gamma_{24}} \frac{\partial G_{k_2}^{k_1}}{\partial n_{\boldsymbol{r}}}(\boldsymbol{r}, \boldsymbol{r}') \psi(\boldsymbol{r}') \, ds_{\boldsymbol{r}'}, \ \boldsymbol{r} \in \Gamma_{ij}.
\end{aligned}
\tag{3.9}
$$

The following lemma establishes the uniqueness of solutions of the integral equation system (3.8):

Lemma 3.2.1. *Under the assumptions laid out in Section 3.1 on the physical parameters* k_j, $j = 1, \ldots, 4$, *the system of integral equations* (3.8) *admits at most one solution, unless the exterior wavenumbers* k_1 *and* k_2 *are such that there exists an interior Dirichlet eigenfunction* $v : \Omega_3 \cup \Omega_4 \to \mathbb{C}$ *that satisfies:*

$$
\begin{cases}
\Delta v + k_1^2 v = 0 & in \quad \Omega_3, \\[4pt]
\Delta v + k_2^2 v = 0 & in \quad \Omega_4, \\[4pt]
v\big|_{y=0^+} = v\big|_{y=0^-} & on \quad \Gamma_{34}, \\[4pt]
\nu_{12} \dfrac{\partial v}{\partial n}\bigg|_{y=0^+} = \dfrac{\partial v}{\partial n}\bigg|_{y=0^-} & on \quad \Gamma_{34}, \\[4pt]
v = 0 & on \quad \Gamma_{13}, \\[4pt]
v = 0 & on \quad \Gamma_{24}.
\end{cases}
\tag{3.10}
$$

Proof. Let ψ_{int} and ψ_{ext} be solutions of the homogeneous ($u^f = 0$) integral equation system (3.8) and assume that, for the given exterior wavenumbers k_1 and k_2, the interior boundary value problem (3.10) admits only the trivial solution. Defining the single-layer potentials

$$
v = \mathcal{S}_{\text{ext}}[\psi_{\text{ext}}] \quad \text{and} \quad w = \mathcal{S}_{\text{int}}[\psi_{\text{int}}],
\tag{3.11}
$$

it then follows, by uniqueness of the PDE boundary value problem (cf. [74]), that $v = 0$ in $\Omega_1 \cup \Omega_2$ and $w = 0$ in $\Omega_3 \cup \Omega_4$. Furthermore, since v satisfies (3.10), it follows by hypothesis that $v = 0$ in $\Omega_3 \cup \Omega_4$. Thus the single layer potential v vanishes throughout $\mathbb{R}^2$ and, in view of the jump relation for the normal derivative of the single-layer potential, we conclude $\psi_{\text{ext}} = 0$ on $\Gamma_{13} \cup \Gamma_{24}$.

On the other hand, the relation $S_{\text{int}}^{\Gamma_{ij}}[\psi_{\text{int}}] = 0$ for $(ij) = (13), (24)$ tells us that w is a solution of the Helmholtz equation in the exterior domain $\Omega_1 \cup \Omega_2$, with wavenumbers k_3 in Ω_1 and k_4 in Ω_2, which satisfies homogeneous Dirichlet boundary conditions on $\Gamma_{13} \cup \Gamma_{24}$ as well as homogeneous transmission conditions on Γ_{12}. But, under the conditions $\operatorname{Re} k_3 > 0$, $\operatorname{Im} k_3 \geq 0$ and $\operatorname{Re} k_4 > 0$, $\operatorname{Im} k_4 \geq 0$ that are generally satisfied by the physical constants (Section 3.1) the exterior Dirichlet problem admits an unique solution (cf. [74]). Consequently, $w = 0$ in

$\Omega_1 \cup \Omega_2$. Thus, the single-layer potential w vanishes throughout $\mathbb{R}^2$. Invoking once again normal-derivative jump relations we conclude that $\psi_{\text{int}} = 0$ on $\Gamma_{13} \cup \Gamma_{24}$. The proof is now complete. $\qquad\square$

3.2.2 Problem Type II

In Problem Type II the domain Ω_2 contains a PEC medium, and the domains Ω_j, $j = 1, 3, 4$ contain dielectric media of finite or zero conductivity. Clearly,

- For the problem of scattering by a *dielectric-filled cavity on PEC half-plane* we have $k_1 = k_3, k_3 \neq k_4$;

- For the problem of scattering by an *overfilled cavity on PEC half-plane* we have $k_1 \neq k_3, k_3 = k_4$; and

- For the problem of scattering by a *void cavity on PEC half-plane* we have $k_1 = k_3, k_3 = k_4$.

For Type II problems we express the total field u by means of the single-layer-potential representation

$$
u = \begin{cases}
\mathcal{S}_{\text{int}}[\psi_{\text{int}}] & \text{in} \quad \Omega_3 \cup \Omega_4, \\[2mm]
\mathcal{S}_{\text{ext}}[\psi_{\text{ext}}] + u^f & \text{in} \quad \Omega_1, \\[2mm]
0 & \text{in} \quad \Omega_2,
\end{cases}
\tag{3.12}
$$

where, defining $G_{k_4}^{k_3}$ as in Section 3.2.1 and letting $G_0^{k_1}$ denote the Green function that satisfies the PEC boundary condition (3.4) on Γ_{12}, the potentials above are defined by

$$
\mathcal{S}_{\text{int}}[\psi](\boldsymbol{r}) = \int_{\Gamma_{13} \cup \Gamma_{24}} G_{k_4}^{k_3}(\boldsymbol{r}, \boldsymbol{r}')\psi(\boldsymbol{r}')\,\mathrm{d}s_{\boldsymbol{r}'},
\tag{3.13a}
$$

$$
\mathcal{S}_{\text{ext}}[\psi](\boldsymbol{r}) = \int_{\Gamma_{13}} G_0^{k_1}(\boldsymbol{r}, \boldsymbol{r}')\psi(\boldsymbol{r}')\,\mathrm{d}s_{\boldsymbol{r}'}.
\tag{3.13b}
$$

As mentioned in Section 3.2.1 the Green function $G_{k_j}^{k_i}$ depends on the polarization; the same is of course true for $G_0^{k_1}$, which is given by $G_0^k(\boldsymbol{r}, \boldsymbol{r}') = G_k(\boldsymbol{r}, \boldsymbol{r}') - G_k(\boldsymbol{r}, \bar{\boldsymbol{r}}')$ in TE-polarization, and $G_0^k(\boldsymbol{r}, \boldsymbol{r}') = G_k(\boldsymbol{r}, \boldsymbol{r}') + G_k(\boldsymbol{r}, \bar{\boldsymbol{r}}')$ in TM-polarization, where $\bar{\boldsymbol{r}}' = (x', -y')$

and where $G_k(\boldsymbol{r}, \boldsymbol{r}') = iH_0^{(1)}(k|\boldsymbol{r} - \boldsymbol{r}'|)/4$ is the free-space Green function. By virtue of the integral representation (3.12) the field satisfies the Helmholtz equation in the domain Ω_j with wavenumber k_j, $j = 1, 3, 4$, the radiation condition at infinity, transmission conditions on Γ_{34} and the PEC boundary conditions on Γ_{12}. Imposing the remaining transmission conditions (3.3) on Γ_{13} and PEC boundary condition (3.4) of Γ_{24}, we obtain the equations

$$
\begin{aligned}
S_{\text{int}}^{\Gamma_{13}}[\psi_{\text{int}}] - S_{\text{ext}}^{\Gamma_{13}}[\psi_{\text{ext}}] &= u^f, \\
\nu_{13} \left\{ \frac{\psi_{\text{int}}}{2} + K_{\text{int}}^{\Gamma_{13}}[\psi_{\text{int}}] \right\} + \frac{\psi_{\text{ext}}}{2} - K_{\text{ext}}^{\Gamma_{13}}[\psi_{\text{ext}}] &= \frac{\partial u^f}{\partial n},
\end{aligned}
\tag{3.14a}
$$

on Γ_{13} (valid for both TE- and TM- polarizations provided the corresponding constant ν_{ij} and Green functions are used) and

$$
\frac{\psi_{\text{int}}}{2} + K_{\text{int}}^{\Gamma_{24}}[\psi_{\text{int}}] = 0 \quad \text{(TE-polarization)}
\tag{3.14b}
$$

$$
S_{\text{int}}^{\Gamma_{24}}[\psi_{\text{int}}] = 0 \quad \text{(TM-polarization)}
\tag{3.14c}
$$

on Γ_{24}. In accordance with the definition of the single-layer potentials (3.13), the boundary integral operators in (3.14) for $(ij) = (13)$ and $(ij) = (24)$ are given by

$$
\begin{aligned}
S_{\text{int}}^{\Gamma_{ij}}[\psi](\boldsymbol{r}) &= \int_{\Gamma_{13} \cup \Gamma_{24}} G_{k_4}^{k_3}(\boldsymbol{r}, \boldsymbol{r}')\psi(\boldsymbol{r}')\, \mathrm{d}s_{\boldsymbol{r}'}, \ \boldsymbol{r} \in \Gamma_{ij}, \\
S_{\text{ext}}^{\Gamma_{ij}}[\psi](\boldsymbol{r}) &= \int_{\Gamma_{13}} G_0^{k_1}(\boldsymbol{r}, \boldsymbol{r}')\psi(\boldsymbol{r}')\, \mathrm{d}s_{\boldsymbol{r}'}, \ \boldsymbol{r} \in \Gamma_{ij}, \\
K_{\text{int}}^{\Gamma_{ij}}[\psi](\boldsymbol{r}) &= \int_{\Gamma_{13} \cup \Gamma_{24}} \frac{\partial G_{k_4}^{k_3}}{\partial n_{\boldsymbol{r}}}(\boldsymbol{r}, \boldsymbol{r}')\psi(\boldsymbol{r}')\, \mathrm{d}s_{\boldsymbol{r}'}, \ \boldsymbol{r} \in \Gamma_{ij}, \\
K_{\text{ext}}^{\Gamma_{ij}}[\psi](\boldsymbol{r}) &= \int_{\Gamma_{13}} \frac{\partial G_0^{k_1}}{\partial n_{\boldsymbol{r}}}(\boldsymbol{r}, \boldsymbol{r}')\psi(\boldsymbol{r}')\, \mathrm{d}s_{\boldsymbol{r}'}, \ \boldsymbol{r} \in \Gamma_{ij}.
\end{aligned}
\tag{3.15}
$$

The following lemma, whose proof is analogous to the one given for Lemma 3.2.1, establishes the conditions for uniqueness of solutions of the integral equation system (3.14).

Lemma 3.2.2. *The system of integral equations* (3.14) *admits at most one solution unless the exterior wavenumber k_1 is such that there exists an interior Dirichlet (in TE-polarization)*

or mixed Dirichlet-Neumann (in TM-polarization) eigenfunction $v : \Omega_3 \to \mathbb{C}$ satisfying

$$
\begin{cases}
\Delta v + k_1^2 v = 0 & in \quad \Omega_3, \\
\quad\quad v = 0 & on \quad \Gamma_{13}, \\
\quad\quad v = 0 & on \quad \Gamma_{34} \quad in\ TE\text{-}polarization, \\
\dfrac{\partial v}{\partial n} = 0 & on \quad \Gamma_{34} \quad in\ TM\text{-}polarization.
\end{cases}
\tag{3.16}
$$

3.2.3 Problem Type III

For Problem Type III the domains Ω_j, $j = 1, 3$, contain dielectric media of finite or zero conductivity and the domains Ω_j, $j = 2, 4$, are filled by a PEC material. Note that

– For the problem of scattering by a *dielectric bump on PEC half-plane* we have $k_3 \neq k_1$.

As in the previous cases, for Type III problems the total field u is expressed by means of the single-layer-potential representation

$$
u =
\begin{cases}
\mathcal{S}_{\text{int}}[\psi_{\text{int}}] & in \quad \Omega_3, \\
\mathcal{S}_{\text{ext}}[\psi_{\text{ext}}] + u^f & in \quad \Omega_1, \\
0 & in \quad \Omega_2 \cup \Omega_4,
\end{cases}
\tag{3.17}
$$

where the potentials above are defined by

$$
\mathcal{S}_{\text{int}}[\psi](\boldsymbol{r}) = \int_{\Gamma_{13}} G_0^{k_3}(\boldsymbol{r}, \boldsymbol{r}')\psi(\boldsymbol{r})\,\mathrm{d}s_{\boldsymbol{r}'}, \tag{3.18a}
$$

$$
\mathcal{S}_{\text{ext}}[\psi](\boldsymbol{r}) = \int_{\Gamma_{13}} G_0^{k_1}(\boldsymbol{r}, \boldsymbol{r}')\psi(\boldsymbol{r})\,\mathrm{d}s_{\boldsymbol{r}'}. \tag{3.18b}
$$

As mentioned in Section 3.2.2, the Green functions $G_0^{k_1}$ and $G_0^{k_3}$ depend on the polarization and satisfy the PEC boundary condition on Γ_{12} and Γ_{34} respectively. The total field, as given by the potentials (3.18), satisfies Helmholtz equations with wavenumber k_j in the domain Ω_j, $j = 1, 3$, PEC boundary condition on Γ_{24} and Γ_{12}, as well as the radiation condition at infinity. Imposing the transmission conditions (3.3) on Γ_{13} the following system of boundary

integral equations is obtained for the unknown density functions ψ_{int} and ψ_{ext}:

$$
\begin{aligned}
S_{\text{int}}^{\Gamma_{13}}[\psi_{\text{int}}] - S_{\text{ext}}^{\Gamma_{13}}[\psi_{\text{ext}}] &= u^f, \\
\frac{\beta_3}{\beta_1}\left\{\frac{\psi_{\text{int}}}{2} - K_{\text{int}}^{\Gamma_{13}}[\psi_{\text{int}}]\right\} + \frac{\psi_{\text{ext}}}{2} - K_{\text{ext}}^{\Gamma_{13}}[\psi_{\text{ext}}] &= \frac{\partial u^f}{\partial n},
\end{aligned}
\tag{3.19}
$$

on Γ_{13}, where the boundary integral operators are defined by

$$
\begin{aligned}
S_{\text{int}}^{\Gamma_{13}}[\psi](\boldsymbol{r}) &= \int_{\Gamma_{13}} G_0^{k_3}(\boldsymbol{r}, \boldsymbol{r}')\psi(\boldsymbol{r}')\,\mathrm{d}s_{\boldsymbol{r}'}, \ \ \boldsymbol{r} \in \Gamma_{13}, \\
S_{\text{ext}}^{\Gamma_{13}}[\psi](\boldsymbol{r}) &= \int_{\Gamma_{13}} G_0^{k_1}(\boldsymbol{r}, \boldsymbol{r}')\psi(\boldsymbol{r}')\,\mathrm{d}s_{\boldsymbol{r}'}, \ \ \boldsymbol{r} \in \Gamma_{13}, \\
K_{\text{int}}^{\Gamma_{13}}[\psi](\boldsymbol{r}) &= \int_{\Gamma_{13}} \frac{\partial G_0^{k_3}}{\partial n_{\boldsymbol{r}}}(\boldsymbol{r}, \boldsymbol{r}')\psi(\boldsymbol{r}')\,\mathrm{d}s_{\boldsymbol{r}'}, \ \ \boldsymbol{r} \in \Gamma_{13}, \\
K_{\text{ext}}^{\Gamma_{13}}[\psi](\boldsymbol{r}) &= \int_{\Gamma_{13}} \frac{\partial G_0^{k_1}}{\partial n_{\boldsymbol{r}}}(\boldsymbol{r}, \boldsymbol{r}')\psi(\boldsymbol{r}')\,\mathrm{d}s_{\boldsymbol{r}'}, \ \ \boldsymbol{r} \in \Gamma_{13}.
\end{aligned}
\tag{3.20}
$$

The conditions under which the integral equation system (3.19) admits a unique solution are the ones established in Lemma 3.2.2 for the uniqueness of solutions of the integral equation system (3.14).

3.3   Nyström method

3.3.1   Discretization of integral equations

The integral equations (3.8), (3.14) and (3.19) involve either a) Integrals over $\Gamma_{13} \cup \Gamma_{24}$ with equality enforced on $\Gamma_{13} \cup \Gamma_{24}$, or given by b) Integrals over Γ_{13} with equality enforced on Γ_{13}. All of these integral equations can be expressed in terms of parametrizations of the curves Γ_{13} and Γ_{24}, or, more precisely, in terms of integrals of the form

$$
\int_0^{2\pi} L(t, \tau)\phi(\tau)\,\mathrm{d}\tau \quad \text{and} \quad \int_0^{2\pi} M(t, \tau)\phi(\tau)\,\mathrm{d}\tau, \tag{3.21}
$$

with kernels

$$
\begin{aligned}
L(t,\tau) &= G(\boldsymbol{r}(t), \boldsymbol{r}'(\tau))|\boldsymbol{r}''(\tau)|, \\
M(t,\tau) &= \nabla_{\boldsymbol{r}}[G](\boldsymbol{r}(t), \boldsymbol{r}'(\tau)) \cdot n(t)|\boldsymbol{r}''(\tau)|,
\end{aligned}
\tag{3.22}
$$

where *i)* each of the functions $\boldsymbol{r}(t)$ and $\boldsymbol{r}'(\tau)$ denote either a parametrization for the curve Γ_{13} or of the curve Γ_{24} with parameters t and τ in the interval $(0, 2\pi)$; *ii)* $n(t) = (x_2'(t), -x_1'(t))/|\boldsymbol{r}'(t)|$ denotes the unit normal on Γ_{13} or Γ_{24}, as appropriate, which points outward from the defect; *iii)* $\phi(\tau) = \psi(\boldsymbol{r}'(\tau))$, where ψ stands for the unknown density function under consideration; and *iv)* G denotes the relevant Green function. Indeed, in case a) above, the integral over $\Gamma_{13} \cup \Gamma_{24}$ can be expressed as a sum of integrals on Γ_{13} and Γ_{24}. In case b), in particular, we take $\boldsymbol{r} = \boldsymbol{r}'$.

Our discretization of the integral equations (3.8), (3.14) and (3.19) is based on corresponding discretizations of the integrals (3.21). Following [44] we thus proceed by expressing the kernels (3.22) in the form

$$
\begin{aligned}
L(t,\tau) &= L_1(t,\tau) \log r^2(t,\tau) + L_2(t,\tau), \tag{3.23a} \\
M(t,\tau) &= M_1(t,\tau) \log r^2(t,\tau) + M_2(t,\tau), \tag{3.23b}
\end{aligned}
$$

where L_j and M_j ($j = 1, 2$) are smooth functions on $(0, 2\pi) \times (0, 2\pi)$ and where $\boldsymbol{r}(t,\tau) = \boldsymbol{r}(t) - \boldsymbol{r}'(\tau)$ and $r(t,\tau) = |\boldsymbol{r}(t,\tau)|$. In cases for which $\boldsymbol{r}(t)$ and $\boldsymbol{r}'(\tau)$ parametrize the same open curve we have

$$
\begin{aligned}
L_1(t,\tau) &= -\frac{1}{4\pi} J_0(kr(t,\tau))|\boldsymbol{r}''(\tau)|, \\
L_2(t,\tau) &= L(t,\tau) - L_1(t,\tau) \log r^2(t,\tau), \\
M_1(t,\tau) &= \frac{k}{4\pi} J_1(kr(t,\tau)) n(t) \cdot \frac{\boldsymbol{r}(t,\tau)}{r} |\boldsymbol{r}''(\tau)|, \\
M_2(t,\tau) &= M(t,\tau) - M_1(t,\tau) \log r^2(t,\tau).
\end{aligned}
$$

The diagonal terms $L_2(t,t)$ and $M_2(t,t)$ can be computed exactly by taking the limit of $L_2(t,\tau)$ and $M_2(t,\tau)$ as $\tau \to t$ (see [44, p. 77] for details). On the other hand, when $\boldsymbol{r}(t)$ and $\boldsymbol{r}'(\tau)$ parametrize different curves, L and M are smooth on $(0, 2\pi) \times (0, 2\pi)$ and, thus,

$L_1 = 0$, $L = L_2$, $M_1 = 0$ and $M = M_2$. (Note that although in the latter case L and M are smooth functions, these functions are in fact *nearly singular*, for t near the endpoints of the parameter interval $(0, 2\pi)$ for the curve $\boldsymbol{r}$, and for τ around the corresponding endpoint of the parameter interval for the curve $\boldsymbol{r'}$.)

Letting K denote one of the integral kernels L or M in equation (3.23), in view of the discussion above K may be expressed in the form $K(t, \tau) = K_1(t, \tau) \log r^2(t, \tau) + K_2(t, \tau)$ for smooth kernels K_1 and K_2. For a fixed t then, there are two types of integrands for which high-order quadratures must be provided, namely integrands that are smooth in $(0, 2\pi)$ but have singularities at the endpoints of the interval (that arise from corresponding singularities of the densities ϕ at the endpoints of the open curves; cf. [32, 88, 130]), and integrands that additionally have a logarithmic singularity at $\tau = t$. To handle both singular integration problems we follow [44, 70] and utilize a combination of a graded-meshes, the trapezoidal quadrature rule, and a quadrature rule that incorporates the logarithmic singularity into its quadrature weights—as described in what follows. Interestingly, the graded meshes and associated changes of variables gives rise to accurate integration even in the near-singular regions mentioned above in this section.

To introduce graded meshes we consider the polynomial change of variables $t = w(s)$ where

$$
\begin{aligned}
w(s) &= 2\pi \frac{[v(s)]^p}{[v(s)]^p + [v(2\pi - s)]^p}, \quad 0 \le s \le 2\pi, \quad (3.24) \\
v(s) &= \left(\frac{1}{p} - \frac{1}{2} \right) \left(\frac{\pi - s}{\pi} \right)^3 + \frac{1}{p} \frac{s - \pi}{\pi} + \frac{1}{2},
\end{aligned}
$$

and where $p \ge 2$. The function w is smooth and increasing on $[0, 2\pi]$, with $w^{(k)}(0) = w^{(k)}(2\pi) = 0$ for $1 \le k \le p - 1$. Using this transformation we express K as

$$
\begin{aligned}
K(t, \tau) &= K(w(s), w(\sigma)) \\
&= K_1(w(s), w(\sigma)) \log \left(4 \sin^2 \frac{s - \sigma}{2} \right) + \widetilde{K}_2(s, \sigma),
\end{aligned}
$$

where

$$\widetilde{K}_2(s,\sigma) = K_1(w(s), w(\sigma)) \log \left(\frac{r^2(w(s), w(\sigma))}{4 \sin^2 \frac{s-\sigma}{2}} \right) + K_2(w(s), w(\sigma)),$$

and where the diagonal term is given by $\widetilde{K}_2(s,\sigma) = 2K_1(t,t) \log(w'(s)|r'(t)|) + K_2(t,t)$. High-order accurate quadrature formulae for the integral operators (3.21) based on the $(2n-1)$–point discretization $\sigma_j = j\pi/n$, $1 \le j \le 2n-1$ (which, via the correspondence $\tau = w(\sigma)$ gives rise to a discrete quadrature formula for the integral over the curve parametrized by $r'(\tau)$) at evaluation points $t = t_i = w(s_i)$ with $s_i = i\pi/q$, $1 \le i \le 2q-1$ (which correspond to evaluation of the integral operator at points on the curve parametrized by $r(t)$) can easily be obtained [44] from the expressions

$$\int_0^{2\pi} f(\sigma) \, d\sigma \approx \frac{\pi}{n} \sum_{j=0}^{2n-1} f(\sigma_j) \tag{3.25}$$

and

$$\int_0^{2\pi} f(\sigma) \log \left(4 \sin^2 \frac{s-\sigma}{2} \right) d\sigma \approx \sum_{j=0}^{2n-1} R_j^{(n)}(s) f(\sigma_j),$$

$0 \le s \le 2\pi$, (which, for smooth functions f, yield high-order accuracy), where the weights $R_j(s)$ are given by

$$R_j(s) = -\frac{2\pi}{n} \sum_{m=1}^{n-1} \frac{1}{m} \cos m(s-\sigma_j) - \frac{\pi}{n^2} \cos n(s-\sigma_j).$$

Clearly setting $s = \sigma_i$ in this equation gives $R_j(\sigma_i) = R_{|i-j|}$, where

$$R_k = -\frac{2\pi}{n} \sum_{m=1}^{n-1} \frac{1}{m} \cos \frac{mk\pi}{n} - \frac{(-1)^k \pi}{n^2}.$$

Using these quadrature points and weights and corresponding parameter values $t = t_i = w(s_i)$ for the observation point ($s_i = i\pi/q$) we obtain the desired discrete approximation for

the integrals (3.21): for an approximation $\phi_j \approx \phi(\tau_j) = \phi(w(\sigma_j))$, we have

$$\int_0^{2\pi} K(t_i, \tau)\phi(\tau)\,\mathrm{d}\tau \approx \sum_{j=1}^{2n-1} \left\{ K_1(t_i, \tau_j)W_{ij} + K_2(t_i, \tau_j)\frac{\pi}{n} \right\} \phi_j\, w'(\sigma_j) \tag{3.26}$$

for $1 \leq i \leq 2q-1$, where $\tau_j = w(\sigma_j)$ and where the quadrature weights are given by

$$W_{ij} = R_{|i-j|} + \frac{\pi}{n} \log\left(\frac{r^2(t_i, t_j)}{4\sin^2(s_i - s_j)/2} \right).$$

Note that for sufficiently large values of p the product $\phi(w(\sigma))w'(\sigma)$, (an approximation of which appears in (3.26)) vanishes continuously at the endpoints of the parameter interval $[0, 2\pi]$—even in cases for which, as it happens for corners or points of junction between multiple dielectric materials, $\phi(w(\sigma))$ tends to infinity at the endpoints.

The systems of boundary integral equations (3.8), (3.14) and (3.19) are discretized by means of applications of the quadrature rule (3.26) to the relevant integral operators (3.9), (3.15) and (3.20), respectively. This procedure leads to linear systems of algebraic equations for the unknown values of the density functions ψ_{int} and ψ_{ext} at the quadrature points. The presence of the weight $w'(\sigma_j)$ in (3.26), which multiplies the unknowns $\phi_j \approx \phi(\tau_j)$ and which is very small for σ_j close to 0 and 2π, however, gives rise to highly ill conditioned linear systems. To avoid this difficulty we resort to the change of unknown $\eta_j = \phi_j w'(\sigma_j)$ in (3.26); for the equations which contain terms of the form $\psi_{\mathrm{int}}/2$ and $\psi_{\mathrm{ext}}/2$ it is additionally necessary to multiply both sides of the equation by $w'(\sigma_j)$ to avoid small denominators. In what follows, the resulting discrete linear systems for the problems under consideration are generically denoted by $\mathbf{A}\boldsymbol{\eta} = \mathbf{f}$ where, in each case $\boldsymbol{\eta}$ is a vector that combines the unknowns that result from the discretization procedure described above in this section for the various boundary portions Γ_{ij} (cf. Figure 3.2). Once $\boldsymbol{\eta}$ has been found, the numerical approximation of the scattered fields at a given point $\boldsymbol{r}$ in space, which in what follows will be denoted by $\tilde{u} = \tilde{u}(\boldsymbol{r})$, can be obtained by consideration of the relevant representation (3.7), (3.13) or (3.18). For evaluation points $\boldsymbol{r}$ sufficiently far from the integration curves these integrals can be accurately approximated using the change of variable $t = w(s)$ together

with the trapezoidal rule (3.25); for observation points near the integration curves, in turn, a procedure based on interpolation along a direction transverse to the curve is used (see [3] for details).

3.3.2   Solution at resonant and near-resonant frequencies

As mentioned in the introduction, despite the fact that each one of the physical problems considered in this contribution admit unique solutions for all frequencies ω and all physically admissible values of the dielectric constant and magnetic permeability, for certain values of ω spurious resonances occur: for such values of ω the systems of integral equations derived in Section 3.2 are not invertible. In fact, as it was shown in Propositions 3.2.1 and 3.2.2, spurious resonances for these systems arise whenever the wavenumber k_1, which will also be denoted by κ in what follows, is such that $-k_1^2 = -\kappa^2$ equals a certain Dirichlet eigenvalue. Note, in particular, that the values of κ for which spurious resonances occur are necessarily real numbers (and, thus, physically realizable), since the eigenvalues $-\kappa^2$ are necessarily negative).

It is important to note that, in addition to the spurious resonances mentioned above, the transmission problems considered in Section 3.1 *themselves* (and, therefore the corresponding systems of integral equations mentioned above) also suffer from non-uniqueness for certain *non-physical* values of κ ($\mathrm{Im}\,(\kappa) < 0$) which are known as "scattering poles" [123]; cf. Figure 3.4 and a related discussion below in this section.

The non-invertibility of the aforementioned continuous systems of integral equations at a spurious-resonance or scattering-pole wavenumber $\kappa = \kappa^*$ manifests itself at the discrete level in non-invertibility or ill-conditioning of the system matrix $\mathbf{A} := \mathbf{A}(\kappa)$ for values of κ close to κ^*. Therefore, for κ near κ^* the numerical solution of the transmission problems under consideration (which, in what follows will be denoted by $\tilde{u} := \tilde{u}_\kappa(\boldsymbol{r})$ to make explicit the solution dependence on the parameter κ) cannot be obtained via direct solution the linear system $\mathbf{A}\boldsymbol{\eta} = \mathbf{f}$. As is known, however [123], the solutions $u = u_\kappa$ of the continuous transmission problems are analytic functions of κ for all real values of κ—including, in particular, for κ equal to any one of the spurious resonances mentioned above and for real values

of κ near a scattering pole—and therefore, the approximate values $\tilde{u}_\kappa(\boldsymbol{r})$ for κ sufficiently far from κ^* can be used, via analytic continuation, to obtain corresponding approximations around $\kappa = \kappa^*$ and even at a spurious resonance $\kappa = \kappa^*$.

In order to implement this strategy for a given value of κ it is necessary for our algorithm to possess a capability to perform two main tasks, namely, Task I: Determination of whether κ is "sufficiently far" from any one of the spurious resonances and scattering poles κ^*; and Task II: Evaluation of analytic continuations to a given real wavenumber κ_0 which is either close or equal to a spurious resonance κ^*, or which lies close to a scattering pole κ^*. Once these capabilities are available the algorithm can be completed readily: if completion of Task I leads to the conclusion that κ is far from all spurious resonances then the solution process proceeds directly via solution of the associated system of integral equations. Otherwise, the solution process is completed by carrying out Task II. Descriptions of the proposed methodologies to perform Tasks I and II are presented in the following two sections.

3.3.2.1   Task I: matrix-singularity detection

Consider a given wavenumber κ' for which a solution to one of the problems under consideration needs to be obtained. As discussed in what follows, in order to determine the level of proximity of κ' to a spurious resonance or scattering pole κ^*, the matrix-singularity detection algorithm utilizes the minimum singular value $\sigma_{\min}(\kappa')$ of $\mathbf{A}(\kappa')$. (Note that in view of the discussion concerning Task I above in the present Section 3.3.2 it is not necessary to differentiate wavenumbers κ' that lie near to either a spurious resonance or to a scattering pole: both cases can be treated equally well by means of one and the same Task II (analytic continuation) algorithm (Section 3.3.2.2).

To introduce the matrix-singularity detection algorithm consider Figure 3.3: clearly, with exception of a sequence of wavenumbers (spurious resonances and/or real wavenumbers close to non-real scattering pole) around which the minimum singular value is small, the function $\sigma_{\min}(\kappa)$ maintains an essentially constant level. This property forms the basis of the matrix-singularity detection algorithm. Indeed, noting that there are no singularities for κ smaller than certain threshold (as it follows from the spectral theory for the Laplace

operator), we choose a wavenumber $\kappa_0 > 0$ close to zero and we compare $\sigma_{\min}(\kappa_0)$ with $\sigma_{\min}(\kappa')$. If $\sigma_{\min}(\kappa') \ll \sigma_{\min}(\kappa_0)$, say $\sigma_{\min}(\kappa') < \xi \cdot \sigma_{\min}(\kappa_0)$ for an adequately chosen value of ξ, κ' is determined to be close to a some singularity κ^*, and therefore the Task-II analytic-continuation algorithm is utilized to evaluate $\tilde{u}_{\kappa'}(\boldsymbol{r})$. The parameter values $\kappa_0 = 0.1$ and $\xi = 10^{-4}$ were used in all the numerical examples presented in this chapter.

(A remark is in order concerning the manifestations of resonances and scattering poles on the plots of the function $\sigma_{\min}(\kappa)$ as a function of the real variable κ. By definition the function $\sigma_{\min}(\kappa)$ vanishes exactly at all spurious resonances. The four sharp peaks shown in Figure 3.3, for example, occur at the spurious resonances listed in the inset of Figure 3.4. The first peak from the left in Figure 3.3, in contrast, is not sharp—as can be seen in the inset close-up included in the figure. The small value $\sigma_{\min}(\kappa) \sim 10^{-7}$ around $\kappa = 0.5708$ is explained by the presence of a scattering pole κ^*: $\sigma_{\min}(\kappa^*) = 0$ at the complex wavenumber $\kappa^* = 0.57807113743881 - 0.000074213015953i$. Thus scattering poles can in practice be quite close to the real κ axis, and thus give rise to rather sharp peaks which are not associated with actual spurious resonances. As mentioned above, however, the analytic continuation algorithm presented in what follows need not differentiate between these two types of singularities: analytic continuation is utilized whenever a sufficiently small value of $\sigma_{\min}$ is detected.)

3.3.2.2 Task II: analytic continuation

Analytic continuation of the numerical solution $\tilde{u}_\kappa(\boldsymbol{r})$ to a given wavenumber κ' detected as a matrix singularity (Section 3.3.2.1) is carried out via interpolation. Note, however, that, since $\mathbf{A}(\kappa)$ is generally extremely ill-conditioned for values of κ in a narrow interval around such wavenumbers κ', fine interpolation meshes cannot be utilized to achieve arbitrary accuracy in the approximation. To overcome this difficulty we utilize an interpolation method based on use of Chebyshev expansions, for which the meshsize is not allowed to be smaller than a certain tolerance, and within which convergence is achieved, in view of the analyticity of the scattered field with respect to the wavenumber κ, by increasing the order of the Chebyshev expansion. To do this for a given wavenumber κ' identified by the

matrix-singularity detection algorithm (Section 3.3.2.1), the analytic continuation algorithm proceeds by introducing a Chebyshev grid of points $\{\kappa_j\}_{j=1}^{2m}$ (cf. [63]) sorted in ascending order such that the two middle points in the grid, κ_m and κ_{m+1}, lie at an appropriately selected distance $\delta > 0$ from the wavenumber κ': $\kappa_m = \kappa' - \delta$ and $\kappa_{m+1} = \kappa' + \delta$.

The accuracy of the numerical evaluation of the field $\tilde{u}_{\kappa_j}$ at each one of the interpolation points κ_j is ensured by running the matrix-singularity detection algorithm at each κ_j and adequately changing the value of δ if a matrix-singularity is detected at one or more of the mesh points κ_j. Letting $\tilde{u}_\kappa^{(m)}$ denote the Chebyshev expansion of order $2m-1$ resulting for a Chebyshev mesh selected as indicated above, the sequence $\tilde{u}_{\kappa'}^{(m)}$ convergences exponentially fast to $\tilde{u}_{\kappa'}$ as m grows—as it befits Chebyshev expansions of analytic functions. If the matrix-singularity condition $\sigma_{\min}(\kappa_{j_\ell}) < \xi \cdot \sigma_{\min}(\kappa_0)$ occurs at one of more of the interpolation points κ_j, say κ_{j_ℓ}, $1 \leq \ell \leq L'$, the algorithm proceeds by selecting the smallest value of the parameter $\delta' > \delta$ and a new set of Chebyshev points $\{\kappa'_j\}_{j=1}^{2m'}$ ($m' \geq m$) satisfying $\kappa'_{m'} = \kappa' - \delta'$, $\kappa'_{m'+1} = \kappa' + \delta'$, such that none of the new interpolation points lie on the region $\bigcup_{\ell=1}^{L'}(\kappa_{j_\ell}-\delta, \kappa_{j_\ell}+\delta)$. If the condition $\sigma_{\min}(\kappa'_j) < \xi \cdot \sigma_{\min}(\kappa_0)$ occurs for some of the new interpolation points, say κ'_{j_ℓ}, $1 \leq \ell \leq L''$, the algorithm proceeds as described above, but for a new value $\delta'' > \delta'$, and so on. Note that in practice the interpolation procedure described above is rarely needed, and when it is needed, a suitable interpolation grid is usually found after a single iteration: in practice the choice $\delta = 0.01$ has given excellent results in all the examples presented in this chapter.

In order to demonstrate the fast convergence of $\tilde{u}_{\kappa'}^{(m)}$ to $\tilde{u}_{\kappa'}$ as m increases we consider the problem of scattering by a dielectric unit-radius semi-circular bump on a PEC half-plane. For this problem the wavenumbers κ^* for which the system of integral equations (3.19) is non-invertible can be computed explicitly: spurious resonances are given by real solutions of the equation $J_n(\kappa) = 0$, $n \geq 0$, where J_n denotes the Bessel function of first kind and order n [134], and scattering poles are complex valued solutions of $\kappa H_n^{(1)}(\kappa)J_n'(k_3) = k_3 J_n(k_3)H_n^{(1)'}(\kappa)$, where $H_n^{(1)}$ denotes the Hankel function of first kind and order n (see Appendix B.2). The function $\sigma_{\min}(\kappa)$ is displayed in Figure 3.3. The κ^* values identified in that figure coincide (up to machine precision) with the first four positive solutions of the equation $J_n(\kappa) = 0$. On
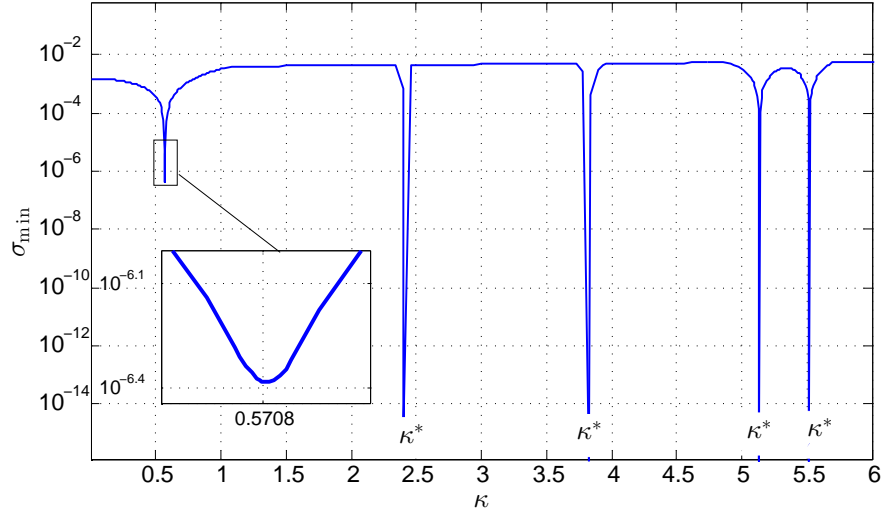
Figure 3.3: Minimum singular value of $\mathbf{A}$ as a function of $\kappa = k_1$ for the problem of scattering by a semi-circular bump on a PEC half-plane in TE-polarization.
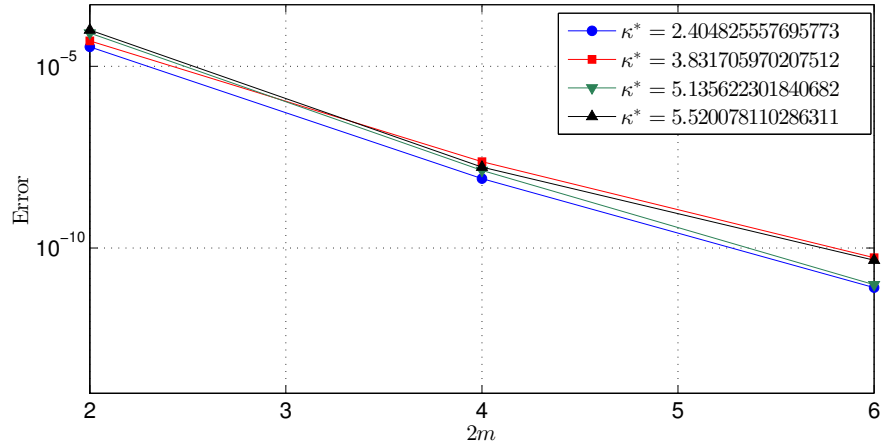
Figure 3.4: Error in the approximation of $\tilde{u}_{\kappa^*}$ by Chebyshev interpolation/analytic-continuation for various spurious resonant frequencies κ^* as a function of the order $2m$ of the Chebyshev expansion.

the other hand, this problem admits an analytical solution u_κ in terms of a Fourier-Bessel expansion (see Appendix B.1). The availability of the exact solution allows us to quantify the magnitude of interpolation error by evaluating the maximum of the error function $E(\boldsymbol{r}) = |\tilde{u}_{\kappa^*}^{(m)}(\boldsymbol{r}) - u_{\kappa^*}(\boldsymbol{r})|$ at a polar grid Π (consisting of points inside, outside and at the boundary of the semi-circular bump). Figure 3.4 shows the error $\max_{\boldsymbol{r} \in \Pi} E(\boldsymbol{r})$ versus the number of points used in the Chebyshev interpolation of $\tilde{u}_{\kappa^*}$, which is computed for the four spurious resonances k^* shown in Figure 3.3, and where a sufficiently fine spatial discretization is used.

In all the calculations $k_3 = 6$, the curve Γ_{13} is discretized using 128 points, and $\delta = 0.01$ is utilized to construct the Chebyshev grids.

3.4 Numerical examples

This section demonstrates the high accuracies and high-order convergence that result as the proposed boundary integral methods are applied to each one of the mathematical problems formulated in Section 3.2. For definiteness all dielectric media are assumed non-magnetic so that $\nu_{ij} = 1$ for TE-polarization and $\nu_{ij} = k_j^2/k_i^2$ for TM-polarization. In all the numerical examples shown in this section the incident plane-wave is parallel to the vector $\boldsymbol{d} = (\cos\alpha, \sin\alpha)^T$, $\alpha = -\pi/3$, and the graded-mesh parameter (3.24) is $p = 8$.

We thus consider the problem of scattering by a dielectric filled cavity on a dielectric half-plane (Problem Type I); the problem of scattering by a dielectric filled cavity on a PEC half-plane (Problem Type II); and the problem of scattering by a dielectric bump on a PEC half-plane (Problem Type III). With reference to Figure 3.2, in the first two examples the cavity is determined by the curve $\Gamma_{24} = \{(x,y) \in \mathbb{R}^2 : x = -\cos(\frac{t}{2}), y = \frac{\cos(4t)}{40}t(t-2\pi) - \sin(\frac{t}{2}), t \in (0, 2\pi)\}$, and the curve Γ_{13} (which, in view of the formulation in Section 3.2, may be selected rather arbitrarily as long as it lies in the upper half plane and has the same endpoints as Γ_{24}) is given by the semicircle of radius one in the upper half plane that joins the points $(1, 0)$ and $(-1, 0)$. For the problem of scattering by a dielectric bump (Type III Problem), in turn, the boundary of the bump is given by $\Gamma_{13} = \{(x,y) \in \mathbb{R}^2 : x = \cos(\frac{t}{2}), y = \frac{\cos(4t)}{40}t(2\pi - t) + \sin(\frac{t}{2}), t \in (0, 2\pi)\}$.

To estimate the error in the aforementioned numerical test problems, the systems of boundary integral equations (3.8), (3.14) and (3.19) were discretized utilizing five different meshes Π_j, $1 \le j \le 5$ consisting of $P = 2^{j+5} - 1$ points distributed along each one of the relevant boundaries: P points on Γ_{24} and P points on Γ_{13} in the case of Type I and II problems, and P points on Γ_{13} in the case of Type III Problem. The sequence of meshes is chosen to be nested ($\Pi_j \subset \Pi_i$ for $j < i$) in order to facilitate the convergence analysis; in what follows the numerical solution that results from the discretization Π_j is denoted by $\tilde{u}_j$.

(a) TM-polarization.

(b) TE-polarization.

(c) TM-polarization.

(d) TE-polarization.

(e) TM-polarization.

(f) TE-polarization.

Figure 3.5: Diffraction pattern resulting from the scattering of a plane-wave by; a dielectric-filled cavity on a dielectric half-plane ((a) and (b)); a dielectric-filled cavity on a PEC half-plane ((c) and (d)); a dielectric bump on a PEC half-plane ((e) and (f)).

The error in the numerical solution $\tilde{u}_j$ is estimated by means of the expression

$$E_j = \frac{\max_{\boldsymbol{r} \in \Pi_1} |\tilde{u}_j(\boldsymbol{r}) - \tilde{u}_5(\boldsymbol{r})|}{\max_{\boldsymbol{r} \in \Pi_1} |\tilde{u}_5(\boldsymbol{r})|}, \quad 1 \le j \le 4.$$

Table 3.1 presents the numerical error estimates E_j, $1 \le j \le 5$ for the three different problem types (including real and complex wavenumbers); clearly high accuracies and fast convergence is achieved in all cases. To further illustrate the results provided by the proposed method, the real part of the total field is presented in Figures 3.5 and 3.6 for the cases considered in Table 3.1, including examples for TM- and TE-polarization. Thus, Figures 3.5a-3.5b

(a) TM-polarization.

(b) TE-polarization.

(c) TM-polarization.

(d) TE-polarization.
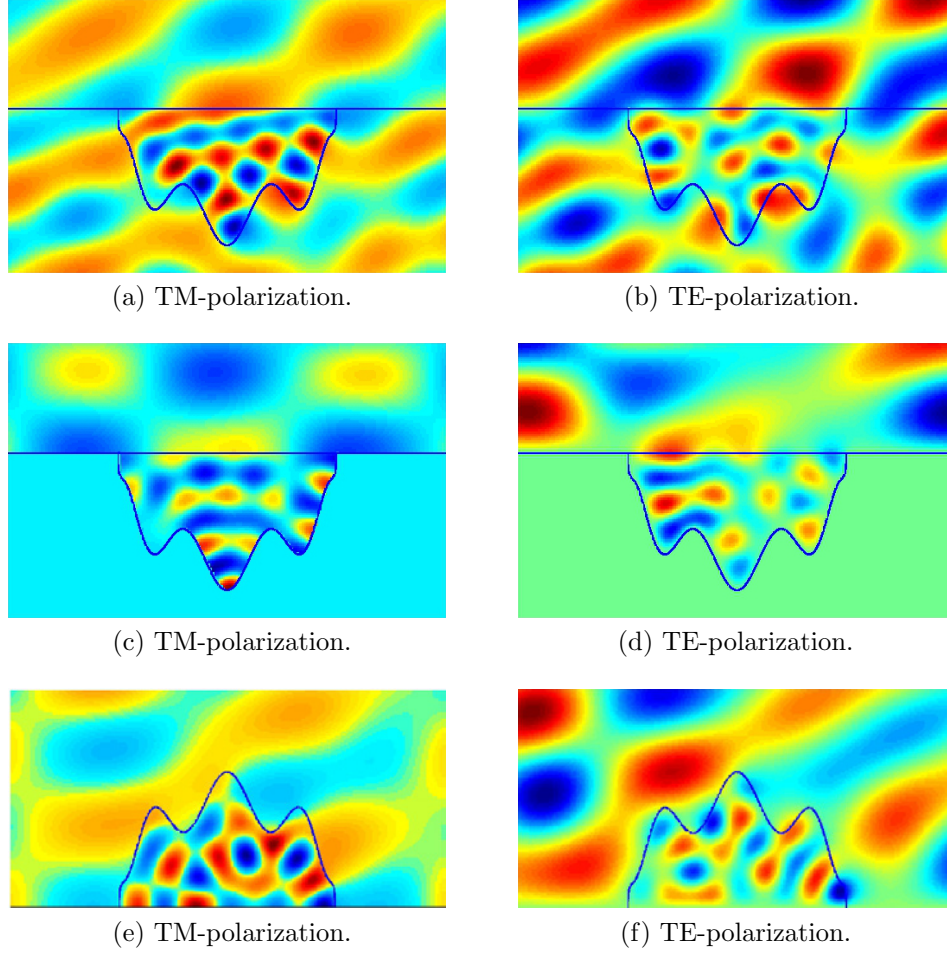
(e) TM-polarization.

(f) TE-polarization.
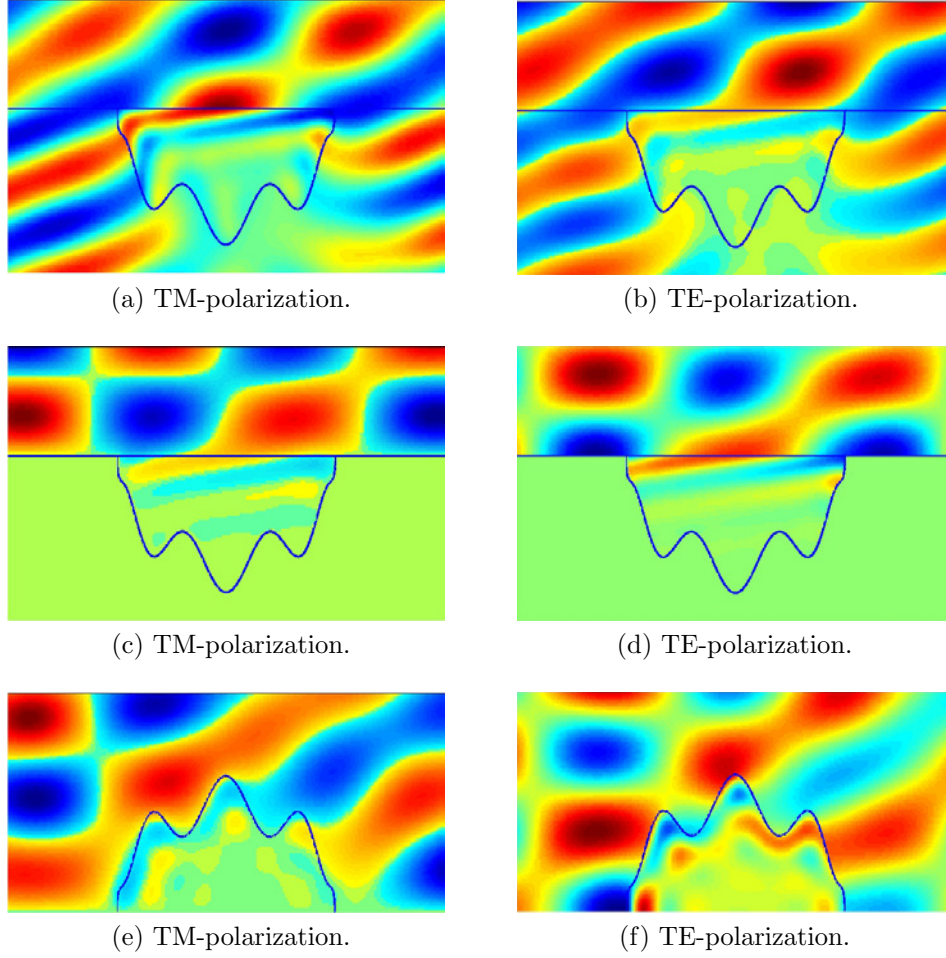
Figure 3.6: Diffraction pattern resulting from the scattering of a plane-wave by; a dielectric-filled cavity on a dielectric half-plane ((a) and (b)); a dielectric-filled cavity on a PEC half-plane ((c) and (d)); a dielectric bump on a PEC half-plane ((e) and (f)).

$(k_4 = 15)$ and Figures 3.6a-3.6b $(k_4 = 15 + 5i)$ present the diffraction pattern for the problem of scattering by the dielectric-filled cavity on the dielectric half-plane (problem Type I); Figures 3.5c-3.5d $(k_4 = 15)$ and Figures 3.6c-3.6d $(k_4 = 15 + 5i)$ present the diffraction pattern for the problem of scattering by the dielectric-filled cavity on the PEC half-plane (problem Type II); and Figures 3.5e-3.5f $(k_3 = 15)$ and Figures 3.6e-3.6f $(k_3 = 15 + 5i)$ present the diffraction pattern for the problem of scattering by the dielectric bump on the PEC half-plane.

Figure 3.7, finally, presents diffraction patterns (real part) for the problem of scattering by a dielectric filled cavity on a dielectric half-plane (Problem Type I) for the wavenumbers

		Type I		Type II		Type III	
		k_4		k_4		k_3	
	P	15	$15 + 5i$	15	$15 + 5i$	15	$15 + 5i$
TM	63	$3 \cdot 10^{-01}$	$6 \cdot 10^{-03}$	$7 \cdot 10^{-01}$	$1 \cdot 10^{-04}$	$2 \cdot 10^{-01}$	$7 \cdot 10^{-02}$
	127	$7 \cdot 10^{-04}$	$4 \cdot 10^{-06}$	$2 \cdot 10^{-03}$	$1 \cdot 10^{-07}$	$2 \cdot 10^{-03}$	$1 \cdot 10^{-03}$
	255	$1 \cdot 10^{-10}$	$7 \cdot 10^{-12}$	$3 \cdot 10^{-11}$	$6 \cdot 10^{-12}$	$5 \cdot 10^{-08}$	$8 \cdot 10^{-08}$
	511	$6 \cdot 10^{-12}$	$5 \cdot 10^{-12}$	$1 \cdot 10^{-12}$	$3 \cdot 10^{-13}$	$1 \cdot 10^{-13}$	$8 \cdot 10^{-13}$
TE	63	$9 \cdot 10^{-02}$	$3 \cdot 10^{-03}$	$2 \cdot 10^{-01}$	$6 \cdot 10^{-04}$	$4 \cdot 10^{-01}$	$4 \cdot 10^{-02}$
	127	$3 \cdot 10^{-04}$	$7 \cdot 10^{-06}$	$1 \cdot 10^{-04}$	$2 \cdot 10^{-07}$	$1 \cdot 10^{-03}$	$3 \cdot 10^{-04}$
	255	$3 \cdot 10^{-12}$	$2 \cdot 10^{-12}$	$3 \cdot 10^{-12}$	$7 \cdot 10^{-12}$	$2 \cdot 10^{-08}$	$2 \cdot 10^{-08}$
	511	$1 \cdot 10^{-12}$	$2 \cdot 10^{-12}$	$4 \cdot 10^{-14}$	$1 \cdot 10^{-14}$	$1 \cdot 10^{-13}$	$2 \cdot 10^{-13}$

Table 3.1: Convergence test for the numerical solution of Problem Type I ($k_3 = 5$, $k_4 = 15$ or $15 + 5i$, $k_1 = 5$, and $k_2 = 7$), II ($k_3 = 5$, $k_4 = 15$ or $15 + 5i$, and $k_1 = 5$) and III ($k_3 = 15$ or $15 + 5i$, and $k_1 = 5$).

$k_1 = k_3 = 15$, $k_4 = 10$, $k_2 = 5$ and the angle of incidence $\alpha = -\pi/3$ in TM- and TE-polarization, as well as the corresponding transmission patterns for the dielectric half-plane in the absence of the cavity. For these specially selected numerical values of the physical constants the phenomenon of total internal reflection [18, 64] takes place: in absence of the cavity the field transmitted below the interface decays exponentially fast with the distance to the interface. Interestingly (although not surprisingly), placement of a defect in this configuration gives rise to transmission of electromagnetic radiation to the lower half plane.

3.5   Applications

This section concerns applications of the LGF method presented above in the present chapter to studies of the effects of surface roughness on the absorption properties of a material surface, and their relation to pseudo-resonant phenomena that take place in open cavities.

(a) TM-polarization.

(b) TM-polarization.

(c) TE-polarization.

(d) TE-polarization.
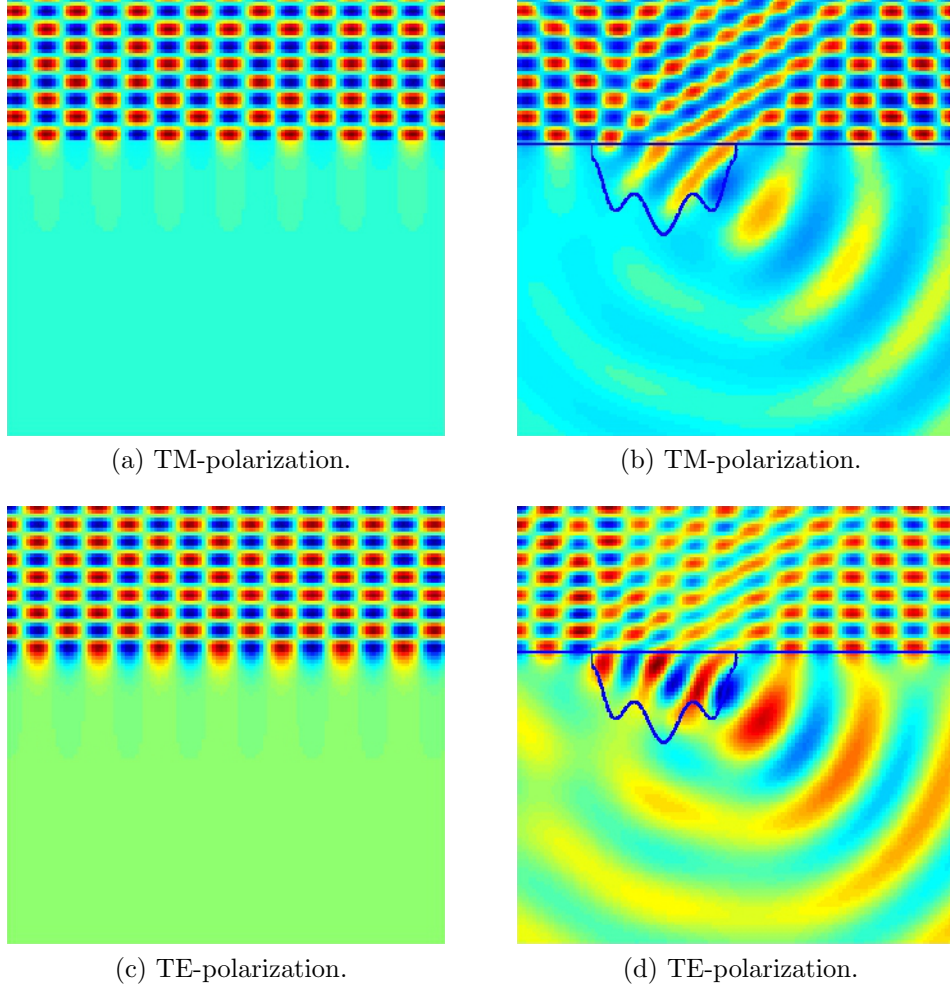
Figure 3.7: Scattering and transmission of an incident plane-wave, with $\alpha = -\pi/4$, by a dielectric half plane in absence (resp. presence) of a dielectric-filled cavity (Problem Type I with wavenumbers $k_1 = k_3 = 15$, $k_4 = 10$ and $k_2 = 5$. The parameters are selected so as to give rise to total internal reflection in absence of the cavity.

3.5.1 Electromagnetic power absorption due to bumps and trenches on flat surfaces

Our first study concerns assessment of the enhanced electromagnetic power absorption due to a small local surface defect, where we assume the size of the defect $a > 0$ is much smaller than the free space wavelength $\lambda > 0$ ($a \ll \lambda$) and the radius of curvature of the surface at the location of the defect (in the absence of the defect) is much larger than λ, so that the surface can be considered as locally flat in the absence of the defect. The 2D surface defect

is assumed to be in the form of either a single semi-cylindrical bump or trench located on an otherwise flat surface, where, letting $\sigma > 0$ denote the conductivity at the RF frequency ω, the (complex) permittivity in the conducting medium equals $\varepsilon_2 = \varepsilon_{2r} + i\sigma/\omega$ in the pristine conducting half-space (see Figure 3.8).
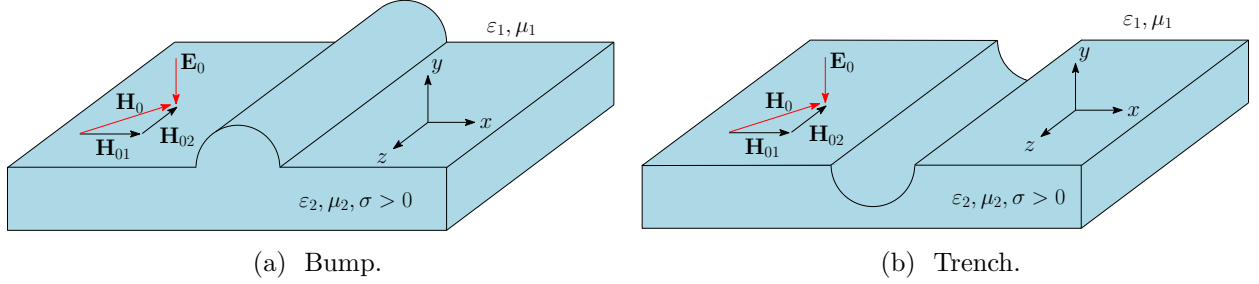
(a) Bump. (b) Trench.

Figure 3.8: A semi-cylindrical (a) bump, and (b) trench, on a conducting surface of finite conductivity. The bump is made of the same material as the flat surface.

The permittivity ε_1 in the region outside the conducting structure is taken as a real constant, and the magnetic permeability $\mu = \mu_1 = \mu_2$ is assumed real and constant throughout space. Clearly, letting $\delta = (2/\omega\mu_1\sigma)^{1/2}$ denote the skin depth associated with the conducting material, the ratio δ/a may take on an arbitrary value ranging from zero to infinity: $\delta \to \infty$ corresponds to an insulating surface and $\delta = 0$ corresponds to a perfectly conducting surface.

We consider the power dissipation that results from three different types of incident electromagnetic fields for which 1) the electric field $\mathbf{E}_0$ is perpendicular to the conducting surface with wavevector $\mathbf{k}$ perpendicular to the cylinder axis, where the complex amplitude of the electric field equal to $(e^{ik_1 x} + e^{-ik_1 x})/2 = \cos(k_1 x)$; 2) the magnetic field $\mathbf{H}$ (denoted in this case by $\mathbf{H}_{01}$) is perpendicular to axis of the defect with wavevector $\mathbf{k}$ perpendicular to the planar interface, where the complex amplitude of the incident magnetic field is equal to $e^{-ik_1 y}$; and 3) the magnetic field $\mathbf{H}$ (denoted in this case by $\mathbf{H}_{02}$) is parallel to the conducting surface and to the axis of the defect, where the complex amplitude of the magnetic field equal to $(e^{ik_1 x} + e^{-ik_1 x})/2 = \cos(k_1 x)$. The resulting problems of scattering are two-dimensional and are solved utilizing the LGF method presented above in this chapter (see also [104]).

For each of the three cases $\mathbf{E}_0$, $\mathbf{H}_{01}$, and $\mathbf{H}_{02}$, we compute the power absorption per unit
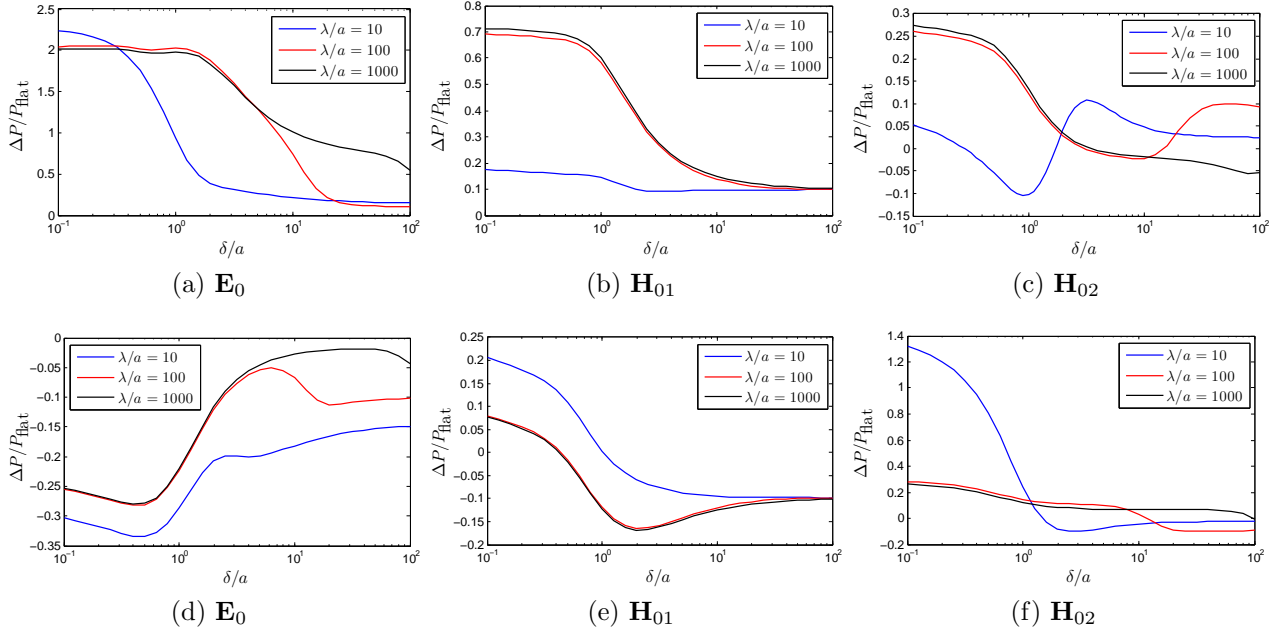
Figure 3.9: $\Delta P/P_{\text{flat}}$ for various values of δ/a for the case of the bump (top row) and the trench (bottom row) on the plane of finite conductivity for the three incidences considered.

axial length, P_{flat}, due to the flat surface (when the defect is absent) using

$$P = \int_D \sigma |\mathbf{E}|^2 \, \mathrm{d}x = \int_D \sigma |u_2|^2 \, \mathrm{d}x \quad \text{or} \quad P = \frac{\sigma}{\omega^2 |\varepsilon_2|^2} \left[\int_{\partial D} \bar{u}_2 \frac{\partial u_2}{\partial n} \, \mathrm{d}s + k_2^2 \int_D |u_2|^2 \, \mathrm{d}x \right] \quad (3.27)$$

depending on the polarization, integrating in the domain $D = D_{\text{flat}} = [-2a, 2a] \times [0, -4a]$. Note that $u_2 = E_z$ or $u_2 = H_z$, depending on the polarization, satisfies Helmholtz equation $\Delta u_2 + k_2^2 u_2 = 0$ in the conducting domain and the boundary of the flat conducting plane is taken to be $\Pi_1 = \{y = 0\}$. Similarly, the power absorption per unit axial length, P_{rough}, due to the rough surface (when the defect is present) is computed using formula (3.27) integrating in the domain $D = D_{\text{rough}} = D_{\text{flat}} \cup B$ in the case of the bump, and $D = D_{\text{rough}} = D_{\text{flat}} \setminus B$ in the case of the trench, where $B = \{(x, y) \in \mathbb{R}^2 : \sqrt{x^2 + y^2} < a\}$. All the required integrals in (3.27) are computed with high-order accuracy by means of a combination of Clenshaw-Curtis quadratures in polar and Cartesian coordinates. Figures 3.9a, 3.9b, and 3.9c (resp. Figures 3.9d, 3.9e, and 3.9f) plot the ratio of the enhanced power absorption due to the
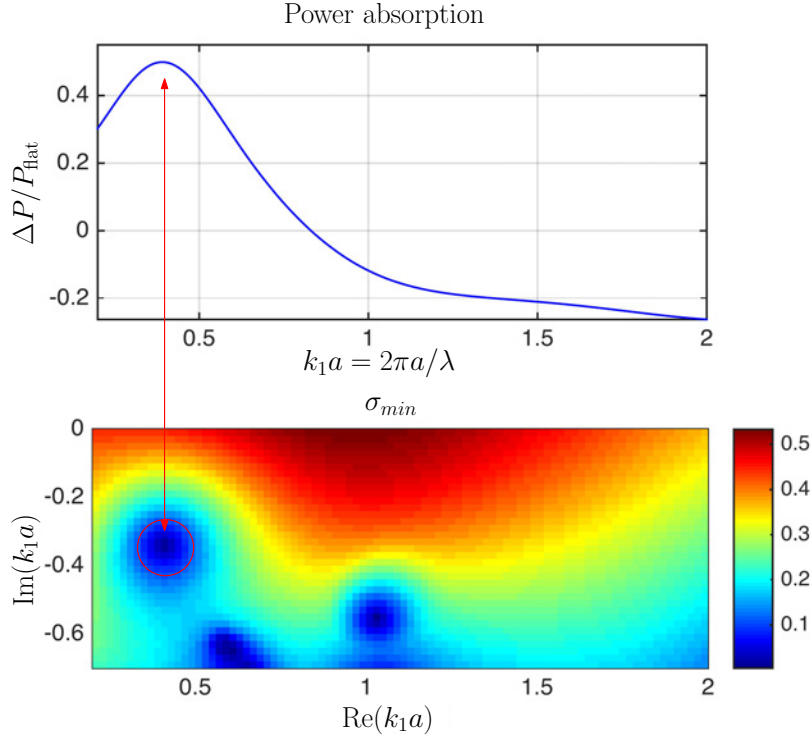
Figure 3.10: Power absorption curve for various values of the dimensionless wavelength λ/a (top) and location of scattering poles (bottom) for the problem of scattering by cavity in conducting plane for $\mathbf{H}_{02}$ incidence.

bump (resp. trench) to the ohmic loss of the pristine flat surface,

$$\frac{\Delta P}{P_{\text{flat}}} = \frac{P_{\text{rough}} - P_{\text{flat}}}{P_{\text{flat}}} = \frac{P_{\text{rough}}}{P_{\text{flat}}} - 1,$$

as a function of δ/a, for various values of λ/a, and for the three incident fields under consideration.

Interestingly, from Figures 3.9c and 3.9f we observe that for the $\mathbf{H}_{02}$ incident field and for large wavelength values ($\lambda/a \gg 10$) the quotient $\Delta P/P_{\text{flat}}$ seems to approach the limit $\Delta L/L_{\text{flat}} = (L_{\text{rough}} - L_{\text{flat}})/L_{\text{flat}} = (\pi - 2)/4 = 0.2854$ as $\delta \to 0$, where $L_{\text{rough}} = a(\pi + 2)$ and $L_{\text{flat}} = 4a$ denote the length of the curve representing the boundary of the conducting surface on which the skin depth effect takes place in presence and absence of the defect respectively. This phenomenon may be explained by the fact that in these cases the skin depth effect produces an uniform boundary layer near the boundary of the conducting surface. Surprisingly,

in Figures 3.9d, 3.9e and 3.9f we observe that, for some values of δ/a, the electromagnetic absorption is actually reduced (not increased!) by the presence of the trench, specially in the cases $\mathbf{E}_0$ and $\mathbf{H}_{01}$.

Another interesting phenomenon observed in this study is that for certain narrow regions in wavenumber space significantly enhanced power absorption occurs. This can be observed in the absorption curve in Figure 3.9f corresponding to $\lambda/a = 10$, for small values of the skin depth δ/a. In order to study this phenomenon in more detail we compute the power absorption for various values of wavelength for a fixed skin depth $\delta/a = 1$. The resulting absorption curve is displayed at the top of Figure 3.10, where a local maximum arises around $k_1 a = 2\pi a/\lambda = 0.4$. A possible explanation for the observed enhanced power absorption concerns the existence of so-called scattering poles near the real axis. The scattering poles correspond to values of the wavenumber at which the homogeneous scattering problem admits non-trivial solutions, or equivalently, they correspond to poles of the meromorphic continuation of solution operator [123]. From the well-posedness of the problem of scattering for physically meaningful values of the wavenumber, it follows that such scattering poles lie in the lower complex half-plane. When the selected (real) wavenumber k_1 is close to one of these scattering poles—which may occur when a scattering pole lies close to the real axis—an incident field can give rise to a total field that results in energy concentration within a certain region of the domain under consideration; a phenomenon that we refer to as "pseudo-resonance". In our case, for example, that region may correspond to the cavity and the resulting pseudo-resonance phenomenon could give rise to enhanced power absorption due to the the large values that the electric field can attain on and around the cavity walls. To establish an actual connection between the pseudo-resonance phenomenon and the enhanced power absorption in this case, we compute some of the scattering poles of the solution operator, which can be numericaly found by searching for complex $k_1 a$-values at which the system matrix (resulting from the LGF method) becomes singular. In order to find such values we resort to a stabilization procedure similar to the one put forth in [4]—which relies on use of certain "interior points" for eigenfunction normalization. The resulting minimum singular $\sigma_{\min}$ function, which vanishes at the scattering poles, is displayed at the bottom of

Figure 3.10. The location of the pick in the absorption curve in this figure corresponds to the projection of the closest scattering pole onto the real $k_1 a$-axis, which suggests a connection may exist between the scattering poles and the enhanced power absorption observed in this case. This interesting question is not pursued any further in this thesis and is left for future work.

3.5.2 Surface plasmon polariton scattering by defects in conducting surfaces

In this study we consider the aforementioned pseudo-resonance phenomenon in the context of problems of scattering of surface plasmon polaritons (SPP) by micro-cavities in conducting surfaces [83, 107]. SPP are waves that travel along an interface and which decay exponentially with the distance to the interface. As an example we consider an SPP given by [83, Section 2.2]

$$H_z^{\text{inc}}(x, y) = \begin{cases} e^{i\beta x - \sqrt{\beta^2 - k_1^2} y}, & y \geq 0, \\ e^{i\beta x + \sqrt{\beta^2 - k_2^2} y}, & y < 0, \end{cases} \qquad \beta = k_1 \sqrt{\frac{\varepsilon_2}{\varepsilon_1 + \varepsilon_2}}, \tag{3.28}$$

(where $\text{Re} \sqrt{\beta^2 - k_1^2} > 0$ and $\text{Re} \sqrt{\beta^2 - k_2^2} > 0$) which effectively amounts to a TM-polarized electromagnetic wave that decays exponentially as $y \to \pm\infty$, and which propagates along the planar interface $\Pi_1 = \{y = 0\}$ between air ($\varepsilon_1 = \varepsilon_0$, where ε_0 denotes the permittivity of the vacuum) and a metal (silver in our example). In our example the frequency dependent permittivity of the conducting medium is assumed to be given by the Drude model [83, Section 1.2]:

$$\varepsilon_2(\omega) = \varepsilon_0 \left(1 - \frac{\omega_p^2}{\omega^2 + i\gamma\omega} \right),$$

where γ and ω_p denote the so-called characteristic collision and plasma frequencies, respectively. Figures 3.11a and 3.11b display the incident magnetic field (3.28) and the total field solution of the problem of scattering of a micro-cavity of aperture $a = 2400\mu$m. The spatial wavelength of the incident field is $\lambda = 600\mu$m $= 2\pi/k_1$, while $\varepsilon_2 = \varepsilon_0(-15.59 + 0.17i)$ and $\beta = k_1(1.033 + 0.004i)$.

In order to study the pseudo-resonance phenomenon in this case we consider the void

(a) Real part of the surface plasmon polariton H_z^{inc} (3.28).

(b) Real part of H_z; the total field solution the problem of scattering of H_z^{inc} by a cavity.
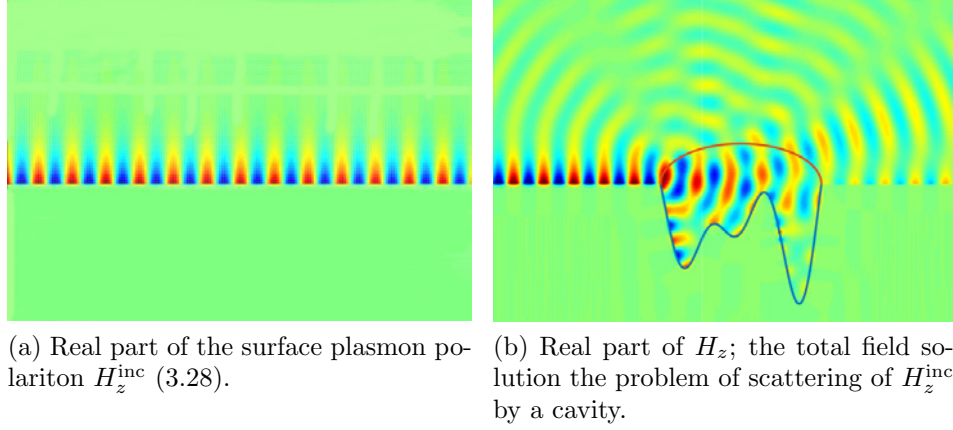
Figure 3.11: Surface plasmon polariton (left) in a flat metallic half-plane, and total field (right) solution of the problem of scattering of the surface plasmon polariton (3.11b) by a void cavity in a metal half-plane. Figure 3.11b displays the artificial curve Γ_{13} utilized by the LGF method.

cavity of Figure 3.11b, for which we compute the power flow, with and without the cavity, through the open artificial curve placed on the upper half-plane that is utilized by the LGF method (Γ_{13} in Figure 3.2, which is shown in Figure 3.11b for this example) for various wavenumbers $k_1 = \sqrt{\varepsilon_1 \mu_1}\omega$. To demonstrate further the influence of pseudo-resonance on the field localization inside the cavity, we consider the plot, presented in Figure 3.12, of the ratio

$$\frac{|P_{\mathrm{cavity}}|}{|P_{\mathrm{flat}}|} = \frac{\left|\int_{\Gamma_{13}} \left(\mathbf{E} \times \overline{\mathbf{H}}\right) \cdot d\mathbf{s}\right|}{\left|\int_{\Gamma_{13}} \left(\mathbf{E}^{\mathrm{inc}} \times \overline{\mathbf{H}^{\mathrm{inc}}}\right) \cdot d\mathbf{s}\right|} = \frac{\left|\int_{\Gamma_{13}} \overline{H}_z \frac{\partial H_z}{\partial n}\, ds\right|}{\left|\int_{\Gamma_{13}} \overline{H}_z^{\mathrm{inc}} \frac{\partial H_z^{\mathrm{inc}}}{\partial n}\, ds\right|}$$

of the power flow through the artificial curve, in presence of the cavity and without any cavity, respectively. This figure shows a number of sharp peaks and valleys. It may thus be conjectured that a correspondence exists between energy-transfer characteristics and pseudo-resonant phenomena; such a study, which lies beyond the scope of this thesis, is left for future work.
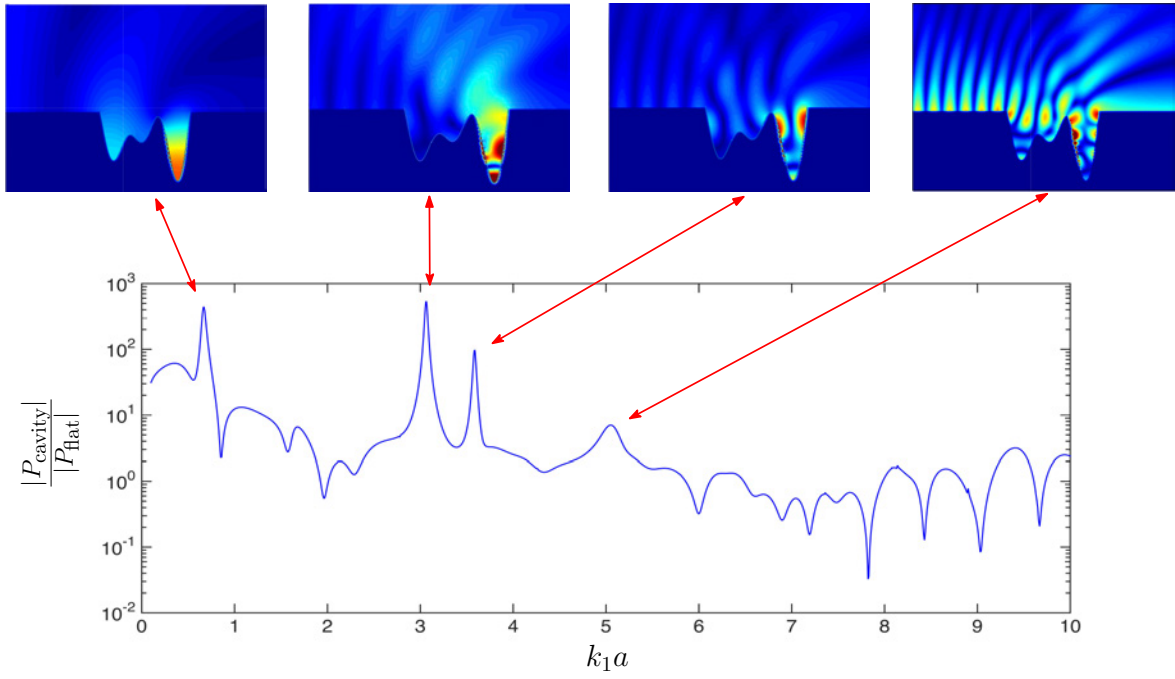
Figure 3.12: Power flow ratio and plots of the absolute value of the total fields resulting from solutions of the problem of scattering of a SPP by a micro-cavity corresponding to the frequencies marked by the red arrows.

Chapter 4

Windowed Green Function Method for layered media scattering

The solution of problems of scattering by obstacles or defects in the presence of planar layered dielectric or conducting media has typically required use of Sommerfeld integrals and associated layer Green functions—which automatically enforce the relevant transmission conditions on the unbounded flat surfaces and thus reduce the scattering problems to integral equations on the obstacles and/or defects (see Section 2.4 and Chapter 3). As is well known, however, the numerical evaluation of layer Green functions and their derivatives, which amounts to computation of certain challenging Fourier integrals [41, 117], are extremely expensive and give rise to a significant bottleneck in layer-media simulations (see e.g. [38] for details). This chapter presents a novel integral-equation approach for problems involving layered media. The new approach, which is based on use of certain "windowing" functions and considerations associated with the method of stationary phase, *does not require use of expensive Sommerfeld integrals.* Our analysis and numerical experiments demonstrate that both the near- and far-field errors resulting from the proposed approach decrease faster than any negative power of the window size.

A variety of methods have been provided for the solution of problems of scattering by obstacles in the presence of layered media. Amongst the most effective such approaches we mention: 1) methods which evaluate Sommerfeld integrals on the basis of path-integration in the complex plane [38, 39, 103, 104] (such approaches require numerical evaluation of integrals of functions that oscillate, grow exponentially in a bounded section of the integration path

and, depending on the relative position of the source and observation points to the interface between the two media, may decay slowly at infinity; 2) the complex images method reviewed in [5] (a discussion indicating certain instabilities and inefficiencies in this method is presented in [39, section 5.5]); 3) the steepest descent method [47, 48] which, provided the steepest descent path is known, reduces the Sommerfeld integral to an integral of an exponentially decaying function (unfortunately, however, the application of the steepest descent method for each observation point can be challenging and expensive [38, 39, 47]); 4) the contribution [80] which, utilizing Laplace transforms in addition to the Fourier transforms in the Sommerfeld method, demonstrates an improved performance over direct integration of the Sommerfeld integrals—but, as the authors stress, this is probably due to the straightforward character of the Sommerfeld integration method they use; and 5) a method [98] that relies on a combination of Sommerfeld integral representations as well as the method of images for a related application to the impedance problem, and which is demonstrated in low-frequency contexts. As is known, in any case, all of these methods entail significant computational costs [38, 80, 98].

The ideas embodied in the windowed Green function method proposed in this chapter are related to apodization techniques used in optics, as well as tapering or Hann functions utilized widely in signal processing. Apodization is used in the design of certain optical devices to eliminate edge effects; the Hann functions, in turn, are used to produce signals of finite duration from infinite-time signals while reducing distortions in the spectrum caused by the windowing process itself. From a computational perspective in a problem related to wave scattering, finally, the approach proposed in this chapter bears similarities with certain "finite-section" methods in the field of rough-surface scattering. These methods utilize approximations based on truncated portions of a given unbounded rough surface [86, 113, 141] and, in some cases, they incorporate a "taper" [92, 118, 141] to eliminate artificial reflections from the edges of the finite sections. In fact the smooth taper function utilized in [92] (Figure 2 in that reference) resembles the smooth windowing function we use (Figure 4.2 below and references [26, 93]). But as indicated in comments provided in Section 4.2.1 in regards to certain slow-rise windowing functions, essential differences exist between the finite-section

approaches and the methods proposed in this chapter. In particular, with exception of the slow-rise windowing function method [26, 93], none of the previous tapered rough surface algorithms has demonstrated high-order convergence as the width of the finite sections tend to infinity.

In Section 4.4 the proposed WGF method is compared to the high-order integral equation method introduced in Chapter 3 (see also [104]), which is based on the accurate and efficient evaluation of Sommerfeld integrals. In the examples considered in that section the proposed method is up to thousands of times faster, for a given accuracy, than the corresponding layer-Green-function method. A similar improvement in computational costs has been observed for problems of electromagnetic scattering by defects and obstacles in multi-layer structures in two and three dimensions; a detailed discussion of such problems is left for Chapters 5 and 6.

This chapter is organized as follows. After some basic preliminaries are presented in Section 4.1, the proposed methodology is introduced in Section 4.2. A formal error analysis of the method, based on multiple-scattering perturbation theory, then follows in Section 4.3. A variety of numerical results presented in Section 4.4, finally, demonstrate the accuracy and speed of the proposed approach.

4.1   Preliminaries

We consider two-dimensional problems of reflection and transmission by dielectric or conducting media under TE and TM polarizations. As was shown in Section 2.2.1, the z components $u = E_z$ and $u = H_z$ of the total electric and magnetic fields satisfy the Helmholtz equation $\Delta u + k_j^2 u = 0$ in Ω_j, $j = 1, 2$ (see Figure 4.1), where calling $\mu_0 > 0$ and $\omega > 0$ the magnetic permeability of vacuum and the temporal frequency, and letting $\varepsilon_j > 0$ and $\sigma_j \geq 0$ ($\sigma_1 = 0$) denote the electric permittivity and the electrical conductivity in Ω_j, the corresponding wavenumbers k_j are defined by $k_j^2 = \omega^2(\varepsilon_j + i\sigma_j/\omega)\mu_0$, $j = 1, 2$. The interface between the two unbounded media Ω_1 and Ω_2 is denoted by Γ. In either case the total field

resulting from a plane-wave incident field

$$u^{\text{inc}}(\boldsymbol{r}) = e^{ik_1(x\cos\alpha + y\sin\alpha)} \tag{4.1}$$

with incidence angle $\alpha \in (-\pi, 0)$ measured from the horizontal (see Figure 4.1) is given by

$$u(\boldsymbol{r}) = \begin{cases} u_1(\boldsymbol{r}) + u^{\text{inc}}(\boldsymbol{r}), & \boldsymbol{r} \in \Omega_1, \\ u_2(\boldsymbol{r}), & \boldsymbol{r} \in \Omega_2, \end{cases} \tag{4.2}$$

where u_1 and u_2 denote the reflected and transmitted waves, respectively. As is known (see e.g. Section 5.2 or [52, Section 5]), the scattered and transmitted fields u_1 and u_2 admit the representations

$$u_1(\boldsymbol{r}) = \mathcal{D}_1\left[u_1|_\Gamma\right](\boldsymbol{r}) - \mathcal{S}_1\left[\left.\frac{\partial u_1}{\partial n}\right|_\Gamma\right](\boldsymbol{r}), \qquad \boldsymbol{r} \in \Omega_1, \tag{4.3a}$$

$$u_2(\boldsymbol{r}) = -\mathcal{D}_2\left[u_2|_\Gamma\right](\boldsymbol{r}) + \mathcal{S}_2\left[\left.\frac{\partial u_2}{\partial n}\right|_\Gamma\right](\boldsymbol{r}) + u^\parallel(\boldsymbol{r}), \quad \boldsymbol{r} \in \Omega_2, \tag{4.3b}$$

where

$$u^\parallel(\boldsymbol{r}) = \begin{cases} e^{ik_1 x\cos\alpha} & \text{if } k_2 = k_1|\cos\alpha|, \\ 0 & \text{if } k_2 \neq k_1|\cos\alpha|, \end{cases} \tag{4.4}$$

and where, letting

$$G_j(\boldsymbol{r}, \boldsymbol{r}') = \frac{i}{4}H_0^{(1)}(k_j|\boldsymbol{r} - \boldsymbol{r}'|), \quad j = 1, 2,$$

denote the free-space Green function for the Helmholtz equation with wavenumber k_j, the single- and double-layer potentials in (4.3) are defined by means of the improper integrals

$$\mathcal{S}_j[\phi](\boldsymbol{r}) = \int_\Gamma G_j(\boldsymbol{r}, \boldsymbol{r}')\phi(\boldsymbol{r}')\,\mathrm{d}s_{\boldsymbol{r}'} \quad \text{and} \quad \mathcal{D}_j[\phi](\boldsymbol{r}) = \int_\Gamma \frac{\partial G_j}{\partial n_{\boldsymbol{r}'}}(\boldsymbol{r}, \boldsymbol{r}')\phi(\boldsymbol{r}')\,\mathrm{d}s_{\boldsymbol{r}'}, \tag{4.5}$$

respectively—whose convergence is conditioned upon the oscillatory behavior of the integrand. Throughout this chapter the interface Γ is assumed to be a piecewise smooth curve that coincides with the flat interface $\Pi = \Pi_1 = \{y = 0\}$ for large enough values of $|x|$; see

e.g. Figure 4.1.
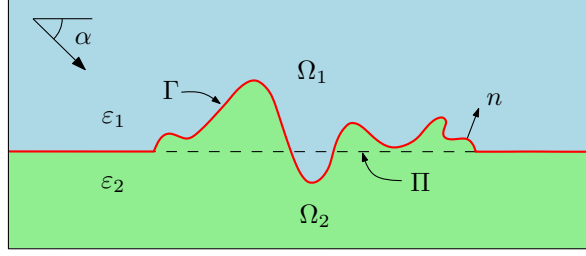
Figure 4.1: Description of the problem under consideration: scattering by a defect on a penetrable planar dielectric or conducting layer. Γ denotes the interface between the two media and Π denotes the interface between the upper- and lower-half planes.

By evaluating the fields (4.3) and their normal derivatives on Γ and using the transmission conditions

$$u_2 - u_1 = u^{\text{inc}}, \quad \nu \frac{\partial u_2}{\partial n} - \frac{\partial u_1}{\partial n} = \frac{\partial u^{\text{inc}}}{\partial n} \quad \text{on} \quad \Gamma,$$

(with $\nu = 1$ and $\nu = \varepsilon_1/\varepsilon_2$ in TE- and TM-polarizations respectively) we obtain the second-kind system of integral equations [68]

$$\mathrm{E}\,\boldsymbol{\phi} + \mathrm{T}\,[\boldsymbol{\phi}] = \boldsymbol{\phi}^{\text{inc}} \quad \text{on} \quad \Gamma \tag{4.6}$$

for the surface currents $\boldsymbol{\phi}$. Here

$$\mathrm{E} = \begin{bmatrix} 1 & 0 \\ 0 & \frac{1+\nu}{2} \end{bmatrix}, \quad \boldsymbol{\phi} = \begin{bmatrix} u_2|_\Gamma \\ \frac{\partial u_2}{\partial n}\Big|_\Gamma \end{bmatrix}, \quad \boldsymbol{\phi}^{\text{inc}} = \begin{bmatrix} (u^{\text{inc}} + u^{\|})|_\Gamma \\ \frac{\partial(u^{\text{inc}} + u^{\|})}{\partial n}\Big|_\Gamma \end{bmatrix}$$

and

$$\mathrm{T} = \begin{bmatrix} D_2 - D_1 & -S_2 + \nu S_1 \\ N_2 - N_1 & -K_2 + \nu K_1 \end{bmatrix}, \tag{4.7}$$

where, using the potentials (4.5), the entries in the matrix operator T are defined by

$$\begin{aligned} S_j[\phi](\boldsymbol{r}) &= \mathcal{S}_j\,[\phi]\,(\boldsymbol{r}), & D_j[\phi](\boldsymbol{r}) &= \int_\Gamma \frac{\partial G_j}{\partial n_{\boldsymbol{r}'}}(\boldsymbol{r}, \boldsymbol{r}')\phi(\boldsymbol{r}')\,\mathrm{d}s_{\boldsymbol{r}'}, \\ N_j[\phi](\boldsymbol{r}) &= \frac{\partial \mathcal{D}_j\,[\phi]}{\partial n}(\boldsymbol{r}), & K_j[\phi](\boldsymbol{r}) &= \int_\Gamma \frac{\partial G_j}{\partial n_{\boldsymbol{r}}}(\boldsymbol{r}, \boldsymbol{r}')\phi(\boldsymbol{r}')\,\mathrm{d}s_{\boldsymbol{r}'} \end{aligned} \tag{4.8}$$

for $r \in \Gamma$ and for $j = 1, 2$.

4.2 Windowed Green Function Method: Basic concepts

Instead of solving the problem (4.6) on the entire infinite interface Γ, a locally windowed problem could be used in an attempt to obtain the local currents over all relevant portions of Γ in an inexpensive manner. To pursue this idea we may utilize a smooth windowing function w_A in Definition 2.3.3 and depicted in Figure 4.2, which is non-zero in an interval of length $2A$, and which has a slow rise—that is

$$w_A(x) = \eta(x/A; c, 1) \tag{4.9}$$

for the fixed window function η defined in (2.78) (see Definition 2.3.3). Clearly, w_A rises from zero to one in regions of length proportional to $A > 0$.

In order to motivate the use of the smooth window function w_A in the following section we consider a highly illustrative integration example.

4.2.1 Slow-rise windowing function

Following example [26] concerning the numerical evaluation of the elementary integral

$$I = \int_0^\infty \frac{e^{ikx}}{\sqrt{x}} \, dx, \quad k > 0, \tag{4.10}$$

which in fact can be computed in closed form: $I = \sqrt{\frac{\pi}{2k}}(1 + i)$. Note that this integral has certain elements in common with the integrals that define the operators S_j, D_j, K_j and N_j in (4.8): as is the case in those operators, the integrand in the present integrand is both slowly decaying (like $1/\sqrt{|x|}$) and oscillatory (like $e^{ik|x|}$). In fact, the integrands in (4.10)(and (4.8)) are not even absolutely integrable, and, as it can be checked directly via integration by parts, it is the oscillatory nature of the integrands that renders these improper integrals convergent.

For our example we consider the approximations

$$I_H = \int_0^A \frac{e^{ikx}}{\sqrt{x}}\, dx \qquad \text{and} \qquad I_W = \int_0^A \eta(x, cA, A)\frac{e^{ikx}}{\sqrt{x}}\, dx, \qquad (4.11)$$

of the integral I in (4.10), where η is the slow rise window function (2.78). Table 4.1

A	$|I - I_H|$	$|I - I_W|$
4	7.9×10^{-2}	4.3×10^{-3}
16	4.0×10^{-2}	9.1×10^{-5}
64	1.9×10^{-2}	9.3×10^{-9}
256	9.1×10^{-3}	1.1×10^{-13}

Table 4.1: Errors in the approximation of I in (4.10) by the definite integrals I_H and I_W in (4.11) for various values of A, for $k = 2\pi$ and $c = 0.5$.

demonstrates the convergence properties of I_H and I_W as A increases. The slow convergence rate of I_H can be easily explained by the simple integration-by-parts calculation mentioned above: we have

$$\begin{aligned}
|I - I_H| &= \left| \int_A^\infty \frac{e^{ikx}}{\sqrt{x}}\, dx \right| = \sqrt{A}\left| \int_1^\infty \frac{e^{ikAt}}{\sqrt{t}}\, dt \right| \\
&= \sqrt{A}\left| -\frac{e^{ikA}}{ikA} + \frac{1}{2ikA}\int_1^\infty \frac{e^{ikAt}}{t^{3/2}}\, dt \right| = \mathcal{O}\left(\frac{1}{\sqrt{k}\sqrt{kA}} \right)
\end{aligned} \qquad (4.12)$$

as $A \to \infty$: the error tends to zero like $A^{-1/2}$.

The extraordinarily fast rate of convergence of I_W that is demonstrated by this example deserves especial mention, and can be explained as follows. Letting $\tilde{\eta} = 1 - \eta$ and noting that by construction of the window function we have $\tilde{\eta}(x, cA, A) = \tilde{\eta}(\frac{x}{cA}, 1, \frac{1}{c})$, we see that the error in this case is given by

$$|I - I_W| = \left| \int_{cA}^\infty \tilde{\eta}(x, cA, A)\frac{e^{ikx}}{\sqrt{x}}\, dx \right| = \sqrt{cA}\left| \int_1^\infty \tilde{\eta}(t, 1, 1/c)\frac{e^{ikcAt}}{\sqrt{t}}\, dt \right|.$$

Upon successive integration by parts that involves multiple differentiation of the smooth bounded function $\tilde{\eta}(t, 1, 1/c)/\sqrt{t}$ that vanishes at $t = 1$ along with all its derivatives (so that

no boundary contributions exist!), we obtain

$$\begin{aligned}
|I - I_W| &= \frac{1}{\sqrt{k}(cAk)^{p-1/2}} \left| \int_1^\infty \frac{\mathrm{d}^p}{\mathrm{d}t^p} \left(\frac{\widetilde{\eta}(t,1,1/c)}{\sqrt{t}} \right) \mathrm{e}^{ikcAt} \, \mathrm{d}t \right| \\
&= \mathcal{O}\left(\frac{1}{\sqrt{k}(cAk)^{p-1/2}} \right) \quad \text{as} \quad A \to \infty, \quad \text{for all} \quad p \geq 1,
\end{aligned}$$

(4.13)

which demonstrates the super-algebraic convergence observed in the example above.

As demonstrated in [26, 93] and in the example above, the slow rise character of the window function w_A is essential to ensure super-algebraically fast convergence (i.e., faster than any power of $1/A$) of windowed oscillatory integrals.

4.2.2 Windowed integral equation: preliminary considerations

In view of the discussion in Section 4.2.1 it is reasonable to attempt to produce an accurate *windowed* version of equation (4.6). Thus, letting $\Gamma_A = \{(x,y) \in \Gamma : w_A(x) \neq 0\}$ (where I is the 2×2 identity matrix) and calling $W_A = w_A \cdot I$, we consider the preliminary approximate equation

$$\mathrm{E}\,\phi^\star + \mathrm{T}\,[W_A\phi^\star] = \phi^{\mathrm{inc}} \quad \text{on} \quad \Gamma_A,$$

(4.14)

where $\phi^\star$ denotes a new unknown defined on Γ_A. In order to assess the errors inherent in the approximation (4.14) we also consider the form

$$\mathrm{E}\,\phi + \mathrm{T}\,[W_A\phi] = \phi^{\mathrm{inc}} - \mathrm{T}\,[(I - W_A)\phi] \quad \text{on} \quad \Gamma_A$$

(4.15)

of the exact equation (4.6).
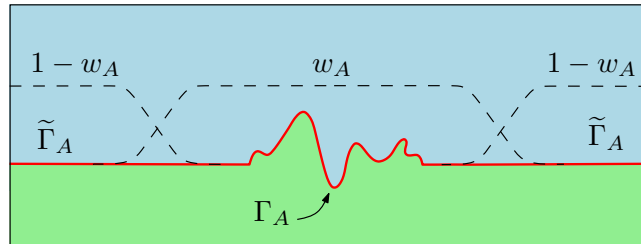
Figure 4.2: Window function w_A and windowed sections Γ_A and $\widetilde{\Gamma}_A$ of the unbounded curve Γ.

Remark 4.2.1. *For notational simplicity our derivations in the remainder of Section 4.2 are presented for cases for which the corrugations on the surface Γ are the only departures from planarity (see e.g. Figure 4.1). Cases in which additional scatterers exist (e.g. Figures 4.13 and 4.16) are considered in Sections 4.3 and 4.4.*

Remark 4.2.2. *Throughout the rest of this thesis the function w_A, which only depends on x, is viewed as a function defined for all values of $(x, y) \in \mathbb{R}^2$ which is constant with respect to y for each fixed value of x.*

Remark 4.2.3. *In what follows, the parts of the boundary Γ where $w_A(x) \neq 0$ and $\widetilde{w}_A(x) = 1 - w_A(x) \neq 0$ will be denoted by Γ_A and $\widetilde{\Gamma}_A$, respectively. With reference to Remark 4.2.2, the window-width $2A > 0$ is only restricted by the requirement that $\widetilde{w}_A(x)$ vanishes on any corrugations that exist on the surface Γ as well as on any additional obstacles that may exist above and/or below Γ. As shown below in this text, solutions converge rapidly as A increases beyond the bound posed by this restriction.*

As indicated below in Section 4.3, arguments based on integration by parts and the concept of stationary-phase can be used to establish that both the right-hand side $\mathrm{T}\left[(I - W_A)\phi\right]$ in (4.15) and the approximation error $|\phi - \phi^\star|$ are super-algebraically small—i.e., smaller than CA^{-m} for any positive integer m as $A \to \infty$, where the constant C is independent of A—throughout the center region $\{w_A = 1\}$ of the surface Γ_A. However, large window sizes may be required in such a scheme to correctly account for all fields reflected and refracted by the planar surface—a difficulty that can be visualized easily for incidence angles approaching grazing.

In order to demonstrate this difficulty (which is in fact overcome in Section 4.2.4 by incorporating certain closed-form and numerically evaluated expressions) here we consider a test case in which equation (4.14) is used to approximate the solution of the TE problem of scattering of a plane-wave by a semi-circular bump of radius $a = 1$ placed directly on top of a planar dielectric surface (see e.g. Figure 4.6). The problem was discretized using a direct generalization of the Nyström method presented in [69] which, relying on graded meshes over the surfaces of the bump and the windowed portion of the planar interface, accurately

accounts for the singularities of the currents at and around corners. For this example the wavenumbers k_1 and k_2 in the regions above and below the plane were set to 4π and 8π, respectively, and approximately 20 points per unit length of the surface of the bump and the surrounding were used.

Figure 4.3 shows that, as suggested above, the naive windowing approach embodied in (4.14) requires, for a given accuracy, large values of A—well beyond the extent of the non-planar local geometry—as the incidence angle decreases. A correction that resolves this difficulty, and which results in super-algebraic convergence uniformly for all incidence angles, is presented in Section 4.2.4.
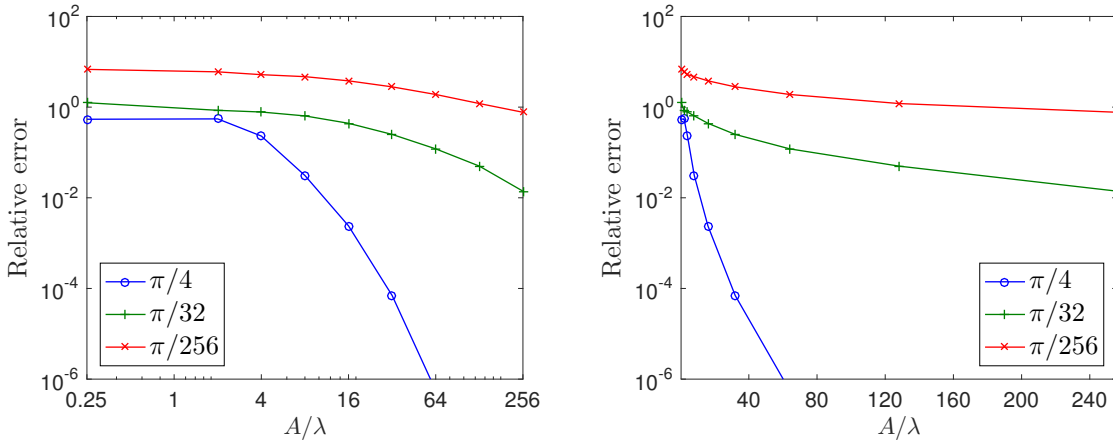
Figure 4.3: Relative errors (see Remark 4.4.1) in the integral densities resulting from numerical solution of (4.14) by means of a naive implementation of the WGF method for a semi-circular bump-shaped defect, for various window sizes (measured in numbers A/λ of wavelengths, where $\lambda = 2\pi/k_1$ denotes the free-space wavelength) and angles of incidence $\alpha = -\pi/4$ (blue), $-\pi/32$ (green) and $-\pi/256$ (red). Left: log-log scale. Right: semi-log scale. Clearly, the window size required by the naive method to produce a given accuracy increases dramatically as the angle of incidence approaches grazing.

4.2.3 Error sources in equation (4.2.2)

In order to provide an insight into the source of the errors displayed in Figure 4.3 we present Figure 4.4. Figure 4.4(a) depicts rays incident on the left planar region as well as their reflection and transmission. Clearly, in view of the incidence angle considered in this example, these reflected fields subsequently illuminate the defect and thus give rise to multiple

scattering.

Remark 4.2.4. *In the present section we make free use of standard geometrical optics nomenclature, with mention, in particular, of shooting and bouncing rays. Additionally, we make reference to the property of super-algebraic convergence that arises from windowing of integral representations of scattered fields around points of stationary-phase [28]. A justification of the geometrical-optics and integral-asymptotics arguments used throughout Section 4.2 is provided in Section 4.3—on the basis of the concept of stationary phase, and the methods of contour integration and multiple-scattering perturbation theory.*

Continuing with our argument concerning Figure 4.4(a), then, let us consider separately the rays shown in blue and red (or, in gray-scale, dark-gray and light-gray, respectively) in that figure. The blue rays represent the reflections that are correctly taken into account in the solution of equation (4.14) (since they impinge within the windowed region), but, clearly, the red arrows represent reflections that are neglected in this equation. Figure 4.4(b), on the other hand, represents reflections by the defect. The color-code in the left figure carries over to the right figure: the blue (resp. red) rays in Figure 4.4(b) represent the fields scattered by the defect which arise from the blue (resp. red) arrows in Figure 4.4(a). It is natural to suggest that, as justified in Section 4.3, the omission of the incident fields represented by the red arrows causes the errors observed in Figure 4.3. We also note that the relatively fast convergence demonstrated by the blue curves in Figure 4.3 can be explained by the fact that for near normal incidence ($\alpha \approx -\pi/2$) there is not a significant "red field" interacting with the defect. In contrast, for incidence near grazing ($\alpha \approx 0$), "red fields" from regions far away from the windowed area do interact with the defect, and therefore give rise to significant errors if neglected. As shown in Section 4.2.4, introduction of adequate corrections in equation (4.14) which account for such neglected terms allows us to establish super-algebraically fast convergence uniformly over the domain $[-\pi, 0]$ of all possible incidence angles.
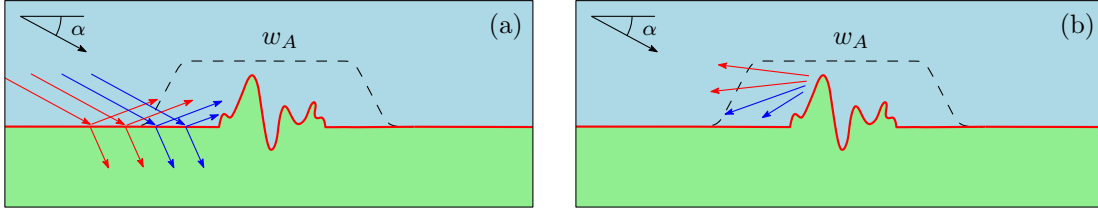
Figure 4.4: Physical concepts underlying the WGF method.

4.2.4 Uniform super-algebraically fast convergence for all incidence angles

To address the difficulties demonstrated in Figure 4.3 we consider again the exact integral equation (4.15), and we replace the unknown density ϕ on the right-hand side of this equation by the corresponding (known) density ϕ_Π^f associated with the problems of scattering and transmission of a plane-wave by a *perfectly-flat infinite interface* $\Pi = \{(x,y) \in \mathbb{R}^2 : y = 0\}$. A closed form expression for the density $\phi_\Pi^f = \phi_\Pi^f(x)$ is derived in Appendix C. We thus obtain the approximate equation

$$\mathrm{E}\,\phi^w + \mathrm{T}\left[W_A \phi^w\right] = \phi^{\mathrm{inc}} - \mathrm{T}\left[(I - W_A)\phi_\Pi^f\right] \quad \text{on} \quad \Gamma_A, \tag{4.16}$$

whose solution ϕ^w is (see Remark 4.2.5) a super-algebraically close approximation of the exact solution ϕ which is valid throughout the region $\Gamma_A \cap \{w_A = 1\}$, and which does not deteriorate as the incidence angle α tends to zero.

In order to evaluate the term $\mathrm{T}\left[(I - W_A)\phi_\Pi^f\right]$ we first consider the flat interface Π and, in view of (4.7), we switch the integrations over Γ of integrands involving $(I - W_A)\phi_\Pi^f$ into integrations over Π. To do this we rely on the fact that, since both ϕ_Π^f and W_A are a functions of x only, these quantities and their product $(I - W_A)\phi_\Pi^f$ can be trivially extended to corresponding functions defined for all values of $(x,y) \in \mathbb{R}^2$—as constant functions of y for each fixed x—which, in fact, vanish whenever $w_A = 1$. The modification is thus straightforward: since $(I - W_A)\phi_\Pi^f$ vanishes on $\Gamma \setminus \Pi$ (at least for A large enough), we may substitute the integration of an integrand equal to zero over the region $\Gamma_A \cap \{w_A = 1\}$ by

the integral over an integrand equal to zero over the region $\Pi \cap \{w_A = 1\}$. We thus obtain

$$\mathrm{T}\left[(I - W_A)\phi_\Pi^f\right](\boldsymbol{r}) = \widetilde{\mathrm{T}}_\Pi\left[(I - W_A)\phi_\Pi^f\right](\boldsymbol{r}), \quad \boldsymbol{r} \in \Gamma,$$

where, letting the layer potentials $\mathcal{S}_j^\Pi$ and $\mathcal{D}_j^\Pi$ $(j = 1, 2)$ be given by

$$\mathcal{S}_j^\Pi[\phi](\boldsymbol{r}) = \int_\Pi G_j(\boldsymbol{r}, \boldsymbol{r}')\phi(\boldsymbol{r}')\,\mathrm{d}s_{\boldsymbol{r}'} \quad \text{and} \quad \mathcal{D}_j^\Pi[\phi](\boldsymbol{r}) = \int_\Pi \frac{\partial G_j}{\partial n_{\boldsymbol{r}'}}(\boldsymbol{r}, \boldsymbol{r}')\phi(\boldsymbol{r}')\,\mathrm{d}s_{\boldsymbol{r}'}, \qquad (4.17)$$

for all $x \in \mathbb{R}^2$, and defining the boundary integral operators

$$\widetilde{S}_j^\Pi[\phi](\boldsymbol{r}) = \mathcal{S}_j^\Pi[\phi](\boldsymbol{r}), \qquad \widetilde{D}_j^\Pi[\phi](\boldsymbol{r}) = \int_\Pi \frac{\partial G_j}{\partial n_{\boldsymbol{r}'}}(\boldsymbol{r}, \boldsymbol{r}')\phi(\boldsymbol{r}')\,\mathrm{d}s_{\boldsymbol{r}'},$$

$$\widetilde{N}_j^\Pi[\phi](\boldsymbol{r}) = \frac{\partial \mathcal{D}_j^\Pi[\phi]}{\partial n}(\boldsymbol{r}), \qquad \widetilde{K}_j^\Pi[\phi](\boldsymbol{r}) = \int_\Pi \frac{\partial G_j}{\partial n_{\boldsymbol{r}}}(\boldsymbol{r}, \boldsymbol{r}')\phi(\boldsymbol{r}')\,\mathrm{d}s_{\boldsymbol{r}'},$$

$$\boldsymbol{r} \in \Gamma,\ j = 1,\ 2,$$

the operator $\widetilde{\mathrm{T}}_\Pi$ is defined by

$$\widetilde{\mathrm{T}}_\Pi = \begin{bmatrix} \widetilde{D}_2^\Pi - \widetilde{D}_1^\Pi & -\widetilde{S}_2^\Pi + \nu\widetilde{S}_1^\Pi \\[2mm] \widetilde{N}_2^\Pi - \widetilde{N}_1^\Pi & -\widetilde{K}_2^\Pi + \nu\widetilde{K}_1^\Pi \end{bmatrix}. \qquad (4.18)$$

An important subtlety to be noted concerns the fact that $\widetilde{\mathrm{T}}_\Pi$ maps density functions defined on Π to functions defined on Γ.

Thus equation (4.16) becomes

$$\mathrm{E}\,\phi^w + \mathrm{T}\left[W_A\phi^w\right] = \phi^{\mathrm{inc}} - \widetilde{\mathrm{T}}_\Pi\left[\phi_\Pi^f\right] + \widetilde{\mathrm{T}}_\Pi\left[W_A\phi_\Pi^f\right] \quad \text{on} \quad \Gamma_A. \qquad (4.19)$$

Clearly the expression $\widetilde{\mathrm{T}}_\Pi\left[W_A\phi_\Pi^f\right]$ can be evaluated by means of numerical integration over the bounded region $\Pi_A = \Pi \cap \{(x, y) \in \mathbb{R}^2 : w_A(x) \neq 0\}$. As shown in Appendix C, on the

other hand, the expression $\widetilde{\mathrm{T}}_\Pi\left[\phi_\Pi^f\right]$ can be computed in closed form:

$$\widetilde{\mathrm{T}}_\Pi\left[\phi_\Pi^f\right] = \phi^{\mathrm{inc}} - \begin{cases} \left[u_2^f, \dfrac{(1+\nu)}{2}\dfrac{\partial u_2^f}{\partial n}\right]^T & \text{on} \quad \Gamma \cap \Pi, \\[4mm] \left[u^f, \dfrac{\partial u^f}{\partial n}\right]^T & \text{on} \quad \Gamma \setminus \Pi. \end{cases} \tag{4.20}$$

The expressions on the right-hand side of equation (4.19) can thus be evaluated numerically throughout the surface Γ_A, and the corresponding bounded-domain integral equation can be solved by means of any available integral equation methodology—such as, for example, the highly accurate Nyström method [44, 69] we use.

Results on the existence and uniqueness of solutions for the second-kind integral equation (4.16) are provided in Appendix D, under the assumption that Γ_A is of class $\mathcal{C}^2$. In practice, it has been observed that (4.16) is uniquely solvable for all physically meaningful wavenumbers k_1 and k_2.

To conclude this section, in Figure 4.5 we demonstrate the fast and angle-independent convergence of ϕ^w to ϕ: clearly the value of A required to obtain an accurate approximation of the exact solution has been reduced substantially and the errors are uniformly small as the incidence angle decreases to zero.

Remark 4.2.5. *As mentioned above in this section, the solution of equation (4.16) is a uniform-in-α, super-algebraically close approximation of the exact solution ϕ throughout the curve $\Gamma_A \cap \{w_A = 1\}$. This is established by means of a formal error analysis in Section 4.3. But a brief rationale may be provided within the geometrical-optics framework considered in the present section. Indeed, notice at first that, in view of the theory of asymptotic evaluation of integrals [16], the value of the surface potentials $\mathcal{S}_j$ and $\mathcal{D}_j$ in (4.5) which, in view of (4.3), are needed to evaluate the field at a point $\mathbf{r}$, can be obtained with super-algebraic accuracy by means of windowed integration in a region which contains all points of stationary phase [16, Section 3.3]. But the points of stationary phase that arise for a given observation point $\mathbf{r}$ are precisely the points on the scattering surface where the rays reflect prior to their incidence upon $\mathbf{r}$. Thus, the windowed region in Figure 4.4, for example, contains (reps. does not*
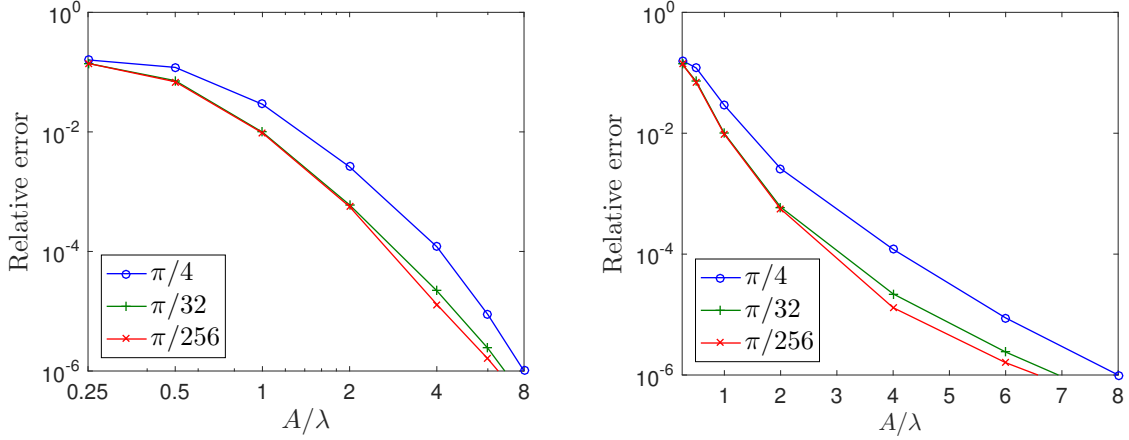
Figure 4.5: Relative errors (see Remark 4.4.1) in the integral densities ϕ^w on the surface of the defect resulting from numerical solution of (4.19), for a semi-circular bump-shaped defect, and for various window sizes and angles of incidence $\alpha = -\pi/4$ (blue), $-\pi/32$ (green) and $-\pi/256$ (red)—including extremely shallow incidences. Left: log-log scale. Right: semi-log scale. Clearly, this version of the WGF method computes integral densities with super-algebraically high (but not exponential) accuracy uniformly for all angles of incidence (cf. Figure 4.3).

contain) the points of stationary phase associated with the blue rays (resp. the red rays). But the contributions from red rays are re-incorporated per equation (4.19), and, thus, all of the incidences that impact upon the curve $\Gamma_A \cap \{w_A = 1\}$ on the first multiple-scattering iteration are taken into account with super-algebraically small errors. There remain fields that are not accounted for in equation (4.19), such as the field reflected by the windowed region which impacts outside of the windowed region. But these fields do not result in significant errors within the windowed region in any of the subsequent multiple-scattering iterations: examination of the associated reflection points shows that only a super-algebraically small portion of the field reflected by the windowed region into the plane outside the windowed region reflects back into the windowed domain. We may thus conclude that the error arising from the substitution of ϕ by ϕ_Π^f ought to give rise to super-algebraically small errors in equation (4.19) throughout the curve $\Gamma_A \cap \{w_A = 1\}$.

As mentioned in Remark 4.2.5, certain fields reflected by the windowed region, which do not affect the accuracy of the solution within the region $\Gamma_A \cap \{w_A = 1\}$, are not taken into account within the formalism described in this section. These neglected fields do affect

near fields and far fields in certain areas, however, as suggested by the ray description used throughout Section 4.2. But, as shown in Sections 4.2.5 and 4.2.6 below, the solution ϕ^w can be used to produce both the associated near field u everywhere in space as well as far fields in all directions.

4.2.5   Field evaluation: Near fields

The discussion in Remark 4.2.5 extends directly to evaluation of near fields. Indeed, that remark tells us that substitution of ϕ by $w_A \phi^w + (1 - w_A)\phi_\Pi^f$ ($\phi_\Pi^f = \left[\varphi^f, \psi^f\right]^T$) in the integral equation (4.15) leads to super-algebraically small errors $\mathbf{e} = \phi - \phi^w$ within the curve $\Gamma_A \cap \{w_A = 1\}$. Similar arguments can be used to establish that an analogous set of substitutions into the representation formula (4.3) produces the near field u with super-algebraically small errors throughout the strip $[-cA, cA] \times \mathbb{R}$ (but see Remark 4.3.1). The necessary substitutions are as follows: substitution of $u_1|_\Gamma$ and $\partial u_1/\partial n|_\Gamma$ by $w_A \varphi^w + (1 - w_A)\varphi^f - u^{\text{inc}}|_\Gamma$ and $\nu(w_A\psi^w + (1 - w_A)\psi^f) - \partial u^{\text{inc}}/\partial n|_\Gamma$, respectively, in (4.3a), and substitution of $u_2|_\Gamma$ and $\partial u_2/\partial n|_\Gamma$ by $w_A\varphi^w + (1 - w_A)\varphi^f$ and $w_A\psi^w + (1 - w_A)\psi^f$, respectively, in (4.3b) (see (C.13)).

These substitutions together with the relation

$$0 = \mathcal{D}_1\left[u^{\text{inc}}|_\Gamma\right] - \mathcal{S}_1\left[\left.\frac{\partial u^{\text{inc}}}{\partial n}\right|_\Gamma\right] \quad \text{in} \quad \Omega_1$$

(see [52]) leads to the expression

$$u^w = \begin{cases} u^{\text{inc}} + \mathcal{D}_1\left[w_A\varphi^w + (1 - w_A)\varphi^f\right] - \nu\mathcal{S}_1\left[w_A\psi^w + (1 - w_A)\psi^f\right] & \text{in} \quad \Omega_1, \\[2mm] u^\| - \mathcal{D}_2\left[w_A\varphi^w + (1 - w_A)\varphi^f\right] + \mathcal{S}_2\left[w_A\psi^w + (1 - w_A)\psi^f\right] & \text{in} \quad \Omega_2, \end{cases} \quad (4.21)$$

for the approximate total near field u^w in terms of the layer potentials defined in (4.5). After some manipulations similar to those presented in the derivation of equation (4.20), and using

the relations (C.1), (C.2a) and (C.2b), the formula in (4.21) is re-expressed in the forms

$$u^w = \mathcal{D}_1\left[w_A\varphi^w\right] - \nu\mathcal{S}_1\left[w_A\psi^w\right]$$

$$+ \begin{cases} u^f - \mathcal{D}_1^\Pi\left[w_A\varphi^f\right] + \nu\mathcal{S}_1^\Pi\left[w_A\psi^f\right] & \text{in} \quad \{y > 0\}, \\ \left(1 - \dfrac{w_A}{2}\right)u^f - D_1^\Pi\left[w_A\varphi^f\right] + \nu S_1^\Pi\left[w_A\psi^f\right] & \text{on} \quad \{y = 0^+\}, \\ \dfrac{w_A}{2}u^f - D_1^\Pi\left[w_A\varphi^f\right] + \nu S_1^\Pi\left[w_A\psi^f\right] & \text{on} \quad \{y = 0^-\}, \\ -\mathcal{D}_1^\Pi\left[w_A\varphi^f\right] + \nu\mathcal{S}_1^\Pi\left[w_A\psi^f\right] & \text{in} \quad \{y < 0\}, \end{cases}$$

(4.22a)

within Ω_1, and

$$u^w = -\mathcal{D}_2\left[w_A\varphi^w\right] + \mathcal{S}_2\left[w_A\psi^w\right]$$

$$+ \begin{cases} \mathcal{D}_2^\Pi\left[w_A\varphi^f\right] - \mathcal{S}_2^\Pi\left[w_A\psi^f\right] & \text{in} \quad \{y > 0\}, \\ \dfrac{w_A}{2}u^f + D_2^\Pi\left[w_A\varphi^f\right] - S_2^\Pi\left[w_A\psi^f\right] & \text{on} \quad \{y = 0^+\}, \\ \left(1 - \dfrac{w_A}{2}\right)u^f + D_2^\Pi\left[w_A\varphi^f\right] - S_2^\Pi\left[w_A\psi^f\right] & \text{on} \quad \{y = 0^-\}, \\ u^f + \mathcal{D}_2^\Pi\left[w_A\varphi^f\right] - \mathcal{S}_2^\Pi\left[w_A\psi^f\right] & \text{in} \quad \{y < 0\}, \end{cases}$$

(4.22b)

within Ω_2, in terms of various surface potentials and operators defined either on Γ or on Π—namely, the potentials $\mathcal{S}_j$ and $\mathcal{D}_j$ defined in (4.5), the potentials $\mathcal{S}_j^\Pi$ and $\mathcal{D}_j^\Pi$ defined in (4.17) and the operators S_j^Π and D_j^Π, $j = 1, 2$, defined in (C.3). Note that, by construction the straight finite-length segments $\Pi \cap \Omega_j$, $j = 1, 2$, are contained in the region $\{-cA \leq x \leq cA\}$ for A large enough; see Figures 4.1 and 4.7. Thus, for such values of A the second and third expressions in both (4.22a) and (4.22b) give rise to an overall continuous and, indeed, smooth solution u^w, across the finite segments $\Pi \cap \Omega_1$ and $\Pi \cap \Omega_2$, respectively (Figure 4.1)—as it behooves a solution of the Helmholtz equation away from the dielectric interface Γ.

Figure 4.6 displays the total near field produced by means of both, the WGF method and the layer-Green-function (LGF) method [104], for the solution of the problem of scattering of a plane-wave by a semi-circular bump of radius $a = 1$ in TE-polarization—with wavenumbers $k_1 = 10$ and $k_2 = 15$, and under two different incidence angles: $\alpha = -\pi/2$ and $\alpha = -\pi/6$.

The WGF solutions were obtained from the integral equation (4.19) followed by evaluation of field values on the basis of (4.22) (but see also the last paragraph is Section 4.2.6 in regards to near-field evaluation with higher accuracy and/or over extended regions). The absolute errors (see Remark 4.4.1) in the WGF solutions displayed in Figures 4.6a and 4.6d over the complete range shown are $1 \cdot 10^{-4}$ and $2 \cdot 10^{-4}$, respectively.

4.2.6 Field evaluation: Far fields

In view of the analysis in Section 4.3 it follows that formulae (4.22) do not generally provide an accurate approximation of either far fields or near fields outside bounded subsets of $[-cA, cA] \times \mathbb{R}$ (see, in particular, Remark 4.3.1). In order to tackle this difficulty we consider the boundary S of a disc B such as the one depicted in Figure 4.7. The curve S encloses the portion of Γ that differs from the flat interface Π; as indicated above, super-algebraic convergence of the fields u_1 and u_2 takes place everywhere on and within such a curve S.

As shown in the following lemma, application of the Green identities, integration over the region exterior to S and use of the layer Green function (2.27) leads to the integral representation

$$u^s(\boldsymbol{r}) = \int_S \left\{ \frac{\partial G}{\partial n_{\boldsymbol{r}'}}(\boldsymbol{r}, \boldsymbol{r}') u^s(\boldsymbol{r}') - G(\boldsymbol{r}, \boldsymbol{r}') \frac{\partial u^s}{\partial n}(\boldsymbol{r}') \right\} \mathrm{d}s_{\boldsymbol{r}'} \qquad (4.23)$$

of the scattered field $u^s = u - u^f$ which is valid for $\boldsymbol{r}$ everywhere outside S. Here G denotes the layer Green function for the Helmholtz equation with wavenumbers k_1 in $D_1 = \{y > 0\}$ and k_2 in $D_2 = \{y < 0\}$. Note that the necessary values of the scattered field u^s and its normal derivative on S can be computed directly utilizing (4.22), since, by construction, S lies inside the region where (4.22) provides an accurate approximation of the total field u.

Lemma 4.2.6. *The scattered field $u^s = u - u^f : \mathbb{R}^2 \backslash \overline{B} \to \mathbb{C}$ admits the integral representation*

$$u^s(\boldsymbol{r}) = \int_S \left\{ \frac{\partial G}{\partial n_{\boldsymbol{r}'}}(\boldsymbol{r}, \boldsymbol{r}') u^s(\boldsymbol{r}') - G(\boldsymbol{r}, \boldsymbol{r}') \frac{\partial u^s}{\partial n}(\boldsymbol{r}') \right\} \mathrm{d}s_{\boldsymbol{r}'} \quad in \quad \mathbb{R}^2 \setminus \overline{B}, \qquad (4.24)$$

in terms of the layer Green function G (2.27).

(a) WGF method. (b) LGF method. (c) Difference.

(d) WGF method. (e) LGF method. (f) Difference.
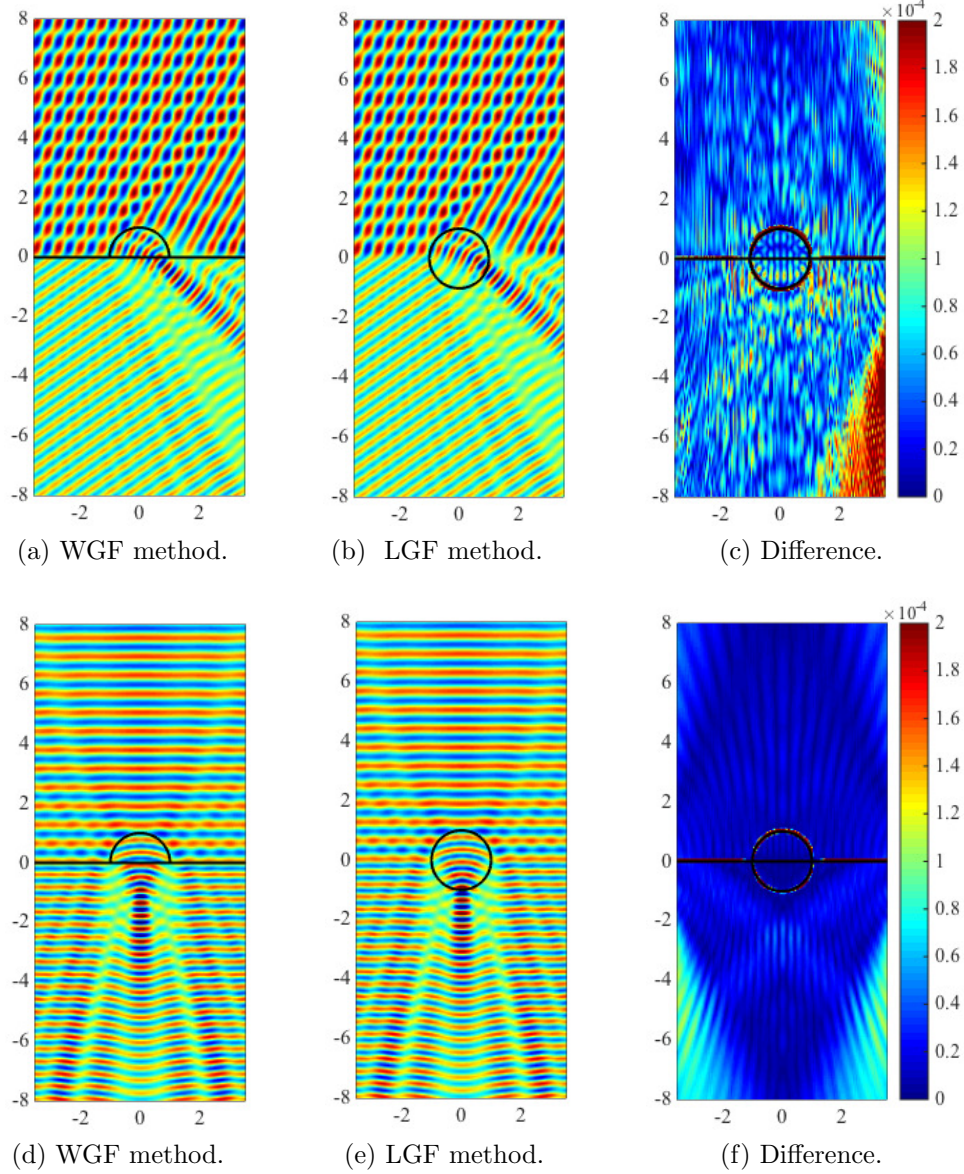
Figure 4.6: Real parts of the total fields produced by the WGF method and the layer-Green-function (LGF) method for the problem of scattering of a plane-wave by a semi-circular bump. Figures 4.6a and 4.6b: $\alpha = -\pi/6$. Figures 4.6d and 4.6e: $\alpha = -\pi/2$. The width of the support of the selected window function is $2A = 16\lambda \approx 10.053$ in all these calculations. The black lines represent the domains where the respective integral equation formulations are posed. (Note that in addition to the surface of the bump itself, the LGF method [104] entails discretization of a certain transparent boundary in the lower half-plane—so that, in the present bump cases, for example, the LGF integral equations are actually posed on the full circles depicted in Figures (b) and (d)).
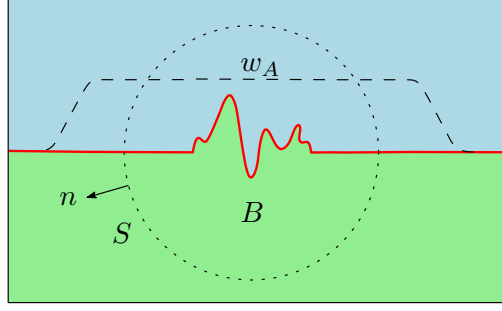
Figure 4.7: Curve S utilized in (4.23).

Proof. As is known [74], u^s is an element of $C^2(\mathbb{R}^2 \setminus \{\overline{B} \cup \Pi\}) \cap C(\mathbb{R}^2 \setminus B)$ which satisfies the equations

$$\Delta u^s + k_j^2 u^s = 0 \qquad \text{in} \quad D_j \setminus \overline{B}, \ j = 1, 2,$$

$$u^s\big|_{y=0+} = u^s\big|_{y=0-} \qquad \text{on} \quad \Pi \setminus \overline{B},$$

$$\frac{\partial u^s}{\partial y}\bigg|_{y=0+} = \nu \frac{\partial u^s}{\partial y}\bigg|_{y=0-} \qquad \text{on} \quad \Pi \setminus \overline{B}$$

as well as the radiation condition

$$\lim_{|\boldsymbol{r}| \to \infty} \sqrt{|\boldsymbol{r}|} \left\{ \frac{\partial u^s}{\partial |\boldsymbol{r}|} - i k_j u^s \right\} = 0 \quad \text{uniformly in all directions} \quad \frac{\boldsymbol{r}}{|\boldsymbol{r}|} \in D_j, \qquad (4.25)$$

where $f, g : S \to \mathbb{C}$ are piecewise continuous functions.

Let $f = u^s|_S$, $g = \partial u^s/\partial n\big|_S$ and $R > 0$, and consider the domains $B_{j,R} = \left(D_j \setminus \overline{B} \right) \cap B_R$ where $B_R = \{|\boldsymbol{r}| < R\}$ for $j = 1, 2$. Let us also call $G^\pm = G|_{y'=0\pm}$, $H^\pm = \frac{\partial G}{\partial y'}\big|_{y'=0\pm}$, $v = u^s\big|_{y=0-}$ and $w = \frac{\partial u^s}{\partial y}\big|_{y=0-}$ the limit values of G and u^s at the planar interface $\Pi \setminus \overline{B}$. From Green's third identity, integrating over the domain $B_{1,R}$, and then taking the limit as $R \to \infty$, we obtain

$$\int_{S_1} \left\{ \frac{\partial G}{\partial n_{\boldsymbol{r}'}}(\boldsymbol{r}, \boldsymbol{r}') f(\boldsymbol{r}') - G(\boldsymbol{r}, \boldsymbol{r}') g(\boldsymbol{r}') \right\} \mathrm{d}s_{\boldsymbol{r}'}$$
$$+ \int_{\Pi \setminus \overline{B}} \left\{ H^+(\boldsymbol{r}, \boldsymbol{r}') v(\boldsymbol{r}') - \nu G^+(\boldsymbol{r}, \boldsymbol{r}') w(\boldsymbol{r}') \right\} \mathrm{d}s_{\boldsymbol{r}'} = \begin{cases} u^s(\boldsymbol{r}), & \boldsymbol{r} \in D_1 \setminus \overline{B}, \\ 0, & \boldsymbol{r} \in D_2 \setminus \overline{B}, \end{cases} \qquad (4.26)$$

where $S_1 = S \cap D_1$. (Note that the integral over $\partial B_R \cap D_1$ vanishes in the $R \to \infty$ limit—a

fact which can be checked by adding and subtracting $ik_1 u^s(\boldsymbol{r}')G(\boldsymbol{r},\boldsymbol{r}')$ to the integrand and appealing to the $|\boldsymbol{r}'| \to \infty$ radiation conditions (4.25) and (2.31) that are satisfied by $u^s(\boldsymbol{r}')$ and $G(\cdot, \boldsymbol{r}')$, respectively. Similarly, from Green's third identity integrating now over $B_{2,R}$, we obtain

$$
\begin{aligned}
\int_{S_2} & \left\{ \frac{\partial G}{\partial n_{\boldsymbol{r}'}}(\boldsymbol{r},\boldsymbol{r}')f(\boldsymbol{r}') - G(\boldsymbol{r},\boldsymbol{r}')g(\boldsymbol{r}') \right\} \, \mathrm{d}s_{\boldsymbol{r}'} \\
& - \int_{\Pi\setminus\overline{B}} \left\{ H^-(\boldsymbol{r},\boldsymbol{r}')v(\boldsymbol{r}') - G^-(\boldsymbol{r},\boldsymbol{r}')w(\boldsymbol{r}') \right\} \, \mathrm{d}s_{\boldsymbol{r}'} =
\begin{cases}
0, & \boldsymbol{r} \in D_1 \setminus \overline{B}, \\
u^s(\boldsymbol{r}), & \boldsymbol{r} \in D_2 \setminus \overline{B}.
\end{cases}
\end{aligned}
\tag{4.27}
$$

Adding the expressions (4.26) and (4.27) we arrive at

$$
\begin{aligned}
u^s(\boldsymbol{r}) = & \int_S \left\{ \frac{\partial G}{\partial n_{\boldsymbol{r}'}}(\boldsymbol{r},\boldsymbol{r}')f(\boldsymbol{r}') - G(\boldsymbol{r},\boldsymbol{r}')g(\boldsymbol{r}') \right\} \, \mathrm{d}s_{\boldsymbol{r}'} \\
& + \int_{\Pi\setminus\overline{B}} \left\{ \left[H^+ - H^- \right](\boldsymbol{r},\boldsymbol{r}')v(\boldsymbol{r}') - \left[G^+ - \nu G^- \right](\boldsymbol{r},\boldsymbol{r}')w(\boldsymbol{r}') \right\} \, \mathrm{d}s_{\boldsymbol{r}'}, \ \boldsymbol{r} \in (D_1 \cup D_2) \setminus \overline{B}.
\end{aligned}
\tag{4.28}
$$

From the transmission conditions (2.30) satisfied by the layer Green function we see that the last integral in the identity above vanishes for $\boldsymbol{r} \in (D_1 \cup D_2) \setminus \overline{B}$. Thus, equation (4.24) follows from (4.28) for $\boldsymbol{r} \in (D_1 \cup D_2) \setminus \overline{B}$, and, by continuity of u^s across $\Pi \setminus \overline{B}$, finally, throughout $\mathbb{R}^2 \setminus \overline{B}$. The proof is now complete. $\qquad \square$

The far-field pattern $u_\infty(\hat{\boldsymbol{r}})$, which is related to the scattered field by the asymptotic formula

$$
u^s(\boldsymbol{r}) = \frac{\mathrm{e}^{ik_1|\boldsymbol{r}|}}{\sqrt{|\boldsymbol{r}|}} u_\infty(\hat{\boldsymbol{r}}) + \mathcal{O}\left(|\boldsymbol{r}|^{-3/2} \right), \quad |\boldsymbol{r}| \to \infty, \quad \hat{\boldsymbol{r}} = \frac{\boldsymbol{r}}{|\boldsymbol{r}|},
$$

can be produced by replacing G and its normal derivative in equation (4.23) by their corresponding leading order asymptotic expansions as $|\boldsymbol{r}| \to \infty$. As shown in Section 2.3.4, the first order term of the asymptotic expansion of the layer Green function in a given direction $\hat{\boldsymbol{r}} = (\cos\theta, \sin\theta), 0 < \theta < \pi$ can be obtained by the method of steepest descent. Substitution

of the result in equation (4.23) yields the expression

$$u_\infty(\hat{\boldsymbol{r}}) = \int_S \left\{ n(\boldsymbol{r}') \cdot \boldsymbol{H}_\infty(\hat{\boldsymbol{r}}, \boldsymbol{r}') u^s(\boldsymbol{r}') - G_\infty(\hat{\boldsymbol{r}}, \boldsymbol{r}') \frac{\partial u^s}{\partial n}(\boldsymbol{r}') \right\} \, \mathrm{d}s_{\boldsymbol{r}'} \tag{4.29}$$

for the far field $u_\infty(\hat{\boldsymbol{r}})$, where the far-field kernels G_∞ and $\boldsymbol{H}_\infty$ are given in (2.59) and (2.60), respectively. Thus, unlike the layer Green function G itself for small values of $|\boldsymbol{r} - \boldsymbol{r}'|$, the far-field associated with G can be computed inexpensively by means of the explicit expressions (2.59) and (2.60). Figure 4.8 provides a comparison of the far-field patterns computed using the LGF and WGF methods for the problem considered in Section 4.2.5.
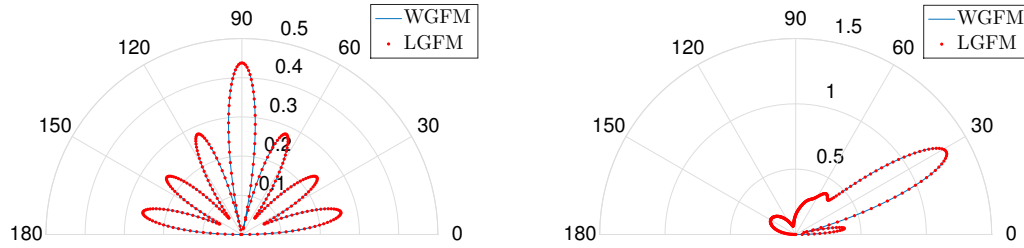
Figure 4.8: Far-field patterns obtained using the layer-Green-function method [104] (red dotted curve) and the WGF method (continuous blue line) for the solution of the problem of scattering considered in this section at incidences $\alpha = -\pi/2$ (left) and $\alpha = -\pi/6$ (right) .

In view Section 4.2.5 and the discussion above in the present Section 4.2.6, equations (4.22) and (4.29) can be used to accurately and efficiently evaluate near-fields and far-fields, respectively. These are typically the quantities of interest in scattering simulations involving layered media. The evaluation of the fields in an intermediate region, such as the complement of a bounded domain within the strip $[-cA, cA]$ (where (4.22) yields an accurate approximation) can be approximated efficiently on the basis of equation (4.23). Indeed, in such cases, for which source points $\boldsymbol{r}'$ lie on S and observation points $\boldsymbol{r}$ are at a large distance away from S, the Sommerfeld integrals in (2.27) (which by Cauchy's theorem can be expressed in terms of complex contour integrals with highly oscillatory and/or exponentially decaying integrands) can be obtained rapidly by means of asymptotic numerical methods [10, 28]— based on localization around critical points and the method of steepest descents in very small regions around saddle points.

4.3 Formal error analysis

A formal multiple-scattering error analysis introduced in Section 4.3.4 validates the ray-based discussions presented in Section 4.2. The arguments presented in Section 4.3.4 rely on the WGF approximation properties for certain simple "obstacle-free problems": the problem of scattering by a planar interface in absence of a defect or obstacle, and including point-source incident fields. Useful insights in these regards can be obtained by consideration of obstacle-free problems under *plane-wave incident fields with possibly complex wavevectors—* which, via integration, can be used to represent an arbitrary point source by complex contour evaluation of the integral in equation (4.41). The preliminary discussion concerning plane-wave incidence is advantageous in a number of ways, as 1) The error of the complete range of relevant plane-wave approximations is dominated by the "worst-case" errors which arise for real wavevectors at normal incidence (see e.g. Figures 4.9 and 4.10); 2) The worst-case errors can be characterized by a single parameter (namely the number of wavelengths $A/\lambda = k_1 A/(2\pi)$ contained in the windowed region; and, as will be shown elsewhere, 3) The windowed obstacle-free problem lends itself more directly to analysis under plane-wave incidence—since, unlike the WGF solutions for point-source problems, the plane-wave WGF solutions (for either real or complex incident wavevector) can be expressed as the product of the incident field times a function whose derivatives decay as $A \to \infty$.

Section 4.3.1 presents a discussion of the WGF method for the plane-wave obstacle-free problem, and Sections 4.3.2 and 4.3.3, further illustrate and augment these discussions through a variety of numerical examples for both plane-wave and point-source illumination. As mentioned above, our formal multiple-scattering error analysis is then presented in Section 4.3.4.

4.3.1 WGF solution of plane-wave-illuminated planar interface

4.3.1.1 WGF error sources

With reference to equation (4.41) and its complex contour representation used in Section 4.3.3, for a given point $\boldsymbol{r'} = (x', y')$, $y' > 0$ and complex wavevector $\left(\xi, -i\gamma_1(\xi)\right)$ we

consider the problem of scattering by a dielectric half-plane illuminated by a (generalized) plane wave u_ξ^{inc} of the form

$$u_\xi^{\text{inc}}(\boldsymbol{r}) = \frac{e^{i\xi(x-x')-\gamma_1(\xi)|y-y'|}}{\gamma_1(\xi)} = C_\xi\, e^{i\xi x + \gamma_1(\xi)y} \tag{4.30}$$

$(C_\xi = \frac{e^{-i\xi y_1 - \gamma_1(\xi)y'}}{\gamma_1(\xi)})$ with $y' > y$ ($y = 0$ for the planar interface considered in this section). Here $\gamma_1(\xi) = \sqrt{\xi^2 - k_1^2} = \sqrt{\xi - k_1}\sqrt{\xi + k_1}$ with branches selected as indicated in Section 2.3.1. Note that the quantity $|y - y'|$ in (4.30) equals $y' - y$ under the $y' > y$ assumption included in the equation, of course, but the absolute values are kept in order to match the form of the integrand in the plane-wave integral expression (4.41) for a point-source incident field.

Following Section 4.1 we obtain the integral equation formulation

$$\mathrm{E}\,\boldsymbol{\phi}_\xi + \mathrm{T}_\Pi[\boldsymbol{\phi}_\xi] = \boldsymbol{\phi}_\xi^{\text{inc}} \quad \text{on} \quad \Pi \tag{4.31}$$

for the present problem, where the operator T_Π is defined as in equations (4.7)–(4.8) with $\Gamma = \Pi$, and where letting $\boldsymbol{\phi}_\xi = [\varphi_\xi, \psi_\xi]^T$, the right-hand-side is given by

$$\boldsymbol{\phi}_\xi^{\text{inc}} = \left[u_\xi^{\text{inc}}|_\Pi, \frac{\mathrm{d}u_\xi^{\text{inc}}}{\mathrm{d}y}\Big|_\Pi \right]^T.$$

The solution of (4.31) can be obtained by letting $\xi = k_1 \cos\alpha$ in the relevant expressions in Appendix C: with this identification we have $\boldsymbol{\phi}_\Pi^{\text{inc}} = \boldsymbol{\phi}_\xi^{\text{inc}}/C_\xi$, and, thus, the exact solution of (4.31) coincides with (C.13). In terms of ξ we thus have

$$\varphi_\xi(t) = C_\xi T_\xi\, e^{i\xi t} \quad \text{and} \quad \psi_\xi(t) = \frac{\gamma_1(\xi)C_\xi(2 - T_\xi)}{\nu}\, e^{i\xi t}, \tag{4.32}$$

where $T_\xi = \dfrac{2\gamma_1(\xi)}{\gamma_1(\xi) + \nu\gamma_2(\xi)}$, and where $\gamma_2(\xi) = \sqrt{\xi^2 - k_2^2}$ (with a choice of branches as specified in Section 2.3.1.

Our analysis relies on use of a certain approximate solution $\boldsymbol{\phi}_\xi^w = \left[\varphi_\xi^w, \psi_\xi^w\right]^T$ of (4.31) which is obtained by means of the windowing approximation but without use of a correction

term akin to $T[(I - W_A)\phi^f_\Pi]$ in (4.16): the density ϕ^w_ξ satisfies

$$\mathrm{E}\,\phi^w_\xi + \mathrm{T}_\Pi[W_A\phi^w_\xi] = \phi^{\mathrm{inc}}_\xi \quad \text{on} \quad \Pi_A, \tag{4.33}$$

where $\Pi_A = \Pi \cap \{-A \leq x \leq A\}$. As shown in what follows, both ϕ^w_ξ itself and the reflected and transmitted fields it produces according to

$$u^w_\xi(\boldsymbol{r}) = \begin{cases} \mathcal{D}^\Pi_1\left[w_A\varphi^w_\xi\right](\boldsymbol{r}) - \nu\mathcal{S}^\Pi_1\left[w_A\psi^w_\xi\right](\boldsymbol{r}), & \{y > 0\}, \\[2mm] -\mathcal{D}^\Pi_2\left[w_A\varphi^w_\xi\right](\boldsymbol{r}) + \mathcal{S}^\Pi_2\left[w_A\psi^w_\xi\right](\boldsymbol{r}), & \{y < 0\}, \end{cases} \tag{4.34}$$

(cf. (4.3)), are highly accurate for a certain range of complex values of ξ—a fact that is relevant in the analysis presented at various points in Section 4.3.4.

In order to appreciate the need for consideration of complex values of ξ we first study the errors that result from use of the approximate equation (4.33) for a given *real* value of ξ. To gain an insight into the extent of such errors we subtract (4.33) from (4.31) and we thus find that the error $\mathbf{e}^w_\xi = \phi_\xi - \phi^w_\xi$ satisfies the equation

$$\mathrm{E}\,\mathbf{e}^w_\xi + \mathrm{T}_\Pi[W_A\mathbf{e}^w_\xi] = \mathrm{T}_\Pi\left[(I - W_A)\phi_\xi\right] \quad \text{on} \quad \Pi_A.$$

The error source $\mathrm{T}_\Pi\left[(I - W_A)\phi_\xi\right]$ provides an important indication of the expected error sizes. For definiteness we focus on one of the various contributions to this quantity, namely $\mathrm{T}_{12}\left[(1 - w_A)\psi_\xi\right]$ (see equation (4.7)); all other contributions can be treated similarly.

The error source term $\mathrm{T}_{12}\left[(1 - w_A)\psi_\xi\right]$ is given by a linear combination of the single-layer potentials

$$\begin{aligned} S_j\left[(1 - w_A(\cdot))\,\mathrm{e}^{i\xi\cdot}\right](t) &= \frac{i}{4}\int_{-\infty}^{\infty} H^{(1)}_0(k_j|t - \tau|)[1 - w_A(\tau)]\,\mathrm{e}^{i\xi\tau}\,\mathrm{d}\tau \\ &= \frac{i}{4}\int_{-\infty}^{-cA} H^{(1)}_0(k_j|t - \tau|)\widetilde{w}_A(\tau)\,\mathrm{e}^{i\xi\tau}\,\mathrm{d}\tau \\ &\quad + \frac{i}{4}\int_{cA}^{\infty} H^{(1)}_0(k_j|t - \tau|\widetilde{w}_A(\tau)\,\mathrm{e}^{i\xi\tau}\,\mathrm{d}\tau, \end{aligned} \tag{4.35}$$

$(j = 1, 2)$. We consider the last term first. Introducing the change of variables $t = As$ and

$\tau = A\sigma$ the last integral in (4.35) is expressed in the form

$$A\,\mathrm{e}^{-iAk_js}\int_c^\infty h_0(Ak_j|s-\sigma|)\widetilde{w}_1(\sigma)\,\mathrm{e}^{iA\sigma(k_j+\xi)}\,\mathrm{d}\sigma, \tag{4.36}$$

which we estimate in what follows for values of s throughout the interval $[-c, c]$ (that is, throughout the region $\{s : w_A(As) = 1\} = \{s : w(s; c, 1) = 1\}$) under the assumption $k_j + \xi \neq 0$. Here, given $k > 0$ and $d > 0$, the (non-oscillatory) function $h_\ell(x) = \mathrm{e}^{-ix}H_\ell^{(1)}(x)$ ($\ell \geq 0$, $x \geq 0$) satisfies the estimates

$$\left|\left(\frac{\mathrm{d}}{\mathrm{d}x}\right)^m [h_\ell(kx)]\right| \leq \begin{cases} C_{m,\ell}(kx)^{-1/2}x^{-m} & \text{if } kx \geq d, \\ C_{m,\ell}(kx)^{-\ell}x^{-m} & \text{if } 0 < kx < d \text{ and } m + \ell > 0, \\ C_{0,0}(1 + |\log kx|) & \text{if } 0 < kx < d \text{ and } m = \ell = 0, \end{cases} \tag{4.37}$$

for some constants $C_{m,\ell} > 0$, $m \geq 0$. (This follows from the well known asymptotic expression [76, Section 5.11] for the Hankel function; see also [50, Lemma 1].)

To estimate the error source (4.36) for a given ξ we note that, in view of the absence points of stationary phase in the region $\{|\sigma| > c\}$, after m integrations by parts we obtain

$$\frac{(-1)^m A\,\mathrm{e}^{-iAk_js}}{[iA(k_j+\xi)]^m}\int_c^\infty \left(\frac{\mathrm{d}}{\mathrm{d}\sigma}\right)^m [h_0(Ak_j|s-\sigma|)\widetilde{w}_1(\sigma)]\,\mathrm{e}^{iA\sigma(k_j+\xi)}\,\mathrm{d}\sigma, \tag{4.38}$$

since all the boundary contributions vanish. This can be checked by taking into account that (a) the function $\widetilde{w}_1$ and its derivatives vanish at $\sigma = c$, and that, in view of (4.37), (b) the function $h_0(Ak_j|s-\sigma|)$ and its derivatives decay as $\sigma \to \infty$.

(The integration-by-parts procedure used above requires that for all $s \in [-c, c]$ the integrand in (4.36) be an infinitely smooth function of σ throughout the integration domain. This is straightforward for $s \in [-c, c)$, and it holds for $s = c$ as well—in spite of the fact that, for $s = c$, $h_0(Ak_j(\sigma - s))$ and its derivatives are singular at $\sigma = c$—since the window function $\widetilde{w}_1(\sigma) = 1 - w(\sigma; c, 1)$ vanishes along with all of its derivatives at the endpoint $\sigma = c$.)

Utilizing (4.37) it additionally follows that the value of the integral in (4.38) remains

bounded for all $A > 0$. We therefore conclude from (4.38) that for $|s| \leq c$ the last integral in (4.35) is a super-algebraically small quantity (it decays faster than any integer power of $1/A$) as long as $k_j + \xi \neq 0$. Similarly, it can be shown the next-to-last integral in (4.35) is super-algebraically small as long as $k_j - \xi \neq 0$, and thus we conclude that provided $k_j \pm \xi \neq 0$ the term $T_{\Pi}\left[(I - W_A)\phi_\xi\right]$ decreases super-algebraically fast as $A \to \infty$ within the interval $[-cA, cA]$.

Clearly, increasingly larger values of A are necessary to keep the error-source term (4.38) below a given tolerance as $|k_j \pm \xi| \to 0$. The last column of Table 4.2 demonstrates that, as expected, the corresponding errors $\mathbf{e}_\xi^w$ arising in the integral equation (4.33) exhibit slow convergence for small values of $|k_j \pm \xi|$ as well. Fortunately, however, small values of $|k_j \pm \xi|$ can be completely avoided in the analysis presented in Section 4.3.4 by representing point sources as a contour integral in the complex ξ plane. A discussion concerning the errors $\mathbf{e}_\xi^w$ that arise in the integral equation (4.33) as a result of the aforementioned errors sources, but with allowance for complex values of ξ, is presented in the following section.

4.3.1.2 Error estimation for complex values of ξ

As mentioned in Section 4.3.1.1, the formal multiple-scattering error analysis presented in Section 4.3.4, which applies to the case in which the WGF method is used to produce the solutions of problems of scattering by a *bounded obstacle in the presence of a planar dielectric layer*, can be established provided corresponding estimates for the error $\mathbf{e}_\xi^w$ on $[-cA, cA]$ for the *obstacle-free problem* are available for certain complex values of ξ. Under certain smoothness assumptions on ϕ_ξ^w, which have been verified numerically, such estimates on $\mathbf{e}_\xi^w$ can be obtained (for $\xi \in \mathbb{C}$, $\operatorname{Re}\xi \cdot \operatorname{Im}\xi \leq 0$, $\xi \neq \pm k_j$) on the basis of the "improper" integral equation

$$E\, \mathbf{e}_\xi + T_{\Pi}[\mathbf{e}_\xi] = (I - W_A)\left\{\phi_\xi^{\text{inc}} - T_{\Pi}[W_A \phi_\xi^w]\right\} \quad \text{on} \quad \Pi \tag{4.39}$$

that is satisfied by a *new* error density $\mathbf{e}_\xi = W_A \phi_\xi^w - \phi_\xi$. Note that, by definition, $\mathbf{e}_\xi = \mathbf{e}_\xi^w$ on $[-cA, cA]$.

We call this integral equation improper in view of its infinite-domain exponentially-growing integrand. Note, for example, that the related integral equation (4.31), which for such complex values of ξ entails a closely related exponentially growing integrand, admits the exact solution (4.32). Equation (4.31) represents the most singular term in (4.39); the remaining terms do not present difficulties. (The numerical values of $\mathbf{e}_\xi$ presented in Table 4.2 for complex values of ξ, for example, were evaluated as the difference of the numerical WGF solution and the exact solution (4.32).) The integral equation (4.39) could alternatively (and more generally) be interpreted via an appeal to analytic contour integration in the complex plane.

Relying on 1) The convolution character of the operator T to explicitly solve (4.39) by means of Fourier transform techniques, together with 2) An extension of the integration-by-parts arguments presented in Section 4.3.1.1 to complex values of ξ, and 3) The aforementioned smoothness assumptions on ϕ_ξ^w, it can be shown that, as illustrated by the numerical examples in Section 4.3.2, the error $\mathbf{e}_\xi$ is super-algebraically small throughout the region $[-cA, cA]$. Additionally, the error estimates can be extended to the values of the scattered fields in certain regions around the windowed domain (but see also Remark 4.3.1). Rigorous proofs of these estimates are currently being completed and will be presented elsewhere. The next section presents a variety of numerical results demonstrating that, as suggested in the present section, the WGF method for the obstacle-free case does give rise to super-algebraically convergent integral-equation solutions and scattered fields.

Remark 4.3.1. *It is important to note that the aforementioned near-field convergence is not uniform in the strip $[-cA, cA] \times \mathbb{R}$: for points in this region with larger and larger values of y, correspondingly larger and larger values of $A > 0$ are necessary to reach a prescribed error tolerance; see also Figures 4.9, 4.10 and 4.12.*

A	Error
	$\xi = 0$	$\xi = 20 - i$	$\xi = 40 - i$	$\xi = 50$	$\xi = 19.99$
2λ	$1.26 \cdot 10^{-2}$	$1.06 \cdot 10^{-3}$	$2.10 \cdot 10^{-17}$	$1.42 \cdot 10^{-22}$	$\mathbf{2.04 \cdot 10^{-0}}$
$2^2\lambda$	$3.29 \cdot 10^{-3}$	$5.72 \cdot 10^{-4}$	$1.04 \cdot 10^{-17}$	$9.21 \cdot 10^{-23}$	$\mathbf{1.95 \cdot 10^{-0}}$
$2^3\lambda$	$5.04 \cdot 10^{-4}$	$8.98 \cdot 10^{-6}$	$1.35 \cdot 10^{-19}$	$1.38 \cdot 10^{-24}$	$\mathbf{3.70 \cdot 10^{-1}}$
$2^4\lambda$	$2.95 \cdot 10^{-5}$	$7.91 \cdot 10^{-7}$	$8.28 \cdot 10^{-21}$	$1.31 \cdot 10^{-25}$	$\mathbf{2.36 \cdot 10^{-1}}$
$2^5\lambda$	$5.57 \cdot 10^{-7}$	$1.57 \cdot 10^{-8}$	$3.68 \cdot 10^{-21}$	$8.65 \cdot 10^{-27}$	$\mathbf{1.45 \cdot 10^{-1}}$

Table 4.2: Errors $\|\mathbf{e}_\xi\|_{L^\infty([-cA,cA])} = \|\mathbf{e}_\xi^w\|_{L^\infty([-cA,cA])} = \|\boldsymbol{\phi}_\xi - \boldsymbol{\phi}_\xi^w\|_{L^\infty([-cA,cA])}$ for various window sizes and values of the parameter ξ obtained in the solution of the problem of scattering of u_ξ^{inc}, defined in (4.30) for $\boldsymbol{r}' = (0, 1)$, by a dielectric plane for wavenumbers $k_1 = 20$ and $k_2 = 40$. As demonstrated by the $\xi = 19.99$ column in this table, which is included for completeness, slow convergence takes place for values of ξ for which $|k_j \pm \xi|$ is small. As indicated in the text, however, such situations are bypassed in the error analysis presented in Section 4.3.4 by an appropriate selection of complex integration contours.

4.3.2 Obstacle-free problem under plane-wave incidence: Numerical illustrations

To illustrate the WGF approximation properties considered in Section 4.3.1, here we present Table 4.2 and Figures 4.9 and 4.10. With reference to the notations in that section, Table 4.2 displays the maximum throughout $[-cA, cA]$ of the numerical errors $\mathbf{e}_\xi^w$ that result for incident waves u_ξ^{inc} with various relevant complex values of ξ (cf. equation (4.30) and associated text). As demonstrated in these experiments, $\boldsymbol{\phi}_\xi^w$ does indeed approximate $\boldsymbol{\phi}_\xi$ with super-algebraically small errors within the region $[-cA, cA]$ for $\xi \in \mathbb{C}$, $\operatorname{Re} \xi \cdot \operatorname{Im} \xi \leq 0$, such that $\xi \neq \pm k_1$ or $\xi \neq \pm k_2$. In accordance with the discussion in Section 4.3.1, it is clear that large values of A are generally required for convergence to a given error whenever $|k_j \pm \xi|$ is small. But this does not impact upon the multiple-scattering error analysis presented in Section 4.3.4 since the complex integration contour used in that section (Figure 4.11) completely avoids a neighborhood of the points $\xi \neq \pm k_1$.

The errors introduced by the obstacle-free WGF method in the *scattered field* for values of ξ along the aforementioned complex contour are also considered in the context of the multiple-scattering error analysis presented in Section 4.3.4. The field errors resulting for a

(a) $\xi = 0$.

(b) $\xi = 20 - i$.

(c) $\xi = 40 - i$.

(d) $\xi = 50$.
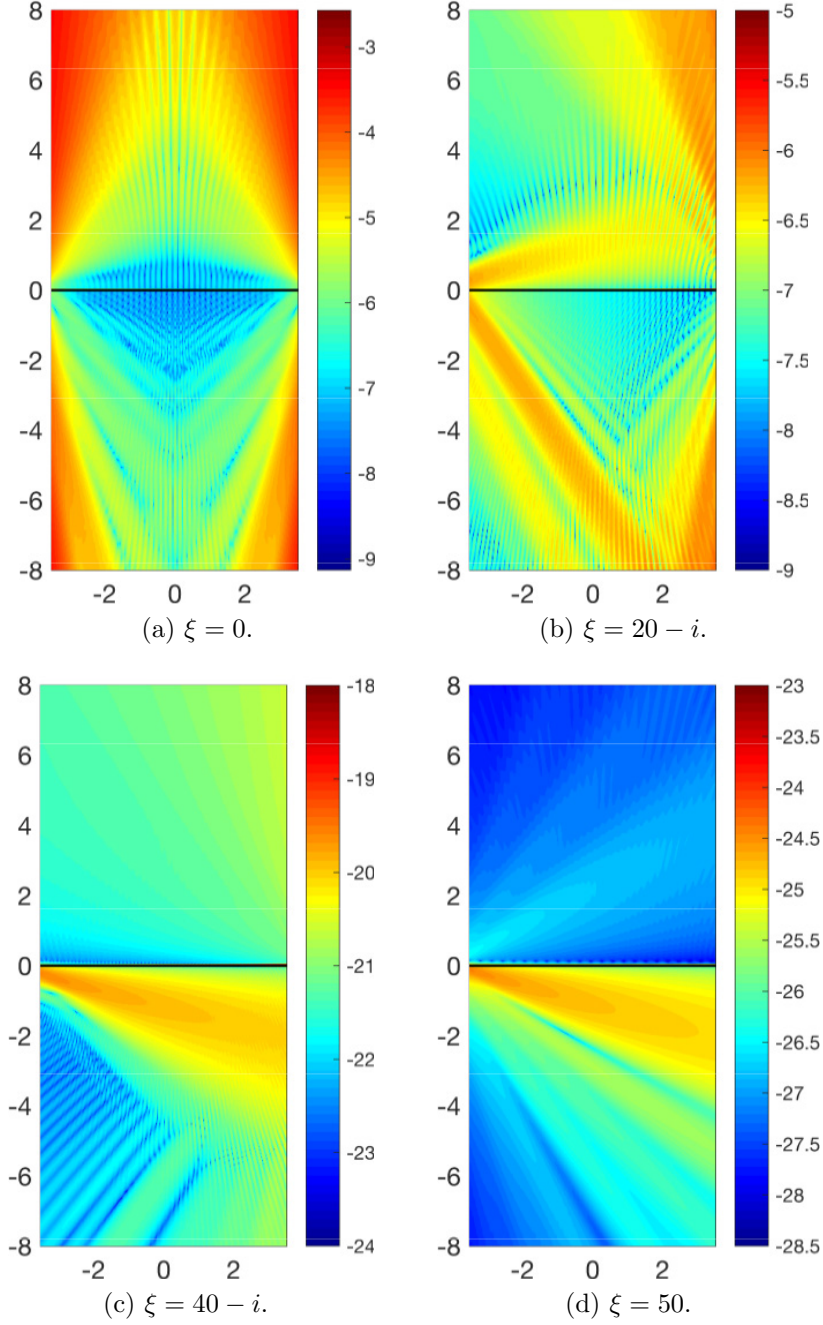
Figure 4.9: Logarithm of the field errors $\log_{10} |u_\xi(\boldsymbol{r}) - u_\xi^w(\boldsymbol{r})|$ obtained by means of WGF method with $A = 16\lambda$ ($\lambda = 2\Pi/k_1$) for the problem of scattering of u_ξ^{inc} defined in (4.30) for $\boldsymbol{r}' = (0, 1)$, by a dielectric plane for various values of ξ and wavenumbers $k_1 = 20$ and $k_2 = 40$. The quantity u_ξ^w is defined in (4.34) and u_ξ equals the exact reflected field $C_\xi(T_\xi - 1) \, \mathrm{e}^{i\xi x - \gamma_1(\xi)y}$ in the upper half-plane $\{y > 0\}$, and the exact transmitted field $C_\xi T_\xi \, \mathrm{e}^{i\xi x + \gamma_2(\xi)y}$ in the lower half-plane $\{y < 0\}$.
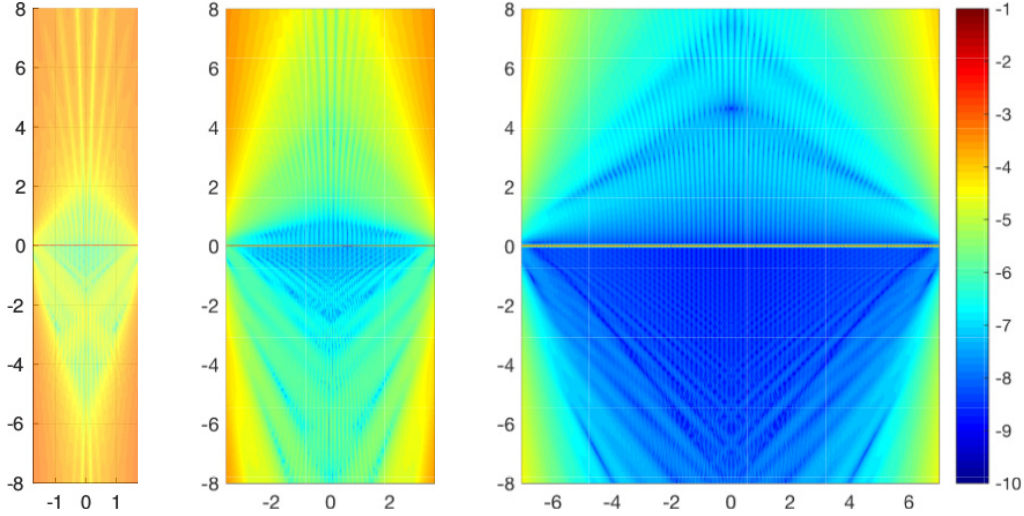
Figure 4.10: Logarithm of the field errors $\log_{10} |u_\xi(\boldsymbol{r}) - u_\xi^w(\boldsymbol{r})|$ obtained by means of WGF method for the problem of scattering of u_ξ^{inc}, $\xi = 0$, defined in (4.30) for $\boldsymbol{r}' = (0,1)$, by a dielectric plane for various window sizes $A = 8\lambda$ (left), 16λ (middle) and 32λ (right) and wavenumbers $k_1 = 20$ and $k_2 = 40$ ($\lambda = 2\Pi/k_1$). As in Figure 4.9, u_ξ^w is defined in (4.34) and u_ξ equals the exact reflected field $C_\xi(T_\xi - 1)\,\mathrm{e}^{i\xi x - \gamma_1(\xi)y}$ in the upper half-plane $\{y > 0\}$, and the exact transmitted field $C_\xi T_\xi\,\mathrm{e}^{i\xi x + \gamma_2(\xi)y}$ in the lower half-plane $\{y < 0\}$. The absolute errors on the segment $\{(x,y) : -1 \le x \le 1 \text{ and } y = 4\}$, for example, are $10^{-3.68}$, $10^{-5.18}$ and $10^{-7.04}$ for $A = 8\lambda$, $A = 16\lambda$ and $A = 32\lambda$, respectively, thus demonstrating super-algebraic convergence. Note that given the highly oscillatory character of the error, in both the horizontal direction and, at a much lower frequency, in the vertical direction, it is difficult to obtain a clean (non-oscillatory) convergence pattern at any given point in space.

few relevant complex-wavevector incidences ξ are presented in Figure 4.9. Note the extremely small field values that arise for the relatively small window size $A = 16\lambda$. In fact, the largest such errors take place for the case $\xi = 0$—which corresponds to an incident field with a *real wavevector* (that is, a physically realizable incident field) under normal incidence. As demonstrated in Figure 4.10, even in this case fast convergence takes place. For example, use of windows of sizes the $A = 8\lambda$, $A = 16\lambda$ and $A = 32\lambda$ suffices to produce solutions with errors of the order of $10^{-3.68}$, $10^{-5.18}$ and $10^{-7.04}$, respectively, on a certain representative segment in space (details are presented in the figure caption).

4.3.3 Obstacle-free problem under point-source incidence: Numerical illustrations

To conclude this section we study the errors introduced by the WGF method in the solution of the problem of scattering of a point-source incident field (where the source is located at a point $\boldsymbol{r}' = (x', y')$ with $y' > 0$) by a flat dielectric half-plane in the region $\{-cA \leq x \leq cA\}$. The resulting integral equation formulation for this problem is once again

$$\mathrm{E}\,\boldsymbol{\phi_{r'}} + \mathrm{T}_\Pi[\boldsymbol{\phi_{r'}}] = \boldsymbol{\phi_{r'}^{\mathrm{inc}}} \quad \text{on} \quad \Pi, \tag{4.40}$$

where the right-hand-side is now given by

$$\boldsymbol{\phi_{r'}^{\mathrm{inc}}} = \frac{i}{4}\left[H_0^{(1)}(k_1|\cdot - \boldsymbol{r}'|)\big|_\Pi, \frac{\partial}{\partial y} H_0^{(1)}(k_1|\cdot - \boldsymbol{r}'|)\big|_\Pi \right]^T.$$
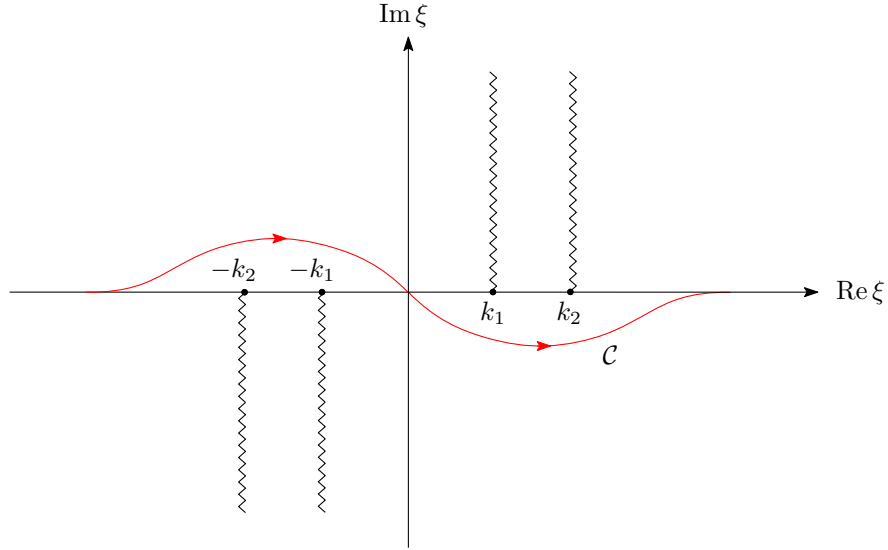
Figure 4.11: Complex integration path utilized in the evaluation of the integral in (4.41).

According to well-known formula

$$\frac{i}{4} H_0^{(1)}(k_j|\boldsymbol{r} - \boldsymbol{r}'|) = \frac{1}{4\pi} \int_{\mathcal{L}} \frac{\mathrm{e}^{-\gamma_j|y-y'|}}{\gamma_j}\, \mathrm{e}^{i\xi(x-y_1)}\, \mathrm{d}\xi \tag{4.41}$$

(where $\mathcal{L} = (-\infty, \infty)$), the field produced by a point source can be expressed as a superposition of incident fields u_ξ^{inc} as defined in (4.30). But, to obtain a superposition which includes favorable plane waves only (that is, plane waves for which, like the ones considered in Section 4.3.1 and above in the present section, the WGF method gives rise to super-algebraic convergence) we resort to Cauchy's theorem to deform the integration contour in the integral (4.41) so that the modified integration contour in the complex plane, denoted by $\mathcal{C}$ (see Figure 4.11), avoids the singular points $\xi = \pm k_2$ and $\xi = \pm k_1$ at which the WGF method fails. According to section 4.3.2, for each $\xi \in \mathcal{C}$ the WGF method approximates, with super-algebraically small errors, the field resulting from the scattering of u_ξ^{inc}. Thus, in view of equation (4.41) with $\mathcal{L} = \mathcal{C}$, we see that the solution of the integral equation (4.40) for point source illumination is also approximated with super-algebraically small errors throughout the interval $[-cA, cA]$.
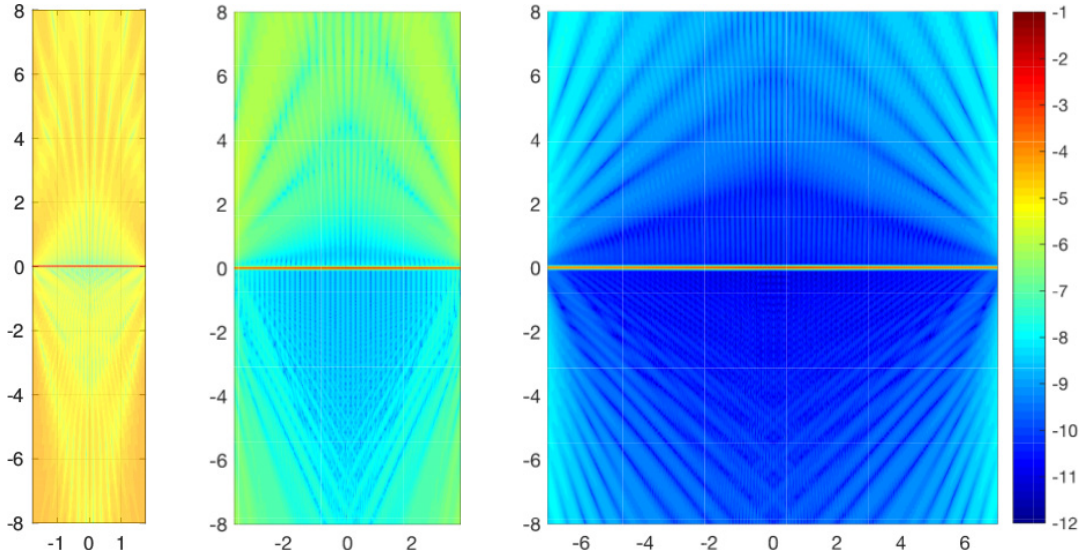
Figure 4.12: Base-10 logarithm of the absolute error (see Remark 4.4.1) in the WGF-computed reflected and transmitted fields for the problem of scattering of a point-source incidence field by a dielectric plane.

Remark 4.3.2. *The approximation properties demonstrated above in this section for incident fields given by point sources can easily be extended to illuminations given by surface*

distributions of point sources of the form

$$\tilde{u}^{\text{inc}}(\boldsymbol{r}) = \frac{i}{4} \int_S H_0^{(1)}(k_1|\boldsymbol{r} - \boldsymbol{r}'|)\sigma(\boldsymbol{r}')\,\mathrm{d}s_{\boldsymbol{r}'}, \tag{4.42}$$

where S is a bounded curve contained in the upper-half plane $\{y > 0\}$ (Figure 4.13), and where σ denotes a given surface density. Indeed, letting $\boldsymbol{\phi}^{\text{inc}} = [\tilde{u}^{\text{inc}}|_\Pi, \partial\tilde{u}^{\text{inc}}/\partial n|_\Pi]^T$, the solutions $\boldsymbol{\phi} = \boldsymbol{\phi}(\boldsymbol{r})$ and $\boldsymbol{\phi}^w = \boldsymbol{\phi}^w(\boldsymbol{r})$ of the exact and windowed integral equations

$$\mathrm{E}\,\boldsymbol{\phi} + \mathrm{T}_\Pi\,[\boldsymbol{\phi}] = \boldsymbol{\phi}^{\text{inc}} \quad on \quad \Pi \tag{4.43}$$

and

$$\mathrm{E}\,\boldsymbol{\phi}^w + \mathrm{T}_\Pi\,[W_A\boldsymbol{\phi}^w] = \boldsymbol{\phi}^{\text{inc}} \quad on \quad \Pi_A, \tag{4.44}$$

are given by integrals of the form

$$\int_S \boldsymbol{\eta}_{\boldsymbol{r}'}(\boldsymbol{r})\sigma(\boldsymbol{r}')\,\mathrm{d}s_{\boldsymbol{r}'},$$

where $\boldsymbol{\eta}_{\boldsymbol{r}'} = \boldsymbol{\phi}_{\boldsymbol{r}'}$ (resp. $\boldsymbol{\eta}_{\boldsymbol{r}'} = \boldsymbol{\phi}_{\boldsymbol{r}'}^w$) is the exact solution (resp. the WGF approximation of the solution) of equation (4.40). Since, in view of the discussion presented above in this section, $\boldsymbol{\phi}_{\boldsymbol{r}'}^w$ is a super-algebraically uniformly accurate approximation of the corresponding solution $\boldsymbol{\phi}_{\boldsymbol{r}'}$ throughout the region $[-cA, cA]$ for all point sources $\boldsymbol{r}' \in S$, it follows that $\boldsymbol{\phi}^w$ must itself be a super-algebraically accurate approximation of $\boldsymbol{\phi}$ within the region $[-cA, cA]$. Similarly, use of the representation formula (4.34) with densities $\boldsymbol{\phi}^w$ produces the associated reflected and transmitted fields with super-algebraically small errors within the strip $[-cA, cA] \times \mathbb{R}$, and, in particular, throughout the curve S. An entirely analogous discussion applies, finally, to illumination by incident fields given by dipole distributions of the form

$$\tilde{u}^{\text{inc}}(\boldsymbol{r}) = \frac{i}{4} \int_S \frac{\partial}{\partial n_{\boldsymbol{r}'}} H_0^{(1)}(k_1|\boldsymbol{r} - \boldsymbol{r}'|)\sigma(\boldsymbol{r}')\,\mathrm{d}s_{\boldsymbol{r}'}, \tag{4.45}$$

The contents of this remark play an important role in the multiple scattering error analysis presented in Section 4.3.4.

4.3.4 Formal error analysis via multiple-scattering

In order to place the descriptive discussions in Section 4.2 within a more mathematically precise framework, this section presents a formal error analysis based on multiple scattering iterations. For clarity and simplicity we limit the discussion in this section to geometrical configurations in which a defect, in the form of a dielectric obstacle bounded by the curve S, lies completely above the dielectric planar interface Π—as depicted in Figure 4.13.
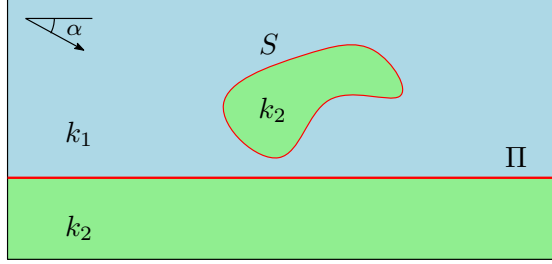
Figure 4.13: Description of the domain consisting of an obstacle above a dielectric half-plane utilized in the multiple-scattering discussion in Section 4.3.4. For notational simplicity the wavenumber within S was selected to equal the "ground" wavenumber k_2. But this is otherwise an absolutely unessential assumption.

The specifics in the context of the configuration in Figure 4.13 are as follows. Upon illumination of such a structure by a plane-wave $u^{\mathrm{inc}}(\boldsymbol{r}) = \mathrm{e}^{ik_1(x\cos\alpha + y\sin\alpha)}$, and letting $\boldsymbol{\phi}_{\Pi}^{\mathrm{inc}} = \left[u^{\mathrm{inc}}|_{\Pi}, \partial u^{\mathrm{inc}}/\partial n|_{\Pi}\right]^{T}$, $\boldsymbol{\phi}_{S}^{\mathrm{inc}} = \left[u^{\mathrm{inc}}|_{S}, \partial u^{\mathrm{inc}}/\partial n|_{S}\right]^{T}$, the integral equations (4.6) may be re-expressed as the equation system

$$\mathrm{E}\,\boldsymbol{\phi}_{\Pi} + \mathrm{T}_{\Pi}\left[\boldsymbol{\phi}_{\Pi}\right] \;=\; \boldsymbol{\phi}_{\Pi}^{\mathrm{inc}} + \mathrm{R}_{S}^{\Pi}\left[\boldsymbol{\phi}_{S}\right] \quad \text{on} \quad \Pi, \tag{4.46a}$$

$$\mathrm{E}\,\boldsymbol{\phi}_{S} + \mathrm{T}_{S}\left[\boldsymbol{\phi}_{S}\right] \;=\; \boldsymbol{\phi}_{S}^{\mathrm{inc}} + \mathrm{R}_{\Pi}^{S}\left[\boldsymbol{\phi}_{\Pi}\right] \quad \text{on} \quad S \tag{4.46b}$$

for the unknowns $\boldsymbol{\phi}_{S} = \left[u_2|_{S}, \partial u_2/\partial n|_{S}\right]^{T}$ and $\boldsymbol{\phi}_{\Pi} = \left[u_2|_{\Pi}, \partial u_2/\partial n|_{\Pi}\right]^{T}$ (whose components are the values of the total field and its normal derivative at the boundaries S and Π, respectively). Here the operators T_{Π} and T_{S} are defined as in equations (4.7)–(4.8) with $\Gamma = \Pi$

and $\Gamma = S$, respectively, and the operators R_S^Π and R_Π^S are given by

$$
R_S^\Pi[\phi](\boldsymbol{r}) = \begin{bmatrix} \int_S \left\{ \dfrac{\partial G_1}{\partial n_{\boldsymbol{r}'}}(\boldsymbol{r}, \boldsymbol{r}')\phi_1(\boldsymbol{r}') - \nu G_1(\boldsymbol{r}, \boldsymbol{r}')\phi_2(\boldsymbol{r}') \right\} \mathrm{d}s_{\boldsymbol{r}'} \\ \int_S \left\{ \dfrac{\partial^2 G_1}{\partial n_{\boldsymbol{r}}\partial n_{\boldsymbol{r}'}}(\boldsymbol{r}, \boldsymbol{r}')\phi_1(\boldsymbol{r}') - \nu \dfrac{\partial G_1}{\partial n_{\boldsymbol{r}}}(\boldsymbol{r}, \boldsymbol{r}')\phi_2(\boldsymbol{r}') \right\} \mathrm{d}s_{\boldsymbol{r}'} \end{bmatrix}, \quad \boldsymbol{r} \in \Pi, \quad (4.47)
$$

$$
R_\Pi^S[\phi](\boldsymbol{r}) = \begin{bmatrix} \int_\Pi \left\{ \dfrac{\partial G_1}{\partial n_{\boldsymbol{r}'}}(\boldsymbol{r}, \boldsymbol{r}')\phi_1(\boldsymbol{r}') - \nu G_1(\boldsymbol{r}, \boldsymbol{r}')\phi_2(\boldsymbol{r}') \right\} \mathrm{d}s_{\boldsymbol{r}'} \\ \int_\Pi \left\{ \dfrac{\partial^2 G_1}{\partial n_{\boldsymbol{r}}\partial n_{\boldsymbol{r}'}}(\boldsymbol{r}, \boldsymbol{r}')\phi_1(\boldsymbol{r}') - \nu \dfrac{\partial G_1}{\partial n_{\boldsymbol{r}}}(\boldsymbol{r}, \boldsymbol{r}')\phi_2(\boldsymbol{r}') \right\} \mathrm{d}s_{\boldsymbol{r}'} \end{bmatrix}, \quad \boldsymbol{r} \in S. \quad (4.48)
$$

In order to estimate the errors that arise as the system (4.46) is solved by means of the WGF method, we reformulate (4.46) in terms of the new unknowns $\widetilde{\phi}_\Pi = \phi_\Pi - \phi_\Pi^f$ on Π and $\widetilde{\phi}_S = \phi_S - \phi_S^f$ on S. Here, denoting by u_2^f and u^f the exact transmitted field and the total field for the obstacle-free problem, respectively (see (C.1)), we have set $\phi_\Pi^f = \left[u_2^f|_\Pi, \partial u_2^f/\partial n|_\Pi\right]^T$ and $\phi_S^f = \left[u^f|_S, \partial u^f/\partial n|_S\right]^T$. Using the identities: $\mathrm{E}\,\phi_\Pi^f + \mathrm{T}_\Pi\left[\phi_\Pi^f\right] = \phi_\Pi^{\mathrm{inc}}$ on Π, $R_S^\Pi\left[\phi_S^f\right] = \boldsymbol{0}$ and $R_\Pi^S\left[\phi_\Pi^f\right] = \phi_S^f - \phi_S^{\mathrm{inc}}$, which follow from Green's theorem (using (C.12) and (C.2)) and replacing $\phi_\Pi = \widetilde{\phi}_\Pi + \phi_\Pi^f$ and $\phi_S = \widetilde{\phi}_S + \phi_S^f$ in (4.46a) and (4.46b), respectively, we obtain the following integral equation system

$$
\mathrm{E}\,\widetilde{\phi}_\Pi + \mathrm{T}_\Pi\left[\widetilde{\phi}_\Pi\right] = R_S^\Pi\left[\widetilde{\phi}_S\right] \quad \text{on} \quad \Pi, \tag{4.49a}
$$

$$
\mathrm{E}\,\widetilde{\phi}_S + \mathrm{T}_S\left[\widetilde{\phi}_S\right] = \phi_S^f + R_\Pi^S\left[\widetilde{\phi}_\Pi\right] \quad \text{on} \quad S. \tag{4.49b}
$$

The multiple-scattering character of the problem embodied in (4.49) (or, equivalently, (4.46)) can be elucidated by means of the formal Neumann series solution

$$
\begin{bmatrix} \widetilde{\phi}_\Pi \\ \widetilde{\phi}_S \end{bmatrix} = \sum_{n=0}^\infty \begin{bmatrix} \widetilde{\phi}_\Pi^{(n)} \\ \widetilde{\phi}_S^{(n)} \end{bmatrix} = \sum_{n=0}^\infty \begin{bmatrix} 0 & (\mathrm{E}+\mathrm{T}_\Pi)^{-1}\,R_S^\Pi \\ (\mathrm{E}+\mathrm{T}_S)^{-1}\,R_\Pi^S & 0 \end{bmatrix}^n \begin{bmatrix} \boldsymbol{0} \\ (\mathrm{E}+\mathrm{T}_S)^{-1}\phi_S^f \end{bmatrix}.
$$

Clearly $\widetilde{\phi}_\Pi^{(0)} = \boldsymbol{0}$, and $\phi_S^{(0)}$ is the solution of the integral equation

$$
\mathrm{E}\,\widetilde{\phi}_S^{(0)} + \mathrm{T}_S\left[\widetilde{\phi}_S^{(0)}\right] = \phi_S^f \quad \text{on} \quad S. \tag{4.50}
$$

The $n > 0$ terms in the series, in turn, satisfy the recurrence relation

$$
\begin{bmatrix} \tilde{\phi}_\Pi^{(n)} \\ \tilde{\phi}_S^{(n)} \end{bmatrix} = \begin{bmatrix} (\mathrm{E} + \mathrm{T}_\Pi)^{-1} & 0 \\ 0 & (\mathrm{E} + \mathrm{T}_S)^{-1} \end{bmatrix} \begin{bmatrix} 0 & \mathrm{R}_\Pi^S \\ \mathrm{R}_S^\Pi & 0 \end{bmatrix} \begin{bmatrix} \tilde{\phi}_\Pi^{(n-1)} \\ \phi_S^{(n-1)} \end{bmatrix},
$$

or, equivalently

$$
\begin{aligned}
\mathrm{E}\,\tilde{\phi}_\Pi^{(n)} + \mathrm{T}_\Pi \left[\tilde{\phi}_\Pi^{(n)} \right] &= \mathrm{R}_S^\Pi \left[\tilde{\phi}_S^{(n-1)} \right] && \text{on} \quad \Pi, && \text{(4.51a)} \\
\mathrm{E}\,\tilde{\phi}_S^{(n)} + \mathrm{T}_S \left[\tilde{\phi}_S^{(n)} \right] &= \mathrm{R}_\Pi^S \left[\tilde{\phi}_\Pi^{(n-1)} \right] && \text{on} \quad S. && \text{(4.51b)}
\end{aligned}
$$

The corresponding "multiple-scattering" form of the windowed integral equations (4.16) for the configuration depicted in Figure 4.13, in turn, is given by the system

$$
\begin{aligned}
\mathrm{E}\,\psi_\Pi + \mathrm{T}_\Pi \left[W_A \psi_\Pi \right] &= \phi_\Pi^{\mathrm{inc}} - \mathrm{T}_\Pi \left[(I - W_A) \phi_\Pi^f \right] + \mathrm{R}_S^\Pi \left[\psi_S \right] && \text{on} \quad \Pi, \\
\mathrm{E}\,\psi_S + \mathrm{T}_S \left[\psi_S \right] &= \phi_S^{\mathrm{inc}} + \mathrm{R}_\Pi^S \left[W_A \psi_\Pi \right] + \mathrm{R}_\Pi^S \left[(I - W_A) \phi_\Pi^f \right] && \text{on} \quad S,
\end{aligned}
$$

which, letting $\widetilde{\psi}_\Pi = \psi_\Pi - \phi_\Pi^f$ on Π_A and $\widetilde{\psi}_S = \psi_S - \phi_S^f$ on S, becomes

$$
\begin{aligned}
\mathrm{E}\,\widetilde{\psi}_\Pi + \mathrm{T}_\Pi \left[W_A \widetilde{\psi}_\Pi \right] &= \mathrm{R}_S^\Pi \left[\widetilde{\psi}_S \right] && \text{on} \quad \Pi_A, && \text{(4.53a)} \\
\mathrm{E}\,\widetilde{\psi}_S + \mathrm{T}_S \left[\widetilde{\psi}_S \right] &= \phi_S^f + \mathrm{R}_\Pi^S \left[W_A \widetilde{\psi}_\Pi \right] && \text{on} \quad S, && \text{(4.53b)}
\end{aligned}
$$

where $\Pi_A = \Pi \cap [-A, A]$. Thus, comparison with (4.49) shows that, similarly, the multiple-scattering recursion for the windowed problem is initialized by $\tilde{\psi}_\Pi^{(0)} = \mathbf{0}$ on Π_A and

$$
\mathrm{E}\,\tilde{\psi}_S^{(0)} + \mathrm{T}_S \left[\tilde{\psi}_S^{(0)} \right] = \phi_S^f \quad \text{on} \quad S, \tag{4.54}
$$

with $n > 0$ terms given by the solutions of the equations

$$
\begin{aligned}
\mathrm{E}\,\tilde{\psi}_\Pi^{(n)} + \mathrm{T}_\Pi \left[W_A \tilde{\psi}_\Pi^{(n)} \right] &= \mathrm{R}_S^\Pi \left[\tilde{\psi}_S^{(n-1)} \right] && \text{on} \quad \Pi_A, && \text{(4.55a)} \\
\mathrm{E}\,\tilde{\psi}_S^{(n)} + \mathrm{T}_S \left[\tilde{\psi}_S^{(n)} \right] &= \mathrm{R}_\Pi^S \left[W_A \tilde{\psi}_\Pi^{(n-1)} \right] && \text{on} \quad S. && \text{(4.55b)}
\end{aligned}
$$

Since equations (4.50) and (4.54) coincide so do their solutions: the $n = 0$ approximation produced by the WGF method, which is given by $\tilde{\boldsymbol{\psi}}_S^{(0)}$, coincides with the exact solution $\tilde{\boldsymbol{\phi}}_S^{(0)}$ throughout S. Similarly, $\tilde{\boldsymbol{\psi}}_\Pi^{(0)} = \mathbf{0}$ coincides with the restriction of $\tilde{\boldsymbol{\phi}}_\Pi^{(0)} = \mathbf{0}$ to Π_A. And, the same is true about the $n = 1$ approximation on S: $\tilde{\boldsymbol{\psi}}_S^{(1)} = \tilde{\boldsymbol{\phi}}_S^{(1)} = \mathbf{0}$. But the $n = 1$ approximation on Π as well as all subsequent approximations do not coincide on either Π or S. As shown in what follows, however, the WGF iterates $\tilde{\boldsymbol{\psi}}_S^{(n)}$ approximate the exact iterates $\tilde{\boldsymbol{\phi}}_S^{(n)}$ with super-algebraic accuracy.

In order to establish this approximation result (and thus complete our multiple-scattering error analysis) we rely on the fact that the right-hand-sides in equations (4.51a), (4.55a), (4.51b) and (4.55b) can be interpreted as scattered field by either S or Π resulting from illumination by fields scattered in previous stages of the multi-scattering recurrence. For example, the right-hand-sides in equations (4.51a) (resp. (4.55a)) coincides with the values on Π (resp. Π_A) of the fields scattered by S under illumination given by $\mathrm{R}_\Pi^S\left[\tilde{\boldsymbol{\phi}}_\Pi^{(n-2)}\right]$ (resp. $\mathrm{R}_\Pi^S\left[W_A\tilde{\boldsymbol{\psi}}_\Pi^{(n-2)}\right]$). Similarly, the right-hand-side in (4.51b) (resp. (4.55b)) coincides with the values on S of the fields scattered by Π (resp. Π_A) under illumination given by $\mathrm{R}_S^\Pi\left[\tilde{\boldsymbol{\phi}}_S^{(n-2)}\right]$ (resp. $\mathrm{R}_S^\Pi\left[\tilde{\boldsymbol{\psi}}_S^{(n-2)}\right]$).

On the strength of this observation, then, let us consider once again the $n = 1$ terms $\tilde{\boldsymbol{\phi}}_\Pi^{(1)}$ and $\tilde{\boldsymbol{\psi}}_\Pi^{(1)}$ (on Π_A) which, as indicated above, do not exactly coincide. Noting that the incident fields in equations (4.51a) and (4.55a) are given by identical distributions of point sources along S, however, Remark 4.3.2 tells us that the WGF solution $\tilde{\boldsymbol{\psi}}_\Pi^{(1)}$ approximates $\tilde{\boldsymbol{\phi}}_\Pi^{(1)}$ with super-algebraically small errors.

Continuing with the multiple-scattering process let us now consider the $n = 2$ instance of equations (4.51b) and (4.55b). Relying once again on Remark 4.3.2, the established super-algebraic convergence of $\tilde{\boldsymbol{\psi}}_\Pi^{(1)}$ to $\tilde{\boldsymbol{\phi}}_\Pi^{(1)}$ throughout $[-cA, cA]$ implies, in turn, that $\mathrm{R}_\Pi^S\left[W_A\tilde{\boldsymbol{\psi}}_\Pi^{(1)}\right]$ approximates $\mathrm{R}_\Pi^S\left[\tilde{\boldsymbol{\phi}}_\Pi^{(1)}\right]$ with super-algebraically small errors as well, and thus the stability of the integral equation posed on S permits us to conclude that $\tilde{\boldsymbol{\psi}}_S^{(2)}$ approximates $\tilde{\boldsymbol{\phi}}_S^{(2)}$ with super-algebraically small errors. In view of equations (4.51a) and (4.55a), on the other hand, we note that $\tilde{\boldsymbol{\phi}}_\Pi^{(2)} = \mathbf{0}$ on Π and $\tilde{\boldsymbol{\psi}}_\Pi^{(2)} = \mathbf{0}$ on Π_A, as both equations have null right-hand

sides.

Clearly, this argument can be carried out to all orders in perturbation theory, allowing us to conclude, within this formal framework, that, at least for the configuration depicted in Figure 4.13, the overall WGF method produces scattering solutions with super-algebraically small errors over the strip $[-cA, cA] \times \mathbb{R}$ (but see Remark 4.3.1). As indicated in Sections 4.2.5 and 4.2.6, once such solutions are available, equally accurate solutions can easily be obtained over prescribed regions in space as well as in the far-field regions.

4.4   Numerical Experiments

This section illustrates the proposed methodology with a variety of numerical results concerning dielectric media, including relevant efficiency and accuracy studies as well as generic application examples. For the sake of definiteness in all the examples considered throughout this section, the value $c = 0.7$ is utilized for the evaluation of the window function (4.9) w_A.

Remark 4.4.1. *In most cases considered in this chapter, errors are reported as "relative errors in the L^∞ norm", or just "relative errors", for short, but absolute L^∞ errors are used as well. The "absolute error" over a given region is defined here as the maximum value of the error over every numerical grid point in that region. The relative error over a region, on the other hand, is defined as the quotient of the absolute error over the region by the maximum value of the solution over the region.*

Our first example demonstrates the efficiency of the new approach by comparing the computing times required to create the systems of equations (which is the operation that dominates the computing time in all of the examples considered) for the WGF method (4.19) and the layer-Green-function method [104, 7]. To do this we consider once again the configuration associated with Figure 4.5, i.e. the problem of scattering by a semi-circular bump defect on a dielectric plane under TE-polarization. Figure 4.14 displays the computing times for various wavenumbers k_1 and $k_2 = 2k_1$ for each method. The discretization density was held proportional to k_1 to properly resolve the oscillatory character of the integrands, and, in order to easily allow for pointwise comparison of the corresponding integral-density
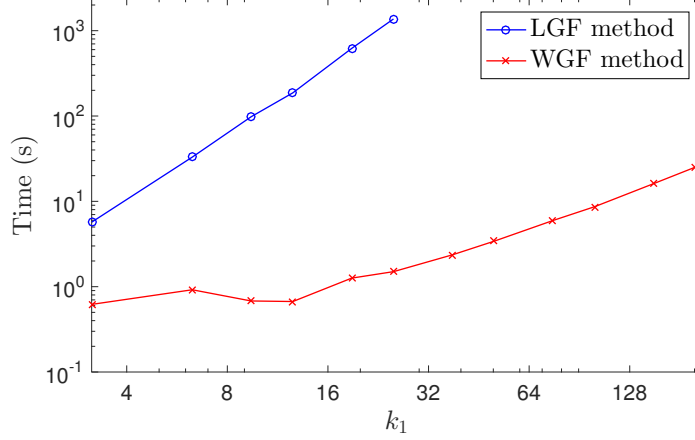
Figure 4.14: Computing times required to form the linear systems of equations resulting from the Nyström discretization of the relevant integral equations for the WGF method (red line) and the layer-Green-function method [104] (blue line), as functions of the wavenumber k_1. The wavenumber k_2 was taken to equal $2k_1$. Comparable ratios in computing times were obtained in cases in which complex k_2 values ($k_2 = \omega\sqrt{(\varepsilon_2 + i\sigma_2/\omega)\mu_0}$) were assumed, with either large or small values of the conductivity σ—including values for materials such as limestone, saturated sand, silt and clay.

k_1	k_2	LGF time	WGF time	ratio
π	2π	588 s.	3.07 s.	192
π	4π	3579 s.	9.10 s.	393

Table 4.3: Computing times required by the layer-Green-function method and the WGF method to produce integral equation solutions with an accuracy better than 5×10^{-3} for the city-like geometry displayed in Figure 4.15. We note that the LGF computing times for this problem are significantly larger than those considered in Figure 4.14 for similar wavenumbers. Such large costs arise in the present problem from the relatively large number of discretization points that need to be used near the plane $y = 0$ to resolve the solution's corner singularity, and from the high cost required by the associated Sommerfeld integral evaluation at such points.

solutions, the same discretization was used for both methods on the semi-circular bump. For each run the WGF parameters were optimized to produce ϕ^w with a relative error which does not exceed 5×10^{-5} on the bump surface. Similarly, the key parameters in the implementation of the layer-Green-function method (including the parameters associated with the numerical evaluation of the Sommerfeld integrals) were adjusted to yield the fastest computation of the corresponding integral density solution within a relative error of 5×10^{-5}. Note that the

data points around $k_1 = 8\pi \approx 25.1$ in Figure 4.14 (which is the last data point presented for the layer-Green-function method) shows that for such frequencies the WGF is approximately three orders of magnitude faster than the layer-Green-function method [104].
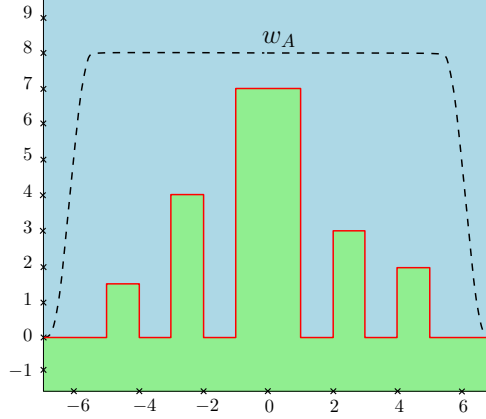

Figure 4.15: City-like geometry and windowing function used. The windowing function w_A was vertically stretched by a factor of 8 for visualization purposes.

The problem of scattering by the city-like structure depicted in Figure 4.15 is considered next. Figure 4.15 also displays the window function utilized in this example. In contrast with the results presented previously in this chapter, the case of TM-polarization was considered for this test. Table 4.3 reports the computing times required to form the relevant system matrices for both the WGF method and the layer-Green-function method. Both solvers were optimized to produce a absolute error of 5×10^{-3} in the solutions of the integral equation, and the same computational grids were utilized to discretize the buildings for both methods.

Table 4.3 compares the computing times required by the WGF method and the layer-Green-function method for two values of k_2. In particular we note that, not only is the new method much faster than the previous approach, but also that the speed-up factor grows: a speed up factor in the hundreds for the value $k_2 = 2\pi$ is doubled as k_2 is itself doubled to the value $k_2 = 4\pi$. Additionally, application of the layer-Green-function method in this context requires use of fictitious curves underneath each building [104] each one of which (curves) must itself be discretized, while the WGF method requires discretization of the ground between the buildings and in the region where the windowing takes place. In the present case the layer-Green-function method produced a system of 2384 unknowns while the WGF

method produced a system of nearly identical size: 2406 unknowns. At higher frequencies, the WGF method requires fewer unknowns than the layer-Green-function method, since, as demonstrated in Table 4.4, at higher frequencies the width of the windowing function can be decreased while maintaining accuracy.

k_1	k_2	A
π	2π	6.5
2π	4π	3.5
4π	8π	1.75
8π	16π	1.1875

Table 4.4: Extent of the windowed region required by the WGF method (4.19) to maintain an accuracy of 5×10^{-5} in the approximation of the surface fields for the problem of scattering from a semi-circular bump of unit radius with various wavenumbers. The angle of incidence was taken to equal $\alpha = -\pi/8$.

In our next numerical example we consider an obstacle over a rough ground which contains indentations below ground level. Figure 4.16 displays the geometry under consideration, together with a selection of window function (which yields an relative error of approximately 1% in the integral equation solution) and corresponding near fields under TE polarized plane-wave illumination with incidence angle $\alpha = -\pi/8$ and with $k_1 = 2\pi$ and $k_2 = 4\pi$. As demonstrated in Figure 4.17 super-algebraic convergence is once again observed as A/λ grows.

In our last example we consider a range of conducting materials with widely varied electrical conductivities. The materials and their corresponding permittivities and electrical conductivities are listed in Table 4.5. The value of the constant for air is included for reference. Table 4.6 presents the ratio of the computing times for each one the examples; these results, which correspond to the value $k_1 = 2.095845023$ of the free-space wavenumber are in rough agreement with the corresponding results presented in Figure 4.14 above, for similar values of k_1. The corresponding values of the wavenumber k_2 are included in the first column of Table 4.6. The fact that k_2 is complex leads to a reduction of the computational cost of the layer Green function, as the overall length of the integration path C_1 in (2.75) is somewhat reduced (as compared to the length of integration path required to evaluate
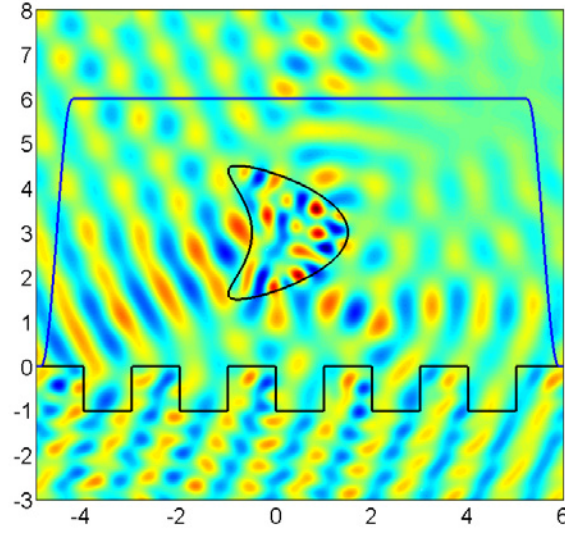
Figure 4.16: Obstacle over a rough ground containing indentations below ground level and associated near fields. Interestingly, the rather narrow window function used (which was scaled vertically in this image for visual clarity) is wide enough to produce a relative error smaller than 1% in the integral equation solution.
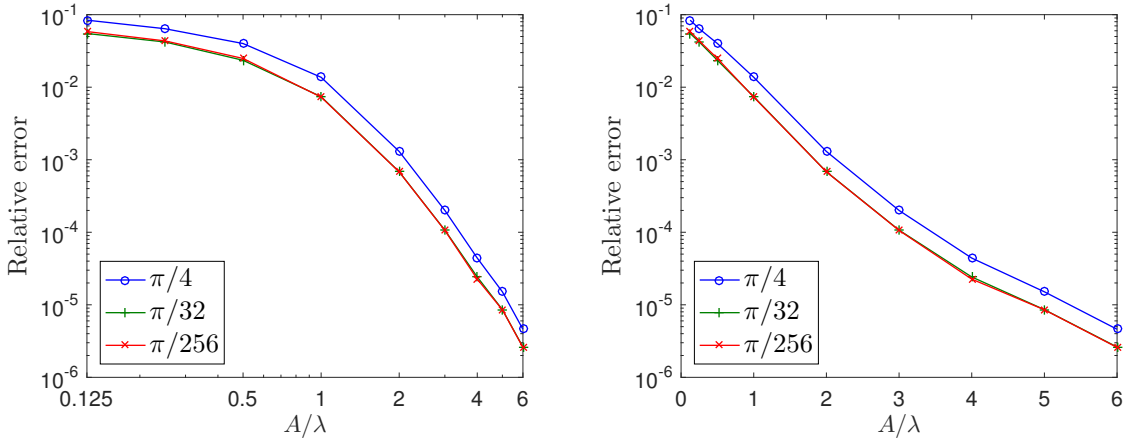
Figure 4.17: Relative errors in the integral densities resulting from numerical solution of (4.19) for the structure depicted in Figure 4.16 by means of the full WGF method, for various window sizes and angles of incidence—including extremely shallow incidences. Left: log-log scale. Right: semi-log scale. Once again we see that, the WGF method computes integral densities with super-algebraically high accuracy uniformly for all angles of incidence.

the Sommerfeld integrals in the case $n = k_2/k_1 > 1$; see Section 2.3.5 for details). As show in Table 4.6, however, this fact does not yield a significant reduction of the overall

computational cost of the LGF method. Table 4.7, in turn, displays the errors in the total field relative to the maximum value of the field, which were obtained by means of the WGF method for the solution of the problem of scattering of a plane-wave by a semi-circular bump for various window sizes $A > 0$.

Material	Relative dielectric constant ε'_r	Electrical conductivity σ (mS/m)
Air	1	0
Limestone	6	2
Saturated sand	20	1
Silt	30	100
Clay	40	1000

Table 4.5: Typical electromagnetic properties of soil materials at 100 MHz [94]. The wave number in the domain Ω_2 is given by $k_2 = \omega\sqrt{\mu_0\varepsilon_0(\varepsilon'_r + \frac{i\sigma}{\omega\varepsilon_0})}$ where $\omega = 2\pi f$, $f = 100 \times 10^6$ Hz, $\varepsilon_0 = 8.8541878176 \times 10^{-12}$F/m and $\mu_0 = 4\pi \times 10^{-7}$H/m. The wavenumber in Ω_1, in turn, is given by $k_1 = \omega\sqrt{\mu_0\epsilon_0}$, and it corresponds to the numerical value $k_1 = 2.095845023 = 2\pi/\lambda$.

Material	Wavenumber k_2	Computing-time ratios Ratio = LGF/WGF
Limestone	$5.136 + 0.1537i$	$23.52 = 84.74s/3.73s$
Sat. sand	$9.373 + 0.0421i$	$28.11 = 83.76s/2.98s$
Silt	$11.95 + 3.3048i$	$17.92 = 72.94s/4.07s$
Clay	$22.19 + 17.793i$	$12.45 = 76.18s/6.12s$

Table 4.6: Comparison of the computing times required for solution of the problem of scattering of a plane-wave by a semi-circular bump of radius 1m using the LGF method and the proposed WGF method. The values of the parameters utilized in the computation of both the WGF solution and the LGF solution were optimized so each one would result, with optimal computational cost, in integral-equation solutions at the surface of the bump which lie within a maximum relative error of 10^{-5} of the exact values. The same quadrature points were used to discretize the surface of the bump for both the LGF and WGF methods. The window size $A = 3.5\lambda$ was utilized in all WGF calculations.

Window	Relative error for $\alpha =$		
size A	$-\pi/4$	$-\pi/32$	$-\pi/256$
1λ	5.19E-03	4.52E-03	4.51E-03
2λ	5.04E-04	4.56E-04	4.55E-04
4λ	2.56E-05	2.40E-05	2.39E-05
8λ	7.57E-08	1.64E-08	2.08E-09

Table 4.7: Relative errors obtained in the solution of the problem of scattering of a semi-circular bump of radius 1m obtained with the WGF method for various window sizes and plane-wave incidences, where the domain Ω_2 is assumed filled with clay for which $k_2 = 22.18765822 + 17.79296274i$ at $f = 100$MHz.

Figures 4.18a, 4.18a and 4.18c, lastly, display the total fields solution of the problem of scattering of the plane-wave with $\alpha = -\pi/4$ by defects in half-planes occupied by limestone, silt and clay, respectively. The clay image (Figure 4.18c) demonstrates that very limited electromagnetic energy penetrates the highly conducting clay ground at this frequency. A small fraction of the energy can be viewed in the Silt image (Figure 4.18b), and a rich electromagnetic pattern in the low-conductivity Limestone image (Figure 4.18a).

(a) Limestone ($k_2 = 20.54 + 0.15i$). (b) Silt ($k_2 = 46.05 + 3.43i$). (c) Clay ($k_2 = 59.33 + 26.62i$).
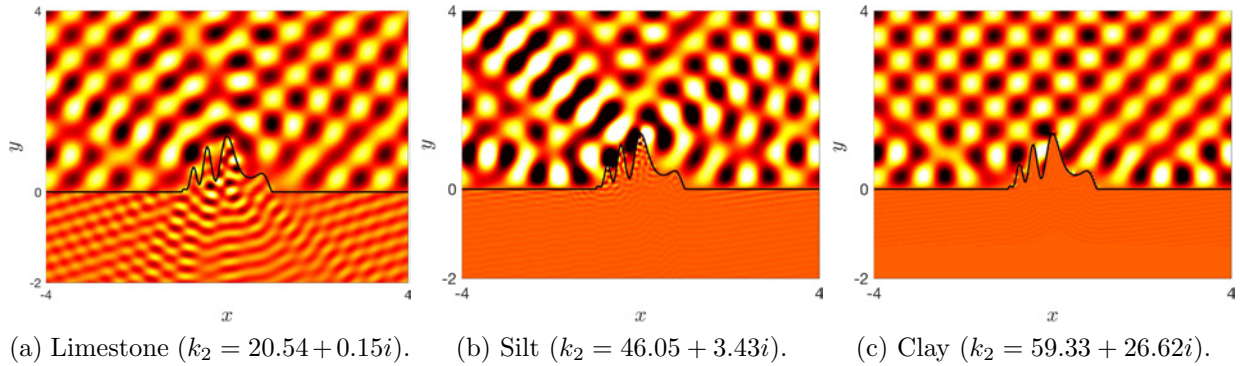
Figure 4.18: Total fields (real part) obtained for the scattering of a plane-wave with $\alpha = -\pi/4$ by defects on conducting planes made of three different materials at $f = 400$MHz.

Chapter 5

Windowed Green Function Method for layered media scattering: Multiple layers

This chapter presents an extension of the Window Green Function (WGF) method introduced in Chapter 4 to two-dimensional problems of electromagnetic scattering by surface defects in the presence of layered media containing an arbitrary number layers. As shown below in this chapter, the main features of the two-layer WGF approach (namely, the super-algebraic convergence of the windowed integral equation solutions as the window size increases and the efficiency of the WGF approach as compared to the LGF approach introduced in Chapter 3) are maintained by the proposed multi-layer solver. Some of the numerical examples presented here, concerning problems of scattering by a surface defect in a three-layer medium, demonstrate that the proposed WGF method is up to hundreds of times faster than the LGF method in producing the corresponding integral equation solution, and it is up to thousands of times faster than the LGF approach in producing the near-fields in a regions around the defect.

This chapter is organized as follows: Section 5.1 introduces notations and necessary multi-layer radiation conditions. The integral representation formulae for the fields are then derived in Section 5.2 on the basis of Green's third identity and the ideas introduced in [52]. Sections 5.3 and 5.4 present the integral equations for the field values at the multiple unbounded material interfaces and the associated windowed integral equations, respectively. The corresponding expressions for the evaluation the near-fields are then presented in Section 5.5.

Section 5.6 deals with a reformulation of the integral equations obtained in Sections 5.3 and 5.4 which significantly simplifies the numerical implementation of the multi-layer WGF method for problems of scattering by smooth surface defects. (This new formulation will be extensively utilized in Chapter 6 to tackle problems of scattering in thee-dimensional space.) Section 5.7, finally, presents a variety of numerical examples which demonstrate the super-algebraic convergence and the high efficiency of multi-layer WGF approach.

5.1 Preliminaries

In this chapter we consider localized (bounded) surface defects in a planar layered dielectric medium composed by $N > 1$ dielectric layers, such as the one depicted in Figure 2.1. The underlying two-dimensional planar dielectric layers are given by $D_j = \mathbb{R} \times (-d_j, -d_{j-1})$ for $j = 1, \ldots, N$, with $d_j > d_{j-1}$ and $d_j \geq 0$ for $j = 1, \ldots, N - 1$, and with $d_0 = -\infty$ and $d_N = \infty$. The planar boundary at the interface between the layers D_j and D_{j+1} is denoted by $\Pi_j = \mathbb{R} \times \{-d_j\}$ where $j = 1, \ldots, N - 1$ (see Figure 2.1). For convenience we set $d_1 = 0$.

The locally perturbed planar dielectric structure results as localized bounded defects are introduced at the planar interfaces Π_j—as illustrated in Figure 5.1 for the particular case $N = 3$. The locally perturbed structure is given by the union of the homogeneous dielectric domains Ω_j, $j = 1, \ldots N$, each one of which amounts to a local perturbation of the corresponding domain D_j. The wavenumber in Ω_j is given by $k_j = \omega \sqrt{\varepsilon_j \mu_j} > 0$. The corresponding local perturbations of the planar interfaces Π_j, $j = 1, \ldots, N - 1$, are denoted by Γ_j, $j = 1, \ldots, N - 1$, respectively. Throughout this chapter it is further assumed that $\Gamma_j \cap \Gamma_i = \emptyset$ for all $i, j = 1, \ldots, N - 1$, so that the boundaries of the subdomains Ω_j are given by $\partial\Omega_1 = \Gamma_1$, $\partial\Omega_j = \Gamma_{j-1} \cup \Gamma_j$, $j = 2, \ldots, N - 1$ and $\partial\Omega_N = \Gamma_{N-1}$.

Our derivations utilize the polar-coordinate systems centered at $(0, -d_1)$, $(0, -(d_{j-1} + d_j)/2)$, $j = 2, \ldots, N - 1$, $(0, -d_{N-1})$ whose radial variables are given by

$$
r_j = \begin{cases}
\sqrt{x^2 + (y + d_1)^2}, & j = 1, \\
\sqrt{x^2 + (y + (d_{j-1} + d_j)/2)^2}, & j = 2, \ldots, N - 1, \\
\sqrt{x^2 + (y + d_{N-1})^2}, & j = N,
\end{cases} \tag{5.1}
$$

(see Figure 5.2). We further consider the domain

$$B_R = ((-R, R) \times (-d_{N-1}, -d_1)) \cup \{(x, y) : r_1 < R\} \cup \{(x, y) : r_N < R\} \tag{5.2}$$

and we select a value of $R > 0$ large enough that B_R contains all of the surface defects, as illustrated in Figure 5.2 for the case $N = 3$. Throughout this chapter, finally, we use the notations $\Omega = \bigcup_{j=1}^{N} \Omega_j$, $D = \bigcup_{j=1}^{N} D_j$ and $\Omega_j^R = \Omega_j \cap B_R$ for $j = 1, \dots, N$.

(a) Planar layered medium.   (b) Locally perturbed planar layered medium.
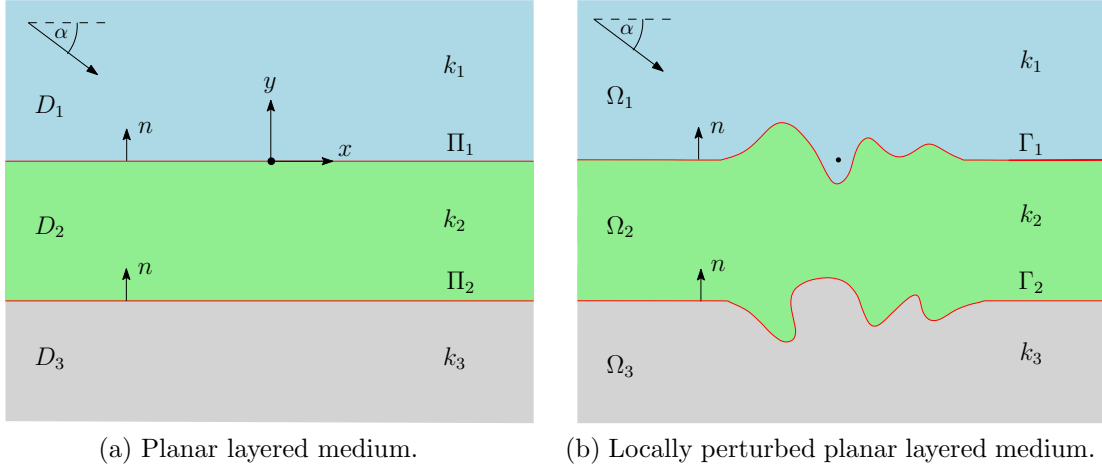
Figure 5.1: Geometry description of a planar layered medium (a) and a locally perturbed planar layered medium (b) for the case $N = 3$.

As in the previous chapters, we consider an incident plane wave $u^{\mathrm{inc}}(\boldsymbol{r}) = \mathrm{e}^{ik_1(x\cos\alpha + y\sin\alpha)}$ that impinges on Γ_1 as indicated in Figure 5.1, where $\alpha \in (-\pi, 0)$ denotes the angle of incidence measured with respect to the x-axis. As shown in Section 2.2.1, $u = E_z$, the z-component of the total electric field in TE-polarization, or $u = H_z$, the z-component of the total magnetic field in TM-polarization, satisfies the homogeneous Helmholtz equation

$$\Delta u + k_j^2 u = 0 \quad \text{in} \quad \Omega_j, \quad j = 1, \dots, N. \tag{5.3}$$

Letting

$$u|_{j^{\pm}}(\boldsymbol{r}) = \lim_{\delta \to 0^+} u(\boldsymbol{r} \pm \delta n(\boldsymbol{r})) \quad \text{and} \quad \left.\frac{\partial u}{\partial n}\right|_{j^{\pm}}(\boldsymbol{r}) = \lim_{\delta \to 0^+} \nabla u(\boldsymbol{r} \pm \delta n(\boldsymbol{r})) \cdot n(\boldsymbol{r}) \quad \text{for} \quad \boldsymbol{r} \in \Gamma_j, \tag{5.4}$$

the transmission conditions at the interfaces between the dielectric media can be expressed in the form

$$u|_{j^+} = u|_{j^-} \quad \text{and} \quad \frac{\partial u}{\partial n}\bigg|_{j^+} = \nu_j \frac{\partial u}{\partial n}\bigg|_{j^-} \quad \text{on} \quad \Gamma_j, \quad j = 1, \ldots, N-1, \tag{5.5}$$

where $\nu_j = \varepsilon_j/\varepsilon_{j+1}$ in TM-polarization and $\nu_j = \mu_j/\mu_{j+1}$ in TE-polarization. Here the unit normal $n = n(\boldsymbol{r})$ at a point $\boldsymbol{r} \in \Gamma_j$ is taken to point into Ω_j.

Outside $B_R = \bigcup_{j=1}^{N} \Omega_j^R$ the total field u can be expressed as

$$u = u^f + u^s \quad \text{in} \quad \Omega \setminus \overline{B_R}, \tag{5.6}$$

where u^f denotes the total field solution of the problem of scattering of the plane-wave u^{inc} by the planar layered media $D = \bigcup_{j=1}^{N} D_j$ (see Section 2.2.3), and where $u^s = u - u^f$ quantifies the scattered field produced by the presence of the local defects.

The solution of the problem of scattering by the unperturbed structure D was obtained in Section 2.2.3. In the TE case, for example, $u^f = E_z$ where E_z is given by (2.16); the corresponding expression for the TM case follows easily as indicated in that section. In particular, in both the TE and TM cases u^f can be expressed in the form

$$u^f = u_j^{\uparrow} + u_j^{\downarrow} \quad \text{in} \quad D_j, \tag{5.7}$$

where letting $k_{jx} = k_1 \cos \alpha$ and $k_{jy} = \sqrt{k_j^2 - k_{jx}^2}$, the up-going and down-going plane-waves (see Sections 2.2.2 and 2.2.3) are given by

$$u_j^{\uparrow}(\boldsymbol{r}) = p_j \, \mathrm{e}^{ik_{jx}x + ik_{jy}y} \quad \text{and} \quad u_j^{\downarrow}(\boldsymbol{r}) = q_j \, \mathrm{e}^{ik_{jx}x - ik_{jy}y}, \tag{5.8}$$

respectively, where the constants $p_j = \mathrm{e}^{2ik_{jy}d_j} A_j^{\text{TE,TM}} \widetilde{R}_{j,j+1}^{\text{TE,TM}}$ and $q_j = A_j^{\text{TE,TM}}$ are expressed in terms of the generalized reflection coefficients $\widetilde{R}_{j,j+1}^{\text{TE,TM}}$ and the amplitudes $A_j^{\text{TE,TM}}$ defined in (2.14a) for the polarization considered (TE or TM). Note that the only down-going wave in the uppermost layer corresponds to the incident field, i.e., $u_1^{\downarrow} = u^{\text{inc}}$, and that there is no

up-going wave in the lowermost layer, i.e., $u_N^\uparrow = 0$ (see Section 2.2.3 for details).

The radiative character of the scattered field u^s is as follows [66]:

$$
u^s = \begin{cases} u_j^{\text{rad}} + u_j^{\text{gui}} & \text{in} \quad \Omega_j \setminus \overline{B_R}, \quad j = 1, N, \\ u_j^{\text{gui}} & \text{in} \quad \Omega_j \setminus \overline{B_R}, \quad j = 2, \dots, N - 1, \end{cases} \tag{5.9}
$$

where

$$
\left| \frac{\partial u_j^{\text{rad}}}{\partial r_j} - i k_j u_j^{\text{rad}} \right| = o\left(r_j^{-1/2} \right) \quad \text{in} \quad \Omega_j \setminus \overline{B_R}, \quad j = 1, N, \tag{5.10}
$$

and

$$
u_j^{\text{gui}}(\boldsymbol{r}) = \sum_{m=1}^{M_j} \alpha_j^m u_j^m(\boldsymbol{r}) + \mathcal{O}\left(r_j^{-\beta_j} \right), \tag{5.11a}
$$

$$
\left| \frac{\partial u_j^{\text{gui}}}{\partial r_j} - i \sum_{m=1}^{M_j} \alpha_j^m \xi_j^m u_j^m \right| = \mathcal{O}\left(r_j^{-\beta_j} \right) \quad \text{in} \quad \Omega_j, \tag{5.11b}
$$

as $r_j \to \infty$, $j = 1, \dots, N$, where $\beta_j = 1$ for $j = 2, \dots, N - 1$ and $\beta_j = 2/3$ for $j = 1, N$ (see (5.1) for the definition of r_j). Here u_j^m denote the guided modes

$$
u_j^m(\boldsymbol{r}) = \begin{cases} \left\{ a_j^m \cosh\left(\gamma_j^m y \right) + b_j^m \sinh\left(\gamma_j^m y \right) \right\} e^{i|x|\xi_j^m}, & j = 2, \dots, N - 1, \\ e^{-\gamma_j^m |y|} e^{i|x|\xi_j^m}, & j = 1, N, \end{cases} \tag{5.12}
$$

which are expressed in terms of the so-called propagation constants $\xi_j^m > 0$, and $\gamma_j^m = \sqrt{(\xi_j^m)^2 - k_j^2}$, $m = 1, \dots, M_j$. The propagation constants ξ_j^m are given by the real poles (sometimes called surface wave poles [39, 42]) of the corresponding N-layer Green function in spectral form. The condition for the existence of the propagative modes in the inner layers Ω_j, $j = 2, \dots, N - 1$, is given by $k_1 < \xi_j^m < k_j$. For the outer layer Ω_1 (resp. Ω_N), on the other hand, it holds that $\xi_1^m = \xi_2^m$ (resp. $\xi_N^m = \xi_{N-1}^m$) and $\xi_1^m > k_1$ (resp. $\xi_N^m > k_N$) so that u_1^m (resp. u_N^m) corresponds to a surface wave that travels along the interface Γ_1 (resp. Γ_{N-1}) and decays exponentially fast towards the interior of Ω_1 (resp. Ω_N).

The rigorous derivation of the radiation condition (5.10)-(5.11) for the scattered u^s should follow from the integral representation of u^s in the region $\Omega \setminus \overline{B_R}$ by means of the layer Green

function of the planar layered medium D—similar to the one presented in Lemma 4.2.6 for $N = 2$—and the asymptotic analysis of the N-layer Green function—similar to the analysis presented in Section 2.3.4 for the case $N = 2$. An analysis of this kind is presented in the reference [66] for a three-layer-medium in three-dimensions.
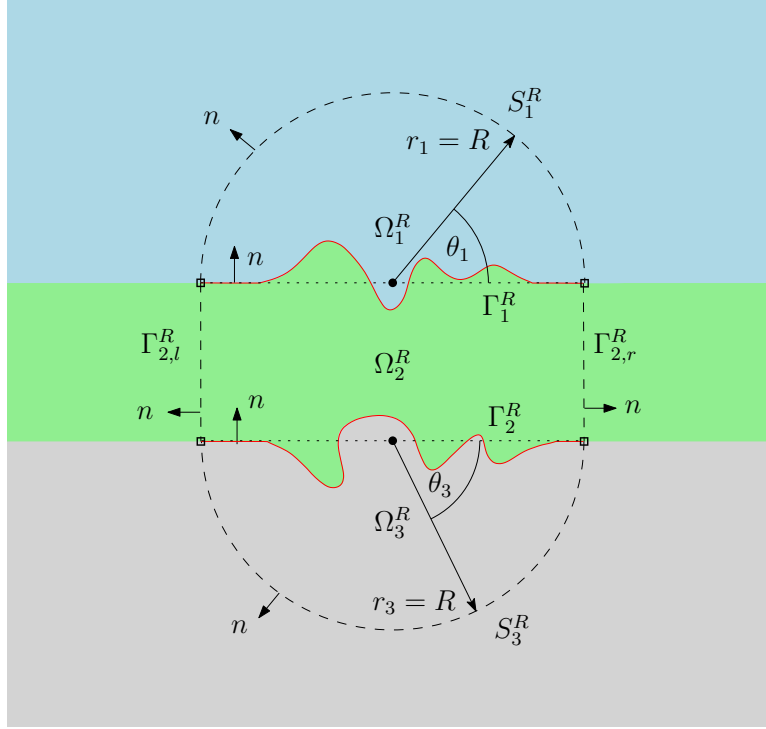
Figure 5.2: Depiction of the various domains, boundaries and variables involved in the derivation of the integral representation formula (5.15). The relevant curves are marked with a dashed line and junctions between the curves are marked with the symbol □.

5.2   Integral representation

We are now in position to derive the integral representation of the total field u. For simplicity we restrict the discussion to the three-layer problem; the general N-layer problem with $N > 3$ can be treated in an analogous manner. Our derivation uses the curves $\Gamma_{2,l}^R$, $\Gamma_{2,r}^R$, S_1^R and S_3^R and corresponding normals n, as depicted in Figure 5.2. Following [52], further, for a given

curve C we define

$$I_j \left[\phi; C\right](\boldsymbol{r}) = \int_C \left\{ \frac{\partial G_{k_j}}{\partial n_{\boldsymbol{r}'}}(\boldsymbol{r}, \boldsymbol{r}')\phi(\boldsymbol{r}') - G_{k_j}(\boldsymbol{r}, \boldsymbol{r}')\frac{\partial \phi}{\partial n}(\boldsymbol{r}') \right\} \mathrm{d}s_{\boldsymbol{r}'}$$

in order to facilitate repeated use of Green's third identity in our calculations; here we have called $G_{k_j}(\boldsymbol{r}, \boldsymbol{r}') = \frac{i}{4}H_0^{(1)}(k_j|\boldsymbol{r} - \boldsymbol{r}'|)$ the free-space Green function for the Helmholtz equation with wavenumber $k_j > 0$. In what follows, finally, we make frequent use of the asymptotic identities

$$
\begin{aligned}
G_k(\boldsymbol{r}, \boldsymbol{r}') &= \frac{i\,\mathrm{e}^{-i\pi/4}}{\sqrt{8\pi k|\boldsymbol{r}'|}}\,\mathrm{e}^{ik(|\boldsymbol{r}'|-\boldsymbol{r}\cdot\hat{\boldsymbol{r}}')}\left\{1 + \mathcal{O}\left(|\boldsymbol{r}'|^{-1}\right)\right\} \\
\nabla_{\boldsymbol{r}'}G_k(\boldsymbol{r}, \boldsymbol{r}') &= -\frac{\sqrt{k}\,\mathrm{e}^{-i\pi/4}}{\sqrt{8\pi|\boldsymbol{r}'|}}\,\mathrm{e}^{ik(|\boldsymbol{r}'|-\boldsymbol{r}\cdot\hat{\boldsymbol{r}}')}\,\hat{\boldsymbol{r}}'\left\{1 + \mathcal{O}\left(|\boldsymbol{r}'|^{-1}\right)\right\}
\end{aligned}
\qquad \left(\hat{\boldsymbol{r}}' = \frac{\boldsymbol{r}'}{|\boldsymbol{r}'|}\right) \quad |\boldsymbol{r}'| \to \infty,
$$

$$(5.13)$$

that are obtained from the asymptotic expansion of the Hankel functions [76] and the relation $|\boldsymbol{r} - \boldsymbol{r}'| = |\boldsymbol{r}'| - \boldsymbol{r}' \cdot \boldsymbol{r}/|\boldsymbol{r}'| + \mathcal{O}\left(|\boldsymbol{r}'|^{-1}\right)$ as $|\boldsymbol{r}'| \to \infty$.

Utilizing Green's third identity, where integration is performed over the domain Ω_1^R, whose boundary is given by $\partial\Omega_1^R = \Gamma_1^R \cup S_1^R$ (see Figure 5.2), we obtain:

$$
I_1\left[u; \Gamma_1^R\right](\boldsymbol{r}) - I_1\left[u; S_1^R\right](\boldsymbol{r}) =
\begin{cases}
u(\boldsymbol{r}), & \boldsymbol{r} \in \Omega_1^R, \\
0, & \boldsymbol{r} \in \mathbb{R}^2 \setminus \Omega_1^R,
\end{cases}
\qquad (5.14\mathrm{a})
$$

where the total field on $\partial\Omega_1^R$ is obtained by taking the limit of u and its gradient (required to evaluate the normal derivative of u at $\partial\Omega_1^R$) from the interior of Ω_1^R. Similarly, integrating over the domains Ω_2^R and Ω_3^R, whose boundaries are given by $\partial\Omega_2^R = \Gamma_2^R \cup \Gamma_{2,r}^R \cup \Gamma_1^R \cup \Gamma_{2,l}^R$ and $\partial\Omega_3^R = \Gamma_2^R \cup S_3^R$, respectively, we obtain

$$
I_2\left[u; \Gamma_2^R\right](\boldsymbol{r}) - I_2\left[u; \Gamma_1^R\right](\boldsymbol{r}) - I_2\left[u; \Gamma_{2,l}^R\right](\boldsymbol{r}) - I_2\left[u; \Gamma_{2,r}^R\right](\boldsymbol{r}) =
\begin{cases}
u(\boldsymbol{r}), & \boldsymbol{r} \in \Omega_2^R, \\
0, & \boldsymbol{r} \in \mathbb{R}^2 \setminus \Omega_2^R,
\end{cases}
$$

$$(5.14\mathrm{b})$$

and

$$-I_3\left[u;\Gamma_2^R\right](\boldsymbol{r}) - I_3\left[u;S_3^R\right](\boldsymbol{r}) = \begin{cases} u(\boldsymbol{r}), & \boldsymbol{r} \in \Omega_3^R, \\ 0, & \boldsymbol{r} \in \mathbb{R}^2 \setminus \Omega_3^R. \end{cases} \tag{5.14c}$$

We now study the limit values of the various integrals in (5.14) as $R \to \infty$. In view of the decay of the integral kernels (5.13) and the fact that the total field u remains bounded throughout Ω_2, it follows that the terms I_2 involving integrals over the vertical curves $\Gamma_{2,r}^R$ and $\Gamma_{2,l}^R$ tend to zero as $R \to \infty$. In fact

$$I_2\left[u;\Gamma_{2,l}^R\right] = I_2\left[u;\Gamma_{2,r}^R\right] = \mathcal{O}\left(R^{-\frac{1}{2}}\right) \quad \text{as} \quad R \to \infty.$$

In order to estimate the values of the terms I_j that involve integrals over the semi-circular curves S_1^R and S_3^R, in turn, we observe that for $\boldsymbol{r}' \in S_j^R$ with $j = 1$ and $j = 3$ we have $|\boldsymbol{r}'| = R + \mathcal{O}(1)$ and $\widehat{\boldsymbol{r}'} = (\cos\theta_j, \sin\theta_j) + \mathcal{O}(R^{-1})$ as $R \to \infty$—where the definition of the angles θ_j given in Figure 5.2. Since u_j^{rad}, $j = 1, 3$, in (5.9) satisfies the Sommerfeld radiation condition (5.10), utilizing standard arguments [45] it can be shown that

$$I_j\left[u_j^{\mathrm{rad}};S_j^R\right] = o\left(1\right), \quad j = 1, 3, \quad \text{as} \quad R \to \infty.$$

Let us now consider $I_j\left[u_1^{\mathrm{gui}};S_1^R\right]$, which is given by a linear combination of terms of the form $I_j\left[u_1^m;S_1^R\right]$, where letting $\gamma_1^m = \sqrt{(\xi_1^m)^2 - k_1^2} > 0$, the surface wave mode is given by $u_1^m(\boldsymbol{r}) = \mathrm{e}^{-\gamma_1^m|y| + i\xi_1^m|x|}$. Thus, from (5.13) and the fact that $u_1^m(\boldsymbol{r}') = \mathrm{e}^{-\gamma_1^m R \sin\theta_1 + i\xi_1^m R|\cos\theta_1|}$ for $\boldsymbol{r}' = R(\cos\theta_1, \sin\theta_1) \in S_1^R$, $\theta_1 \in [0, \pi]$, we obtain

$$I_1\left[u_1^m;S_1^R\right](\boldsymbol{r}) \sim \sqrt{\frac{k_1 R}{8\pi}}\, \mathrm{e}^{ik_1 R - i\frac{\pi}{4}} \times$$

$$\int_0^\pi \left\{ \frac{i\gamma_1^m \sin\theta_1 + |\cos\theta_1|\xi_1^m}{k_1} - 1 \right\} \mathrm{e}^{-ik_1\boldsymbol{r}\cdot\widehat{\boldsymbol{r}}' - R(\gamma_1^m \sin\theta_1 - i\xi_1^m|\cos\theta_1|)}\, \mathrm{d}\theta_1$$

as $R \to \infty$. Therefore

$$\left|I_1\left[u_1^m;S_1^R\right](\boldsymbol{r})\right| \le \sqrt{\frac{k_1 R}{2\pi}} \left\{ 1 + \frac{|\gamma_1^m| + \xi_1^m}{k_1} \right\} \int_0^{\pi/2} \mathrm{e}^{-\gamma_1^m R \sin\theta_1}\, \mathrm{d}\theta_1.$$

The integral in the expression on the right-hand-side can be bounded utilizing the inequality $\sin\theta \geq 2\theta/\pi$, $\theta \in [0, \pi]$. Doing so we conclude that $I_1\left[u_1^m; S_1^R\right] = \mathcal{O}\left(R^{-\frac{1}{2}}\right)$ as $R \to \infty$. Similarly, it can be shown that $I_3\left[u_3^m; S_3^R\right] = \mathcal{O}\left(R^{-\frac{1}{2}}\right)$, and consequently, in view of (5.11), we conclude that $I_j\left[u_j^{\text{gui}}; S_j^R\right] = \mathcal{O}\left(R^{-\frac{1}{3}}\right)$, $j = 1, 3$, as $R \to \infty$.

Next we consider the term $I_1\left[u_1^\uparrow; S_1^R\right]$ which involves the up-going plane-wave $u_1^\uparrow(\boldsymbol{r}) = e^{ik_{1x}x + ik_{1y}y}$. Thus we have that $u_1^\uparrow(\boldsymbol{r}') = e^{ik_1 R\cos(\theta_1 + \alpha)}$ for $\boldsymbol{r}' \in S_1^R$, and consequently integration by parts yields

$$
\begin{aligned}
I_1\left[u_1^\uparrow; S_1^R\right](\boldsymbol{r}) \sim{}& \sqrt{\frac{k_1 R}{8\pi}}\, e^{ik_1 R - i\frac{\pi}{4}} \int_0^\pi \left\{\cos(\theta_1 + \alpha) - 1\right\} e^{-ik_1 \boldsymbol{r}\cdot\hat{\boldsymbol{r}}'}\, e^{ik_1 R\cos(\theta_1 + \alpha)}\, \mathrm{d}\theta_1 \\
={}& -\frac{e^{ik_1 R + i\frac{\pi}{4}}}{\sqrt{8\pi k_1 R}} \int_0^\pi \frac{\sin(\theta_1 + \alpha)}{1 + \cos(\theta_1 + \alpha)}\, e^{-ik_1 \boldsymbol{r}\cdot\hat{\boldsymbol{r}}'}\, \frac{\mathrm{d}}{\mathrm{d}\theta_1}\, e^{ik_1 R\cos(\theta_1 + \alpha)}\, \mathrm{d}\theta_1 \\
={}& -\frac{e^{ik_1 R + i\frac{\pi}{4}}}{\sqrt{8\pi k_1 R}} \left\{ \frac{\sin(\theta_1 + \alpha)\, e^{ik_1(-\boldsymbol{r}\cdot\hat{\boldsymbol{r}}' + R\cos(\theta_1 + \alpha))}}{1 + \cos(\theta_1 + \alpha)} \Bigg|_0^\pi - \right. \\
& \left. \int_0^\pi e^{ik_1 R\cos(\theta_1 + \alpha)}\, \frac{\mathrm{d}}{\mathrm{d}\theta_1}\left(\frac{\sin(\theta_1 + \alpha)\, e^{-ik_1 \boldsymbol{r}\cdot\hat{\boldsymbol{r}}'}}{1 + \cos(\theta_1 + \alpha)} \right) \mathrm{d}\theta_1 \right\} \\
={}& \mathcal{O}\left(R^{-\frac{1}{2}}\right) \quad \text{as} \quad R \to \infty.
\end{aligned}
$$

Considering now the term $I_1\left[u_1^\downarrow; S_1^R\right]$ with $u_1^\downarrow(\boldsymbol{r}) = e^{ik_{1x}x - ik_{1y}y}$, we have that the down-going plane-wave is given by $u_1^\downarrow(\boldsymbol{r}') = e^{ik_1 R\cos(\theta_1 - \alpha)}$ for $\boldsymbol{r}' \in S_1^R$. Thus

$$
I_1\left[u_1^\downarrow; S_1^R\right](\boldsymbol{r}) \sim \sqrt{\frac{k_1 R}{8\pi}}\, e^{ik_1 R - i\frac{\pi}{4}} \int_0^\pi \left\{\cos(\theta_1 - \alpha) - 1\right\} e^{-ik_1 \boldsymbol{r}\cdot\hat{\boldsymbol{r}}'}\, e^{ik_1 R\cos(\theta_1 - \alpha)}\, \mathrm{d}\theta_1.
$$

Notice that since $\alpha \in (-\pi, 0)$, we have that $0 < \theta_1 - \alpha < 2\pi$. Thus, there is only one point of stationary phase within the domain of integration, which is given by $\theta_1 = \alpha + \pi$. Therefore, the application of the method of stationary phase [16] yields

$$
I_1\left[u_1^\downarrow; S_1^R\right](\boldsymbol{r}) = -e^{ik_1(x\cos\alpha + y\sin\alpha)} + \mathcal{O}\left(R^{-\frac{1}{2}}\right) = -u^{\text{inc}}(\boldsymbol{r}) + \mathcal{O}\left(R^{-\frac{1}{2}}\right) \quad \text{as} \quad R \to \infty.
$$

(Notice that integrating by parts yields that the limit points of the integral give rise to contributions that decay as R^{-1}.)

Finally, we consider the term $I_3\left[u_3^{\downarrow}; S_3^R\right]$ with $u_3^{\downarrow}(\boldsymbol{r}') = \mathrm{e}^{ik_{3x}x - ik_{3y}y}$, where $k_{3x} = k_1 \cos \alpha$ and $k_{3y} = \sqrt{k_3^2 - k_{3x}^2}$. We distinguish three possible cases, namely: (a) $k_3 < k_1 |\cos \alpha|$, (b) $k_3 = k_1 |\cos \alpha|$ ($k_3 = -k_1 \cos \alpha$ for $\alpha \in (-\pi, -\pi/2]$ or $k_3 = k_1 \cos \alpha$ for $\alpha \in (-\pi/2, 0)$), and (c) $k_3 > k_1 |\cos \alpha|$. Since in case (a) we have that $k_{3y} = i\sqrt{k_1^2 \cos^2 \alpha - k_3^2}$, a calculation completely analogous to the one carried in the estimation of the term $I_j\left[u_1^m; S_1^R\right]$ allows us to show that $I_3\left[u_3^{\downarrow}; S_3^R\right] = \mathcal{O}\left(R^{-\frac{1}{2}}\right)$. In case (b), in turn, we first consider $\alpha \in (-\pi/2, 0)$. In this case we have $u_3^{\downarrow}(\boldsymbol{r}') = \mathrm{e}^{ik_3 R \cos \theta_3}$ for $\boldsymbol{r}' \in S_3^R$, and consequently

$$I_3\left[u_3^{\downarrow}; S_3^R\right](\boldsymbol{r}) \sim \sqrt{\frac{k_3 R}{8\pi}}\, \mathrm{e}^{ik_3 R - i\frac{\pi}{4}} \int_{-\pi}^{0} \{\cos \theta_3 - 1\}\, \mathrm{e}^{-ik_2(d_2 \sin \theta_3 + \boldsymbol{r}\cdot\hat{\boldsymbol{r}}') + iRk_3 \cos \theta_3}\, \mathrm{d}\theta_3.$$

Splitting the integration domain and using the identity $\cos \theta - 1 = -\sin^2 \theta/(1 + \cos \theta)$ we obtain

$$I_3\left[u_3^{\downarrow}; S_3^R\right](\boldsymbol{r}) \sim \sqrt{\frac{k_3 R}{8\pi}}\, \mathrm{e}^{ik_3 R - i\frac{\pi}{4}} \left\{ -\int_{-\frac{\pi}{2}}^{0} \frac{\sin^2 \theta_3}{1 + \cos \theta_3}\, \mathrm{e}^{-ik_3(d_2 \sin \theta_3 - \boldsymbol{r}\cdot\hat{\boldsymbol{r}}') + iRk_3 \cos \theta_3}\, \mathrm{d}\theta_3 + \right.$$
$$\left. \int_{-\pi}^{-\frac{\pi}{2}} \{\cos \theta_3 - 1\}\, \mathrm{e}^{-ik_3(d_2 \sin \theta_3 + \boldsymbol{r}\cdot\hat{\boldsymbol{r}}') + iRk_3 \cos \theta_3}\, \mathrm{d}\theta_3 \right\}.$$

Integration by parts yields that the first integral above amounts to a quantity of order $\mathcal{O}\left(R^{-\frac{1}{2}}\right)$. The stationary point at $\theta = -\pi$ in the second integral, on the other hand, leads to

$$I_3\left[u_3^{\downarrow}; S_3^R\right](\boldsymbol{r}) \sim -\frac{\mathrm{e}^{ik_3 x}}{2} + \mathcal{O}\left(R^{-\frac{1}{2}}\right).$$

Similarly it can be shown that $I_3\left(u_3^{\downarrow}; S_3^R\right) \sim -\mathrm{e}^{-ik_3 x}/2 + \mathcal{O}\left(R^{-\frac{1}{2}}\right)$ in the case $k_3 = -k_1 \cos \alpha$ for $\alpha \in (-\pi, \pi/2]$. For case (c), the transmitted wave to the lowermost layers is a plane-wave which can be expressed as $u_3^{\downarrow}(\boldsymbol{r}') = a\, \mathrm{e}^{ik_3 R \cos(\theta_3 - \alpha')}$, $\boldsymbol{r}' \in S_3^R$, where $a = \mathrm{e}^{-ik_3 d_2 \sin \alpha'}$ and where the angle $\alpha' \in (-\pi, 0)$ is determined by the Snell's law $k_3 \cos \alpha' = k_1 \cos \alpha$. Thus, once again,

integration by parts yields

$$I_3\left[u_3^\downarrow; S_3^R\right](\boldsymbol{r}) \sim a\sqrt{\frac{k_3 R}{8\pi}}\, e^{ik_3 R - i\frac{\pi}{4}} \int\limits_{-\pi}^{0} \{\cos(\theta_3 - \alpha') - 1\}\, e^{-ik_3(d_2 \sin\theta_3 + \boldsymbol{r}\cdot\hat{\boldsymbol{r}}')}\, e^{ik_3 R \cos(\theta_3 - \alpha')}\, d\theta_3$$

$$= \mathcal{O}\left(R^{-\frac{1}{2}}\right).$$

Therefore we conclude that taking the limit as $R \to \infty$ in (5.14) we obtain

$$I_1\left[u; \Gamma_1\right](\boldsymbol{r}) + u^{\mathrm{inc}}(\boldsymbol{r}) = \begin{cases} u(\boldsymbol{r}), & \boldsymbol{r} \in \Omega_1, \\ 0, & \boldsymbol{r} \in \mathbb{R}^2 \setminus \overline{\Omega}_1, \end{cases} \tag{5.15a}$$

$$I_2\left[u; \Gamma_2\right](\boldsymbol{r}) - I_2\left[u; \Gamma_1\right](\boldsymbol{r}) = \begin{cases} u(\boldsymbol{r}), & \boldsymbol{r} \in \Omega_2, \\ 0, & \boldsymbol{r} \in \mathbb{R}^2 \setminus \overline{\Omega}_2, \end{cases} \tag{5.15b}$$

$$-I_3\left[u; \Gamma_2\right](\boldsymbol{r}) + u_3^\|(\boldsymbol{r}) = \begin{cases} u(\boldsymbol{r}), & \boldsymbol{r} \in \Omega_3, \\ 0, & \boldsymbol{r} \in \mathbb{R}^2 \setminus \overline{\Omega}_3, \end{cases} \tag{5.15c}$$

where $u_3^\|$ in (5.15c) is given by

$$u_N^\|(\boldsymbol{r}) = \begin{cases} \dfrac{q_N\, e^{ik_1 x \cos\alpha}}{2} & \text{if } k_N = k_1|\cos\alpha|, \\ 0 & \text{if } k_N \neq k_1|\cos\alpha|, \end{cases} \tag{5.16}$$

for $N = 3$.

Remark 5.2.1. *The total field representation (5.15) presented above in this section for the three-layer problem can easily be extended to problems of scattering by defects in the presence of layer media composed by $N > 3$ dielectric layers. In fact, as in (5.15b), the total field within an inner layer Ω_j, $j = 2, \ldots, N-1$, can be expressed as a linear combination of layer-potentials applied to the total field and its normal derivative at the relevant interfaces*

Γ_{j-1} and Γ_j. Consequently, such generalization leads to

$$I_1\left[u;\Gamma_1\right](\boldsymbol{r}) + u^{\mathrm{inc}}(\boldsymbol{r}) = \begin{cases} u(\boldsymbol{r}), & \boldsymbol{r}\in\Omega_1, \\ 0, & \boldsymbol{r}\in\mathbb{R}^2\setminus\overline{\Omega}_1, \end{cases} \tag{5.17a}$$

$$I_j\left[u;\Gamma_j\right](\boldsymbol{r}) - I_j\left[u;\Gamma_{j-1}\right](\boldsymbol{r}) = \begin{cases} u(\boldsymbol{r}), & \boldsymbol{r}\in\Omega_j, \\ 0, & \boldsymbol{r}\in\mathbb{R}^2\setminus\overline{\Omega}_j, \end{cases} \quad j=2,\ldots,N-1, \tag{5.17b}$$

$$-I_N\left[u;\Gamma_{N-1}\right](\boldsymbol{r}) + u_N^{\|}(\boldsymbol{r}) = \begin{cases} u(\boldsymbol{r}), & \boldsymbol{r}\in\Omega_N, \\ 0, & \boldsymbol{r}\in\mathbb{R}^2\setminus\overline{\Omega}_N. \end{cases} \tag{5.17c}$$

5.3 Integral equation formulation

In this section we establish an integral equation for the unknown values of total field u and its normal derivative at each one of the dielectric interfaces Γ_j, $j = 1,\ldots,N-1$. As in Chapter 4 we utilize the improper-integral single- and double-layer potentials

$$\mathcal{S}_j^{(i)}[\phi](\boldsymbol{r}) = \int_{\Gamma_i} G_{k_j}(\boldsymbol{r},\boldsymbol{r}')\phi(\boldsymbol{r}')\,\mathrm{d}s_{\boldsymbol{r}'} \quad\text{and}\quad \mathcal{D}_j^{(i)}[\phi](\boldsymbol{r}) = \int_{\Gamma_i} \frac{\partial G_{k_j}}{\partial n_{\boldsymbol{r}'}}(\boldsymbol{r},\boldsymbol{r}')\phi(\boldsymbol{r}')\,\mathrm{d}s_{\boldsymbol{r}'}, \tag{5.18}$$

respectively, whose convergence is conditioned upon the oscillatory behavior of the integrand. Throughout this chapter the interfaces Γ_j are assumed to be piecewise smooth curves that coincide with the flat interfaces Π_j sufficiently far from the origin; see e.g. Figure 5.1b.

As is known [45], the layer potentials (5.18) satisfy the jump relations

$$\left.\mathcal{S}_j^{(i)}[\phi]\right|_{\ell\pm} = S_j^{(\ell,i)}[\phi], \qquad \left.\frac{\partial}{\partial n}\mathcal{S}_j^{(i)}[\phi]\right|_{\ell\pm} = \begin{cases} \mp\dfrac{\phi}{2} + K_j^{(\ell,i)}[\phi] & \text{if } i=\ell, \\[2mm] K_j^{(\ell,i)}[\phi] & \text{if } i\neq\ell, \end{cases}$$

$$\left.\frac{\partial}{\partial n}\mathcal{D}_j^{(i)}[\phi]\right|_{\ell\pm} = N_j^{(\ell,i)}[\phi], \qquad \left.\mathcal{D}_j^{(i)}[\phi]\right|_{\ell\pm} = \begin{cases} \pm\dfrac{\phi}{2} + D_j^{(\ell,i)}[\phi] & \text{if } i=\ell, \\[2mm] D_j^{(\ell,i)}[\phi] & \text{if } i\neq\ell, \end{cases} \tag{5.19}$$

where the relevant integral operators are defined as

$$
S_j^{(\ell,i)}[\phi](\boldsymbol{r}) = \int_{\Gamma_i} G_{k_j}(\boldsymbol{r},\boldsymbol{r}')\phi(\boldsymbol{r}')\,\mathrm{d}s_{\boldsymbol{r}'}, \qquad D_j^{(\ell,i)}[\phi](\boldsymbol{r}) = \int_{\Gamma_i} \frac{\partial G_{k_j}}{\partial n_{\boldsymbol{r}'}}(\boldsymbol{r},\boldsymbol{r}')\phi(\boldsymbol{r}')\,\mathrm{d}s_{\boldsymbol{r}'},
$$
$$
\qquad\qquad\qquad\qquad\qquad\qquad\qquad\qquad\qquad\qquad\qquad\qquad\qquad\qquad\qquad\boldsymbol{r} \in \Gamma_\ell.
$$
$$
K_j^{(\ell,i)}[\phi](\boldsymbol{r}) = \int_{\Gamma_i} \frac{\partial G_{k_j}}{\partial n_{\boldsymbol{r}}}(\boldsymbol{r},\boldsymbol{r}')\phi(\boldsymbol{r}')\,\mathrm{d}s_{\boldsymbol{r}'}, \quad N_j^{(\ell,i)}[\phi](\boldsymbol{r}) = \frac{\partial}{\partial n_{\boldsymbol{r}}}\int_{\Gamma_i} \frac{\partial G_{k_j}}{\partial n_{\boldsymbol{r}'}}(\boldsymbol{r},\boldsymbol{r}')\phi(\boldsymbol{r}')\,\mathrm{d}s_{\boldsymbol{r}'},
$$

$$(5.20)$$

Note that according to the notation (5.20) the super-index (ℓ, i) refers to the fact that integration is performed over the curve Γ_i, while evaluation is performed over the curve Γ_ℓ. The sub-index j indicates that the wavenumber k_j is used in the integral kernel.

In order to formulate an integral equation for the total field we define the unknown density functions $\varphi_j : \Gamma_j \to \mathbb{C}$ and $\psi_j : \Gamma_j \to \mathbb{C}$ $(j = 1, \ldots, N-1)$ by

$$
\varphi_j = u|_{j^-} \quad \text{and} \quad \psi_j = \left.\frac{\partial u}{\partial n}\right|_{j^-} \quad \text{on} \quad \Gamma_j, \tag{5.21}
$$

where the notation (5.4) was used. Similarly, we call $\varphi^{\mathrm{inc}} = u^{\mathrm{inc}}|_{1^-}$ and $\psi^{\mathrm{inc}} = \partial u^{\mathrm{inc}}/\partial n|_{1^-}$ the values of the incident field and its normal derivative on Γ_1, and we denote by $\varphi^{\|} = u_N^{\|}|_{N-1}$ and $\psi^{\|} = \partial u_N^{\|}/\partial n|_{N-1}$ the values of $u_N^{\|}$ (equation (4.4)) and its normal derivative on Γ_N.

Utilizing the notations (5.19), (5.20) and (5.21) and using the transmission conditions (5.5), equation (5.17) becomes

$$
\mathcal{D}_1^{(1)}[\varphi_1](\boldsymbol{r}) - \nu_1 \mathcal{S}_1^{(1)}[\psi_1](\boldsymbol{r}) + u^{\mathrm{inc}}(\boldsymbol{r}) = \begin{cases} u(\boldsymbol{r}), & \boldsymbol{r} \in \Omega_1, \\[2mm] 0, & \boldsymbol{r} \in \mathbb{R}^2 \setminus \overline{\Omega_1}, \end{cases} \tag{5.22a}
$$

$$
\mathcal{D}_j^{(j)}[\varphi_j](\boldsymbol{r}) - \nu_j \mathcal{S}_j^{(j)}[\psi_j](\boldsymbol{r}) - \mathcal{D}_j^{(j-1)}[\varphi_{j-1}](\boldsymbol{r}) + \mathcal{S}_j^{(j-1)}[\psi_{j-1}](\boldsymbol{r}) = \begin{cases} u(\boldsymbol{r}), & \boldsymbol{r} \in \Omega_j, \\[2mm] 0, & \boldsymbol{r} \in \mathbb{R}^2 \setminus \overline{\Omega_j}, \end{cases}
$$

$$(5.22b)$$

for $j = 2, \ldots, N-1$, and

$$
-\mathcal{D}_N^{(N-1)}[\varphi_{N-1}](\boldsymbol{r}) + \mathcal{S}_N^{(N-1)}[\psi_{N-1}](\boldsymbol{r}) + u_N^{\|}(\boldsymbol{r}) = \begin{cases} u(\boldsymbol{r}), & \boldsymbol{r} \in \Omega_N, \\[2mm] 0, & \boldsymbol{r} \in \mathbb{R}^2 \setminus \overline{\Omega_N}. \end{cases} \tag{5.22c}
$$

We are now in position to derive the equations that govern the field interactions at the interfaces Γ_j, $j = 1, \ldots, N - 1$. Indeed, evaluating the layer-potentials in (5.22a) and their normal derivatives on Γ_1 (taken from the interior of Ω_1) and utilizing the jump relations (5.19) we obtain

$$\begin{aligned}
\frac{\varphi_1}{2} - \varphi^{\text{inc}} &= D_1^{(1,1)}[\varphi_1] - \nu_1 S_1^{(1,1)}[\psi_1], \\
\nu_1 \frac{\psi_1}{2} - \psi^{\text{inc}} &= N_1^{(1,1)}[\varphi_1] - \nu_1 K_1^{(1,1)}[\psi_1].
\end{aligned} \tag{5.23a}$$

Similarly, evaluating the expression in (5.22b) as well as its normal derivative on Γ_{j-1} taken from the interior of Ω_j for $j = 2, \ldots, N - 1$ we obtain

$$\begin{aligned}
\frac{\varphi_{j-1}}{2} &= D_j^{(j-1,j)}[\varphi_j] - \nu_j S_j^{(j-1,j)}[\psi_j] - D_j^{(j-1,j-1)}[\varphi_{j-1}] + S_j^{(j-1,j-1)}[\psi_{j-1}], \\
\frac{\psi_{j-1}}{2} &= N_j^{(j-1,j)}[\varphi_j] - \nu_j K_j^{(j-1,j)}[\psi_j] - N_j^{(j-1,j-1)}[\varphi_{j-1}] + K_j^{(j-1,j-1)}[\psi_{j-1}],
\end{aligned} \tag{5.23b}$$

on Γ_{j-1}, $j = 2, \ldots, N - 1$, while evaluating the expression in (5.22b) and their normal derivatives on Γ_j, $j = 2, \ldots, N - 1$, yields

$$\begin{aligned}
\frac{\varphi_j}{2} &= D_j^{(j,j)}[\varphi_j] - \nu_j S_j^{(j,j)}[\psi_j] - D_j^{(j,j-1)}[\varphi_{j-1}] + S_j^{(j,j-1)}[\psi_{j-1}], \\
\nu_j \frac{\psi_j}{2} &= N_j^{(j,j)}[\varphi_j] - \nu_j K_j^{(j,j)}[\psi_j] - N_j^{(j,j-1)}[\varphi_{j-1}] + K_j^{(j,j-1)}[\psi_{j-1}].
\end{aligned} \tag{5.23c}$$

Evaluating the expression in (5.43c) and its normal derivative on Γ_{N-1} (taken from the interior of Ω_N), finally, we obtain

$$\begin{aligned}
\frac{\varphi_{N-1}}{2} - \varphi^{\parallel} &= -D_N^{(N-1,N-1)}[\varphi_{N-1}] + S_N^{(N-1,N-1)}[\psi_{N-1}], \\
\frac{\psi_{N-1}}{2} - \psi^{\parallel} &= -N_N^{(N-1,N-1)}[\varphi_{N-1}] + K_N^{(N-1,N-1)}[\psi_{N-1}].
\end{aligned} \tag{5.23d}$$

In order to express the integral equations satisfied by the integral densities at Γ_j in a

more compact form, we introduce the following notation:

$$\phi_j = \begin{bmatrix} \varphi_j \\ \psi_j \end{bmatrix}, \quad \phi^{\mathrm{inc}} = \begin{bmatrix} \varphi^{\mathrm{inc}} \\ \psi^{\mathrm{inc}} \end{bmatrix}, \quad \phi^{\|} = \begin{bmatrix} \varphi^{\|} \\ \psi^{\|} \end{bmatrix}, \quad E_j = \begin{bmatrix} 1 & 0 \\ 0 & \frac{1+\nu_j}{2} \end{bmatrix}, \tag{5.24a}$$

$$R_{j,j+1} = \begin{bmatrix} -D_{j+1}^{(j,j+1)} & \nu_{j+1} S_{j+1}^{(j,j+1)} \\ -N_{j+1}^{(j,j+1)} & \nu_{j+1} K_{j+1}^{(j,j+1)} \end{bmatrix}, \quad R_{j,j-1} = \begin{bmatrix} D_j^{(j,j-1)} & -S_j^{(j,j-1)} \\ N_j^{(j,j-1)} & -K_j^{(j,j-1)} \end{bmatrix}, \tag{5.24b}$$

$$\text{and} \quad T_j = \begin{bmatrix} D_{j+1}^{(j,j)} - D_j^{(j,j)} & -S_{j+1}^{(j,j)} + \nu_j S_j^{(j,j)} \\ N_{j+1}^{(j,j)} - N_j^{(j,j)} & -K_{j+1}^{(j,j)} + \nu_j K_j^{(j,j)} \end{bmatrix}. \tag{5.24c}$$

Using these notations and adding the expressions in (5.23a) and the expressions in (5.23b) for $j = 2$ we obtain

$$E_1 \, \phi_1 + T_1 \, [\phi_1] + R_{12} \, [\phi_2] = \phi^{\mathrm{inc}} \quad \text{on} \quad \Gamma_1. \tag{5.25a}$$

Similarly, adding the $j = 3, \ldots, N - 1$ instances of the equations in (5.23b) and the $j = 2, \ldots, N - 2$ instances of the equations in (5.23c), we obtain

$$E_j \, \phi_j + R_{j,j-1} \, [\phi_{j-1}] + T_j \, [\phi_j] + R_{j,j+1} \, [\phi_{j+1}] = 0 \quad \text{on} \quad \Gamma_j, \tag{5.25b}$$

for $j = 2, \ldots, N - 2$. Finally, combining the expressions (5.23c) for $j = N - 1$ and (5.23d) we obtain

$$E_{N-1} \, \phi_{N-1} + R_{N-1,N-2} \, [\phi_{N-2}] + T_{N-1} \, [\phi_{N-1}] = \phi^{\|} \quad \text{on} \quad \Gamma_{N-1}. \tag{5.25c}$$

The coupled systems of integral equations (5.25) can be further compressed into one large system of integral equations. Letting $\mathscr{E}$ and $\mathscr{T}_\Gamma$ denote the block-diagonal matrix and the

block-tridiagonal integral operator whose block components are given by

$$[\mathscr{E}]_{i,j} = \begin{cases} \mathrm{E}_i & \text{if } j = i, \\ 0 & \text{otherwise}, \end{cases} \quad \text{and} \quad [\mathscr{T}_\Gamma]_{i,j} = \begin{cases} \mathrm{R}_{i,i-1} & \text{if } j = i - 1 \text{ and } 2 \le i \le N - 1, \\ \mathrm{T}_i & \text{if } j = i \text{ and } 1 \le i \le N - 1, \\ \mathrm{R}_{i,i+1} & \text{if } j = i + 1 \text{ and } 1 \le i \le N - 2, \\ 0 & \text{otherwise}, \end{cases}$$

(5.26a)

respectively, and letting $\boldsymbol{\phi}$ and $\boldsymbol{\phi}^{\text{inc}}$ denote the block-vectors of unknown densities and right-hand sides, whose block-components are given by

$$[\boldsymbol{\phi}]_j = \phi_j, \ j = 1, \dots, N - 1, \quad \text{and} \quad \left[\boldsymbol{\phi}^{\text{inc}}\right]_j = \begin{cases} \phi^{\text{inc}} & \text{if } j = 1, \\ \phi^{\parallel} & \text{if } j = N, \\ \mathbf{0} & \text{otherwise}, \end{cases}$$

(5.26b)

respectively, the equations in (5.25) can be combined into the following integral equation system:

$$\mathscr{E}\boldsymbol{\phi} + \mathscr{T}_\Gamma[\boldsymbol{\phi}] = \boldsymbol{\phi}^{\text{inc}} \quad \text{on} \quad \Gamma = \bigcup_{j=1}^{N-1} \Gamma_j.$$

(5.27)

5.4 Multilayer Windowed Green Function Method

Following the ideas presented in Chapter 4, instead of attempting to solve the problem (5.27) on the unbounded interfaces Γ_j, $j = 1, \dots, N - 1$, a locally windowed problem is used to obtain the local currents over all relevant portions of Γ_j, $j = 1, \dots, N - 1$. In order to do so we first introduce the block-diagonal matrix function $\mathscr{W}_A : \mathbb{R} \mapsto \mathbb{R}^{2(N-1) \times 2(N-1)}$ whose block components are given by

$$[\mathscr{W}_A]_{i,j} = \begin{cases} \begin{bmatrix} w_A & 0 \\ 0 & w_A \end{bmatrix} & \text{if } i = j, \\ \begin{bmatrix} 0 & 0 \\ 0 & 0 \end{bmatrix} & \text{if } i \ne j, \end{cases}$$

(5.28)

in terms of a smooth window function w_A defined in (4.9). (In fact, different values of A_j of the window-size A could advantageously be used for the various layers. For notational simplicity, however, the following discussion does not include this additional degree of generality.)

Utilizing $\mathscr{W}_A$ we obtain the windowed version

$$\mathscr{E}\boldsymbol{\phi} + \mathscr{T}_\Gamma\left[\mathscr{W}_A\boldsymbol{\phi}\right] = \boldsymbol{\phi}^{\mathrm{inc}} - \mathscr{T}_\Gamma\left[(\mathscr{I} - \mathscr{W}_A)\boldsymbol{\phi}\right] \quad \text{on} \quad \Gamma_A = \bigcup_{j=1}^{N-1}\Gamma_{j,A}, \qquad (5.29)$$

of equation (5.27), where $\mathscr{I} \in \mathbb{R}^{(2N-2)\times(2N-2)}$ denotes the identity matrix, and where

$$\Gamma_{j,A} = \Gamma_j \cap \{w_A \neq 0\} = \Gamma_j \cap \{[-A, A] \times \mathbb{R}\}.$$

In order to provide an approximation for $\mathscr{T}_\Gamma\left[(\mathscr{I} - \mathscr{W}_A)\boldsymbol{\phi}\right]$ in terms of known expressions, we introduce an integral operator that maps density functions defined on the flat interfaces Π_j to density functions defined on Γ_j. Such operator is denoted by $\mathscr{T}_\Pi = [\mathscr{T}_\Pi]_{i,j}$, $i,j = 1,\ldots,N-1$, and is given by

$$[\mathscr{T}_\Pi]_{i,j} = \begin{cases} \widetilde{\mathrm{R}}_{i,i-1} & \text{if } j = i-1 \text{ and } 2 \leq i \leq N-1, \\ \widetilde{\mathrm{T}}_i & \text{if } j = i \text{ and } 1 \leq i \leq N-1, \\ \widetilde{\mathrm{R}}_{i,i+1} & \text{if } j = i+1 \text{ and } 1 \leq i \leq N-2, \\ 0 & \text{otherwise,} \end{cases} \qquad (5.30)$$

where the block integral operators in (5.30) are given by

$$\widetilde{\mathrm{R}}_{j,j+1} = \begin{bmatrix} -\widetilde{D}_{j+1}^{(j,j+1)} & \nu_{j+1}\widetilde{S}_{j+1}^{(j,j+1)} \\ -\widetilde{N}_{j+1}^{(j,j+1)} & \nu_{j+1}\widetilde{K}_{j+1}^{(j,j+1)} \end{bmatrix}, \quad \widetilde{\mathrm{R}}_{j,j-1} = \begin{bmatrix} \widetilde{D}_j^{(j,j-1)} & -\widetilde{S}_j^{(j,j-1)} \\ \widetilde{N}_j^{(j,j-1)} & -\widetilde{K}_j^{(j,j-1)} \end{bmatrix},$$

$$\text{and} \quad \widetilde{\mathrm{T}}_j = \begin{bmatrix} \widetilde{D}_{j+1}^{(j,j)} - \widetilde{D}_j^{(j,j)} & -\widetilde{S}_{j+1}^{(j,j)} + \nu_j\widetilde{S}_j^{(j,j)} \\ \widetilde{N}_{j+1}^{(j,j)} - \widetilde{N}_j^{(j,j)} & -\widetilde{K}_{j+1}^{(j,j)} + \nu_j\widetilde{K}_j^{(j,j)} \end{bmatrix},$$

in terms of the integral operators

$$\widetilde{S}_j^{(\ell,i)}[\phi](\boldsymbol{r}) = \int_{\Pi_i} G_{k_j}(\boldsymbol{r},\boldsymbol{r}')\phi(\boldsymbol{r}')\,\mathrm{d}s_{\boldsymbol{r}'}, \qquad \widetilde{D}_j^{(\ell,i)}[\phi](\boldsymbol{r}) = \int_{\Pi_i} \frac{\partial G_{k_j}}{\partial n_{\boldsymbol{r}'}}(\boldsymbol{r},\boldsymbol{r}')\phi(\boldsymbol{r}')\,\mathrm{d}s_{\boldsymbol{r}'},$$
$$\boldsymbol{r} \in \Gamma_\ell.$$
$$\widetilde{K}_j^{(\ell,i)}[\phi](\boldsymbol{r}) = \int_{\Pi_i} \frac{\partial G_{k_j}}{\partial n_{\boldsymbol{r}}}(\boldsymbol{r},\boldsymbol{r}')\phi(\boldsymbol{r}')\,\mathrm{d}s_{\boldsymbol{r}'}, \quad \widetilde{N}_j^{(\ell,i)}[\phi](\boldsymbol{r}) = \frac{\partial}{\partial n_{\boldsymbol{r}}}\int_{\Pi_i} \frac{\partial G_{k_j}}{\partial n_{\boldsymbol{r}'}}(\boldsymbol{r},\boldsymbol{r}')\phi(\boldsymbol{r}')\,\mathrm{d}s_{\boldsymbol{r}'},$$

$$(5.31)$$

We also the consider the scalar densities φ_j^f and ψ_j^f for $j = 1, \ldots, N-1$, which are defined as

$$\varphi_j^f(\boldsymbol{r}) = \lim_{\delta \to 0^+} u^f(x, y-\delta) \quad \text{and} \quad \psi_j^f(\boldsymbol{r}) = \lim_{\delta \to 0^+} \frac{\partial u^f}{\partial y}(x, y-\delta), \quad \boldsymbol{r} = (x,y) \in \Pi_j,$$

in terms of u^f defined in (5.7): u^f denotes the total field (2.16) that results from the scattering of the plane electromagnetic wave u^{inc} by the planar layer medium $D = \bigcup_{j=1}^N D_j$.

Following the procedure in Chapter 4 we now express the correction term $\mathscr{T}_\Pi\left[(\mathscr{I} - \mathscr{W}_A)\boldsymbol{\phi}^f\right]$ on the right-hand-side of equation (5.29) as

$$\mathscr{T}_\Pi\left[(\mathscr{I} - \mathscr{W}_A)\boldsymbol{\phi}^f\right] = -\mathscr{T}_\Pi\left[\mathscr{W}_A\boldsymbol{\phi}^f\right] + \mathscr{T}_\Pi\left[\boldsymbol{\phi}^f\right]. \tag{5.32}$$

Thus, the windowed integral equation (5.29) becomes

$$\mathscr{E}\boldsymbol{\phi}^w + \mathscr{T}_\Gamma\left[\mathscr{W}_A\boldsymbol{\phi}^w\right] = \boldsymbol{\phi}^{\text{inc}} + \mathscr{T}_\Pi\left[\mathscr{W}_A\boldsymbol{\phi}^f\right] - \mathscr{T}_\Pi\left[\boldsymbol{\phi}^f\right] \quad \text{on} \quad \Gamma_A, \tag{5.33}$$

which can be solved numerically provided the quantity $\mathscr{T}_\Pi\left[\boldsymbol{\phi}^f\right]$ can be evaluated. A convenient closed form expression for this quantity is derived in what follows.

Utilizing the integral representation formulae (5.22) with φ_j^f, ψ_j^f, D_j and Π_j instead of φ, ψ, Ω_j and Γ_j, respectively, we obtain

$$\widetilde{\mathcal{D}}_1^{(1)}\left[\varphi_1^f\right](\boldsymbol{r}) - \nu_1\widetilde{\mathcal{S}}_1^{(1)}\left[\psi_1^f\right](\boldsymbol{r}) + u^{\text{inc}}(\boldsymbol{r}) = \begin{cases} u^f(\boldsymbol{r}), & \boldsymbol{r} \in D_1, \\ 0, & \boldsymbol{r} \in \mathbb{R}^2 \setminus \overline{D_1}, \end{cases} \tag{5.34a}$$

$$\widetilde{\mathcal{D}}_j^{(j)}\left[\varphi_j^f\right](\boldsymbol{r}) - \nu_j \widetilde{\mathcal{S}}_j^{(j)}\left[\psi_j^f\right](\boldsymbol{r}) - \widetilde{\mathcal{D}}_j^{(j-1)}\left[\varphi_{j-1}^f\right](\boldsymbol{r}) + \widetilde{\mathcal{S}}_j^{(j-1)}\left[\psi_{j-1}^f\right](\boldsymbol{r})$$

$$= \begin{cases} u^f(\boldsymbol{r}), & \boldsymbol{r} \in D_j, \\ \\ 0, & \boldsymbol{r} \in \mathbb{R}^2 \setminus \overline{D_j}, \end{cases} \quad \text{for} \quad j = 2, \ldots, N-1, \tag{5.34b}$$

$$\text{and} \quad -\widetilde{\mathcal{D}}_N^{(N-1)}\left[\varphi_{N-1}^f\right](\boldsymbol{r}) + \widetilde{\mathcal{S}}_N^{(N-1)}\left[\psi_{N-1}^f\right](\boldsymbol{r}) + u_N^{\|}(\boldsymbol{r}) = \begin{cases} u^f(\boldsymbol{r}), & \boldsymbol{r} \in D_N, \\ \\ 0, & \boldsymbol{r} \in \mathbb{R}^2 \setminus \overline{D_N}, \end{cases} \tag{5.34c}$$

in terms of the layer potentials:

$$\widetilde{\mathcal{S}}_j^{(i)}[\phi](\boldsymbol{r}) = \int_{\Pi_i} G_{k_j}(\boldsymbol{r}, \boldsymbol{r}')\phi(\boldsymbol{r}')\,\mathrm{d}s_{\boldsymbol{r}'} \quad \text{and} \quad \widetilde{\mathcal{D}}_j^{(i)}[\phi](\boldsymbol{r}) = \int_{\Pi_i} \frac{\partial G_{k_j}}{\partial n_{\boldsymbol{r}'}}(\boldsymbol{r}, \boldsymbol{r}')\phi(\boldsymbol{r}')\,\mathrm{d}s_{\boldsymbol{r}'}. \tag{5.35}$$

Thus, evaluating the expressions in (5.34) as well as their normal derivatives on the curves Γ_j we obtain the following closed-form expression for $\mathscr{T}_\Pi\left[\boldsymbol{\phi}^f\right]$ in (5.32): calling $\boldsymbol{\mu} = \mathscr{T}_\Pi\left[\boldsymbol{\phi}^f\right]$ we have

$$[\boldsymbol{\mu}]_1 = \widetilde{\mathrm{T}}_1\left[\phi_1^f\right] + \widetilde{\mathrm{R}}_{1,2}\left[\phi_2^f\right] = \phi^{\mathrm{inc}} - \begin{cases} \mathrm{E}_1\,\phi_1^f & \text{on} \quad \Gamma_1 \cap \Pi_1, \\ \\ \begin{bmatrix} u^f \\ \\ \nabla u^f \cdot n \end{bmatrix} & \text{on} \quad \Gamma_1 \cap (D_1 \cup D_2), \end{cases} \tag{5.36a}$$

$$[\boldsymbol{\mu}]_j = \widetilde{\mathrm{R}}_{j,j-1}\left[\phi_{j-1}^f\right] + \widetilde{\mathrm{T}}_j\left[\phi_j^f\right] + \widetilde{\mathrm{R}}_{j,j+1}\left[\phi_{j+1}^f\right] = -\begin{cases} \mathrm{E}_j\,\phi_j^f & \text{on} \quad \Gamma_j \cap \Pi_j, \\ \\ \begin{bmatrix} u^f \\ \\ \nabla u^f \cdot n \end{bmatrix} & \text{on} \quad \Gamma_j \cap (D_j \cup D_{j+1}) \end{cases}$$
$$\tag{5.36b}$$

for $j = 2, \ldots, N-2$, and

$$[\boldsymbol{\mu}]_{N-1} = \widetilde{\mathrm{R}}_{N-1,N-2}\left[\phi_{N-2}^f\right] + \widetilde{\mathrm{T}}_{N-1}\left[\phi_{N-1}^f\right] = \phi^{\|} - \begin{cases} \mathrm{E}_{N-1}\,\phi_{N-1}^f & \text{on} \quad \Gamma_{N-1} \cap \Pi_{N-1}, \\ \\ \begin{bmatrix} u^f \\ \\ \nabla u^f \cdot n \end{bmatrix} & \text{on} \ \Gamma_{N-1} \cap (D_{N-1} \cup D_N). \end{cases}$$
$$\tag{5.36c}$$

As demonstrated in Section 5.7 through a variety of numerical examples, the vector

density function $\boldsymbol{\phi}^w$, which is the solution of the windowed integral equation (5.33), converges super-algebraically fast to the exact solution $\boldsymbol{\phi}$ of (5.27) within $\Gamma_A \cap \{w_A = 1\}$ as the window size $A > 0$ increases. This observation can be justified via arguments analogous to those presented in Chapter 4 above.

Remark 5.4.1. *Note that the terms $N_{j+1}^{(j,j)} - N_j^{(j,j)}$ that arise along the diagonal blocks of $\mathscr{T}_\Gamma$, which are given the difference of two hypersingular operators, are in fact weakly singular integral operators. Therefore, the windowed integral equation system (5.33) can be discretized utilizing the Nyström method presented in Section 3.3, which accurately accounts for possible corner singularities of the integral equation solutions that arise due to the presence of corners on the defect itself and at the junctions of the defect and the flat portions of Γ_j.*

Remark 5.4.2. *A difficulty arises in the evaluation of the correction term $\mathscr{T}_\Pi \left[\mathscr{W}_A \boldsymbol{\phi}^f \right]$ in (5.33) whenever a curve Γ_j $(\Gamma_j \neq \Pi_j)$, for some $j = 1, \ldots, N-1$, is smooth. This difficulty stems from the cusps that take place at the points at which the curves Γ_j and Π_j depart from each other. Since the numerical evaluation of $\mathscr{T}_\Pi \left[\mathscr{W}_A \boldsymbol{\phi}^f \right]$ entails integration on Π_j and evaluation Γ_j, the presence of cusps at the junctions of Γ_j and Π_j gives to boundary integrals involving nearly-singular kernels for which graded meshes (such as the ones introduced in Section 3.3) are not sufficient to render high-order accuracy. Section 5.6 introduces a reformulation of the integral equation system (5.33) that completely avoids this difficulty.*

5.5 Field evaluation

In order to provide expressions for the numerical evaluation of total near-fields, we approximate the exact solution $\boldsymbol{\phi}$ of the integral equation system (5.27) by $\mathscr{W}_A \boldsymbol{\phi}^w + (\mathscr{I} - \mathscr{W}_A) \boldsymbol{\phi}^f$, where $\boldsymbol{\phi}^w$ is the solution of the windowed integral equation system (5.33). Thus, letting $[\boldsymbol{\phi}^w]_j = \left[\varphi_j^w, \psi_j^w \right]^T$, $j = 1, \ldots, N-1$, denote the block components of $\boldsymbol{\phi}^w$, we substitute the scalar densities φ_j and ψ_j by the approximate densities $w_A \varphi_j^w + (1 - w_A) \varphi_j^f$ and $w_A \psi_j^w + (1 - w_A) \psi_j^f$, respectively, in the field representation formulae (5.22). In view of the expressions in (5.34)—which suffice to evaluate explicitly the terms involving integrals over

unbounded curves for all operators in equation (5.22) —such substitutions yield:

$$u^w = \mathcal{D}_1^{(1)}\left[w_A\varphi_1^w\right] - \nu_1\mathcal{S}_1^{(1)}\left[w_A\psi_1^w\right]$$

$$+ \begin{cases} u^f - \widetilde{\mathcal{D}}_1^{(1)}\left[w_A\varphi_1^f\right] + \nu_1\widetilde{\mathcal{S}}_1^{(1)}\left[w_A\psi_1^f\right] & \text{in} \quad D_1, \\[2ex] -\widetilde{\mathcal{D}}_1^{(1)}\left[w_A\varphi_1^f\right] + \nu_1\widetilde{\mathcal{S}}_1^{(1)}\left[w_A\psi_1^f\right] & \text{in} \quad \mathbb{R}^2\setminus\overline{D_1}, \\[2ex] \left(1 - \dfrac{w_A}{2}\right)\varphi_1^f - D_1^{\Pi_1}\left[w_A\varphi_1^f\right] + \nu_1 S_1^{\Pi_1}\left[w_A\psi_1^f\right] & \text{on} \quad \Pi_1^+, \\[2ex] \dfrac{w_A}{2}\varphi_1^f - D_1^{\Pi_1}\left[w_A\varphi_1^f\right] + \nu_1 S_1^{\Pi_1}\left[w_A\psi_1^f\right] & \text{on} \quad \Pi_1^-, \end{cases} \quad (5.37\text{a})$$

within Ω_1,

$$u^w = \mathcal{D}_j^{(j)}[w_A\varphi_j^w] - \nu_j\mathcal{S}_j^{(j)}[w_A\psi_j^w] - \mathcal{D}_j^{(j-1)}[w_A\varphi_{j-1}^w] + \mathcal{S}_j^{(j-1)}[w_A\psi_{j-1}^w]$$

$$+ \begin{cases} u^f - \widetilde{\mathcal{D}}_j^{(j)}\left[w_A\varphi_j^f\right] + \nu_j\widetilde{\mathcal{S}}_j^{(j)}\left[w_A\psi_j^f\right] + \\[1ex] \qquad\qquad \widetilde{\mathcal{D}}_j^{(j-1)}\left[w_A\varphi_{j-1}^f\right] - \widetilde{\mathcal{S}}_j^{(j-1)}\left[w_A\psi_{j-1}^f\right] \quad \text{in} \quad D_j, \\[2ex] -\widetilde{\mathcal{D}}_j^{(j)}\left[w_A\varphi_j^f\right] + \nu_j\widetilde{\mathcal{S}}_j^{(j)}\left[w_A\psi_j^f\right] + \\[1ex] \qquad\qquad \widetilde{\mathcal{D}}_j^{(j-1)}\left[w_A\varphi_{j-1}^f\right] - \widetilde{\mathcal{S}}_j^{(j-1)}\left[w_A\psi_{j-1}^f\right] \quad \text{in} \quad \mathbb{R}^2\setminus\overline{D_j}, \\[2ex] \left(1 - \dfrac{w_A}{2}\right)\varphi_{j-1}^f - \widetilde{\mathcal{D}}_j^{(j)}\left[w_A\varphi_j^f\right] + \nu_j\widetilde{\mathcal{S}}_j^{(j)}\left[w_A\psi_j^f\right] + \\[1ex] \qquad\qquad D_j^{\Pi_{j-1}}\left[w_A\varphi_{j-1}^f\right] - S_j^{\Pi_{j-1}}\left[w_A\psi_{j-1}^f\right] \quad \text{on} \quad \Pi_{j-1}^-, \\[2ex] \dfrac{w_A}{2}\varphi_{j-1}^f - \widetilde{\mathcal{D}}_j^{(j)}\left[w_A\varphi_j^f\right] + \nu_j\widetilde{\mathcal{S}}_j^{(j)}\left[w_A\psi_j^f\right] + \\[1ex] \qquad\qquad D_j^{\Pi_{j-1}}\left[w_A\varphi_{j-1}^f\right] - S_j^{\Pi_{j-1}}\left[w_A\psi_{j-1}^f\right] \quad \text{on} \quad \Pi_{j-1}^+, \\[2ex] \left(1 - \dfrac{w_A}{2}\right)\varphi_j^f - D_j^{\Pi_j}\left[w_A\varphi_j^f\right] + \nu_j S_j^{(\Pi_j)}\left[w_A\psi_j^f\right] + \\[1ex] \qquad\qquad \widetilde{\mathcal{D}}_j^{(j-1)}\left[w_A\varphi_{j-1}^f\right] - \widetilde{\mathcal{S}}_j^{(j-1)}\left[w_A\psi_{j-1}^f\right] \quad \text{on} \quad \Pi_j^+, \\[2ex] \dfrac{w_A}{2}\varphi_{j-1}^f - \widetilde{\mathcal{D}}_j^{(j)}\left[w_A\varphi_j^f\right] + \nu_j\widetilde{\mathcal{S}}_j^{(j)}\left[w_A\psi_j^f\right] + \\[1ex] \qquad\qquad D_j^{\Pi_{j-1}}\left[w_A\varphi_{j-1}^f\right] - S_j^{\Pi_{j-1}}\left[w_A\psi_{j-1}^f\right] \quad \text{on} \quad \Pi_j^-, \end{cases} \quad (5.37\text{b})$$

within Ω_j, $j = 2, \ldots, N - 1$, and

$$u^w = -\mathcal{D}_N^{(N-1)}\left[w_A\varphi_{N-1}^w\right] + \mathcal{S}_N^{(N-1)}\left[w_A\psi_{N-1}^w\right]$$

$$+ \begin{cases} u^f + \widetilde{\mathcal{D}}_N^{(N-1)}\left[w_A\varphi_{N-1}^f\right] - \widetilde{\mathcal{S}}_N^{(N-1)}\left[w_A\psi_{N-1}^f\right] & \text{in} \quad D_N, \\[2mm] \widetilde{\mathcal{D}}_N^{(N-1)}\left[w_A\varphi_{N-1}^f\right] - \widetilde{\mathcal{S}}_N^{(N-1)}\left[w_A\psi_{N-1}^f\right] & \text{in} \quad \mathbb{R}^2 \setminus \overline{D_N}, \\[2mm] \dfrac{w_A}{2}\varphi_{N-1}^f + D_N^{\Pi_{N-1}}\left[w_A\varphi_{N-1}^f\right] - S_N^{\Pi_{N-1}}\left[w_A\psi_{N-1}^f\right] & \text{on} \quad \Pi_{N-1}^+, \\[2mm] \left(1 - \dfrac{w_A}{2}\right)\varphi_{N-1}^f + D_N^{\Pi_{N-1}}\left[w_A\varphi_{N-1}^f\right] - S_N^{\Pi_{N-1}}\left[w_A\psi_{N-1}^f\right] & \text{on} \quad \Pi_{N-1}^-. \end{cases} \quad (5.37\text{c})$$

within Ω_N, in terms of the layer potentials $\widetilde{\mathcal{D}}_j^{(i)}$ and $\widetilde{\mathcal{S}}_j^{(i)}$ defined (5.35) and the boundary integral operators $D_j^{\Pi_i}$ and $S_j^{\Pi_i}$ which are defined as

$$S_j^{\Pi_i}[\phi] = \int_{\Pi_i} G_{k_j}(\boldsymbol{r}, \boldsymbol{r}')\phi(\boldsymbol{r}')\,\mathrm{d}s_{\boldsymbol{r}'} \quad \text{and} \quad D_j^{\Pi_i}[\phi] = \int_{\Pi_i} \frac{\partial G_{k_j}}{\partial n_{\boldsymbol{r}'}}(\boldsymbol{r}, \boldsymbol{r}')\phi(\boldsymbol{r}')\,\mathrm{d}s_{\boldsymbol{r}'}, \quad \boldsymbol{r} \in \Pi_i.$$

Numerical examples presented in Section 5.7 demonstrate that formulae (5.37) provide an accurate approximation (in fact, super-algebraically accurate approximation) of the total near-fields within a region containing the surface defects. Once again, this observation can be better understood by following the arguments presented in Chapter 4.

A procedure for evaluation of the far-field pattern, similar to the one presented in Section 4.2.6 for the two-layer case, can then be obtained by utilizing suitable generalizations to the multi-layer case of the the two-layer expressions (2.59) and (2.60) for the far-field of the layer Green function.

Although perhaps most natural, the formulations used in Chapter 4 and above in this chapter lead to the somewhat complicated formulae (5.37) for the evaluation of the total near-field. In the following section we present a slightly different integral formulation of the problem which not only gives rise to significantly simpler near-field expressions, but which also greatly facilitates the developement of numerical methods for smooth surface defects.

5.6 Alternative integral equation formulation

This section presents an alternative representation formula for which the resulting integral equation formulation does not suffer from the difficulties mentioned in Remark 5.4.2.

We start then by expressing the total field as $u = u^s + \widetilde{u}^f$ where the function $\widetilde{u}^f$ is given by

$$\widetilde{u}^f = u_j^{\uparrow} + u_j^{\downarrow} \quad \text{in} \quad \Omega_j, \quad j = 1, \ldots, N,$$

in terms of the up-going $(u_j^{\uparrow})$ and down-going $(u_j^{\downarrow})$ plane-waves defined in (5.8). Notice that $\widetilde{u}^f = u^f$ in $D_j \setminus \Omega_j$ for $j = 1, \ldots, N$.

Clearly $\widetilde{u}^f$ satisfies the Helmholtz equation with wavenumber k_j within the layer Ω_j for $j = 1, \ldots, N$. Consequently, from the derivations presented in Section 5.2 we infer that $\widetilde{u}^f$ admits an integral representation in terms of the layer-potentials $\mathcal{D}_j^{(i)}$ and $\mathcal{S}_j^{(i)}$ defined in (5.18). Letting

$$\widetilde{\varphi}^f = \widetilde{u}^f|_{j^-}, \qquad \widetilde{\psi}^f = \left. \frac{\partial \widetilde{u}^f}{\partial n} \right|_{j^-},$$

and

$$f_j = \widetilde{u}^f\big|_{j^+} - \widetilde{u}^f\big|_{j^-}, \qquad g_j = \left. \frac{\partial \widetilde{u}^f}{\partial n} \right|_{j^+} - \nu_j \left. \frac{\partial \widetilde{u}^f}{\partial n} \right|_{j^-}, \tag{5.38}$$

we thus obtain:

$$\mathcal{D}_1^{(1)} \left[\widetilde{\varphi}_1^f + f_j \right] (\boldsymbol{r}) - \mathcal{S}_1^{(1)} \left[\nu_1 \widetilde{\psi}_1^f + g_j \right] (\boldsymbol{r}) + u^{\text{inc}}(\boldsymbol{r}) = \begin{cases} \widetilde{u}^f(\boldsymbol{r}), & \boldsymbol{r} \in \Omega_1, \\ 0, & \boldsymbol{r} \in \mathbb{R}^2 \setminus \overline{\Omega_1}, \end{cases} \tag{5.39a}$$

$$\mathcal{D}_j^{(j)} \left[\widetilde{\varphi}_j^f + f_j \right] (\boldsymbol{r}) - \mathcal{S}_j^{(j)} \left[\nu_j \widetilde{\psi}_j^f + g_j \right] (\boldsymbol{r})$$
$$- \mathcal{D}_j^{(j-1)} \left[\widetilde{\varphi}_{j-1}^f \right] (\boldsymbol{r}) + \mathcal{S}_j^{(j-1)} \left[\widetilde{\psi}_{j-1}^f \right] (\boldsymbol{r}) = \begin{cases} \widetilde{u}^f(\boldsymbol{r}), & \boldsymbol{r} \in \Omega_j, \\ 0, & \boldsymbol{r} \in \mathbb{R}^2 \setminus \overline{\Omega_j}, \end{cases} \tag{5.39b}$$

for $j = 2, \ldots, N - 1$, and

$$- \mathcal{D}_N^{(N-1)} \left[\widetilde{\varphi}_{N-1}^f \right] (\boldsymbol{r}) + \mathcal{S}_N^{(N-1)} \left[\widetilde{\psi}_{N-1}^f \right] (\boldsymbol{r}) + u_N^{\parallel}(\boldsymbol{r}) = \begin{cases} \widetilde{u}^f(\boldsymbol{r}), & \boldsymbol{r} \in \Omega_N, \\ 0, & \boldsymbol{r} \in \mathbb{R}^2 \setminus \overline{\Omega_N}. \end{cases} \tag{5.39c}$$

Evaluating the expressions (5.39) as well as their normal derivatives—utilizing the jump relations (5.19)—at the dielectric interfaces Γ_j, and letting $\widetilde{\boldsymbol{\phi}}^f = \left[\widetilde{\boldsymbol{\phi}}^f\right]_j = \left[\widetilde{\varphi}_j^f, \widetilde{\psi}_j^f\right]^T$, $j = 1, \ldots, N-1$, we obtain

$$\mathscr{E}\widetilde{\boldsymbol{\phi}}^f + \mathscr{T}_\Gamma\left[\widetilde{\boldsymbol{\phi}}^f\right] = \boldsymbol{\phi}^{\mathrm{inc}} + \mathscr{M}\left[\boldsymbol{\psi}\right] \quad \text{on} \quad \Gamma, \tag{5.40}$$

where

$$[\boldsymbol{\psi}]_j = \boldsymbol{\psi}_j \quad \text{and} \quad [\mathscr{M}]_{i,j} = \begin{cases} \frac{1}{2}\,\mathrm{I}_d + \mathrm{M}_{j,j} & \text{if} \quad i = j, \\ \mathrm{M}_{j,j+1} & \text{if} \quad j = i+1, \\ 0 & \text{otherwise,} \end{cases}$$

for $i, j = 1, \ldots, N-1$, with

$$\boldsymbol{\psi}_j = \begin{bmatrix} f_j \\ g_j \end{bmatrix}, \quad \mathrm{M}_{j,j} = \begin{bmatrix} D_j^{(j,j)} & -S_j^{(j,j)} \\ N_j^{(j,j)} & -K_j^{(j,j)} \end{bmatrix} \quad \text{and} \quad \mathrm{M}_{j,j+1} = \begin{bmatrix} D_{j+1}^{(j,j+1)} & -S_{j+1}^{(j,j+1)} \\ N_{j+1}^{(j,j+1)} & -K_{j+1}^{(j,j+1)} \end{bmatrix}.$$

Subtracting (5.40) from (5.27) we thus obtain the exact integral equation

$$\mathscr{E}\boldsymbol{\phi}^s + \mathscr{T}_\Gamma\left[\boldsymbol{\phi}^s\right] = -\mathscr{M}\left[\boldsymbol{\psi}\right] \quad \text{on} \quad \Gamma, \tag{5.41}$$

for the new unknown vector density function $\boldsymbol{\phi}^s$ which is defined as $\boldsymbol{\phi}^s = \boldsymbol{\phi} - \widetilde{\boldsymbol{\phi}}^f$.

Similarly, subtracting (5.40) from (5.33) and utilizing the identity $\mathscr{T}_\Pi\left[(\mathscr{I} - \mathscr{W}_A)\widetilde{\boldsymbol{\phi}}^f\right] = \mathscr{T}_\Pi\left[(\mathscr{I} - \mathscr{W}_A)\boldsymbol{\phi}^f\right]$—which follows directly from the fact that $\widetilde{\boldsymbol{\phi}}^f = \boldsymbol{\phi}^f$ on $\Gamma \setminus \Pi$—we obtain the windowed integral equation

$$\mathscr{E}\boldsymbol{\phi}^{sw} + \mathscr{T}_\Gamma\left[\mathscr{W}\boldsymbol{\phi}^{sw}\right] = -\mathscr{M}\left[\boldsymbol{\psi}\right] \quad \text{on} \quad \Gamma_A, \tag{5.42}$$

whose solution $\boldsymbol{\phi}^{sw}$, which equals $\boldsymbol{\phi}^w - \widetilde{\boldsymbol{\phi}}^f$, approximates $\boldsymbol{\phi}^s$ with super-algebraically small errors within $\Gamma_A \cap \{w_A = 1\}$.

Remark 5.6.1. *A difficulty offsets, at least to some extent, the benefits provided by the formulation* (5.42)*: The presence of hypersingular operators $N_j^{(j,j)}$ along the block-diagonal of*

the right-hand side operator $\mathscr{M}$ gives rise to significant challenges in the numerical solution of the integral equation system (5.42) in the non-smooth case. The integral equations presented above in the previous section, in contrast, completely avoid such challenges.

Remark 5.6.2. *Note that since $\widetilde{u}^f$ satisfies the transmission conditions at the planar interfaces Π_j, so it does at the planar portions of Γ_j for $j = 1, \ldots, N-1$. Thus the functions f_j and g_j, which are defined in (5.38) in terms of the jumps of $\widetilde{u}^f$ at Γ_j, are supported on $\Gamma_j \setminus \Pi_j$ as they vanish exactly on $\Gamma_j \cap \Pi_j$, $j = 1, \ldots, N-1$. Furthermore, for smooth dielectric interfaces of class $\mathcal{C}^\infty$, we have that $f_j, g_j \in C_0^\infty(\Gamma_j)$; this fact makes it possible to regularize the hypersingular operator $N_j^{(i,i)}$ that arises in the right-hand-side term $\mathscr{M}[\boldsymbol{\psi}]$ and it facilitates the use of the Nyström method to solve (5.42) (see Remark 5.6.3 below).*

Remark 5.6.3. *Unlike (5.33), the new system of integral equations (5.42) where the curves Γ_j, $j = 1, \ldots, N-1$, are assumed to be smooth of class $\mathcal{C}^\infty$, can be discretized by means of the original Nyström method introduced by Martensen [84] and Kussmaul [75] (cf. [44]) which yields super-algebraic convergence as the number of discretization (trapezoidal quadrature) points increases. Such Nyström method, which relies on the smoothness and periodicity of the relevant density functions, is suitable to discretize (5.42) as the functions $w_A \varphi_j^{sw}$, $w_A \psi_j^{sw}$, f_j and g_j, can be extended periodically as smooth functions of the parameter $s \in [0, 2\pi]$ utilized to parametrize the curve $\Gamma_{j,A}$. Note, however, that an additional difficulty arises in the evaluation of $\mathscr{M}[\boldsymbol{\psi}]$ as it is needed to evaluate the hypersingular operators $N_j^{j,j}[f_j]$ (see Remark 5.6.1). In order to do so in the present context, we resort to Maue's identity [71, 85]:*

$$N_j^{j,j}[f_j] = k_j^2 n \cdot S_j^{j,j}[n \, f_j] + \frac{\mathrm{d}}{\mathrm{d}\tau} S_j^{j,j}\left[\frac{\mathrm{d}f_j}{\mathrm{d}\tau}\right],$$

where n denotes the unit normal vector to the curve $\Gamma_{j,A}$ and where $\mathrm{d}/\mathrm{d}\tau$ denotes the tangential derivative along the curve $\Gamma_{j,A}$. Since f_j can be viewed as a smooth periodic function, the numerical evaluation of the terms $n \cdot S_j^{(j,j)}[n \, f_j]$ and $S_j^{j,j}[\mathrm{d}f_j/\mathrm{d}\tau]$ from values of f_j at an equispaced grid $\{s_\ell\} \subset [0, 2\pi]$ is straightforward. The numerical evaluation of $\mathrm{d}S_j^{j,j}[\mathrm{d}f_j/\mathrm{d}\tau]/\mathrm{d}\tau$, however, requires special treatment. Since $S_j^{j,j}[\mathrm{d}f_j/\mathrm{d}\tau]$ can not in general be smoothly extended as periodic function of the parameter $s \in [0, 2\pi]$, the direct numerical differentiation

of the $S_j^{j,j}[\mathrm{d}f_j/\mathrm{d}\tau]$ obtained from its point-values at $\{s_\ell\}$ gives rise to Gibbs phenomenon that destroys the accuracy of the numerical evaluation of right-hand-side $\mathscr{M}[\boldsymbol{\psi}]$, thus leading to numerical errors in integral equation solution $\boldsymbol{\phi}^{sw}$.

In order evaluate $\mathrm{d}S_j^{j,j}[\mathrm{d}f_j/\mathrm{d}\tau]/\mathrm{d}\tau$ with high (super-algebraic) accuracy, we first evaluate the trigonometric interpolant of $S_j^{j,j}[\mathrm{d}f_j/\mathrm{d}\tau]$ —which is explicitly provided by the Nyström method—on a Chebyshev grid $\{\tilde{s}_\ell\} \subset [0, 2\pi]$. Differentiating the Chebyshev interpolating polynomial, which is constructed from the approximate values of $S_j^{j,j}[\mathrm{d}f_j/\mathrm{d}\tau]$ at $\{\tilde{s}_\ell\}$, and evaluating it back on the equispaced grid $\{s_\ell\}$, we obtain the desired values of $\mathrm{d}S_j^{j,j}[\mathrm{d}f_j/\mathrm{d}\tau]/\mathrm{d}\tau$ at the original equispaced grid $\{s_\ell\}$ with super-algebraically small errors.

We now derive expressions for the evaluation of the total near fields. Letting

$$\varphi_j^s = u^s|_{j^-} \quad \text{and} \quad \psi_j^s = \partial u^s/\partial n|_{j^-},$$

we obtain that the scattered field $u^s = u - \widetilde{u}^f$ satisfies the following jump conditions at Γ_j:

$$u^s|_{j^+} = \varphi_j^s - f_j \quad \text{and} \quad \left.\frac{\partial u^s}{\partial n}\right|_{j^+} = \nu\psi_j^s - g_j.$$

From the derivations presented in Section 5.2, it thus follows that u^s admits the integral representation:

$$\mathcal{D}_1^{(1)}\left[\varphi_1^s - f_1\right](\boldsymbol{r}) - \mathcal{S}_1^{(1)}\left[\nu_1\psi_1^s - g_1\right](\boldsymbol{r}) = \begin{cases} u^s(\boldsymbol{r}), & \boldsymbol{r} \in \Omega_1, \\ 0, & \boldsymbol{r} \in \mathbb{R}^2 \setminus \overline{\Omega_1}, \end{cases} \tag{5.43a}$$

$$\begin{aligned} \mathcal{D}_j^{(j)}\left[\varphi_j^s - f_j\right](\boldsymbol{r}) - \mathcal{S}_j^{(j)}\left[\nu_j\psi_j^s - g_j\right](\boldsymbol{r}) & \\ -\mathcal{D}_j^{(j-1)}\left[\varphi_{j-1}^s\right](\boldsymbol{r}) + \mathcal{S}_j^{(j-1)}\left[\psi_{j-1}^s\right](\boldsymbol{r}) &= \begin{cases} u^s(\boldsymbol{r}), & \boldsymbol{r} \in \Omega_j, \\ 0, & \boldsymbol{r} \in \mathbb{R}^2 \setminus \overline{\Omega_j}, \end{cases} \end{aligned} \tag{5.43b}$$

for $j = 2, \ldots, N-1$, and

$$-\mathcal{D}_N^{(N-1)}\left[\varphi_{N-1}^s\right](\boldsymbol{r}) + \mathcal{S}_N^{(N-1)}\left[\psi_{N-1}^s\right](\boldsymbol{r}) = \begin{cases} u^s(\boldsymbol{r}), & \boldsymbol{r} \in \Omega_N, \\ 0, & \boldsymbol{r} \in \mathbb{R}^2 \setminus \overline{\Omega_N}. \end{cases} \tag{5.43c}$$

Therefore, the substitutions: φ_j^s by $w_A \varphi_j^{sw}$, and ψ_j^s by $w_A \psi_j^{sw}$ in the formulae (5.43) yield the following expression for the total near-field:

$$u^w = \widetilde{u}^f + u^{sw}$$

$$= \widetilde{u}^f + \begin{cases} \mathcal{D}_1^{(1)} \left[w_A \varphi_1^{sw} - f_1 \right] - \nu_1 \mathcal{S}_1^{(1)} \left[w_A \psi_1^{ws} - g_1 \right] & \text{in} \quad \Omega_1, \\[2mm] \mathcal{D}_j^{(j)} \left[w_A \varphi_j^{sw} - f_j \right] - \nu_j \mathcal{S}_j^{(j)} \left[w_A \psi_j^{sw} - g_j \right] \\ \quad - \mathcal{D}_j^{(j-1)} \left[w_A \varphi_{j-1}^{sw} \right] + \mathcal{S}_j^{(j-1)} \left[w_A \psi_{j-1}^{sw} \right] & \text{in} \quad \Omega_j, \ j = 2, \dots, N-1, \\[2mm] - \mathcal{D}_N^{(N-1)} \left[w_A \varphi_{N-1}^{sw} \right] + \mathcal{S}_N^{(N-1)} \left[w_A \psi_{N-1}^{sw} \right] & \text{in} \quad \Omega_N, \end{cases} \tag{5.44}$$

where we have set $[\boldsymbol{\phi}^{sw}]_j = [\varphi_j^{sw}, \psi_j^{sw}]^T$, $j = 1, \dots, N-1$. Here the field u^{sw} approximates u^s with super-algebraically small errors within a region around the surface defects.

Notice that the densities φ_j^{sw} and ψ_j^{sw}, $j = 1, \dots, N-1$, needed to produce the near-fields utilizing (5.44) can also be obtained from the windowed integral equation (5.33) by setting $\varphi_j^{sw} = \varphi_j^w - \widetilde{\varphi}_j^f$ and $\psi_j^{sw} = \psi_j^w - \widetilde{\psi}_j^f$ in (5.44). Thus, clearly, formula (5.44) provides a much simpler formula than (5.37) to numerically evaluate the near-fields.

Remark 5.6.4. *Note that, of course, the problem of scattering by smooth defects in a two-layer problem can also be tackled by this method. In this case the resulting windowed integral equation reads*

$$\mathrm{E}_1 \, \boldsymbol{\phi}_1^{sw} + \mathrm{T}_1 \left[\mathrm{W}_A \, \boldsymbol{\phi}_1^{sw} \right] = - \mathrm{M}_{1,1} \left[\boldsymbol{\psi} \right] \quad on \quad \Gamma_{1,A}, \tag{5.45}$$

and the near-field approximation is given by

$$u^w = \widetilde{u}^f + \begin{cases} \mathcal{D}_1^{(1)} \left[w_A \varphi_1^{sw} - f_1 \right] - \nu_1 \mathcal{S}_1^{(1)} \left[w_A \psi_1^{ws} - g_1 \right] & in \quad \Omega_1, \\[2mm] - \mathcal{D}_2^{(1)} \left[w_A \varphi_1^{sw} \right] + \mathcal{S}_2^{(2)} \left[w_A \psi_1^{sw} \right] & in \quad \Omega_2. \end{cases} \tag{5.46}$$
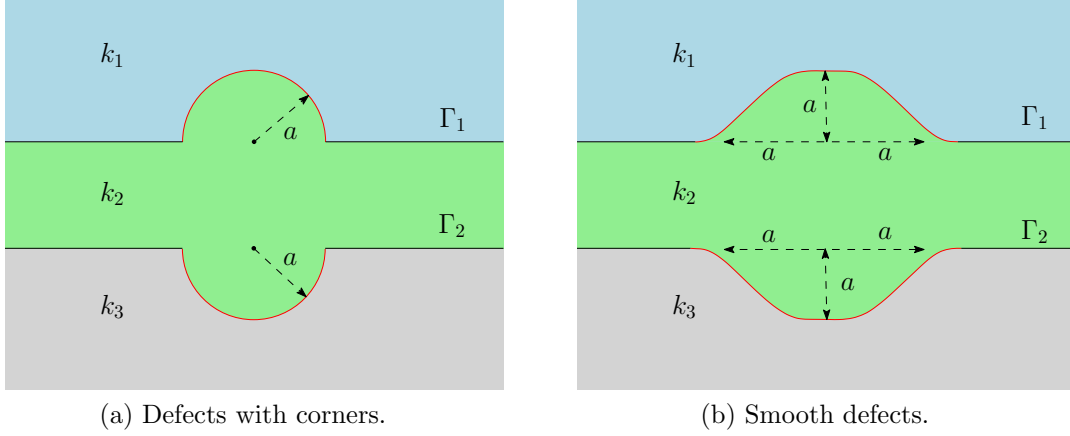
(a) Defects with corners. (b) Smooth defects.

Figure 5.3: Dielectric structures utilized in the numerical examples presented in the present Chapter 5.

5.7   Numerical examples

In this section we present a set of numerical examples designed to demonstrate the accuracy and efficiency of the proposed multi-layer WGF method. In all the illustrations presented in this section we consider problems of scattering of a plane electromagnetic TE-polarized wave that impinges on a layered medium which contains localized surface defects (both smooth and non-smooth) at the dielectric planar interfaces Π_j. The numerical results reported in this section were produced using a Matlab implementation of our algorithms in a MacBook Air laptop (early 2014 model). For the sake of definiteness, in all the examples considered throughout this section, the value $c = 0.7$ is utilized for the evaluation of the window function (4.9) w_A.

This section presents numerical results for the various LGF and WGF algorithms introduced in this thesis. Numerical errors for both the LGF and the WGF method were evaluated by resorting to convergence analyses based on numerical-resolution/convergence studies and/or increases in window sizes. Additionally, adequately accurate LGF solutions (with accuracy guaranteed by convergence studies) were used to evaluate the accuracy of the WGF approach. All of these methods for error evaluation are considered in this section. Brief indications will be provided when necessary to indicate which method is being used in each case.
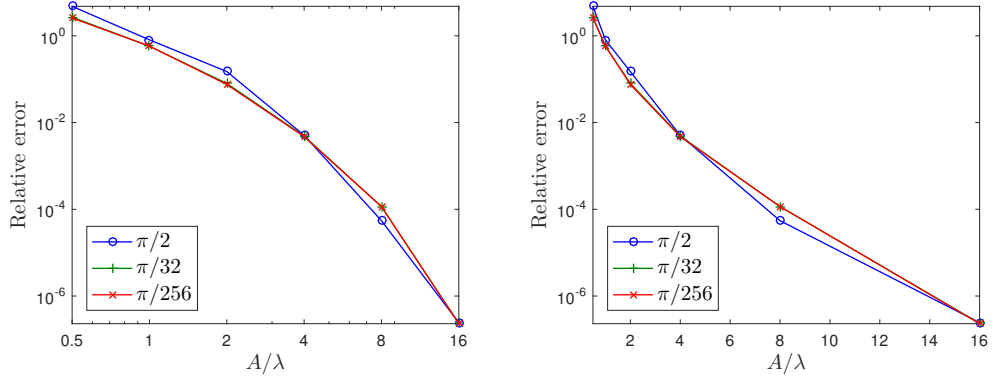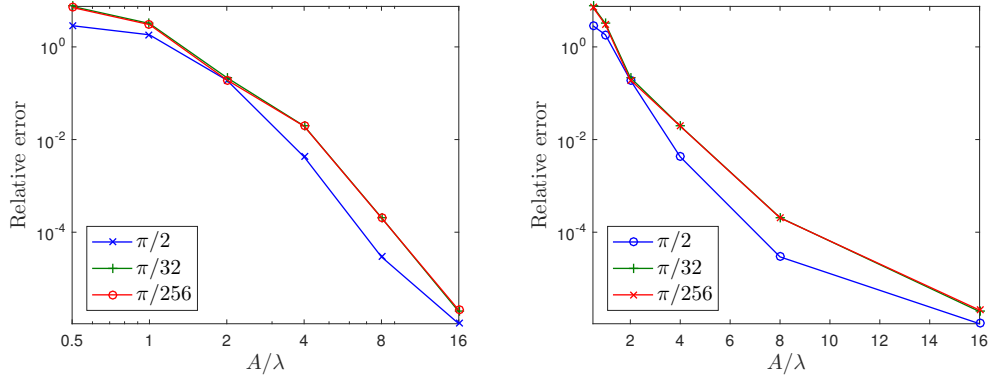
(a) Defect on Γ_1.

(b) Defect on Γ_2.

Figure 5.4: Relative errors in the integral densities resulting from numerical solution of (5.33) for the structure depicted in Figure 5.3a by means of the WGF method, for various window sizes and angles of incidence—including extremely shallow incidences. Left: log-log scale. Right: semi-log scale. Once again we see that, the WGF method computes integral densities with super-algebraically high accuracy uniformly for all angles of incidence.

In our first example we consider the dielectric structure depicted in Figure 5.3a, in which semi-circular defects of radii $a = 1$ are placed at the planar interfaces $\Pi_1 = \mathbb{R} \times \{0\}$ and $\Pi_2 = \mathbb{R} \times \{-3/2\}$ of the three-layer dielectric medium with wavenumbers $k_1 = 10$, $k_2 = 20$ and $k_3 = 30$. Since the junctions of the defect with the planar interfaces give rise dielectric interfaces Γ_1 and Γ_2 with corners (see Figure 5.3a), we utilize the windowed integral equation system (5.33) which is discretized by means of the Nyström method described in Section 3.3 for various windows sizes $A > 0$ and incidences α. Figure 5.4 displays the maximum relative errors in the total field produced by the WGF method on the surface of the semi-circular defects (the curves marked in red in Figure 5.3a). Errors in log-log and semi-log scales for the

various window sizes considered are provided in the left and right graphs, respectively. The number of quadrature points was selected in such a way that for any given $A > 0$ the Nyström discretization error in the integral equation solution is not larger than 10^{-9}. The WGF solution obtained for $A = 32\lambda$ is utilized as the reference for the error estimation. As it can be inferred from the error curves displayed in Figure 5.4, super-algebraic but not exponential convergence is observed as A increases. These results, on the other hand, demonstrate that the fast convergence of the WGF is independent of the plane-wave incidence.

(a) $\alpha = -\pi/2$. (b) $\alpha = -\pi/32$. (c) $\alpha = -\pi/256$.
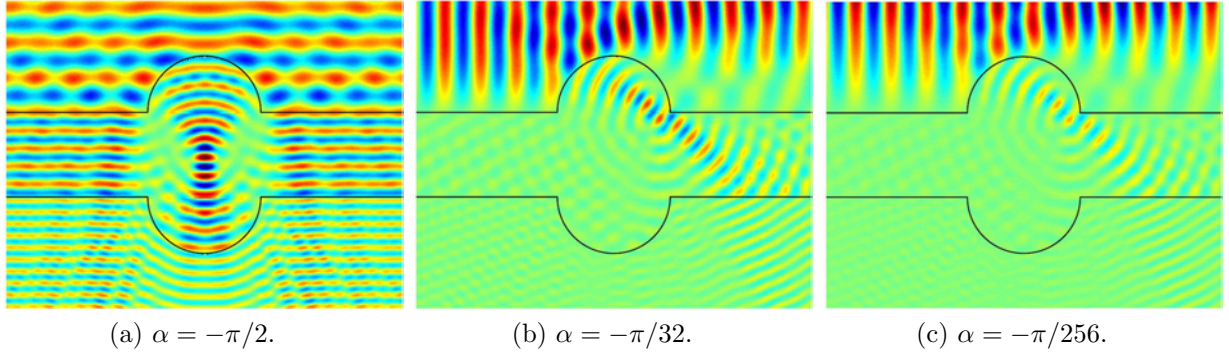
Figure 5.5: Total near field obtained for the solution of the problem of scattering by the structure depicted in Figure 5.3a for various incidences. The near fields were computed utilizing the expression (5.37)

In our second example we consider the three-layer medium presented in Figure 5.3b, with the same interplane distances and layer dielectric constants, but for which the defects do not give rise to corners: the overall scattering surfaces are *smooth*. The dielectric interfaces Γ_1 and Γ_2 displayed in that figure are infinitely-smooth curves which are constructed by suitably utilizing the graph of the function $\eta(t; ca, a)$, $t \in \mathbb{R}$, with $a = 1$ and $c = 0.1$, where η is the function defined in (2.78). The windowed integral equation system (5.42) is utilized in this case, which is discretized by means of the classical Nyström method as none of the dielectric interfaces has corners (see Remark 5.6.3). As in the previous example, the integral equation system (5.42) is solved for various window sizes $A > 0$ and incidences $\alpha \in (-\pi, 0)$. Once again, the maximum relative errors in the total field values on the surface of the smooth defects—which correspond to the curves marked in red in Figure 5.3b—are reported. The number of quadrature points is selected in such a way that for any given

$A > 0$ the Nyström discretization error in the integral equation solution is not larger than 10^{-10}. The reference solution utilized to estimate the error corresponds to the WGF solution obtained with $A = 32\lambda$. The resulting error curves are displayed in Figure 5.6 in log-log and semi-log scales, which, once again, clearly demonstrate super-algebraic but not exponential convergence as A increases.
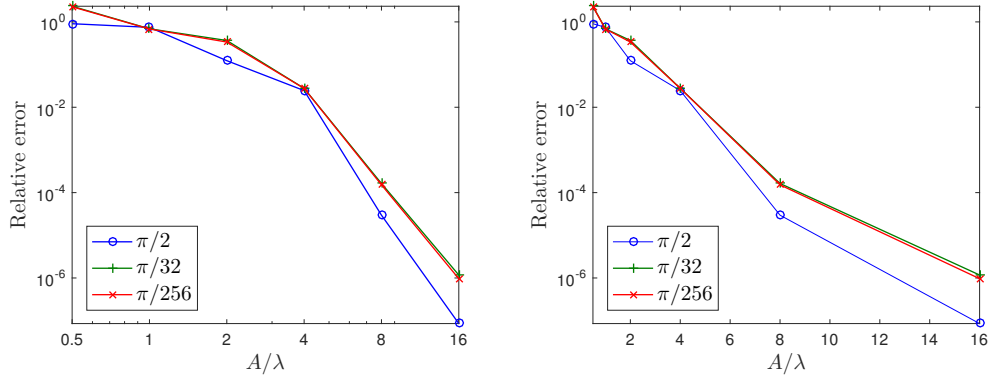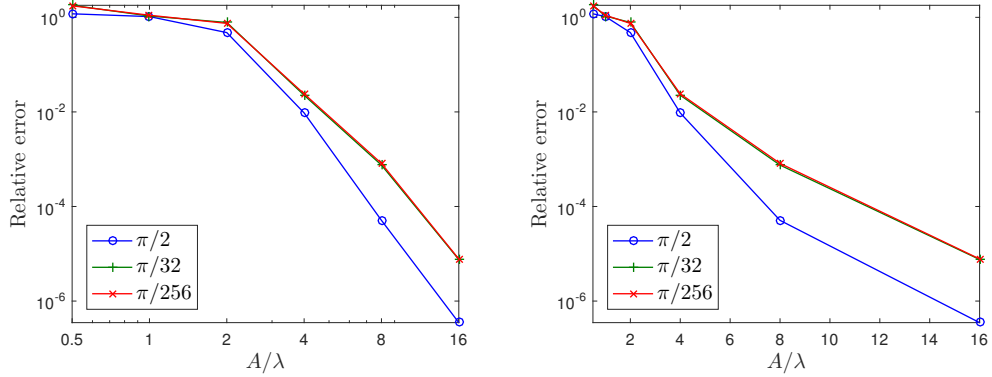

(a) Defect on Γ_1.

(b) Defect on Γ_2.

Figure 5.6: Relative errors in the integral densities resulting from numerical solution of (5.33) for the structure depicted in Figure 5.3b by means of the full WGF method, for various window sizes and angles of incidence—including extremely shallow incidences. Left: log-log scale. Right: semi-log scale. Once again we see that, the WGF method computes integral densities with super-algebraically high accuracy uniformly for all angles of incidence.

In our third example, for which we compare the computational cost of the LGF and WGF methods for a given accuracy, we consider a planar three-layer structure similar to those considered previously, but now containing only one surface defect: a semi-circular cavity of radius $a = 1$ at Π_1. (The use of a single defect reduces somewhat the LGF cost which seemed

(a) $\alpha = -\pi/2$.   (b) $\alpha = -\pi/32$.   (c) $\alpha = -\pi/256$.
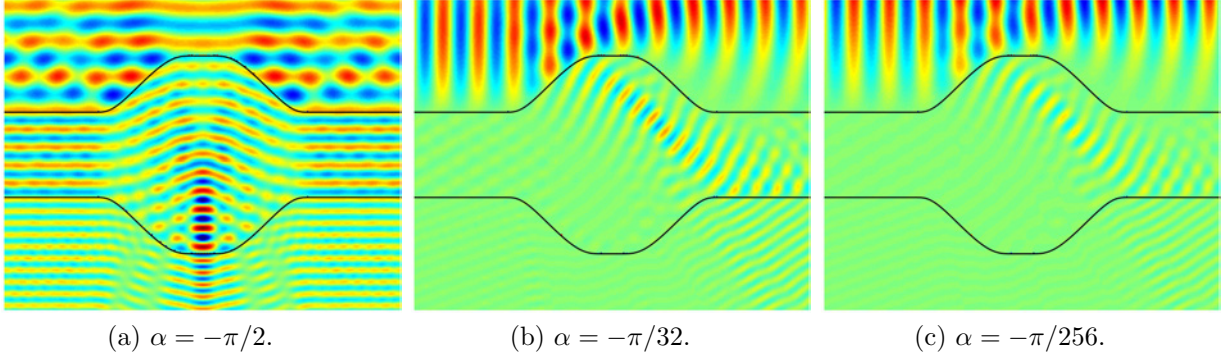
Figure 5.7: Total near field obtained for the solution of the problem of scattering by the structure depicted in Figure 5.3b for various incidences. Near fields were computed utilizing the expression (5.44)

κ	WGF method					LGF method				
	2	4	8	16	32	2	4	8	16	32
Number of unknowns	1232	1272	1348	1496	1800	68	148	300	596	1204
Matrix construction (s)	3.44	3.53	3.98	5.78	7.29	6.49	22.15	82.86	319.46	$1.9 \cdot 10^3$

Table 5.1: Computing times required by the WGF and LGF methods to construct the system matrices for the numerical solution of the problem of scattering of a plane-wave by a semi-circular cavity or radius $a = 1$ on a three-layer medium with wavenumbers $k_1 = \kappa$, $k_2 = 2\kappa$ and $k_3 = 3\kappa$, with $\kappa = 2^j$, $j = 1, \ldots 5$.

inordinately large for the two-defect problem.) A plane-wave u^{inc} with $\alpha = -\pi/6$ illuminates the dielectric structure. Five sets of wavenumbers given by $k_1 = \kappa$, $k_2 = 2\kappa$ and $k_3 = 3\kappa$ with $\kappa = 2^j$, $j = 1, \ldots, 5$ are considered. The resulting problems of scattering are then solved by employing a Nyström discretization of the WGF equations (5.33), and a numerical version of (5.37) is used to evaluate near-fields. The same problem of scattering is then solved, with a relative error not larger than 10^{-4}, by means of a generalization to the present three-layer case, of the two-layer LGF method presented in Chapter 3. The necessary layer Green function for the three-layer medium was obtained in Section 2.3.3. The three-layer Green function is numerically evaluated using a direct extension of the method described in Section 2.3.5. The reference solution used to estimate the accuracy of the LGF solution is obtained by solving the resulting LGF integral equation with an error not larger 10^{-9}

(this accuracy is achieved by utilizing a large number of Nyström quadrature points and evaluating the layer Green function with an error not larger than 10^{-10}).
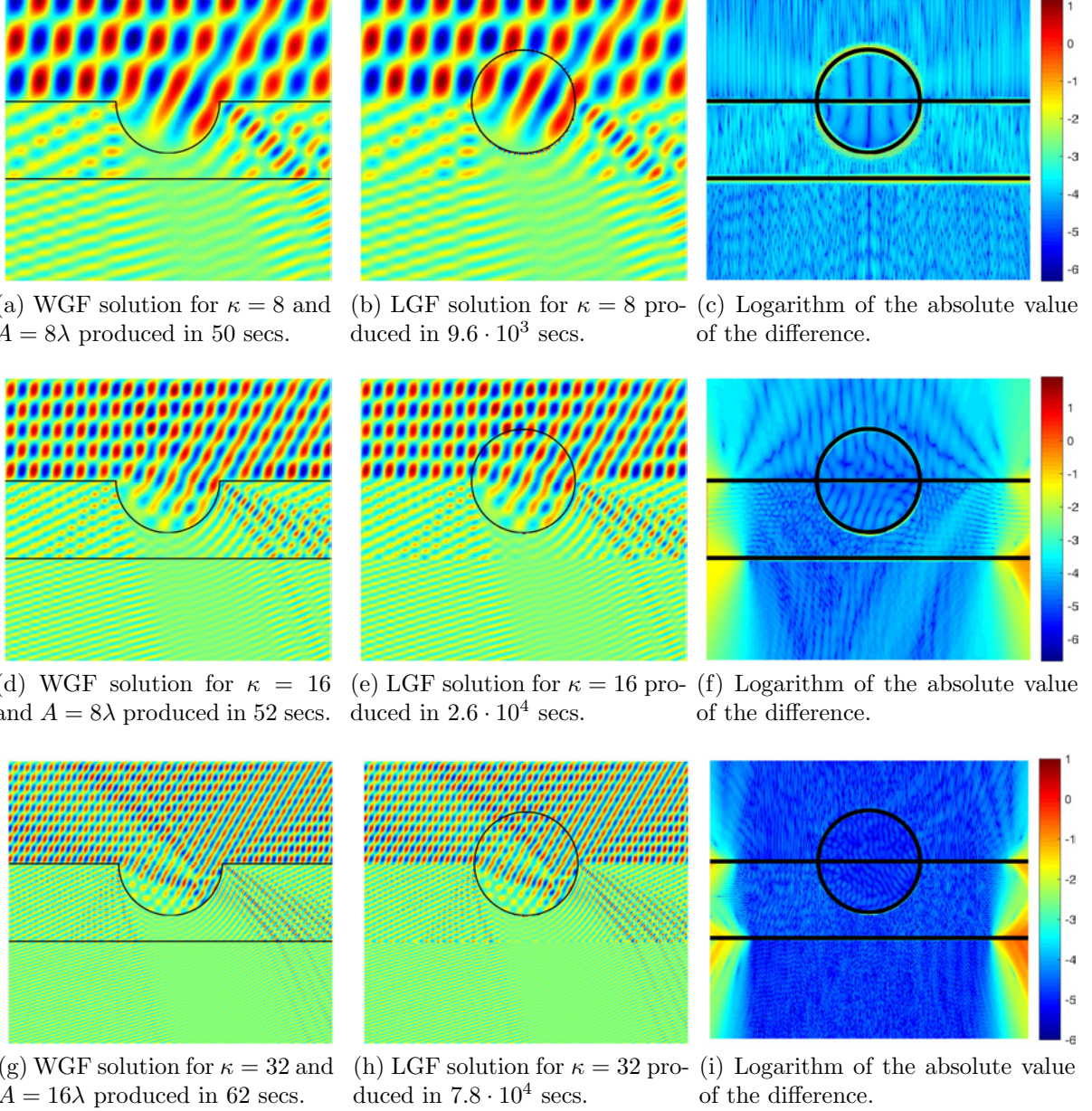

(a) WGF solution for $\kappa = 8$ and $A = 8\lambda$ produced in 50 secs.

(b) LGF solution for $\kappa = 8$ produced in $9.6 \cdot 10^3$ secs.

(c) Logarithm of the absolute value of the difference.

(d) WGF solution for $\kappa = 16$ and $A = 8\lambda$ produced in 52 secs.

(e) LGF solution for $\kappa = 16$ produced in $2.6 \cdot 10^4$ secs.

(f) Logarithm of the absolute value of the difference.

(g) WGF solution for $\kappa = 32$ and $A = 16\lambda$ produced in 62 secs.

(h) LGF solution for $\kappa = 32$ produced in $7.8 \cdot 10^4$ secs.

(i) Logarithm of the absolute value of the difference.

Figure 5.8: Total near fields (real part) and logarithm of the absolute value of the difference of the total near fields obtained by means of the WGF and LGF methods for the solution of the problem of scattering of a semi-circular cavity of radius $a = 1$ on a three-layer medium. The angle of incidence is $\alpha = -\pi/6$ and the wavenumbers considered are $k_1 = \kappa$, $k_2 = 2\kappa$ and $k_3 = 3\kappa$ for $\kappa = 8$ (1st row), 16 (2nd row) and 32 (3rd row). The black lines represent the domains where the respective integral equation formulations are posed.

Table 5.1 displays the computing times needed by both methods to construct the system matrices. In order to allow for a fair comparison of the computing times and the field values on the surface defect, the same set of quadrature points is utilized to discretize the currents on the surface of the cavity in each case. The number of quadrature points was increased in direct proportion to the value of κ. The maximum of the absolute value of the difference between the LGF and WGF solutions (using $A = 8\lambda$) on the surface of the defect is no larger than 10^{-4} in all the examples considered. Remarkably, in the $\kappa = 32$ case the proposed WGF method is 260 times faster than the LGF method.

Continuing with the single cavity problem, Figure 5.8 now presents a comparison of the near fields obtained by means of the WGF and LGF methods for some of the wavenumbers considered in Table 5.1. The first two columns in Figure 5.8 display the real-part of the total near-fields produced by the WGF method (1st column) and by the LGF method (2nd column), while the third column displays the (base ten) logarithm of the absolute value of the difference between the LGF and WGF solutions for three different sets of wavenumbers. The fields are evaluated in the rectangular region $[-3, 3] \times [-7/2, 2]$ at an uniform grid of 280×200 points. Note that, as it follows from consideration of the figure captions, in the $\kappa = 32$ case the WGF near field evaluation procedure is up to 1200 times faster than the corresponding LGF near field evaluation procedure—in spite of the fact that a (larger) window size $A = 16\lambda$ had to be used to produce accurate near fields throughout the plotted region.

Our next example considers a dielectric structure consisting of nested circular surface defects in a 9-layer medium given by $\Pi_j = \mathbb{R} \times \{(j-1)/5\}$, $j = 1, \ldots, 8$. The corresponding wavenumbers are $k_{2j-1} = 15$ for $j = 1, \ldots, 5$ and $k_{2j} = 30$ for $j = 1, \ldots 4$. The structure is illuminated by a plane-wave at normal incidence. The total field solution of the problem of scattering is obtained by solving the integral equation system (5.33) with $A = 12\lambda$. Formulae (5.37) are utilized to evaluate the near field. The real part and the absolute value of the total field are displayed in Figures 5.9a and 5.9b, respectively. A 97 seconds overall computing time sufficed to compute the solution and produce the near field presented in Figure 5.9. Note that, interestingly, a propagative mode that travels within the fourth layer

is excited by the plane-wave incidence considered.

In the last example of this chapter we consider a 18-layer dielectric structure consisting of smooth surface defects in a planar-layered medium given by $\Pi_j = \mathbb{R} \times \{(j-1)/4\}$, $j = 1, \ldots, 17$. The wavenumbers in this example are given by $k_{2j-1} = 15$ and $k_{2j} = 30$, $j = 1, \ldots, 9$. The dielectric structure is illuminated by a plane-wave at normal incidence. The total field is approximated by solving the integral equation system (5.42) with $A = 12\lambda$. The expression (5.44) is utilized to evaluate the near field. The real part and the absolute value of the total field are displayed in Figures 5.10a and 5.10b, respectively. The overall computing time required to produce the solution displayed in the Figure 5.10 was 241 seconds.

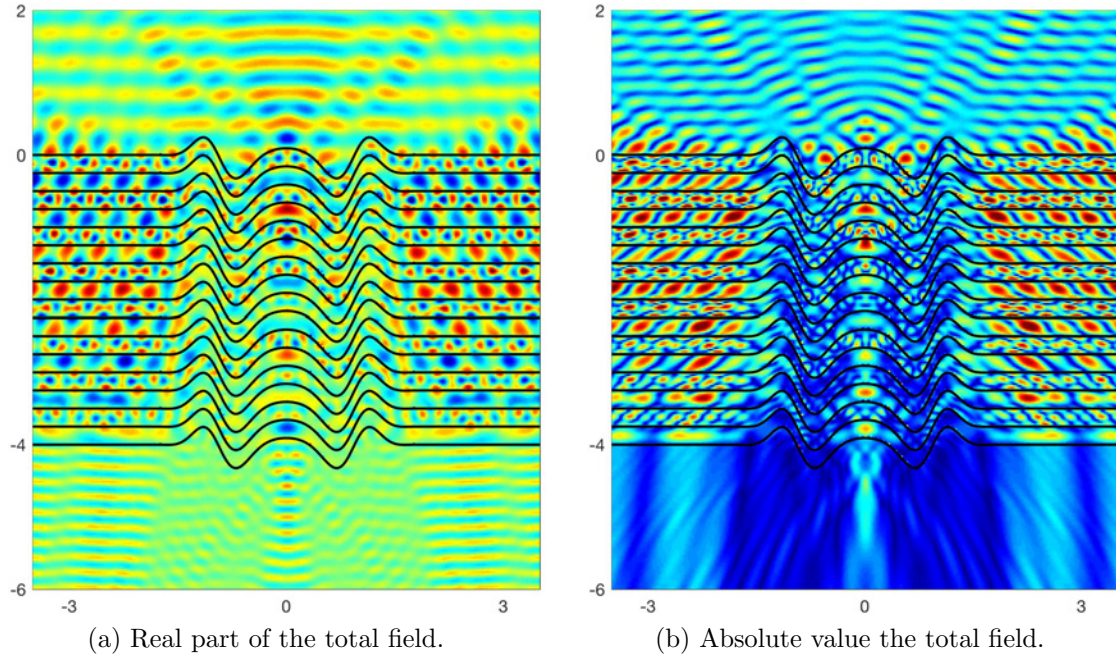(a) Real part of the total field. (b) Absolute value the total field.
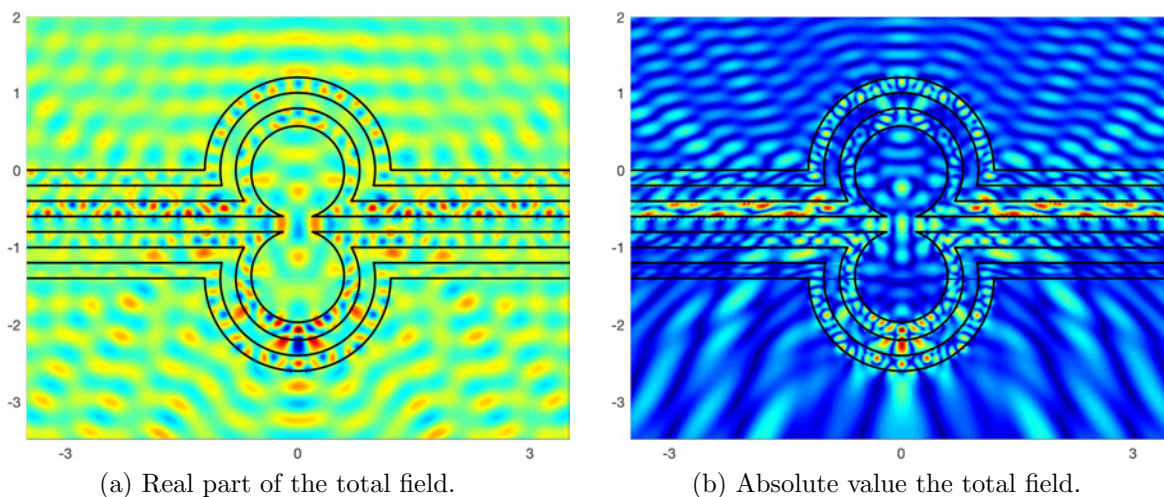
Figure 5.9: Real part (a) and absolute value (b) of the total field solution of the problem of scattering of a plane electromagnetic wave impinging on a layered medium composed of 9 layers: $k_{2j-1} = 15$, $j = 1, \ldots, 5$ and $k_{2j} = 30$, $j = 1, \ldots, 4$ and $\Pi_j = \mathbb{R} \times \{(j-1)/5\}$, $j = 1, \ldots, 8$.

(a) Real part of the total field. (b) Absolute value the total field.

Figure 5.10: Real part (a) and absolute value (b) of the total field solution of the problem of scattering of a plane electromagnetic wave impinging on a layered medium composed of 18 layers: $k_{2j-1} = 15$ and $k_{2j} = 30$, $j = 1, \ldots, 9$ and $\Pi_j = \mathbb{R} \times \{(j-1)/4\}$, $j = 1, \ldots, 17$.

Chapter 6

Windowed Green Function Method for layered media scattering: Three dimensional case

This chapter extends the WGF method introduced in Chapters 4 and 5 to problems of acoustic and electromagnetic scattering in three spatial dimensions. Integral field representations and equations are presented for both acoustic and electromagnetic scattering problems. The main features of the WGF approach are demonstrated through numerical examples for problems of acoustic scattering. Once again, errors are evaluated as indicated in the second paragraph of Section 5.7. In particular, the accuracy and performance of the proposed WGF method are established in Section 6.1.4 by means of convergence studies as well as comparisons with solutions produced by means of the LGF method introduced in Section 2.4 for problems of scattering by sound-hard obstacles in two-layer media.

This chapter is structured as follows: Section 6.1 presents the WGF method for acoustic three-dimensional scattering problems in the presence of two-layer media, including problems of scattering by smooth defects and obstacles, and Section 6.2 extends these methods to the electromagnetic case.

6.1 Acoustics scattering

This section extends the WGF method to acoustic three-dimensional scattering problems by obstacles and surface defects in the presence of layered media. Such problems play important

roles in a variety of contexts—in underwater ocean acoustics, for example, where the ocean acoustic environment is often modeled as a layered medium; cf. [33, 65].

The problems of three-dimensional acoustic scattering bear many similarities with the two-dimensional problems of electromagnetic scattering (or, equivalently, two-dimensional acoustic scattering) considered in Chapters 3, 4 and 5. As a matter of fact, most of the results presented in those chapters can be directly extended to three-dimensional acoustic problems. For variety, this section presents examples incuding different types of configurations—such as scattering problems involving two-layer waveguides and sound-hard bounded obstacles.

Throughout this section the fluid pressure in a layered acoustic medium is denoted by u. The pressure field satisfies Helmholtz equation $\Delta u + k^2 u = 0$ with wavenumber $k = \omega/c$ where, as usual, $\omega > 0$ denotes the angular frequency, and where $c > 0$ denotes the speed of sound of the fluid layer. The Dirichlet boundary condition $u = 0$ is satisfied at sound-soft surfaces such as, for example, the interface between a liquid and a gas; while the Neumann boundary condition $\partial u/\partial n = 0$ is satisfied at sound-hard surfaces such as, for example, the interface between a liquid and a solid. Transmission conditions, on the other hand, which correspond to the continuity of the pressure field u and continuity of the normal velocity $\varrho^{-1}\partial u/\partial n$ (where ϱ denotes the fluid density) are satisfied at the interface between two different fluids; cf. [72].

6.1.1   Surface defect in a two-layer medium

We first consider the problem of scattering of a plane acoustic wave $u^{\mathrm{inc}}(\boldsymbol{r}) = \mathrm{e}^{ik_{1x}x - ik_{1y}y}$, where $k_{1x} = k_1 \cos\alpha$ and $k_{1y} = \sqrt{k_1^2 - k_{1x}^2} = -k_1 \sin\alpha$, with incidence angle $\alpha = (-\pi, 0)$, by a smooth localized surface defect at the interface Π_1 between the half-spaces $D_1 = \{y > 0\}$ and $D_2 = \{y < 0\}$. The resulting layered medium is composed by the unbounded domains Ω_1 and Ω_2 whose common interface is denoted by Γ_1, which is assumed of class $\mathcal{C}^\infty$.

The total acoustic field u—which satisfies the Helmholtz equation $\Delta u + k_j^2 u = 0$ in Ω_j, $j = 1, 2$, and the transmission conditions $u|_{1^+} = u|_{1^-}$ and $\partial u/\partial n|_{1^+} = \nu \partial u/\partial n|_{1^-}$ on Γ_1,

where ν equals ϱ_1/ϱ_2—is expressed as

$$u = u^s + \widetilde{u}^f \quad \text{in} \quad \Omega_1 \cup \Omega_2, \tag{6.1}$$

where, letting: $k_{2x} = k_{1x}$ and $k_{2y} = \sqrt{k_2^2 - k_{2x}^2}$ if $k_2 > k_{2x}$ and $k_{2y} = i\sqrt{k_{2x}^2 - k_2^2}$ if $k_2 < k_{2x}$, the field $\widetilde{u}^f$ is given by

$$\widetilde{u}^f(\boldsymbol{r}) = \begin{cases} e^{ik_{1x}x - ik_{1y}y} + R_{12}\, e^{ik_{1x}x + ik_{1y}y} & \text{in} \quad \Omega_1, \\ T_{12}\, e^{ik_{2x}x - ik_{2y}y} & \text{in} \quad \Omega_2, \end{cases} \tag{6.2}$$

in terms of the reflection and transmission coefficients

$$R_{12} = \frac{k_{1y} - \nu k_{2y}}{k_{1y} + \nu k_{2y}} \quad \text{and} \quad T_{12} = \frac{2k_{1y}}{k_{1y} + \nu k_{2y}},$$

respectively. In view of the derivations presented in Section 2.2.2, it is clear that $\widetilde{u}^f$ coincides with the total field solution of the problem of scattering of a plane wave u^{inc} by the planar two-layer medium composed by the half-spaces D_1 and D_2, in the regions $D_1 \cap \Omega_2$ and $D_2 \cap \Omega_1$. In particular, $\widetilde{u}^f$ satisfies the Helmholtz equation with wavenumber k_j in Ω_j and, furthermore, it satisfies the transmission conditions $\widetilde{u}^f|_{1+} = \widetilde{u}^f|_{1-}$ and $\partial\widetilde{u}^f/\partial n|_{1+} = \nu \partial\widetilde{u}^f/\partial n|_{1-}$ at the planar portions of the interface Γ_1: $\Gamma_1 \cap \Pi_1$.

We thus obtain that $u^s = u - \widetilde{u}^f$, which we refer to as the scattered field, satisfies:

$$\begin{cases} \Delta u^s + k_j^2 u^s = 0 & \text{in} \quad \Omega_j,\ j = 1, 2, \\ u^s\big|_{1+} = u^s\big|_{1-} + f & \text{on} \quad \Gamma_1, \\ \dfrac{\partial u^s}{\partial n}\bigg|_{1+} = \nu\dfrac{\partial u^s}{\partial y}\bigg|_{1-} + g & \text{on} \quad \Gamma_1, \\ \displaystyle\lim_{|r|\to\infty} |\boldsymbol{r}|\left\{\dfrac{\partial u^s}{\partial|\boldsymbol{r}|} - ik_j u^s\right\} = 0 & \text{in} \quad \Omega_j,\ j = 1, 2, \end{cases} \tag{6.3}$$

where the functions f and g are given by

$$f = \widetilde{u}^f\big|_{1+} - \widetilde{u}^f\big|_{1-} \quad \text{and} \quad g = \frac{\partial\widetilde{u}^f}{\partial n}\bigg|_{1+} - \nu\frac{\partial\widetilde{u}^f}{\partial n}\bigg|_{1-}. \tag{6.4}$$

Note that $f, g \in C_0^\infty(\Gamma_1)$ are supported on the (bounded) surface defect $\Gamma_1 \setminus \Pi_1$.

From the results put forth in the contribution [53], which concern the integral representation of scalar fields scattered from two-dimensional unbounded rough surfaces, we obtain that u^s admits the integral representations:

$$
\mathcal{D}_1\left[\varphi^s - f\right](\boldsymbol{r}) - \mathcal{S}_1\left[\nu\psi^s - g\right](\boldsymbol{r}) = \begin{cases} u^s(\boldsymbol{r}), & \boldsymbol{r} \in \Omega_1, \\ 0, & \boldsymbol{r} \in \mathbb{R}^3 \setminus \overline{\Omega_1}, \end{cases} \tag{6.5a}
$$

$$
-\mathcal{D}_2\left[\varphi^s\right](\boldsymbol{r}) + \mathcal{S}_2\left[\psi^s\right](\boldsymbol{r}) = \begin{cases} u^s(\boldsymbol{r}), & \boldsymbol{r} \in \Omega_2, \\ 0, & \boldsymbol{r} \in \mathbb{R}^3 \setminus \overline{\Omega_2}, \end{cases} \tag{6.5b}
$$

where $\varphi^s = u^s|_{1-}$ and $\psi^s = \partial u^s/\partial n|_{1-}$. The layer potentials in (6.5) are defined by the two-dimensional (conditionally convergent) integrals

$$
\mathcal{S}_j[\phi](\boldsymbol{r}) = \int_{\Gamma_1} G_{k_j}(\boldsymbol{r}, \boldsymbol{r}')\phi(\boldsymbol{r}')\,\mathrm{d}s_{\boldsymbol{r}'} \quad \text{and} \quad \mathcal{D}_j[\phi](\boldsymbol{r}) = \int_{\Gamma_1} \frac{\partial G_{k_j}}{\partial n_{\boldsymbol{r}'}}(\boldsymbol{r}, \boldsymbol{r}')\phi(\boldsymbol{r}')\,\mathrm{d}s_{\boldsymbol{r}'}, \tag{6.6}
$$

in terms of the three-dimensional free-space Green function:

$$
G_{k_j}(\boldsymbol{r}, \boldsymbol{r}') = \frac{\mathrm{e}^{ik_j|\boldsymbol{r} - \boldsymbol{r}'|}}{4\pi|\boldsymbol{r} - \boldsymbol{r}'|}. \tag{6.7}
$$

In view of the discussion presented by DeSanto and Martin in [53], no additional terms involving plane- or cylindrical-waves arise in the expressions (6.5), as the scattered field u^s satisfies the Sommerfeld radiation condition, and both surface densities f and g are compactly supported functions.

Hence, following the procedure described in Section 5.6, which entails combining the expressions that result from evaluating (6.5) and their normal derivatives on Γ_1 and using the jump relations:

$$
\mathcal{S}_j[\phi]|_{1\pm} = S_j[\phi], \qquad \frac{\partial}{\partial n}\mathcal{S}_j[\phi]\bigg|_{1\pm} = \mp\frac{\phi}{2} + K_j[\phi],
$$

$$
\frac{\partial}{\partial n}\mathcal{D}_j[\phi]\bigg|_{1\pm} = N_j[\phi], \qquad \mathcal{D}_j[\phi]|_{1\pm} = \pm\frac{\phi}{2} + D_j[\phi], \tag{6.8}
$$

where

$$S_j[\phi](\boldsymbol{r}) = \int_{\Gamma_1} G_{k_j}(\boldsymbol{r}, \boldsymbol{r}')\phi(\boldsymbol{r}')\,\mathrm{d}s_{\boldsymbol{r}'}, \qquad D_j[\phi](\boldsymbol{r}) = \int_{\Gamma_1} \frac{\partial G_{k_j}}{\partial n_{\boldsymbol{r}'}}(\boldsymbol{r}, \boldsymbol{r}')\phi(\boldsymbol{r}')\,\mathrm{d}s_{\boldsymbol{r}'},$$

$$K_j[\phi](\boldsymbol{r}) = \int_{\Gamma_1} \frac{\partial G_{k_j}}{\partial n_{\boldsymbol{r}}}(\boldsymbol{r}, \boldsymbol{r}')\phi(\boldsymbol{r}')\,\mathrm{d}s_{\boldsymbol{r}'}, \quad N_j[\phi](\boldsymbol{r}) = \frac{\partial}{\partial n_{\boldsymbol{r}}}\int_{\Gamma_1} \frac{\partial G_{k_j}}{\partial n_{\boldsymbol{r}'}}(\boldsymbol{r}, \boldsymbol{r}')\phi(\boldsymbol{r}')\,\mathrm{d}s_{\boldsymbol{r}'},$$

$$(6.9)$$

for $\boldsymbol{r} \in \Gamma_1$ and for $j = 1, 2$, we arrive at the integral equation system

$$\mathrm{E}\,\boldsymbol{\phi}^s + \mathrm{T}\,[\boldsymbol{\phi}^s] = -\,\mathrm{M}\,[\boldsymbol{\psi}] \quad \text{on} \quad \Gamma_1, \tag{6.10}$$

where

$$\boldsymbol{\phi}^s = \begin{bmatrix} \varphi^s \\ \psi^s \end{bmatrix}, \quad \boldsymbol{\psi} = \begin{bmatrix} f \\ g \end{bmatrix}, \quad \mathrm{E} = \begin{bmatrix} 1 & 0 \\ 0 & \frac{1+\nu}{2} \end{bmatrix},$$

$$\mathrm{M} = \frac{1}{2}\mathrm{I}_d + \begin{bmatrix} D_1 & -S_1 \\ N_1 & -K_1 \end{bmatrix} \quad \text{and} \quad \mathrm{T} = \begin{bmatrix} D_2 - D_1 & -S_2 + \nu S_1 \\ N_2 - N_1 & -K_2 + \nu K_1 \end{bmatrix}.$$

Letting $W_A = \mathrm{w}_A I$, where I is the 2×2 identity matrix and

$$\mathrm{w}_A(x, z) = w_A(x)w_A(z) = \eta\left(\frac{x}{A}; c, 1\right)\eta\left(\frac{z}{A}; c, 1\right), \tag{6.11}$$

with η denoting the window function defined in (2.78), the resulting windowed integral equation system is then given by

$$\mathrm{E}\,\boldsymbol{\phi}^{sw} + \mathrm{T}\,[W_A\boldsymbol{\phi}^{sw}] = -\,\mathrm{M}\,[\boldsymbol{\psi}] \quad \text{on} \quad \Gamma_{1A}. \tag{6.12}$$

As in the two-dimensional case presented in Chapter 4, the window size $A > 0$ is selected in such a way that the truncated interface $\Gamma_{1A} = \Gamma_1 \cap \{\mathrm{w}_A \neq 0\}$ contains the surface defect $\Gamma_1 \setminus \Pi_1$.

Results on the existence and uniqueness of solutions for the integral equation (6.12) can be obtained, at least for smooth surfaces Γ_{1A}, in view of the fact that the integral operators $D_2 - D_1$, $S_2 - \nu S_1$, $N_2 - N_1$ and $K_2 - \nu K_1$ are given in terms of weakly singular (integrable) kernels (cf. Appendix D).

Letting then $\boldsymbol{\phi}^{sw} = [\varphi^{sw}, \psi^{sw}]^T$ denote the solution (6.12) and following the substitutions: φ^s by $\mathrm{w}_A \varphi^{sw}$ and ψ^s by $\mathrm{w}_A \psi^{sw}$ in the representation formula (6.6), we obtain the following expression for the total near-field:

$$u^w = \widetilde{u}^f + \begin{cases} \mathcal{D}_1 \left[\mathrm{w}_A \varphi^{sw} - f\right] - \nu \mathcal{S}_1 \left[\mathrm{w}_A \psi^{ws} - g\right] & \text{in} \quad \Omega_1, \\[2ex] -\mathcal{D}_2 \left[\mathrm{w}_A \varphi^{sw}\right] + \mathcal{S}_2 \left[\mathrm{w}_A \psi^{sw}\right] & \text{in} \quad \Omega_2, \end{cases} \tag{6.13}$$

where the function $\widetilde{u}^f$ is defined in (6.2).

6.1.2 Two-layer waveguide

In this section we consider the open waveguide structure composed by the acoustic media $D_1 = \{y > 0\}$ and $D_2 = \{-d_2 < y < 0\}$, with wavenumbers $k_1 > 0$ and $k_2 > 0$, respectively, and the half-space $D_3 = \{y < -d_2\}$ which is assumed such that either sound-hard (Neumann) or sound-soft (Dirichlet) boundary conditions are satisfied at the planar boundary $\Pi_2 = \{y = -d_2\}$. For the sake of presentation simplicity we only consider the sound-hard boundary condition (the case of the sound-soft boundary condition is completely analogous). Structures of this kind receive various names in the literature, including two-layer waveguide, Pekeris waveguide, and acoustic substrate.

As is well-known, the finite thickness layer D_2 can support modes that propagate along any horizontal direction such as e.g., the direction of the x-axis. These modes u_m are obtained by solving the Helmholtz equation by the method of separation of variables and enforcing the conditions $\partial u_m / \partial n = 0$ at Π_2, boundedness as $y \to +\infty$ and continuity across Π_1; the result is

$$u_m(x, y) = e^{i\xi_m x} \begin{cases} e^{-\sqrt{\xi_m^2 - k_1^2}\, y} & \text{in} \quad D_1, \\[2ex] \dfrac{\cos\left(\sqrt{k_2^2 - \xi_m^2}(x + d_2)\right)}{\cos\left(\sqrt{k_2^2 - \xi_m^2}\, d_2\right)} & \text{in} \quad D_2. \end{cases} \tag{6.14}$$

Enforcing the condition $\partial u_m / \partial n|_{\Pi_1^+} = \nu \partial u_m / \partial n|_{\Pi_1^-}$ at $\Pi_1 = \{y = 0\}$ we thus obtain the

following algebraic equation for the constants ξ_m:

$$\sqrt{\xi_m^2 - k_1^2} = \nu \sqrt{k_2^2 - \xi_m^2} \tan\left(\sqrt{k_2^2 - \xi_m^2} d_2\right). \tag{6.15}$$

Solutions $\xi_m > 0$ of (6.15) satisfying the condition $k_1 \leq \xi_m \leq k_2$ are known as propagation constants and the associated solutions u_m are known as propagation modes.

We thus consider the problem of scattering of a propagation mode u_m by a surface defect at the planar interface Π_1. In order to formulate the corresponding integral equation we express the total field u in the form $u = u^s + \widetilde{u}^f$ where $\widetilde{u}^f$ is now given by

$$\widetilde{u}^f(x, y) = e^{i\xi_m x} \begin{cases} e^{-\sqrt{\xi_m^2 - k_1^2} y} & \text{in} \quad \Omega_1, \\[2ex] \dfrac{\cos\left(\sqrt{k_2^2 - \xi_m^2}(x + d_2)\right)}{\cos\left(\sqrt{k_2^2 - \xi_m^2} d_2\right)} & \text{in} \quad \Omega_2. \end{cases} \tag{6.16}$$

Utilizing the results put forth in [53] once again, it can be shown u^s admits the representation (6.6) in terms of the functions f and g in (6.4) (with $\widetilde{u}^f$ defined in (6.16)) and the layer potentials $\mathcal{D}_2$ and $\mathcal{S}_2$ in (6.5b) which are defined by the expression that is obtained as the Green function

$$\widetilde{G}_{k_2}(\boldsymbol{r}, \boldsymbol{r}') = G_{k_2}(\boldsymbol{r}, \boldsymbol{r}') + G_{k_2}(\boldsymbol{r}, \overline{\boldsymbol{r}}'), \quad \overline{\boldsymbol{r}}' = (x', -y' - 2d_2, z'),$$

is used instead of the free-space Green function in equation (6.6). Thus, the unknown field values $u^s|_{1^-} = \varphi^s$ and $\partial u^s / \partial n|_{1^-} = \psi^s$ at the interface Γ_1 can be approximated by solving the WGF integral equation system (6.12), and the near-field can be evaluated utilizing the expressions in (6.13).

6.1.3 Sound-hard obstacle in a two-layer medium

We now consider the problem of scattering of a plane acoustic wave by a sound-hard obstacle in a two-layer medium. The obstacle, which is denoted by D, is assumed to be completely

embedded in one of the layers. The total field thus satisfies

$$\frac{\partial u}{\partial n} = \frac{\partial u^s}{\partial n} + \frac{\partial \widetilde{u}^f}{\partial n} = 0 \quad \text{on} \quad \partial D = S.$$

In this case the integral representation formula for the scattered field $u^s = u - \widetilde{u}^f$ (with $\widetilde{u}^f$ defined in (6.2)) in the exterior of the obstacle $\mathbb{R}^3 \setminus \overline{D}$, is given by

$$\mathcal{D}_1 \left[\varphi^s - f\right](\boldsymbol{r}) - \mathcal{S}_1 \left[\nu \psi^s - g\right](\boldsymbol{r}) + \mathcal{D}_1^S \left[\mu\right](\boldsymbol{r}) - \mathcal{S}_1^S \left[\sigma\right](\boldsymbol{r}) = \begin{cases} u^s(\boldsymbol{r}), & \boldsymbol{r} \in \Omega_1 \setminus \overline{D}, \\ 0, & \boldsymbol{r} \in \mathbb{R}^3 \setminus \overline{\Omega_1}, \end{cases} \tag{6.17a}$$

$$-\mathcal{D}_2 \left[\varphi^s\right](\boldsymbol{r}) + \mathcal{S}_2 \left[\psi^s\right](\boldsymbol{r}) = \begin{cases} u^s(\boldsymbol{r}), & \boldsymbol{r} \in \Omega_2, \\ 0, & \boldsymbol{r} \in \mathbb{R}^3 \setminus \overline{\Omega_2}, \end{cases} \tag{6.17b}$$

if $D \subset \Omega_1$, and

$$\mathcal{D}_1 \left[\varphi^s - f\right](\boldsymbol{r}) - \mathcal{S}_1 \left[\nu \psi^s - g\right](\boldsymbol{r}) = \begin{cases} u^s(\boldsymbol{r}), & \boldsymbol{r} \in \Omega_1, \\ 0, & \boldsymbol{r} \in \mathbb{R}^3 \setminus \overline{\Omega_1}, \end{cases} \tag{6.18a}$$

$$-\mathcal{D}_2 \left[\varphi^s\right](\boldsymbol{r}) + \mathcal{S}_2 \left[\psi^s\right](\boldsymbol{r}) + \mathcal{D}_2^S \left[\mu\right](\boldsymbol{r}) - \mathcal{S}_2^S \left[\sigma\right](\boldsymbol{r}) = \begin{cases} u^s(\boldsymbol{r}), & \boldsymbol{r} \in \Omega_2 \setminus \overline{D}, \\ 0, & \boldsymbol{r} \in \mathbb{R}^3 \setminus \overline{\Omega_2}, \end{cases} \tag{6.18b}$$

if $D \subset \Omega_2$, where $u^s|_S = \mu$ and $\partial u^s / \partial n \big|_S = -\partial \widetilde{u}^f / \partial n \big|_S = \sigma$. The layer potentials $\mathcal{D}_j^S$ and $\mathcal{S}_j^S$ are defined by the expression that is obtained as the surface of the bounded obstacle S is used instead of the interface Γ_1 in equation (6.6).

Letting

$$R_j^S[\mu] = - \begin{bmatrix} \mathcal{D}_j^S[\mu]\big|_\Gamma \\ \frac{\partial}{\partial n} \mathcal{D}_j^S[\mu]\big|_\Gamma \end{bmatrix} \quad \text{and} \quad R_j^\Gamma \begin{bmatrix} \varphi \\ \psi \end{bmatrix} = \{\mathcal{D}_j[\varphi] - \mathcal{S}_j[\psi]\}\big|_S,$$

for $j = 1, 2$, the resulting WGF integral equation system (for the unknown densities φ^{sw} and

ψ^{sw} defined on Γ_{1A}, and the density μ^w defined on the surface of the obstacle S) is given by

$$
\begin{cases}
\mathrm{E}\,\boldsymbol{\phi}^{sw} + \mathrm{T}\left[W_A\boldsymbol{\phi}^{sw}\right] + \mathrm{R}_1^{\Gamma}[\mu^w] = -\,\mathrm{M}\begin{bmatrix} f \\ g \end{bmatrix} - \begin{bmatrix} \left.\mathcal{S}_1^S[\sigma]\right|_{\Gamma} \\ \dfrac{\partial}{\partial n}\mathcal{S}_1^S[\sigma]\Big|_{\Gamma} \end{bmatrix} & \text{on} \quad \Gamma_{1A}, \\[4mm]
\dfrac{\mu^w}{2} + D_1^S[\mu^w] + R_1^S\begin{bmatrix} \mathrm{w}_A\varphi^{sw} \\ \nu\mathrm{w}_A\psi^{sw} \end{bmatrix} = S_1^S[\sigma] + \left\{\mathcal{D}_1[f] - \mathcal{S}_1[g]\right\}\big|_S & \text{on} \quad S,
\end{cases}
$$

$$\tag{6.19a}$$

if $D \subset \Omega_1$, and it is given by

$$
\begin{cases}
\mathrm{E}\,\boldsymbol{\phi}^{sw} + \mathrm{T}\left[W_A\boldsymbol{\phi}^{sw}\right] + \mathrm{R}_2^S[\mu^w] = -\,\mathrm{M}\begin{bmatrix} f \\ g \end{bmatrix} - \begin{bmatrix} \left.\mathcal{S}_2^S[\sigma]\right|_{\Gamma} \\ \dfrac{\partial}{\partial n}\mathcal{S}_2^S[\sigma]\Big|_{\Gamma} \end{bmatrix} & \text{on} \quad \Gamma_{1A}, \\[4mm]
\dfrac{\mu^w}{2} + D_2^S[\mu^w] - R_2^{\Gamma}\begin{bmatrix} \mathrm{w}_A\varphi^{sw} \\ \mathrm{w}_A\psi^{sw} \end{bmatrix} = S_2^S[\sigma] & \text{on} \quad S,
\end{cases}
$$

$$\tag{6.19b}$$

if $D \subset \Omega_2$, where the integral operators S_j^S and D_j^S are defined as in (6.9) but in terms of integrals over S instead of Γ_1.

The total near-field can then be approximated by means of the expressions

$$
u^w = \widetilde{u}^f + \begin{cases}
\mathcal{D}_1\left[\mathrm{w}_A\varphi^{sw} - f\right] - \nu\mathcal{S}_1\left[\mathrm{w}_A\psi^{ws} - g\right] + \mathcal{D}_1^S[\mu^w](\boldsymbol{r}) - \mathcal{S}_1^S[\sigma](\boldsymbol{r}) & \text{in} \quad \Omega_1\setminus\overline{D}, \\[3mm]
-\mathcal{D}_2\left[\mathrm{w}_A\varphi^{sw}\right] + \mathcal{S}_2\left[\mathrm{w}_A\psi^{sw}\right] & \text{in} \quad \Omega_2,
\end{cases}
$$

$$\tag{6.20}$$

if $D \subset \Omega_1$, and

$$
u^w = \widetilde{u}^f + \begin{cases}
\mathcal{D}_1\left[\mathrm{w}_A\varphi^{sw} - f\right] - \nu\mathcal{S}_1\left[\mathrm{w}_A\psi^{ws} - g\right] & \text{in} \quad \Omega_1, \\[3mm]
-\mathcal{D}_2\left[\mathrm{w}_A\varphi^{sw}\right] + \mathcal{S}_2\left[\mathrm{w}_A\psi^{sw}\right] + \mathcal{D}_2^S[\mu^w](\boldsymbol{r}) - \mathcal{S}_2^S[\sigma](\boldsymbol{r}) & \text{in} \quad \Omega_2\setminus\overline{D},
\end{cases}
$$

$$\tag{6.21}$$

if $D \subset \Omega_2$.

For problems of scattering by obstacles in a planar layered medium without surface defects ($\Gamma_1 = \Pi_1$) the far-field pattern of the scattered field u^s can be directly evaluated from the

field values at the surface of the obstacle. In fact, following the derivation in Lemma 4.2.6 but utilizing the two-layer Green function in three-dimensions (2.40), it can be shown that the scattered field is given by the expression

$$u^s(\boldsymbol{r}) = \int_S \left\{ \frac{\partial G}{\partial n_{\boldsymbol{r'}}}(\boldsymbol{r}, \boldsymbol{r'})\mu(\boldsymbol{r'}) + G(\boldsymbol{r}, \boldsymbol{r'})\sigma(\boldsymbol{r'}) \right\} \, \mathrm{d}s_{\boldsymbol{r'}}, \quad \boldsymbol{r} \in \mathbb{R}^3 \setminus \overline{D}.$$

Thus, using the far-field pattern of the layer Green function (2.73) and its gradient (2.74) we obtain

$$u_\infty(\hat{\boldsymbol{r}}) = \int_S \left\{ n(\boldsymbol{r'}) \cdot \boldsymbol{H}_\infty(\hat{\boldsymbol{r}}, \boldsymbol{r'})\mu(\boldsymbol{r'}) + G_\infty(\hat{\boldsymbol{r}}, \boldsymbol{r'})\sigma(\boldsymbol{r'}) \right\} \, \mathrm{d}s_{\boldsymbol{r'}}. \tag{6.22}$$

6.1.4 Numerical examples

This section presents numerical examples concerning the acoustic problems described above in this section. The relevant systems of integral equations are discretized by means of (an unaccelerated version of) the high-order Nyström method put forth in the contributions [27, 29] which has been coded in Fortran 90. The material interfaces present in these examples are assumed to be infinitely smooth. For the sake of definiteness in all the examples considered throughout this section, the value $c = 0.7$ is utilized for the evaluation of the window function (4.9) w_A. The resulting linear systems of equations are solved iteratively by means of the GMRES algorithm. For simplicity, no acceleration of any kind has been utilized to perform the matrix-vector products, so that a cost of $\mathcal{O}(N^2)$ operations, where N is the number of unknowns, is required for each GMRES iteration. Much better computational times would be obtained, of course, should an accelerated iterative or non-iterative linear algebra solvers were used; cf. [13, 17, 29, 59].

Our first example deals with the problem of scattering of the plane-wave $u^{\mathrm{inc}}(\boldsymbol{r}) = e^{ik_1(x\cos\alpha + y\sin\alpha)}$, with $\alpha = -\pi/4$, by a sound-hard sphere (of radius 1 and centered at $(0, 3, 0)$) above a flat penetrable acoustic half-space. The wavenumbers are $k_1 = 5$ and $k_2 = 10$ in the upper and lower half-spaces $D_1 = \{y > 0\}$ and $D_2 = \{y < 0\}$ respectively (see Figure 6.1c). The scattering solution is obtained by means of the integral equation (6.20) for various window sizes $A > 0$. Figures 6.1a and 6.1b display the resulting maximum field
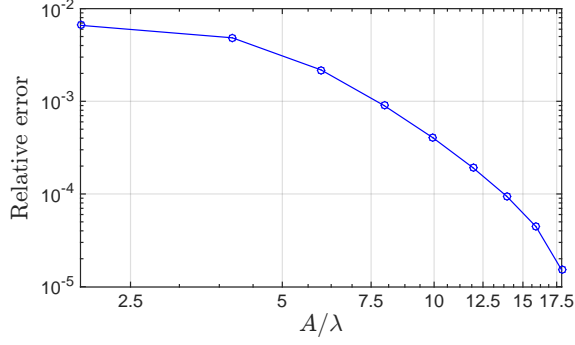
(a) Relative maximum error on the obstacle in log-log scale.
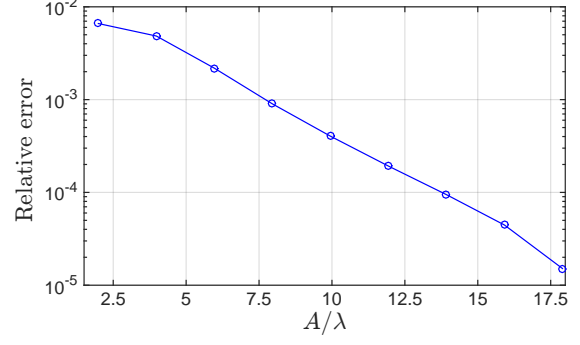
(b) Relative maximum error on the obstacle in semi-log scale.
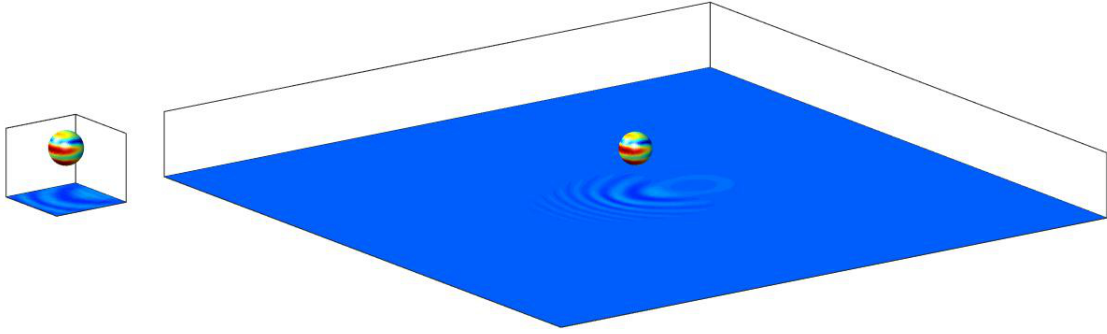
(c) Absolute value of the total field for the smallest (left) and largest (right) windowed regions considered. The section of the planar interface shown in each case coincides with the region in the plane where the corresponding windowing function w_A does not vanish.

Figure 6.1: Convergence of the WGF method applied to a problem of scattering of a spherical sound-hard obstacle in a two-layer medium of wavenumbers $k_1 = 5$ and $k_2 = 10$, at an incidence of $\alpha = -\pi/4$ with respect to the planar interface.

errors on the surface of the sphere in log-log and semi-log scales, respectively. The reference solution used for error estimation is the WGF solution obtained with $A = 25 \approx 19.9\lambda$. The number of quadrature points is selected in such a way that for any given $A > 0$ the Nyström discretization error in the integral equation solution is not larger than 10^{-6}. The GMRES tolerance utilized in this example was set at 10^{-6}. Clearly, super-algebraic convergence is observed as the window size $A > 0$ increases. Figure 6.1c, on the other hand, displays the absolute value of the total fields $\varphi^{sw} + \widetilde{u}^f$ on Γ_{1A} and $\mu^w + \widetilde{u}^f$ on S for $A = 2.5$ (left) and $A = 25$ (right)—where, remarkably, the WGF field is produced with an accuracy better than 10^{-2} for the small window size displayed in left image in Figure 6.1c $A/\lambda = 1.99$.

(a) Far-field pattern $u_\infty(\hat{r})$ in absolute value.

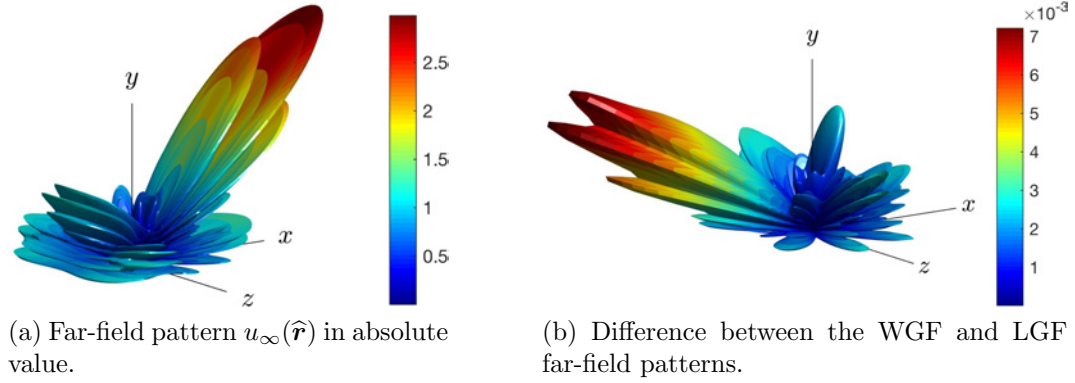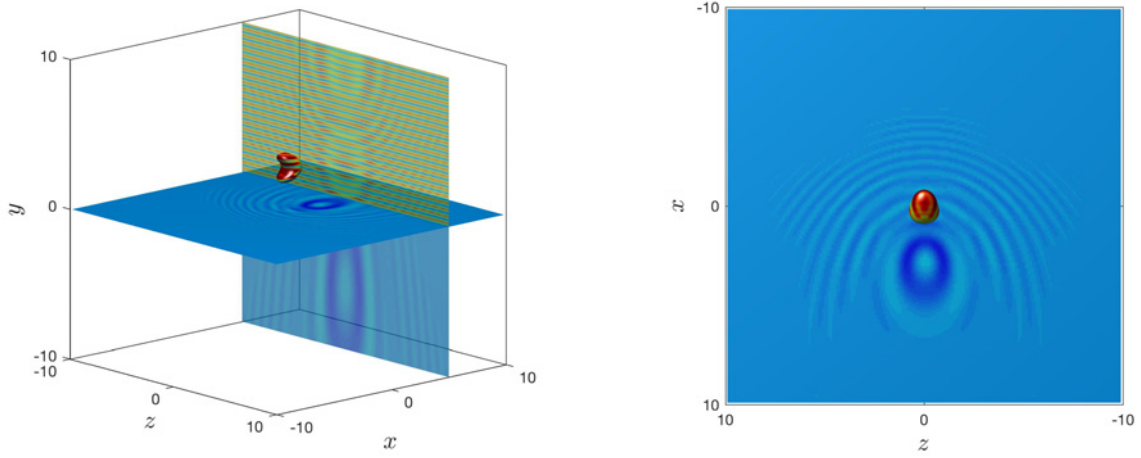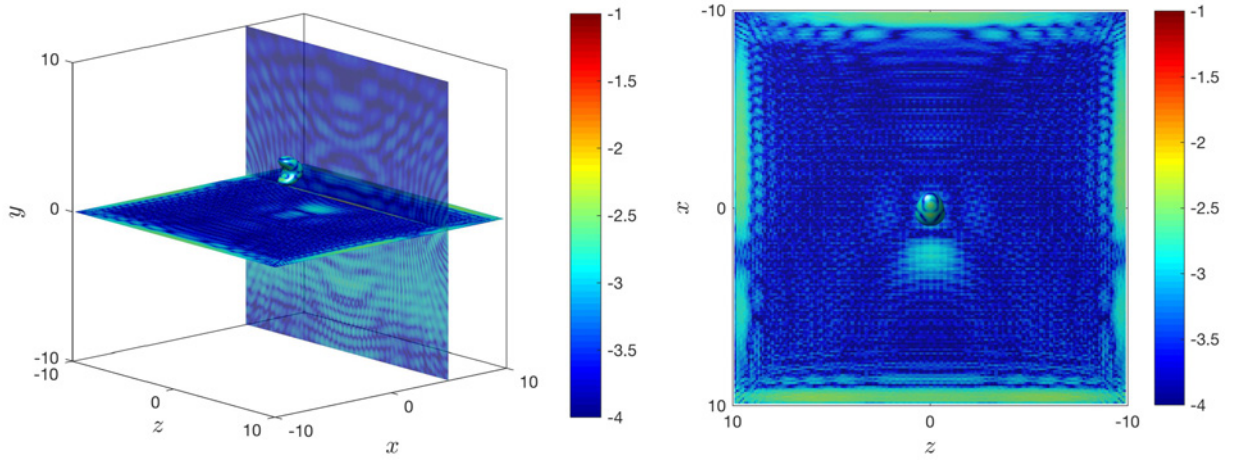(b) Difference between the WGF and LGF far-field patterns.

Figure 6.2: Far-field pattern obtained by means of the WGF and LGF methods for the solution of the problem of scattering of a sound-hard bean-like obstacle in a two-layer medium with wavenumbers $k_1 = 10$ and $k_2 = 20$. Only the WGF pattern is displayed in (a); the LGF pattern appears identical.

In our second example we consider the problem of scattering by a sound-hard bean-like (see Figure 2.10) scatterer centered at $(0, 3, 0)$ in the two-layer medium of the example above with wavenumbers $k_1 = 10$ and $k_2 = 20$ under plane-wave illumination with $\alpha = -\pi/4$. The resulting problem of scattering is solved by means of the WGF method, using the integral equation (6.20) and the formulae (6.20) for the near-field evaluation; and by means of the LGF method described in Section 2.4.

The layer Green function (2.40) used for the LGF method is approximated with a relative error of at most 10^{-4} by means of the algorithm presented in Section 2.3.5. In the present example the obstacle is located relatively far from the interface Π_1, which implies that the integrands in the corresponding Sommerfeld integrals (2.41b) decay exponentially. Consequently, the needed Sommerfeld integrals are easier to evaluate than those arising in problems of scattering by surface defects, such as the ones considered in Chapters 3, 4 and 5. The exact same Nyström quadrature points are utilized by both WGF and LGF methods to discretize the surface of the bean obstacle, which is parametrized using two overlapping patches containing 100×100 quadrature points each. The maximum value of the difference between the far-field patterns, given by (6.22) in the case of the WGF method and by (2.88) in the case of LGF method, is 7.2×10^{-3} (Figure 6.2 displays the far-field pattern as well as the absolute value of the difference). Utilizing a GMRES residual tolerance of 10^{-4} the

(a) Two views of the absolute value of the total field.

(b) Two views of logarithm of the absolute value of the difference between the WGF and LGF solutions.

Figure 6.3: Solution of the problem of scattering of a plane acoustic wave by a sound-hard obstacle in a two-layer medium using the WGF method. First row: total fields. Second row: solution errors, evaluated as the absolute value of the difference between the WGF solution and a well-resolved LGF solution. Wavenumbers $k_1 = 10$ and $k_2 = 20$.

WGF linear system for $A = 5 \approx 4\lambda$, with 40,000 unknowns, required 66 iterations to achieve the imposed tolerance; while the LGF linear system with 20,000 unknowns required only 36 iterations to achieve the tolerance. In spite of the differences in the number of unknowns and the number of GMRES iterations, the proposed WGF method was 94 times faster than the LGF method in producing the corresponding integral equation solution (the WGF method was 173 times faster than the LGF method in performing one GMRES iteration). For the same scattering configuration with the obstacle now centered at $(0, 3/2, 0)$, the WGF method
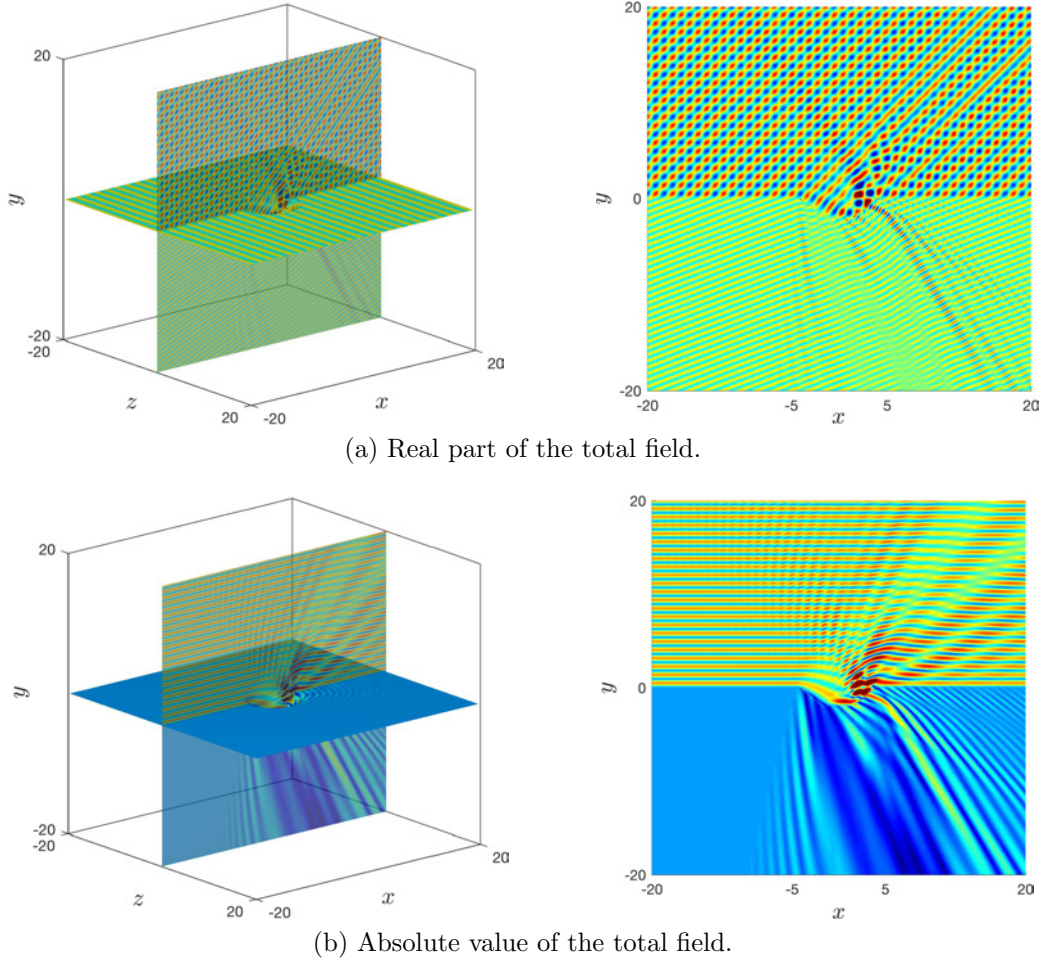
(a) Real part of the total field.

(b) Absolute value of the total field.

Figure 6.4: Total field solution of the problem of scattering of the plane acoustic wave $u^{\text{inc}}(\boldsymbol{r}) = \mathrm{e}^{ik_1(x\cos\alpha + y\sin\alpha)}$, with $\alpha = -\pi/4$, by a cavity in a two-layer medium with wavenumbers $k_1 = 5$ and $k_2 = 10$.

computes the solution 123 times faster than the LGF method. Figures 6.3a, finally, display the absolute value of the fields obtained by the WGF method on Γ_{1A} (for $A = 10 \approx 8\lambda$), S and a plane-perpendicular to Π_1, while Figures 6.3b display the logarithm of the absolute value of the difference between the WGF and LGF solutions on the same aforementioned surfaces.

Our next example concerns the problem of scattering of a cavity in a two-layer medium with wavenumbers $k_1 = 5$ and $k_2 = 10$ under plane wave illumination: $u^{\text{inc}}(\boldsymbol{r}) = \mathrm{e}^{ik_1(x\cos\alpha + y\sin\alpha)}$ with $\alpha = -\pi/4$. The smooth material interface Γ_1 coincides with the graph of the function $y = -2\eta\left(\sqrt{x^2 + z^2}, ca, a\right)$, where η is the window function defined in (2.78) with $a = 5$ and
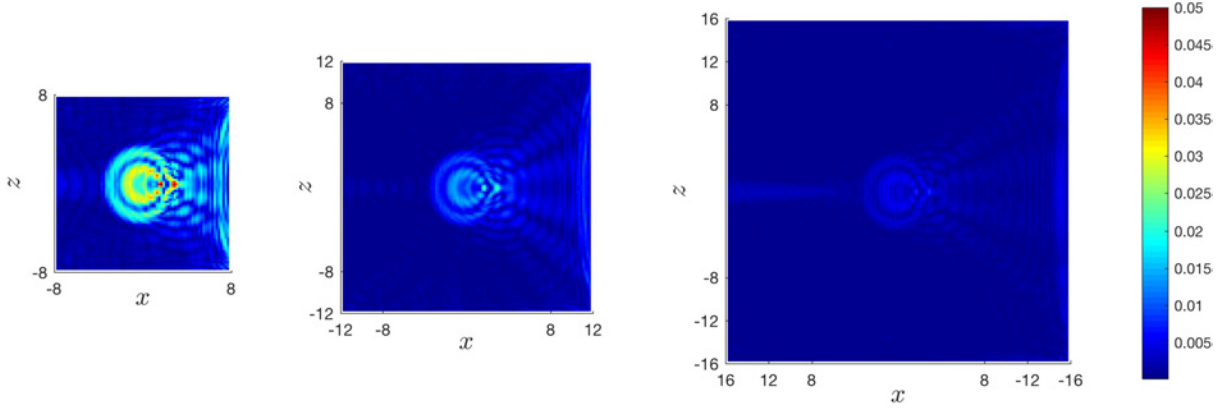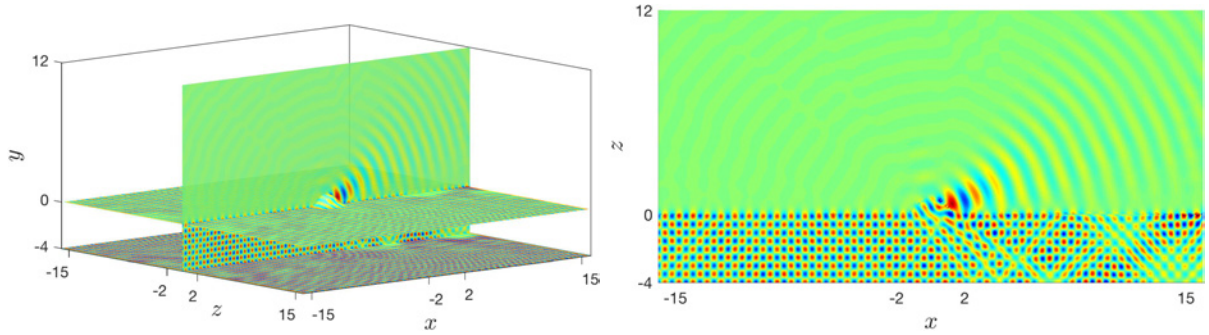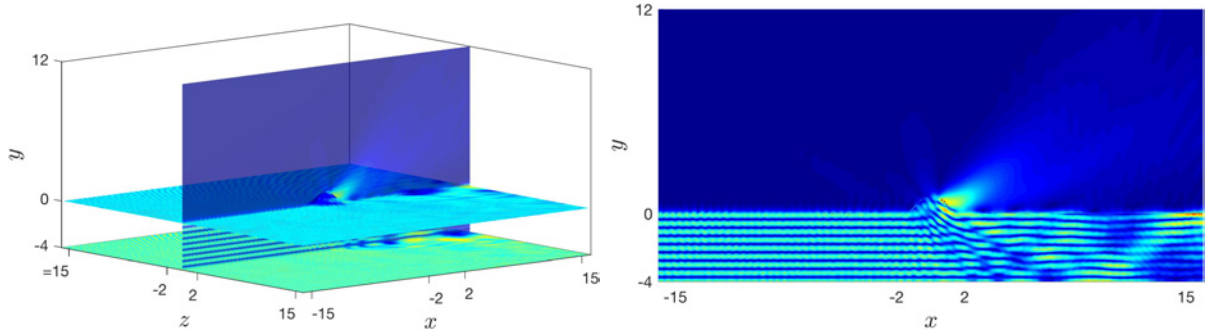
Figure 6.5: Absolute errors for the three-dimensional surface defect problem described in the caption of Figure 6.4 for $A = 8, 12$ and 16. The section of the planar interface shown in each case coincides with the region in the plane where the corresponding windowing function w_A used does not vanish.

(a) Real part of the total field.

(b) Absolute value of the total field.

Figure 6.6: Total field solution of the problem of scattering of a plane acoustic wave $u^{\text{inc}}(\boldsymbol{r}) = e^{ik_1(x\cos\alpha + y\sin\alpha)}$, with $\alpha = -\pi/4$, by a bump on a two-layer waveguide, with wavenumbers $k_1 = 5$ and $k_2 = 10$.

$c = 10^{-3}$. The problem of scattering is solved by means of the windowed integral equation (6.10) and the near field is evaluated by means of (6.13). Two different views of the real

part and the absolute value of the total field are displayed in Figure 6.4. In order to assess the error in the scattering solution we consider various window sizes: $A = 8, 12$ and 16. The resulting scattering solutions for the aforementioned three window sizes are compared against the solution obtained for $A = 20$ in Figure 6.5, which displays the absolute value of the difference of the fields values on Γ_{1A}.

The final example of this section concerns the problem of scattering by a surface bump in a two-layer waveguide with wavenumbers $k_1 = 5$ and $k_2 = 10$ in the $D_1 = \{y > 0\}$ and $D_2 = \{-4 < y < 0\}$. A Neumann boundary condition is enforced at $\Pi_2 = \{y = -4\}$. The incident field is taken to be equal to the the mode u_m defined in (6.14) for $\xi_m = 7.62899157$, which is obtained by solving equation (6.15). Figure 6.6 displays two views of the real part and the absolute value of the total field.

6.2 Electromagnetic scattering

This section presents our derivation of the WGF method for the numerical solution of problems of electromagnetic scattering of plane waves by surface defects in the presence of planar two-layer media. These derivations can easily be generalized to problems of scattering by defects in multi-layer media and two-layer waveguides as well as problems of scattering by PEC bounded obstacles in the presence of layered media in three spatial dimensions, by following the procedures described in Section 5.6 for the two-dimensional electromagnetic and in Section 6.1 for three-dimensional acoustic scattering problems.

We thus consider the underlying two-layer flat-interface medium containing the dielectric or conducting half-spaces $D_1 = \{y > 0\}$ and $D_2 = \{y < 0\}$ with material properties as described in Section 2.2.2. The incident plane-electromagnetic wave $(\mathbf{E}^{\mathrm{inc}}, \mathbf{H}^{\mathrm{inc}})$ we use is defined in (2.12). The dielectric interface bearing the bounded surface defect, which is assumed infinitely smooth, is denoted by Γ_1. The resulting layered medium is composed by the domains Ω_1 and Ω_2.

Following the ideas presented in Section 6.1.1 for the three-dimensional acoustic case, we express the total electromagnetic field $(\mathbf{E}, \mathbf{H})$—which satisfies Maxwell's equations (2.1)—in

the form

$$(\mathbf{E}, \mathbf{H}) = (\mathbf{E}^s, \mathbf{H}^s) + \left(\widetilde{\mathbf{E}}^f, \widetilde{\mathbf{H}}^f\right),$$

where $(\mathbf{E}^f, \mathbf{H}^f)$ is given by

$$\widetilde{\mathbf{E}}^f = \frac{i}{\omega\varepsilon}\frac{\partial \widetilde{H}_z^f}{\partial y}\mathbf{e}_x - \frac{i}{\omega\varepsilon}\frac{\partial \widetilde{H}_z}{\partial x}\mathbf{e}_y + \widetilde{E}_z\mathbf{e}_z, \tag{6.23}$$

$$\widetilde{\mathbf{H}}^f = -\frac{i}{\omega\mu}\frac{\partial \widetilde{E}_z}{\partial y}\mathbf{e}_x + \frac{i}{\omega\mu}\frac{\partial \widetilde{E}_z}{\partial x}\mathbf{e}_y + \widetilde{H}_z\mathbf{e}_z, \tag{6.24}$$

in terms of

$$\widetilde{E}_z(x,y) = E_0\, e^{ik_{1x}x} \begin{cases} e^{-ik_{1y}y} + R_{12}^{\mathrm{TE}}\, e^{ik_{1y}y} & \text{in} \quad \Omega_1, \\[2mm] T_{12}^{\mathrm{TE}}\, e^{-ik_{2y}y} & \text{in} \quad \Omega_2, \end{cases} \tag{6.25}$$

and

$$\widetilde{H}_z(x,y) = H_0\, e^{ik_{1x}x} \begin{cases} e^{-ik_{1y}y} + R_{12}^{\mathrm{TM}}\, e^{ik_{1y}y} & \text{in} \quad \Omega_1, \\[2mm] T_{12}^{\mathrm{TM}}\, e^{-ik_{2y}y} & \text{in} \quad \Omega_2, \end{cases} \tag{6.26}$$

and where, as detailed in equation (6.27) below, $(\mathbf{E}^s, \mathbf{H}^s)$ satisfies a condition of radiation at infinity. (The definitions of the constants k_{jx}, k_{jy} for $j = 1, 2$, and R_{12}^{TM}, R_{12}^{TE}, T_{12}^{TE} and T_{12}^{TM} are given in Section 2.2.2.) In view of derivations presented in Section 2.2.2 we find that, in the domains $D_1 \cap \Omega_1$ and $D_2 \cap \Omega_2$, $(\widetilde{\mathbf{E}}^f, \widetilde{\mathbf{H}}^f)$ coincides with the exact solution $(\mathbf{E}^f, \mathbf{H}^f)$ of the problem of scattering by the flat plane.

In what follows we seek an integral equation for the scattered field $(\mathbf{E}^s, \mathbf{H}^s)$. This field satisfies the equations

$$\begin{cases} \operatorname{curl}\mathbf{E}^s - i\omega\mu_j\mathbf{H}^s &=\ \mathbf{0} \quad \text{in} \qquad \Omega_j, \quad j = 1, 2, \\[2mm] \operatorname{curl}\mathbf{H}^s + i\omega\varepsilon_j\mathbf{E}^s &=\ \mathbf{0} \quad \text{in} \qquad \Omega_j, \quad j = 1, 2, \\[2mm] \mathbf{n}\times\mathbf{E}^s\big|_+ - \mathbf{n}\times\mathbf{E}^s\big|_- &=\ \mathbf{f} \quad \text{on} \qquad \Gamma_1, \\[2mm] \mathbf{n}\times\mathbf{H}^s\big|_+ - \mathbf{n}\times\mathbf{H}^s\big|_- &=\ \mathbf{g} \quad \text{on} \qquad \Gamma_1, \\[2mm] \displaystyle\lim_{|r|\to\infty}\left(\mathbf{H}^s\times\boldsymbol{r} - |\boldsymbol{r}|\sqrt{\frac{\varepsilon_j}{\mu_j}}\mathbf{E}^s\right) &=\ \mathbf{0}, \quad \boldsymbol{r}\in\Omega_j, \quad j = 1, 2, \\[4mm] \displaystyle\lim_{|r|\to\infty}\left(\mathbf{E}^s\times\boldsymbol{r} + |\boldsymbol{r}|\sqrt{\frac{\mu_j}{\varepsilon_j}}\mathbf{H}^s\right) &=\ \mathbf{0}, \quad \boldsymbol{r}\in\Omega_j, \quad j = 1, 2, \end{cases} \tag{6.27}$$

where the tangential vector fields $\mathbf{f}, \mathbf{g} \in C_0^\infty(\Gamma_1)$, which are given by

$$\mathbf{f} = \mathbf{n} \times \widetilde{\mathbf{E}}^f\big|_- - \mathbf{n} \times \widetilde{\mathbf{E}}^f\big|_+ \quad \text{and} \quad \mathbf{g} = \mathbf{n} \times \widetilde{\mathbf{H}}^f\big|_- - \mathbf{n} \times \widetilde{\mathbf{H}}^f\big|_+,$$

are supported on the defect $\Gamma_1 \setminus \Pi_1$. Here, for a field $\mathbf{F}$ defined around the surface Γ_1 we have used the notation

$$\mathbf{F}\big|_{\pm} = \lim_{\substack{h \to 0 \\ h > 0}} \mathbf{F}(\mathbf{r} \pm h\mathbf{n}), \quad \mathbf{r} \in \Gamma_1.$$

Existence and uniqueness results for the solution $\mathbf{E}^s, \mathbf{H}^s \in H_{\text{loc}}(\text{curl}; \mathbb{R}^3)$ can obtained by a slight generalization of the results presented in the contribution [49].

From the Stratton-Chu integral representation formulae [45, 121] and the ideas put forth in the contribution [53] for the integral representation of the scattered field by a two-dimensional rough surface, it can be shown that the electromagnetic scattered field satisfies

$$\text{curl} \int_{\Gamma_1} G_{k_1}(\mathbf{r}, \mathbf{r}') \left[\mathbf{m}(\mathbf{r}') + \mathbf{f}(\mathbf{r}')\right] \mathrm{d}s_{\mathbf{r}'} + \frac{i}{\omega \varepsilon_1} \text{curl}\, \text{curl} \int_{\Gamma_1} G_{k_1}(\mathbf{r}, \mathbf{r}') \left[\mathbf{j}(\mathbf{r}') + \mathbf{g}(\mathbf{r}')\right] \mathrm{d}s_{\mathbf{r}'}$$

$$= \begin{cases} \mathbf{E}^s(\mathbf{r}), & \mathbf{r} \in \Omega_1, \\ \mathbf{0}, & \mathbf{r} \in \mathbb{R}^3 \setminus \overline{\Omega_1}, \end{cases}$$

$$\text{curl} \int_{\Gamma_1} G_{k_1}(\mathbf{r}, \mathbf{r}') \left[\mathbf{j}(\mathbf{r}') + \mathbf{g}(\mathbf{r}')\right] \mathrm{d}s_{\mathbf{r}'} - \frac{i}{\omega \mu_1} \text{curl}\, \text{curl} \int_{\Gamma_1} G_{k_1}(\mathbf{r}, \mathbf{r}') \left[\mathbf{m}(\mathbf{r}') + \mathbf{f}(\mathbf{r}')\right] \mathrm{d}s_{\mathbf{r}'}$$

$$= \begin{cases} \mathbf{H}^s(\mathbf{r}), & \mathbf{r} \in \Omega_1, \\ \mathbf{0}, & \mathbf{r} \in \mathbb{R}^3 \setminus \overline{\Omega_1} \end{cases}$$

$$\tag{6.28a}$$

and

$$\text{curl} \int_{\Gamma_1} G_{k_2}(\mathbf{r}, \mathbf{r}')\mathbf{m}(\mathbf{r}') \, \mathrm{d}s_{\mathbf{r}'} + \frac{i}{\omega \varepsilon_2} \text{curl}\, \text{curl} \int_{\Gamma_1} G_{k_2}(\mathbf{r}, \mathbf{r}')\mathbf{j}(\mathbf{r}') \, \mathrm{d}s_{\mathbf{r}'} = \begin{cases} -\mathbf{E}^s(\mathbf{r}), \ \mathbf{r} \in \Omega_2, \\ \mathbf{0}, \ \mathbf{r} \in \mathbb{R}^3 \setminus \overline{\Omega_2}, \end{cases}$$

$$\text{curl} \int_{\Gamma_1} G_{k_2}(\mathbf{r}, \mathbf{r}')\mathbf{j}(\mathbf{r}') \, \mathrm{d}s_{\mathbf{r}'} - \frac{i}{\omega \mu_2} \text{curl}\, \text{curl} \int_{\Gamma_1} G_{k_2}(\mathbf{r}, \mathbf{r}')\mathbf{m}(\mathbf{r}') \, \mathrm{d}s_{\mathbf{r}'} = \begin{cases} -\mathbf{H}^s(\mathbf{r}), \ \mathbf{r} \in \Omega_2, \\ \mathbf{0}, \ \mathbf{r} \in \mathbb{R}^3 \setminus \overline{\Omega_2}, \end{cases}$$

$$\tag{6.28b}$$

where

$$\mathbf{j} = \mathbf{n} \times \mathbf{H}^s|_- \quad \text{and} \quad \mathbf{m} = \mathbf{n} \times \mathbf{E}^s|_-$$

denote the tangential component of the magnetic and electric fields respectively and where G_k denotes the free-space Green function (6.7).

From the identity $\operatorname{curl}\operatorname{curl}\mathbf{A} = \nabla\operatorname{div}\mathbf{A} - \Delta\mathbf{A}$ and the fact that $G_k(\cdot - \boldsymbol{r})$ satisfies the homogeneous Helmholtz equation in $\mathbb{R}^3 \setminus \{\boldsymbol{r} \neq \boldsymbol{r}'\}$ and $\nabla_{\boldsymbol{r}} G_k(\boldsymbol{r}, \boldsymbol{r}') = -\nabla_{\boldsymbol{r}'} G_k(\boldsymbol{r}, \boldsymbol{r}')$, we obtain

$$\operatorname{curl}\operatorname{curl}\int_{\Gamma_1} G_k(\boldsymbol{r}, \boldsymbol{r}')\mathbf{a}(\boldsymbol{r}')\, \mathrm{d}s_{\boldsymbol{r}'} = -\nabla\int_{\Gamma_1} \nabla_{\boldsymbol{r}'} G_k(\boldsymbol{r}, \boldsymbol{r}') \cdot \mathbf{a}(\boldsymbol{r}')\, \mathrm{d}s_{\boldsymbol{r}'} + k^2\int_{\Gamma_1} G_k(\boldsymbol{r}, \boldsymbol{r}')\mathbf{a}(\boldsymbol{r}')\, \mathrm{d}s_{\boldsymbol{r}'}.$$

Utilizing the surface integration-by-parts formula in [45, Equation 2.73] this identity becomes

$$\operatorname{curl}\operatorname{curl}\int_{\Gamma_1} G_k(\boldsymbol{r}, \boldsymbol{r}')\mathbf{a}(\boldsymbol{r}')\, \mathrm{d}s_{\boldsymbol{r}'} = \nabla\int_{\Gamma_1} G_k(\boldsymbol{r}, \boldsymbol{r}')\operatorname{div}\mathbf{a}(\boldsymbol{r}')\, \mathrm{d}s_{\boldsymbol{r}'} + k^2\int_{\Gamma_1} G_k(\boldsymbol{r}, \boldsymbol{r}')\mathbf{a}(\boldsymbol{r}')\, \mathrm{d}s_{\boldsymbol{r}'},$$

where $\mathbf{a}$ and $\operatorname{div}\mathbf{a}$ are assumed to be continuous on Γ_1.

Evaluating the expressions (6.28)—utilizing the jump relations of the associated potentials [45, Theorems 2.17 and 2.26]—and taking cross product with the normal $\mathbf{n}$ from the left, we obtain the identities

$$-\frac{\mathbf{m}}{2} + \mathbf{K}_1[\mathbf{m}] + \frac{i}{\omega\varepsilon_1}\mathbf{T}_1[\mathbf{j}] = \frac{\mathbf{f}}{2} - \mathbf{K}_1[\mathbf{f}] - \frac{i}{\omega\varepsilon_1}\mathbf{T}_1[\mathbf{g}], \tag{6.29a}$$

$$-\frac{\mathbf{j}}{2} + \mathbf{K}_1[\mathbf{j}] - \frac{i}{\omega\mu_1}\mathbf{T}_1[\mathbf{m}] = \frac{\mathbf{g}}{2} - \mathbf{K}_1[\mathbf{g}] + \frac{i}{\omega\mu_1}\mathbf{T}_1[\mathbf{f}], \tag{6.29b}$$

$$\frac{\mathbf{m}}{2} + \mathbf{K}_2[\mathbf{m}] + \frac{i}{\omega\varepsilon_2}\mathbf{T}_2[\mathbf{j}] = \mathbf{0}, \tag{6.29c}$$

$$\frac{\mathbf{j}}{2} + \mathbf{K}_2[\mathbf{j}] - \frac{i}{\omega\mu_2}\mathbf{T}_2[\mathbf{m}] = \mathbf{0}, \tag{6.29d}$$

on Γ_1, in terms of the boundary integral operators

$$\mathbf{K}_j[\mathbf{a}](\mathbf{r}) = \mathbf{n}(\mathbf{r}) \times \int_{\Gamma_1} \operatorname{curl}_{\mathbf{r}} G_{k_j}(\mathbf{r}, \mathbf{r}') \mathbf{a}(\mathbf{r}') \, \mathrm{d}s_{\mathbf{r}'}, \tag{6.30a}$$

$$\mathbf{S}_j[\mathbf{a}](\mathbf{r}) = \mathbf{n}(\mathbf{r}) \times \int_{\Gamma_1} G_{k_j}(\mathbf{r}, \mathbf{r}') \mathbf{a}(\mathbf{r}') \, \mathrm{d}s_{\mathbf{r}'}, \tag{6.30b}$$

$$\mathbf{N}_j[\mathbf{a}](\mathbf{r}) = \mathbf{n}(\mathbf{r}) \times \int_{\Gamma_1} \nabla_{\mathbf{r}} G_{k_j}(\mathbf{r}, \mathbf{r}') \operatorname{div}_{\Gamma_1} \mathbf{a}(\mathbf{r}') \, \mathrm{d}s_{\mathbf{r}'}, \tag{6.30c}$$

$$\mathbf{T}_j[\mathbf{a}](\mathbf{r}) = \mathbf{n}(\mathbf{r}) \times \operatorname{curl} \operatorname{curl} \int_{\Gamma_1} G_k(\mathbf{r}, \mathbf{r}') \mathbf{a}(\mathbf{r}') \, \mathrm{d}s_{\mathbf{r}'} \tag{6.30d}$$

$$= \mathbf{N}_j[\mathbf{a}](\mathbf{r}) + k_j^2 \mathbf{S}_j[\mathbf{a}](\mathbf{r}),$$

defined for $\mathbf{r} \in \Gamma_1$ and $j = 1, 2$. Clearly, as corresponding operators in the two- and three-dimensional acoustic cases, the scattering operators in (6.30) are given by integrals which are only conditionally convergent.

Suitably combining the identities in (6.29) we obtain

$$\left(\frac{\varepsilon_1 + \varepsilon_1}{2}\right) \mathbf{m} + (\varepsilon_2 \mathbf{K}_2 - \varepsilon_1 \mathbf{K}_1)[\mathbf{m}] + \frac{i}{\omega}(\mathbf{T}_2 - \mathbf{T}_1)[\mathbf{j}] = -\frac{\varepsilon_1}{2}\mathbf{f} + \varepsilon_1 \mathbf{K}_1[\mathbf{f}] + \frac{i}{\omega}\mathbf{T}_1[\mathbf{g}],$$

$$\left(\frac{\mu_1 + \mu_2}{2}\right) \mathbf{j} + (\mu_2 \mathbf{K}_2 - \mu_1 \mathbf{K}_1)[\mathbf{j}] - \frac{i}{\omega}(\mathbf{T}_2 - \mathbf{T}_1)[\mathbf{m}] = -\frac{\mu_1}{2}\mathbf{g} + \mu_1 \mathbf{K}_1[\mathbf{f}] - \frac{i}{\omega}\mathbf{T}_1[\mathbf{g}]. \tag{6.31}$$

The system of integral equations (6.31) for the surface currents $\mathbf{j}$ and $\mathbf{m}$ can be expressed in the form

$$\mathrm{E}\,\boldsymbol{\phi} + \mathrm{T}\,[\boldsymbol{\phi}] = -\,\mathrm{M}[\boldsymbol{\psi}] \quad \text{on} \quad \Gamma_1, \tag{6.32}$$

where

$$\boldsymbol{\phi}^s = \begin{bmatrix} \mathbf{m} \\ \mathbf{j} \end{bmatrix}, \qquad \boldsymbol{\psi} = \begin{bmatrix} \mathbf{f} \\ \mathbf{g} \end{bmatrix}, \qquad \mathrm{E} = \begin{bmatrix} \left(\dfrac{\varepsilon_2 + \varepsilon_1}{2}\right) & 0 \\ 0 & \left(\dfrac{\mu_2 + \mu_1}{2}\right) \end{bmatrix},$$

$$\mathrm{T} = \begin{bmatrix} \varepsilon_2 \mathbf{K}_2 - \varepsilon_1 \mathbf{K}_1 & \dfrac{i}{\omega}(\mathbf{T}_2 - \mathbf{T}_1) \\ -\dfrac{i}{\omega}(\mathbf{T}_2 - \mathbf{T}_1) & \mu_2 \mathbf{K}_2 - \mu_1 \mathbf{K}_1 \end{bmatrix} \quad \text{and} \quad \mathrm{M} = \begin{bmatrix} -\frac{\varepsilon_1}{2}\mathrm{I}_d + \varepsilon_1 \mathbf{K}_1 & \dfrac{i}{\omega}\mathbf{T}_1 \\ -\dfrac{i}{\omega}\mathbf{T}_1 & -\frac{\mu_1}{2}\mathrm{I}_d + \mu_1 \mathbf{K}_1 \end{bmatrix}.$$

Therefore, the resulting windowed integral equation system for the three-dimensional elec-

tromagnetic scattering problem is given by

$$\mathrm{E}\,\boldsymbol{\phi}^{sw} + \mathrm{T}\left[W_A \boldsymbol{\phi}^{sw}\right] = -\,\mathrm{M}[\boldsymbol{\psi}] \quad \text{on} \quad \Gamma_{1A}, \tag{6.33}$$

where, using the 2×2 identity matrix I together with the window function w_A defined in (6.11), we have denoted $W_A = \mathrm{w}_A I$ and $\Gamma_{1A} = \Gamma_1 \cap \{\mathrm{w}_A \neq 0\}$.

Remark 6.2.1. *The operators* $\mathbf{K}_j$, $j = 1, 2$, *(equation* (6.30a)*) and* $\mathbf{T}_2 - \mathbf{T}_1$ *(see equations* (6.31) *and* (6.30d)*) are weakly singular. This follows directly for* $\mathbf{K}_j$ *by consideration of the identity*

$$\mathbf{n}(\boldsymbol{r}) \times \operatorname{curl} \int_{\Gamma_1} G_k(\boldsymbol{r}, \boldsymbol{r}')\mathbf{a}(\boldsymbol{r}')\,\mathrm{d}s_{\boldsymbol{r}'} = \int_{\Gamma_1} \mathbf{n}(\boldsymbol{r}) \times \operatorname{curl}_{\boldsymbol{r}} \left\{\mathbf{a}(\boldsymbol{r}')G_k(\boldsymbol{r}, \boldsymbol{r}')\right\}\,\mathrm{d}s_{\boldsymbol{r}'}$$

$$= \int_{\Gamma_1} \left\{(\mathbf{n}(\boldsymbol{r}) - \mathbf{n}(\boldsymbol{r}')) \cdot \mathbf{a}(\boldsymbol{r}')\nabla_{\boldsymbol{r}}G_k(\boldsymbol{r}, \boldsymbol{r}') - \frac{\partial G_k}{\partial n_{\boldsymbol{r}}}(\boldsymbol{r}, \boldsymbol{r}')\mathbf{a}(\boldsymbol{r}')\right\}\,\mathrm{d}s_{\boldsymbol{r}'}.$$

To establish the corresponding property for $\mathbf{T}_2 - \mathbf{T}_1$, *on the other hand, we define the scalar function* $\phi = G_{k_2}(\cdot, \boldsymbol{r}') - G_{k_1}(\cdot, \boldsymbol{r}')$ *and we consider a vector field* $\mathbf{a}(\boldsymbol{r}')$ *tangential to the surface* Γ_1 *at the point* $\boldsymbol{r}' \in \Gamma_1$. *Then, utilizing the identity*

$$\operatorname{curl}\operatorname{curl}(\phi\,\mathbf{a}) = \operatorname{curl}(\nabla\phi \times \mathbf{a}) = -\mathbf{a}\,\Delta\phi + (\mathbf{a} \cdot \nabla)\nabla\phi$$

we obtain

$$\operatorname{curl}\operatorname{curl}(\phi\,\mathbf{a}) = \mathbf{a}\left\{k_2^2 G_{k_2}(\cdot, \boldsymbol{r}') + \delta_{\boldsymbol{r}'} - k_1^2 G_{k_1}(\cdot, \boldsymbol{r}') - \delta_{\boldsymbol{r}'}\right\}$$

$$+ (\mathbf{a} \cdot \nabla)\nabla\left\{G_{k_2}(\cdot, \boldsymbol{r}') - G_{k_1}(\cdot, \boldsymbol{r}')\right\} \tag{6.34}$$

$$= \mathbf{a}\left\{k_2^2 G_{k_2}(\cdot, \boldsymbol{r}') - k_1^2 G_{k_1}(\cdot, \boldsymbol{r}')\right\} + (\mathbf{a} \cdot \nabla)\nabla\left\{G_{k_2}(\cdot, \boldsymbol{r}') - G_{k_1}(\cdot, \boldsymbol{r}')\right\}.$$

Letting $\boldsymbol{r} = (x_1, x_2, x_3)$ *and* $\boldsymbol{r}' = (y_1, y_2, y_2)$, *the second partial derivatives of the free-space Green function can be expressed as*

$$\frac{\partial^2 G_k}{\partial x_j \partial x_i}(\cdot, \boldsymbol{r}') = \frac{f'(r)}{r}\delta_{ij} + \frac{r f'' - f'(r)}{r^3}(x_i - y_i)(x_j - y_j)$$

$$= \frac{\mathrm{e}^{ikr}}{4\pi r^3}(ikr - 1)\delta_{ij} - \frac{\mathrm{e}^{ikr}(r^2 k^2 + 3ikr - 3)}{4\pi r^5}(x_i - y_i)(x_j - y_j), \quad i, j = 1, 2, 3,$$

where $f(r) = e^{ikr}/(4\pi r)$, $r = |\boldsymbol{r}|$ and $\boldsymbol{r} = \boldsymbol{r} - \boldsymbol{r}'$. Therefore we have

$$
\begin{aligned}
(\mathbf{a} \cdot \nabla)\nabla\phi &= \frac{1}{4\pi r^3} \left\{ e^{ik_2 r}(ik_2 r - 1) - e^{ik_1 r}(ik_1 r - 1) \right\} \mathbf{a} \\
&\quad - \frac{1}{4\pi r^5} \left\{ e^{ik_2 r}(r^2 k_2^2 + 3ik_2 r - 3) - e^{ik_1 r}(r^2 k_1^2 + 3ik_1 r - 3) \right\} (\mathbf{a} \cdot \boldsymbol{r})\boldsymbol{r} \\
&= -\frac{k_2^2 - k_1^2}{8\pi r}\mathbf{a} + \frac{k_2^2 - k_1^2}{8\pi r^3}(\mathbf{a} \cdot \boldsymbol{r})\,\boldsymbol{r} + \mathcal{O}(1)
\end{aligned}
$$

as $r \to 0$, and consequently

$$
\operatorname{curl}\operatorname{curl}(\phi\,\mathbf{a}) = \frac{(k_2^2 - k_1^2)}{8\pi r}\mathbf{a} + \frac{k_2^2 - k_1^2}{8\pi r^3}(\mathbf{a} \cdot \boldsymbol{r})\,\boldsymbol{r} + \mathcal{O}(1) \quad as \quad r \to 0,
$$

which embodies the weakly singular character of the operator $\mathbf{T}_2 - \mathbf{T}_1$.

Results on the existence and uniqueness of solutions for the integral equation (6.12) can be obtained, at least for smooth surfaces Γ_{1A}, in view of the fact that the integral operators $\varepsilon_2 \mathbf{K}_2 - \varepsilon_1 \mathbf{K}_1$, $\mathbf{T}_2 - \mathbf{T}_1$ and $\mu_2 \mathbf{K}_2 - \mu_1 \mathbf{K}_1$ are given in terms of weakly singular (integrable) kernels (cf. Appendix D).

Once the solution $\boldsymbol{\phi}^{sw} = [\mathbf{m}^w, \mathbf{j}^w]^T$ of the windowed integral equations (6.33) have been obtained, the corresponding near fields can be by substituting $\mathbf{m}^s$ by $\mathrm{w}_A \mathbf{m}^w$ and $\mathbf{j}$ by $\mathrm{w}_A \mathbf{j}^w$ in (6.28). We thus obtain the near-field expressions

$$
\begin{aligned}
\mathbf{E}^w(\boldsymbol{r}) &= \widetilde{\mathbf{E}}^f(\boldsymbol{r}) + \operatorname{curl} \int_{\Gamma_1} G_{k_1}(\boldsymbol{r}, \boldsymbol{r}')\left\{\mathrm{w}_A\mathbf{m}^w(\boldsymbol{r}') + \mathbf{f}(\boldsymbol{r}')\right\}\,\mathrm{d}s_{\boldsymbol{r}'} \\
&\quad + \frac{i}{\omega\varepsilon_1}\operatorname{curl}\operatorname{curl}\int_{\Gamma_1} G_{k_1}(\boldsymbol{r}, \boldsymbol{r}')\left\{\mathrm{w}_A\mathbf{j}^s(\boldsymbol{r}') + \mathbf{g}(\boldsymbol{r}')\right\}\,\mathrm{d}s_{\boldsymbol{r}'}, \\
\mathbf{H}^w(\boldsymbol{r}) &= \widetilde{\mathbf{H}}^f(\boldsymbol{r}) + \operatorname{curl}\int_{\Gamma_1} G_{k_1}(\boldsymbol{r}, \boldsymbol{r}')\left\{\mathrm{w}_A\mathbf{j}^w(\boldsymbol{r}') + \mathbf{g}(\boldsymbol{r}')\right\}\,\mathrm{d}s_{\boldsymbol{r}'} \\
&\quad - \frac{i}{\omega\mu_1}\operatorname{curl}\operatorname{curl}\int_{\Gamma_1} G_{k_1}(\boldsymbol{r}, \boldsymbol{r}')\left\{\mathrm{w}_A\mathbf{m}^w(\boldsymbol{r}') + \mathbf{f}(\boldsymbol{r}')\right\}\,\mathrm{d}s_{\boldsymbol{r}'},
\end{aligned}
$$

$$(6.35\mathrm{a})$$

in Ω_1, and

$$\mathbf{E}^w(\boldsymbol{r}) = \widetilde{\mathbf{E}}^f(\boldsymbol{r}) - \operatorname{curl} \int_{\Gamma_1} G_{k_2}(\boldsymbol{r}, \boldsymbol{r}') \mathrm{w}_A \mathbf{m}^w(\boldsymbol{r}') \, \mathrm{d}s_{\boldsymbol{r}'}$$

$$- \frac{i}{\omega \varepsilon_2} \operatorname{curl} \operatorname{curl} \int_{\Gamma_1} G_{k_2}(\boldsymbol{r}, \boldsymbol{r}') \mathrm{w}_A \mathbf{j}(\boldsymbol{r}') \, \mathrm{d}s_{\boldsymbol{r}'},$$

$$\mathbf{H}^w(\boldsymbol{r}) = \widetilde{\mathbf{H}}^f(\boldsymbol{r}) - \operatorname{curl} \int_{\Gamma_1} G_{k_2}(\boldsymbol{r}, \boldsymbol{r}') \mathrm{w}_A \mathbf{j}^w(\boldsymbol{r}') \, \mathrm{d}s_{\boldsymbol{r}'}$$

$$+ \frac{i}{\omega \mu_2} \operatorname{curl} \operatorname{curl} \int_{\Gamma_1} G_{k_2}(\boldsymbol{r}, \boldsymbol{r}') \mathrm{w}_A \mathbf{m}^w(\boldsymbol{r}') \, \mathrm{d}s_{\boldsymbol{r}'},$$

$$(6.35\mathrm{b})$$

in Ω_2.

Chapter 7

Conclusions and future work

7.1 Conclusions

This thesis has introduced a variety of highly-efficient high-order boundary integral equation methods, including, most notably, the WGF method, for the numerical solution of problems of acoustic and electromagnetic scattering in the presence of planar layered media in two and three dimensions. The WGF method, which is based on use of smooth windowing functions and integral kernels that can be expressed directly in terms of the free-space Green function, does not require evaluation of expensive Sommerfeld integrals. It was shown that, indeed, the WGF approach is fast, accurate, flexible and easy to implement. The formal analysis and numerical experiments presented throughout this thesis demonstrate that both the near- and far-field errors resulting from the proposed WGF approach decrease faster than any negative power of the window size.

A number of other efficient algorithms and studies applicable to various layered media scattering problems have been also presented in this thesis, including a Sommerfeld-integral-based high-order integral equation method for problems of scattering by defects in presence of PEC half-planes and dielectric/conducting layered media as well as studies of resonances and near resonances at surface defects and their impact on the absorptive properties of rough surfaces.

7.2 Future work

This thesis work points to a variety of interesting future research projects. For example, unlike the LGF method, the WGF method can directly be utilized in conjunction with the convolution quadrature method put forth in [82], to effectively tackle layered-media scattering problems in the time domain. In order to construct a time-domain solution, the convolution quadrature approach requires solution of a large number of time-harmonic problems that can be efficiently solved by means of the WGF method. Another promising research direction concerns an extension of the WGF method to wave propagation and scattering problems in linear elasticity (cf. [56]). For example, a WGF method in this context would be well suited to handle various problems in geophysics and seismology. Yet another possible extension of the WGF method would make it applicable to problems of scattering by complex highly heterogeneous obstacles in layered media, by coupling the WGF method with a finite element method or other volumetric solver through an artificial boundary enclosing the obstacle.

The multi-scattering phenomenon that naturally arises in the multi-layer configurations—as the fields inside finite-thickness layers might get reflected infinitely many times by the unbounded dielectric interfaces—leads to larger number of GMRES iterations. The design of the an efficient preconditioners to accelerate the convergence of the GMRES algorithm, in this case, is indeed another topic that should be addressed in future contributions.

The pseudo-resonance phenomenon and its connection to electromagnetic power absorption in rough conducting surfaces, discussed in Section 3.5, certainly deserves further study. It would be interesting, for instance, to establish a clear mathematical connection between the location of the scattering poles and the enhancement of electromagnetic power absorption that takes place at certain anomalous frequencies. From a numerical analysis perspective, in turn, the problem of finding the scattering poles by analyzing the (non-linear) spectrum of the relevant integral operators poses a challenging but tractable problem which could additionally give rise to potentially important understanding in the area of power absorption by rough surfaces.

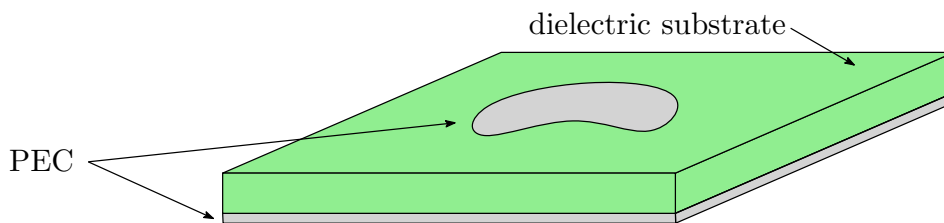To conclude this section we mention, among a variety of possible future applications and

Figure 7.1: Idealized microstrip antenna configuration.

extensions, the important problem of simulation of printed circuit boards and microstrip antennas (sometimes called patch antennas). A more detailed description of this problem and the progress so far achieved in these regards are presented in the following section.

7.2.1 Accurate and efficient microstrip-antenna simulation

Dielectric layer-media models are often utilized in the analysis of printed circuits and microstrip antennas [6, 43, 67, 95, 96]. A microstrip antenna, for example, consists of a radiating patch on one side a dielectric substrate, which has a PEC plane on the other side (see Figure 7.1). Microstrip antennas enjoy several advantages compared to conventional micro-wave antennas: they are lightweight, they require a reduced volume, they can be fabricated inexpensively, and they can be designed for dual-frequency and dual polarization operation [57].

As is known, the numerical simulation of patch antennas encounters two main mathematical difficulties, namely, the singular character of the surface currents along the edge of PEC patches, and the presence of the air-substrate dielectric interface (often assumed to be flat and unbounded) at which suitable transmission conditions have to be enforced. In fact, standard analyses of microstrip antennas rely on the layer Green function and associated integral equation on the PEC patches. Typically, such integral equations are then discretized by means of (low-order) boundary element methods [108]. This solution procedure suffers from several difficulties. On one hand it does not accurately account for the singularity of the surface currents at PEC patches and, on the other hand, it is extremely costly (as the Sommerfeld integrals have to be numerically approximated for the source and observation

points right at the dielectric interface; see discussion in Section 2.3.5).

This problem can in fact be efficiently and accurately solved by means of the WGF method. To illustrate this fact in the two-dimensional case, we consider the problem of scattering by a PEC patch placed at the planar interface between two dielectric half-planes. The windowed integral equation (4.19) is suitably modified to enforce the corresponding (TE or TM) PEC boundary conditions on the patch. The resulting new integral equation system is then discretized by means of a Nyström method that properly resolves the edge singularities of the surface currents at the patch endpoints. Figure 7.2 displays the diffraction patterns that result from the scattering of a point-source (Figures 7.2a) and a pane-wave (Figure 7.2b) by the aforementioned structure.
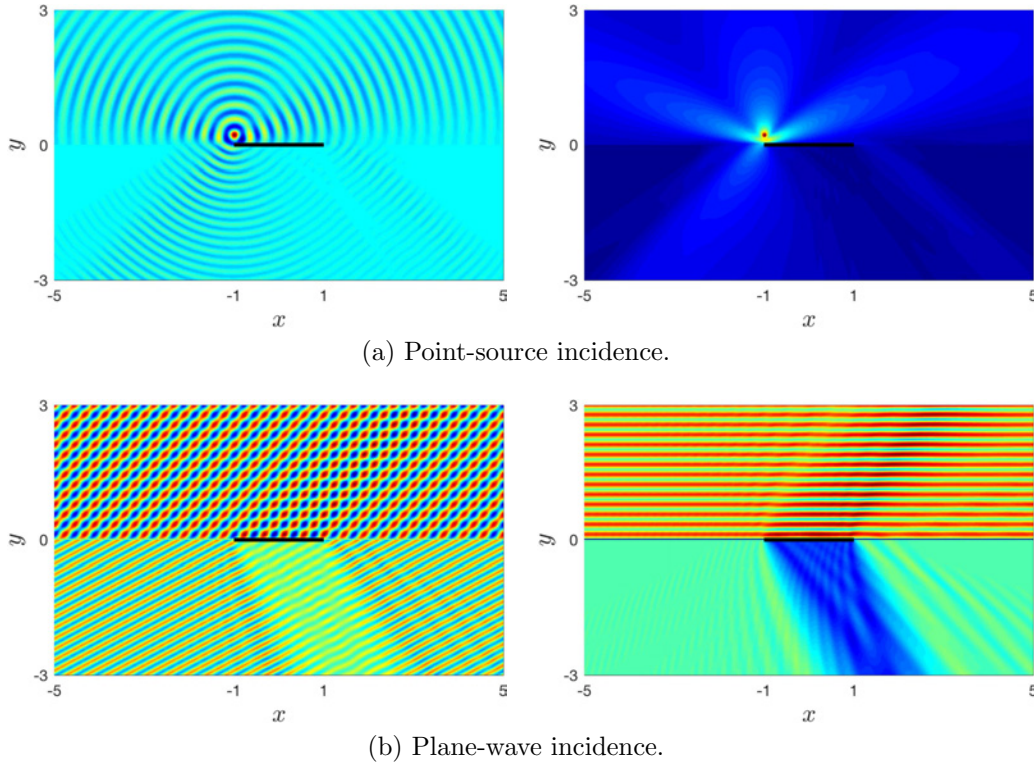

(a) Point-source incidence.

(b) Plane-wave incidence.

Figure 7.2: Scattering by the PEC patch $S = \{(x,y) \in \mathbb{R}^2 : |x| < 1, y = 0\}$ at the interface $\Pi_1 = \{y = 0\}$ of a two-layer medium with wavenumbers $k_1 = 20$ and $k_2 = 30$ in TE polarization. First row: real part (left) and absolute value (right) of the total field solution of the problem of scattering of a point source (centered at $\boldsymbol{r'} = (-1, 0.2)$). Second row: real part (left) and absolute value (right) of the total field solution of the problem of scattering of a plane-wave ($\alpha = -\pi/4$).

In order to extend this solution procedure to the three dimensional case, a suitable open

surface scattering solver is required. The following section presents our progress in this direction. The resulting open surface scattering solver could then be suitably combined with the three-dimensional electromagnetic WGF method presented in Section 7.2.2 to provide an effective solver for the patch antenna problem.

7.2.2 Electromagnetic scattering by three-dimensional open surfaces

Let $S \subset \mathbb{R}^3$ be a bounded open infinitely smooth surface that models an infinitely thin perfect electric conductor (PEC) sheet, and consider an incoming time-harmonic electromagnetic field $(\mathbf{E}^{\text{inc}}, \mathbf{H}^{\text{inc}})$ (2.12) that impinges on S, giving rise to a scattered electromagnetic field denoted by $(\mathbf{E}^s, \mathbf{H}^s)$. As the surface is assumed perfectly conducting, the total electric field tangent to the surface, $\mathbf{n} \times (\mathbf{E}^s + \mathbf{E}^{\text{inc}})$ (where $\mathbf{n}$ denotes the unit normal on S), vanishes on S. The scattered electric field is then determined as the solution of the Maxwell's problem

$$
\begin{aligned}
\operatorname{curl}\operatorname{curl}\mathbf{E}^s - k^2\mathbf{E}^s &= \mathbf{0} &&\text{in}\quad \mathbb{R}^3 \setminus \overline{S}, \\
\mathbf{n} \times \mathbf{E}^s &= -\mathbf{n} \times \mathbf{E}^{\text{inc}} &&\text{on}\quad S, \\
\lim_{|\boldsymbol{r}|\to\infty} (\operatorname{curl}\mathbf{E}^s \times \boldsymbol{r} - ik|\boldsymbol{r}|\mathbf{E}^s) &= \mathbf{0}.
\end{aligned}
\tag{7.1}
$$

In view of the Stratton-Chu formula, on the other hand, the scattered electric field admits the integral representation

$$
\mathbf{E}^s(\boldsymbol{r}) = ik \int_S G_k(\boldsymbol{r}, \boldsymbol{r}')\,\mathbf{j}(\boldsymbol{r}')\,\mathrm{d}s_{\boldsymbol{r}'} + \frac{i}{k}\nabla \int_S G_k(\boldsymbol{r}, \boldsymbol{r}')\operatorname{div}_S \mathbf{j}(\boldsymbol{r}')\,\mathrm{d}s_{\boldsymbol{r}'}, \qquad \boldsymbol{r} \in \mathbb{R}^3 \setminus \overline{S}, \quad (7.2)
$$

in terms of the surface current density $\mathbf{j}$. From the boundary condition on the PEC surface it follows that $\mathbf{j}$ (which physically corresponds to the jump of the tangential magnetic field: $\mathbf{j} = \sqrt{\varepsilon/\mu}\,[\mathbf{n} \times \mathbf{H}^s]$ on S) is a solution of the boundary integral equation

$$
\mathbf{T}[\mathbf{j}] := ik\,\mathbf{S}[\mathbf{j}] + \frac{i}{k}\mathbf{N}[\mathbf{j}] = -\mathbf{n} \times \mathbf{E}^{\text{inc}} \quad \text{on}\quad S, \tag{7.3}
$$

where for $\boldsymbol{r} \in S$ we have denoted

$$\mathbf{S}[\mathbf{j}](\boldsymbol{r}) = \mathbf{n}(\boldsymbol{r}) \times \int_S G_k(\boldsymbol{r}, \boldsymbol{r}')\mathbf{j}(\boldsymbol{r}')\,\mathrm{d}s_{\boldsymbol{r}'} \quad \text{and}$$

$$\mathbf{N}[\mathbf{j}](\boldsymbol{r}) = \mathbf{n}(\boldsymbol{r}) \times \text{p.v.} \int_S \nabla_{\boldsymbol{r}} G_k(\boldsymbol{r}, \boldsymbol{r}')\mathrm{div}_S\mathbf{j}(\boldsymbol{r}')\,\mathrm{d}s_{\boldsymbol{r}'}. \tag{7.4}$$

The integral equation (7.3), usually known as the Electric Field Integral Equation (EFIE), has been extensively studied. In particular, it has been shown that the operator $\mathbf{T}$: $\widetilde{H}_{\mathrm{curl}}^{-1/2}(S) \to H_{\mathrm{curl}}^{-1/2}(S)$ defined in (7.3), is an isomorphism for all wavenumbers $k \in \mathbb{R}$, from where it has been further shown that the problem of scattering (2.1) by an open PEC surface has an unique solution in $H_{\mathrm{loc}}(\mathrm{curl}, \mathbb{R}^3 \setminus \overline{S})$ (see Abboud & Starling [1] and Buffa & Christiansen [35]). These results establish the well-posedness and regularity of solutions of both the integral equation (7.3) and the boundary value problem (2.1); however, they do not provide an explicit form of the edge singularity of the current, which has been long known in the physics literature for certain particular cases (cf. [87]). This issue was resolved by Costabel et al. [46] who proved that the tangential j_t and normal j_ν components of the current with respect to the edge, satisfy

$$j_t := \mathbf{j}(\boldsymbol{r}) \cdot \mathbf{t}(\boldsymbol{r}') = \mathcal{O}(d^{-1/2}) \quad \text{and} \quad j_\nu := \{\mathbf{n}(\boldsymbol{r}) \times \mathbf{j}(\boldsymbol{r})\} \cdot \mathbf{t}(\boldsymbol{r}') = \mathcal{O}(d^{1/2}) \tag{7.5}$$

as $d \to 0$, where $d(\boldsymbol{r}) = |\boldsymbol{r} - \boldsymbol{r}'| = \inf_{\boldsymbol{z} \in \partial S}|\boldsymbol{r} - \boldsymbol{z}|$ denotes the distance from a point $\boldsymbol{r} \in S$ to the edge ∂S, and $\mathbf{t}(\boldsymbol{r}')$ denotes the tangent vector at the point $\boldsymbol{r}' \in \partial S$. Furthermore, [46] established that, in fact

$$j_t = \omega(d)J_t \quad \text{and} \quad j_\nu = J_\nu/\omega(d) \tag{7.6}$$

where $\omega(d) \sim \sqrt{d}$ as $d \to 0$ and where J_t and J_ν are infinitely differentiable functions in a neighborhood on the edge.

We thus see that the numerical solution of the integral equation (7.3) poses several challenges. On one hand the edge singularity (7.5) prevents the use of both standard boundary element (BE) methods based on the polynomial spline approximation of the unknown current density, and existing high-order Nyström methods (cf. [23]) that rely on the global

smoothness of the integral equation solution. Without special treatment of edge singularities the problem becomes severely numerically ill posed. A treatment of the edge singularity significantly improves the situation, although some of the resulting methods possess a very low order of convergence and, to the best of our knowledge, none of these methods have been implemented in practice in the context of *electromagnetic* scattering; some relevant background in these regards can be found in [14, 35], and related results in the scalar case can be found in [119]. On the other hand, the numerical discretization of vectorial integral equations in three dimensional space yields linear systems of large dimensionality, whose solution is impractical by means of direct methods (in view of their sizes), but which cannot be treated by means of iterative linear-algebra solvers such as GMRES—owing to the poor spectral properties of the EFIE (7.3) and resulting extremely large numbers of iterations. The contributions [30, 31, 81] tackle the related acoustic problem for both the cases of sound-soft and sound-hard problems (Dirichlet and Neumann boundary conditions, respectively). These methods, which incorporate the edge singularity and which completely eliminate all negative spectral characteristics, do not directly generalize to the full electromagnetic problem: in view of its boundary conditions which couple all field components, the electromagnetic problem does not easily allow for application of the spectral regularization techniques introduced in [30, 31, 81]. But significant progress in these regards has been obtained as part of this thesis work; preliminary results in these regards, including a novel high-order super-algebraically convergent Nyström method that tackles both difficulties in the full electromagnetic case, is briefly described in what follows.

In order to provide high-order approximations of each one of the integral operators defined in (7.4), we introduce an overlapping-patch representation of the open surface $\overline{S} = \left(\bigcup_{q=1}^{Q_1} \mathcal{P}_1^q \right) \cup \left(\bigcup_{q=1}^{Q_2} \mathcal{P}_2^q \right)$, where $\mathcal{P}_1^q$ and $\mathcal{P}_2^q$ denote interior and edge patches respectively. Associated to each patch there is a C^∞ invertible mapping $\boldsymbol{r}_j^q : \mathcal{H}_j \to \mathcal{P}_j^q$, $j = 1, 2$, where $\mathcal{H}_1 = (-1, 1) \times (-1, 1)$ and $\mathcal{H}_2 = (-1, 1) \times [0, 1) \subset \partial S$. The mappings $\boldsymbol{r}_2^q$, $q = 1, \ldots, Q_2$, associated to the edge patches are such that the section of the edge contained in a patch $\mathcal{P}_2^q$ corresponds to the set $\{\boldsymbol{r}_2^q(u, v) \in \mathbb{R}^3 : v = 0, u \in (-1, 1)\}$. In view of the edge singularity (7.6), on an edge patch $\mathcal{P}_2^q$ the surface current $\mathbf{j}$ can be expressed in terms of a smooth

vector field $\mathbf{J} = J_u \boldsymbol{r}_u + J_v \boldsymbol{r}_v$ and the tensor V defined by

$$\mathbf{j} = V\mathbf{J} = \frac{1}{\omega} \left\{ J_u - \frac{(1+\omega^2)F}{E} J_v \right\} \boldsymbol{r}_u + \frac{1}{\omega} \left\{ \omega^2 J_v \right\} \boldsymbol{r}_v, \tag{7.7}$$

where $\boldsymbol{r}_u = \partial \boldsymbol{r}_2^q / \partial u$, $\boldsymbol{r}_v = \partial \boldsymbol{r}_2^q / \partial v$, and where $E = \boldsymbol{r}_u \cdot \boldsymbol{r}_u$, $F = \boldsymbol{r}_u \cdot \boldsymbol{r}_v$ and $G = \boldsymbol{r}_v \cdot \boldsymbol{r}_v$ denote the first fundamental coefficients. The purpose of tensor V is to factor out the edge singularity of both the tangential and the normal components of the current (note that the functions inside the curly brackets are smooth functions of u and v). In fact, from (7.7) it can be easily shown that

$$J_t = J_u E - J_v F \quad \text{and} \quad J_\nu = -J_v \sqrt{EG - F^2}$$

are smooth functions of u and v. On the other hand, by letting $\omega = \sqrt{v}$ we get that the surface divergence of the current density is given by the following expression

$$\text{div}_S \mathbf{j} = \text{div}_S V\mathbf{J}$$
$$= \frac{1}{\omega \sqrt{EG - F^2}} \left[\frac{\partial}{\partial u} \left\{ \sqrt{EG - F^2} \left(J_t - \frac{(1+\omega^2)F}{E} J_\nu \right) \right\} + \frac{1}{2} \frac{\partial}{\partial v} \left\{ \sqrt{EG - F^2} \, \omega^2 J_\nu \right\} \right], \tag{7.8}$$

that involves partial derivatives of smooth functions only. Identities (7.7) and (7.8) and the use of the partition-of-unity functions defined on each patch allow to redefine the singular unknown vector field $\mathbf{j}$ in the EFIE (7.3), as the smooth vector field $\mathbf{J}$ in the regularized electric field integral equation (V-EFIE):

$$\mathbf{T}_V[\mathbf{J}] := \mathbf{T}[V\mathbf{J}] = -\mathbf{n} \times \mathbf{E}^{\text{inc}} \quad \text{on} \quad S. \tag{7.9}$$

The integral kernels involved in the definition of $\mathbf{T}_V$ possess two kinds of singularities: singularities due to free-space Green function (6.7), and $1/\omega$ singularities arising from the tensor V. High-order quadrature rules we produced for these problems, which significantly extend the methodologies [23, 31] and which are thus applicable to the full vector problem,
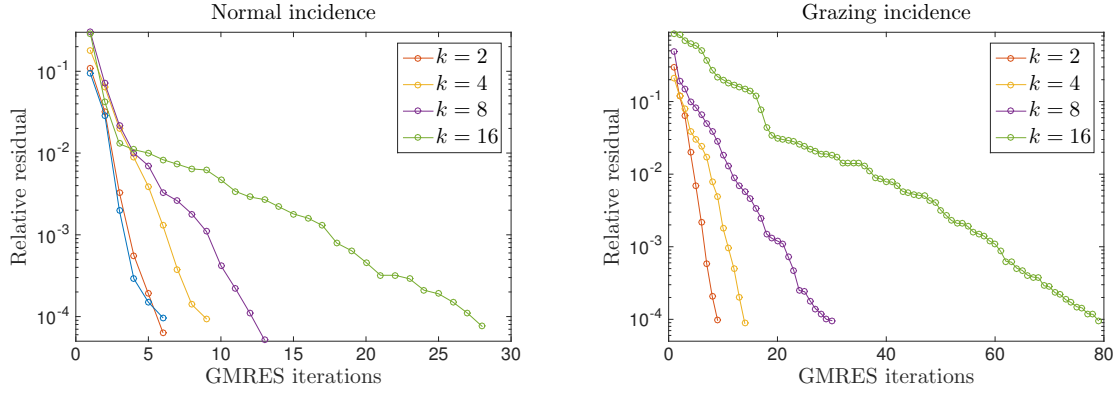
Figure 7.3: GMRES convergence history in the solution of the discretized integral equation (7.10) for various wavenumber and incidences.

were developed and implemented as part of the work leading to this thesis.

Numerical experiments demonstrate that the V-EFIE (7.9) maintains the poor spectral properties of the EFIE (7.3), and thus direct use of the GMRES algorithm leads to an extremely large, highly impractical number of GMRES iterations for convergence. Inspired by the two-dimensional case, for which the spectral properties of the relevant integral operators are well-understood [22, 23, 81], we propose the operator preconditioner

$$\mathbf{T}_\omega[\mathbf{J}] = ik\mathbf{S}\left[V\mathbf{J}\right] + \frac{i}{k}\mathbf{N}\left[\omega\mathbf{J}\right]$$

(early versions of which were outlined in [125]). In order to demonstrate the character of the resulting solvers we consider various problems of scattering of plane electromagnetic waves by a unit PEC disc for various wavenumbers at normal and grazing incidence. Figure 7.3 displays the GMRES convergence history that occurred in the solutions of the discretized preconditioned regularized electric field integral equation (R-EFIE)

$$\left(\mathbf{T}_\omega \circ \mathbf{T}_V\right)[\mathbf{J}] = -\mathbf{T}_\omega\left[\mathbf{n} \times \mathbf{E}^{\text{inc}}\right] \quad \text{on} \quad S. \tag{7.10}$$

We emphasize: without use of the preconditioner no convergence takes place—and, thus, the new preconditioner actually amounts to an enabling technique in this context. Current work, however, does seek to further reduce the required numbers of iterations, and to produce a

preconditioned equation which requires iteration numbers that do not grow as the frequency increases.

The corresponding diffraction patterns are shown in Figure 7.4. Interestingly, the normal-incidence near-field images in Figure 7.4 clearly demonstrate the existence of the famous Poisson spot (also known as Arago spot and Fresnel bright spot). This is a small circular illuminated region at the center of any orthogonal cross-section of the disc shadow, that, in fact, played a fundamental role in the discovery of the wave nature of light. Table 7.1 demonstrates the high-order convergence in each one of the components of the electric field solution of (2.1) that resulted from use of this method for the test problem in which a plane wave impinging normally on a unit disc for $k = 10$. The error is evaluated on a plane parallel to the disc at certain distance away from the disc.

(a) $k = 2$ (b) $k = 4$
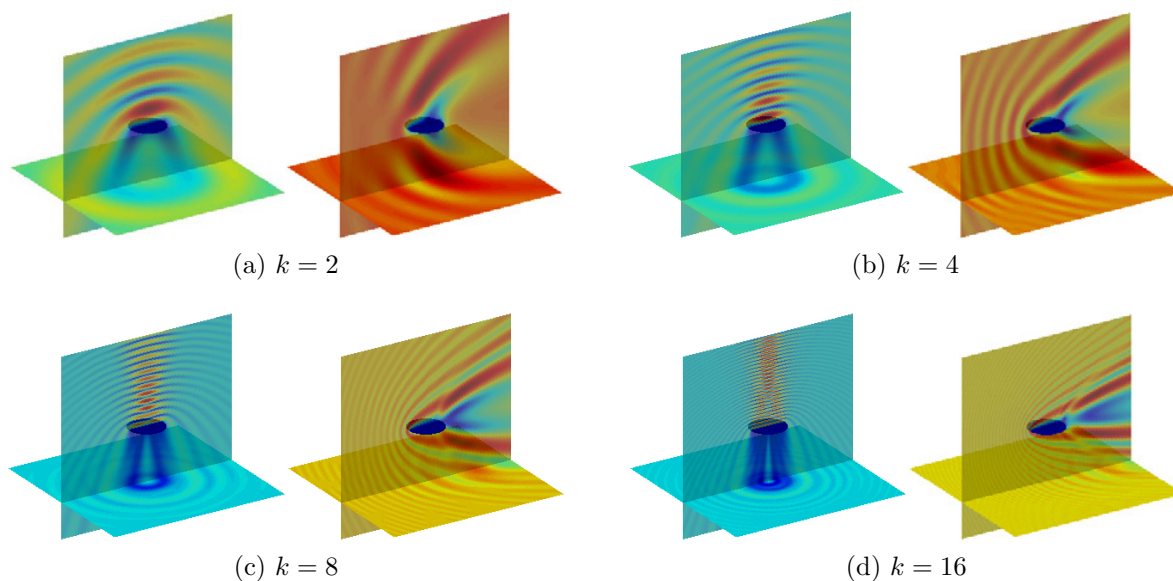
(c) $k = 8$ (d) $k = 16$

Figure 7.4: Magnitude of the total electric field $|\mathbf{E}|$ for the problem of scattering of a plane electromagnetic wave by a PEC disc under normal incidence (columns one and three) and grazing incidence (columns two and four).

$N_1 + 2 \cdot N_2$	E_x	E_y	E_z
$16^2 + 2 \cdot 20 \times 16$	1.62×10^{-2}	3.20×10^{-2}	2.08×10^{-2}
$32^2 + 2 \cdot 40 \times 32$	5.12×10^{-4}	1.07×10^{-3}	6.45×10^{-4}
$64^2 + 2 \cdot 80 \times 64$	1.14×10^{-5}	1.04×10^{-5}	8.42×10^{-6}
$128^2 + 2 \cdot 160 \times 128$	reference		

Table 7.1: Convergence of the solution of the problem of scattering of a plane electromagnetic wave by a unit PEC disc at normal incidence with $k = 10$. Here $N_1 = n^2$ denotes the number of grid points on the interior square patch, and $N_2 = n_u \times n_v$ denotes the number of grid points on the edge patches.

(a) $|\mathbf{E}|$.   (b) $|\mathbf{E}|$.   (c) $|\mathbf{E}|$.

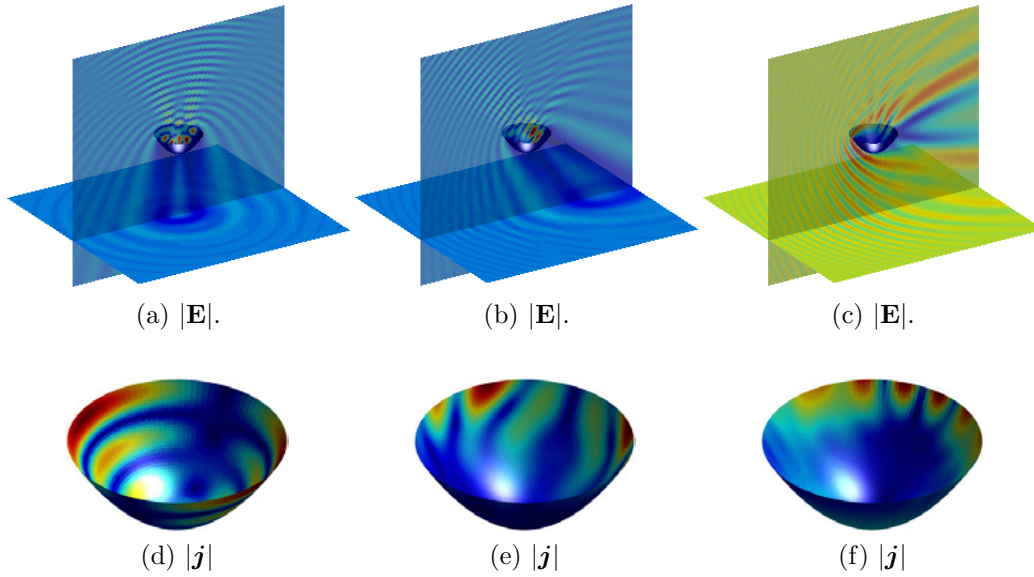(d) $|\boldsymbol{j}|$ (e) $|\boldsymbol{j}|$ (f) $|\boldsymbol{j}|$

Figure 7.5: Solution of the problem of scattering of a plane electromagnetic wave by a paraboloidal PEC open surface. Magnitude of the total electric field (first row) and magnitude of the regularized smooth surface current (second row) for various incidences.

Appendix A

Method of steepest descents

The Sommerfeld integrals in (2.46) can be expressed as a contour integral

$$I(\lambda) = \int_C g(z) \, e^{\lambda\phi(z)} \, dz, \tag{A.1}$$

where the contour C corresponds to an indented path along the real axis. In order to apply the method of steepest descents we first find all the critical points of the phase function ϕ on the path C. As we will show below in this subsection the only the critical points of the phase function (2.47c) are saddle points and, in fact, there is only one simple saddle point on C. Subsequently we determine the path of steepest descent, D, that passes through the saddle point and proceed to deform C into D. By means of Cauchy-Goursat theorem and Jordan's Lemma [15], it can be shown that this process maintains the value of the integral $I(\lambda)$ unchanged. Two main asymptotic contributions arise from this analysis; one due to a localized integral around the saddle point and, possibly, another one arising from integration around one of the branch cuts.

As is well-known [15, Section 7.3], the leading-order asymptotics of an integral I_1 of the form of equation (A.1) but along the path of steepest descent passing through a simple saddle point z_0 and directed towards one of the two steepest descent directions is given by [15, Equation 7.3.11]

$$I_1(\lambda) \sim g(z_0)\sqrt{\frac{2\pi}{\lambda|\phi''(z_0)|}} \, e^{\lambda\phi(z_0)+i\alpha_p} \left\{1 + \mathcal{O}\left(\frac{1}{\lambda}\right)\right\} \quad \text{as} \quad \lambda \to \infty, \tag{A.2}$$

provided the function g is continuous at z_0 and $g(z_0) \neq 0$. Here, using the principal argument function $\arg z \in (-\pi, \pi]$, the two steepest-descent directions are given by $\alpha_p = -\alpha/2 + (2p + 1)\pi/2$, with $p = 0, 1$ and $\alpha = \arg \phi''(z_0)$.

For a function of the form $g(z) = g_0(z - z_0)^{\beta-1}$ $(\beta \in \mathbb{R})$, on the other hand, z_0 is a branch point of g and the value of g at $z = z_0$ is either zero or infinity. The leading-order asymptotics of I_1 along the steepest-descent path for such a function g are given by [15, Equation 7.3.14]

$$I_1(\lambda) \sim \frac{g_0}{2} \left(\frac{2}{\lambda|\phi''(z_0)|} \right)^{\beta/2} S\left(\frac{\beta}{2}\right) e^{\lambda\phi(z_0) - i\beta\alpha/2} \left\{ e^{i\beta\pi/2} - e^{i3\beta\pi/2} \right\} \quad \text{as} \quad \lambda \to \infty. \quad (\text{A.3})$$

The second important contribution may arise when the path of steepest descent intersects one of the various branch cuts. In this case D has to be deformed locally around the branch cut and, consequently, the resulting path is no longer a path of steepest descent but rather a path of descent only. The contribution of a localized integral starting at the branch point along a direction of descent gives rise to a contribution that amounts to [15, Equation 7.3.16]

$$I_2(\lambda) \sim \frac{[g_0]S(\beta)}{[\lambda|\phi'(z_0)|]^\beta} e^{\lambda\phi(z_0) + i\beta(\pi-\alpha)} \quad \text{as} \quad \lambda \to \infty, \quad (\text{A.4})$$

where the function $[g](z)$, which corresponds to the jump of the integrand g at the branch cut, satisfies $[g](z) = [g_0](z-z_0)^{\beta-1}$ as z approaches the branch point z_0, and where $\alpha = \arg \phi'(z_0)$.

Appendix B

A dielectric semi-circular bump on a PEC half-plane

B.1   Exact solution

For reference and testing we consider the problem of scattering of a plane-wave by a unit-radius semi-circular dielectric bump $\Omega_3 = \{(r\cos\theta, r\sin\theta) \in \mathbb{R}^2, 0 \leq r < 1, 0 \leq \theta \leq \pi\}$ on a PEC half-plane Ω_2 (Problem Type III), for which an exact solution in terms of a Fourier-Bessel expansion exists. In detail, the solution of (3.1) can expressed as

$$
\begin{aligned}
u_1(r,\theta) &= \sum_{n=0}^{\infty} b_n H_n^{(1)}(k_1 r)\Phi_n(\theta) \quad \text{in} \quad \Omega_1, & \text{(B.1a)} \\
u_3(r,\theta) &= \sum_{n=0}^{\infty} a_n J_n(k_3 r)\Phi_n(\theta) \quad \text{in} \quad \Omega_3, & \text{(B.1b)}
\end{aligned}
$$

where J_n and $H_n^{(1)}$ are the Bessel and Hankel functions of the first kind and order n, where $\Phi_n(\theta) = \cos(n\theta)$ in TM-polarization and $\Phi_n(\theta) = \sin(n\theta)$ in TE-polarization. The Fourier coefficients in (B.1) are given by

$$
\begin{aligned}
a_n &= \frac{c_n k_1 + (d_n - nc_n)A_n}{[\nu_{13}k_3 J_n'(k_3) - nJ_n(k_3)]A_n + k_1 J_n(k_3)}, \\
b_n &= -\frac{c_n k_3 + (\nu_{31}d_n - nc_n)B_n}{\left[\nu_{31}k_1 H_n^{(1)'}(k_1) - nH_n^{(1)}(k_1)\right]B_n + k_3 H_n^{(1)}(k_1)},
\end{aligned}
$$

$$\text{where} \qquad A_n = \frac{H_n^{(1)}(k_1)}{H_{n+1}^{(1)}(k_1)}, \qquad B_n = \frac{J_n(k_3)}{J_{n+1}(k_3)},$$

$$c_n = \frac{2}{(1+\delta_{n0})\pi} \int_0^\pi f(1,\theta)\Phi_n(\theta)\,d\theta \quad \text{and} \quad d_n = \frac{2}{(1+\delta_{n0})\pi} \int_0^\pi \frac{\partial f}{\partial r}(1,\theta)\Phi_n(\theta)\,d\theta.$$

B.2 Scattering poles

As discussed in Section 3.3.2, scattering poles are complex wavenumbers k for which there exists a non-trivial solution of a transmission problem without sources. In the context of the problem of a dielectric bump on a PEC half plane, for example, scattering poles correspond to existence of non-zero solutions of Problem Type III with $f = 0$. In the particular case considered in Appendix B.1 (semi-circular bump), the problem of evaluation of scattering poles can be further reduced to the problem of finding zeroes of certain nonlinear equations. Indeed, in order for k_1 to be a scattering pole the conditions

$$u_1 = u_3 \quad \text{and} \quad \nu_{13}\frac{\partial u_1}{\partial r} = \frac{\partial u_3}{\partial r}$$

must be satisfied on the boundary $r = 1$ of the bump. From Equation (B.1) it follows that k_1 is a scattering pole if and only if there exist non-trivial constants a_n and b_n such that

$$\begin{aligned} a_n J_n(k_3) - b_n H_n^{(1)}(k_1) &= 0, \\ a_n \nu_{13} k_3 J_n'(k_3) - b_n k_1 H_n^{(1)'}(k_1) &= 0, \end{aligned}$$

for some non-negative integer n. Clearly such constants exist if and only if the determinant of the matrix associated to the linear system above vanishes at k_1. Therefore, scattering poles are given by complex valued solutions k_1 of the equation

$$\nu_{13} k_3 H_n^{(1)}(k_1) J_n'(k_3) = k_1 J_n(k_3) H_n^{(1)'}(k_1)$$

for some non-negative integer n.

Appendix C

Dielectric half-plane under plane-wave illumination

The derivations presented in Chapter 4 rely on the exact solution for the problem of scattering by a flat dielectric half-plane illuminated by the incident field (4.1). This appendix presents an integral equation formulation and associated exact solution for this problem.

As is shown in Section 2.2.2 the corresponding exact expression for the total field is given by the Fresnel formulas

$$
u^f(\boldsymbol{r}) = \begin{cases} u_1^f(\boldsymbol{r}) + u^{\text{inc}}(\boldsymbol{r}) & \text{in} \quad D_1 = \{y > 0\}, \\ u_2^f(\boldsymbol{r}) & \text{in} \quad \overline{D_2} = \{y \le 0\}, \end{cases} \tag{C.1}
$$

where letting

$$
R_\alpha = \frac{ik_1 \sin\alpha - \nu\sqrt{k_1^2 \cos^2\alpha - k_2^2}}{ik_1 \sin\alpha + \nu\sqrt{k_1^2 \cos^2\alpha - k_2^2}} \quad \text{and} \quad T_\alpha = \frac{2ik_1 \sin\alpha}{ik_1 \sin\alpha + \nu\sqrt{k_1^2 \cos^2\alpha - k_2^2}},
$$

we have

$$
u_1^f(\boldsymbol{r}) = R_\alpha\, e^{ik_1(x\cos\alpha - y\sin\alpha)} \quad \text{and} \quad u_2^f(\boldsymbol{r}) = T_\alpha\, e^{ik_1 x\cos\alpha + y\sqrt{k_1^2 \cos^2\alpha - k_2^2}} .
$$

The square root branches in these expressions are determined so as to ensure that $\operatorname{Re} \sqrt{k_1^2 \cos^2\alpha - k_2^2} \ge 0$ and $\operatorname{Im} \sqrt{k_1^2 \cos^2\alpha - k_2^2} \le 0$.

In order to produce the desired integral formulation we use the relations

$$\mathcal{D}_1^\Pi \left[u_1^f |_\Pi \right] (\boldsymbol{r}) - \mathcal{S}_1^\Pi \left[\frac{\partial u_1^f}{\partial n} \Big|_\Pi \right] (\boldsymbol{r}) = \begin{cases} u_1^f(\boldsymbol{r}) & \text{in} \quad D_1, \\ \\ 0 & \text{in} \quad D_2, \end{cases} \tag{C.2a}$$

$$-\mathcal{D}_2^\Pi \left[u_2^f |_\Pi \right] (\boldsymbol{r}) + \mathcal{S}_2^\Pi \left[\frac{\partial u_2^f}{\partial n} \Big|_\Pi \right] (\boldsymbol{r}) + u^\|(\boldsymbol{r}) = \begin{cases} 0 & \text{in} \quad D_1, \\ \\ u_2^f(\boldsymbol{r}) & \text{in} \quad D_2, \end{cases} \tag{C.2b}$$

$$-\mathcal{D}_1^\Pi \left[u^{\text{inc}} |_\Pi \right] (\boldsymbol{r}) + \mathcal{S}_1^\Pi \left[\frac{\partial u^{\text{inc}}}{\partial n} \Big|_\Pi \right] (\boldsymbol{r}) = \begin{cases} 0 & \text{in} \quad D_1, \\ \\ u^{\text{inc}}(\boldsymbol{r}) & \text{in} \quad D_2, \end{cases} \tag{C.2c}$$

for the reflected, transmitted and incident fields, respectively, in terms of the quantity $u^\|$ defined in (4.4) as well as the layer potentials $\mathcal{D}_j^\Pi$ and $\mathcal{S}_j^\Pi$ in (4.17). These relations constitute straightforward generalizations of corresponding expressions presented in [52, Sec. 5].

Defining the boundary integral operators

$$\begin{aligned} S_j^\Pi[\eta](\boldsymbol{r}) = \mathcal{S}_j^\Pi [\eta] (\boldsymbol{r}), \qquad & D_j^\Pi[\eta](\boldsymbol{r}) = \int_\Pi \frac{\partial G_j}{\partial n_{\boldsymbol{r}'}}(\boldsymbol{r}, \boldsymbol{r}')\eta(\boldsymbol{r}') \, \mathrm{d}s_{\boldsymbol{r}'}, \\ N_j^\Pi[\eta](\boldsymbol{r}) = \frac{\partial \mathcal{D}_j^\Pi [\eta]}{\partial n}(\boldsymbol{r}), \qquad & K_j^\Pi[\eta](\boldsymbol{r}) = \int_\Pi \frac{\partial G_j}{\partial n_{\boldsymbol{r}}}(\boldsymbol{r}, \boldsymbol{r}')\eta(\boldsymbol{r}') \, \mathrm{d}s_{\boldsymbol{r}'} \end{aligned} \tag{C.3}$$

for $\boldsymbol{r} \in \Pi$ and for $j = 1, 2$, and utilizing the well-known jump conditions satisfied by the single- and double-layer potentials [45], we obtain

$$\frac{u_1^f}{2} = D_1^\Pi \left[u_1^f |_\Pi \right] - S_1^\Pi \left[\frac{\partial u_1^f}{\partial n} \Big|_\Pi \right] \quad \text{on} \quad \Pi, \tag{C.4}$$

$$\frac{u_2^f}{2} = u^\| - D_2^\Pi \left[u_2^f |_\Pi \right] + S_2^\Pi \left[\frac{\partial u_2^f}{\partial n} \Big|_\Pi \right] \quad \text{on} \quad \Pi, \tag{C.5}$$

$$\frac{u^{\text{inc}}}{2} = -D_1^\Pi \left[u^{\text{inc}} |_\Pi \right] + S_1^\Pi \left[\frac{\partial u^{\text{inc}}}{\partial n} \Big|_\Pi \right] \quad \text{on} \quad \Pi, \tag{C.6}$$

for the fields, and

$$\frac{1}{2}\frac{\partial u_1^f}{\partial n} = N_1^{\Pi}\left[u_1^f|_{\Pi}\right] - K_1^{\Pi}\left[\frac{\partial u_1^f}{\partial n}\Big|_{\Pi}\right] \quad \text{on} \quad \Pi, \tag{C.7}$$

$$\frac{1}{2}\frac{\partial u_2^f}{\partial n} = \frac{\partial u^{\|}}{\partial n} - N_2^{\Pi}\left[u_2^f|_{\Pi}\right] + K_2^{\Pi}\left[\frac{\partial u_2^f}{\partial n}\Big|_{\Pi}\right] \quad \text{on} \quad \Pi, \tag{C.8}$$

$$\frac{1}{2}\frac{\partial u^{\text{inc}}}{\partial n} = -N_1^{\Pi}\left[u^{\text{inc}}|_{\Pi}\right] + K_1^{\Pi}\left[\frac{\partial u^{\text{inc}}}{\partial n}\Big|_{\Pi}\right] \quad \text{on} \quad \Pi, \tag{C.9}$$

for their normal derivatives. Therefore, subtracting the expression for u^{inc} in (C.6) from the expression for u_1^f in (C.4) and using the transmission conditions $u_2^f = u_1^f + u^{\text{inc}}$ and $\nu \partial u_2^f/\partial n = \partial u_1^f/\partial n + \partial u^{\text{inc}}/\partial n$ on Π, we obtain

$$\frac{\varphi^f}{2} - u^{\text{inc}} = D_1^{\Pi}\left[\varphi^f\right] - \nu S_1^{\Pi}\left[\psi^f\right] \quad \text{on} \quad \Pi, \tag{C.10}$$

where we have set $\varphi^f = u_2^f|_{\Pi}$ and $\psi^f = \partial u_2^f/\partial n|_{\Pi}$. Similarly, combining the normal derivatives of the fields we obtain

$$\frac{\nu \psi^f}{2} - \frac{\partial u^{\text{inc}}}{\partial n} = N_1^{\Pi}\left[\varphi^f\right] - \nu K_1^{\Pi}\left[\psi^f\right] \quad \text{on} \quad \Pi. \tag{C.11}$$

Now, adding (C.10) to (C.5) and adding (C.11) to (C.8) we obtain the integral equation

$$\text{E}\,\phi_{\Pi}^f + \text{T}_{\Pi}\left[\phi_{\Pi}^f\right] = \phi_{\Pi}^{\text{inc}} \quad \text{on} \quad \Pi \tag{C.12}$$

for the vector density

$$\phi_{\Pi}^f = \left[\varphi^f, \psi^f\right]^T = \left[u_2^f|_{\Pi}, \frac{\partial u_2^f}{\partial n}\Big|_{\Pi}\right]^T, \tag{C.13}$$

where $\phi_{\Pi}^{\text{inc}} = \left[(u^{\text{inc}} + u^{\|})|_{\Pi}, \partial(u^{\text{inc}} + u^{\|})/\partial n|_{\Pi}\right]^T$ and where the operator T_{Π} is defined by

$$\text{T}_{\Pi} = \begin{bmatrix} D_2^{\Pi} - D_1^{\Pi} & -S_2^{\Pi} + \nu S_1^{\Pi} \\ N_2^{\Pi} - N_1^{\Pi} & -K_2^{\Pi} + \nu K_1^{\Pi} \end{bmatrix}.$$

Equations (C.2), (C.12) and (C.13) provide the desired integral formulation and correspond-

ing integral equation and exact solution for the planar interface problem.

To conclude this section we mention that since $\widetilde{T}_\Pi[\phi^f]$ coincides with $T_\Pi[\phi^f]$ on $S \cap \Pi$, the first line in the correction term (4.20) follows directly from (C.12). The second line in (4.20), in turn, can be obtained by means of expression

$$u^f = u^{\text{inc}} + u^\| - \left(\mathcal{D}_2^\Pi - \mathcal{D}_1^\Pi \right) \left[\varphi^f \right] + \left(\mathcal{S}_2^\Pi - \nu \mathcal{S}_1^\Pi \right) \left[\psi^f \right] \quad \text{in} \quad \mathbb{R}^2 \setminus \Pi, \tag{C.14}$$

which results from addition of equations (C.2a), (C.2b) and (C.2c). Indeed, using (C.14) to evaluate the fields and (by differentiation) their normal derivatives on $S \setminus \Pi$, directly yields the second line in equation (4.20).

Appendix D

Existence and uniqueness

In this appendix we establish existence and uniqueness of a solution $\boldsymbol{\phi} \in C(\overline{\Gamma}_A) \times C(\overline{\Gamma}_A) = C(\overline{\Gamma}_A)^2$ of the windowed integral equation

$$\mathrm{E}\,\boldsymbol{\phi} + \mathrm{T}[W_A \boldsymbol{\phi}] = \boldsymbol{\psi} \quad \text{on} \quad \Gamma_A \tag{D.1}$$

for a smooth curve Γ_A, as defined in Chapter 4 (which here we additionally assume is of class $\mathcal{C}^2$) provided the contrast $n = k_2/k_1$ is sufficiently close to one. The right-hand side is assumed to be continuous, $\boldsymbol{\psi} \in C(\overline{\Gamma}_A)^2$, where $C(\overline{\Gamma}_A)$ denotes the Banach space of continuous complex-valued functions on the closure $\overline{\Gamma}_A$ of Γ_A equipped with the maximum norm $\|\varphi\| = \max_{\boldsymbol{r} \in \overline{\Gamma}_A} |\varphi(\boldsymbol{r})|$. This result on the existence and uniqueness of a solution $\boldsymbol{\phi}$ of the windowed integral equation is then further extended to $L^2(\Gamma_A) \times L^2(\Gamma) = L^2(\Gamma_A)^2$.

Letting $\varphi : \Gamma_A \to \mathbb{C}$ and T^w be the block operator matrix

$$[\mathrm{T}^w]_{ij} = T_{ij}^w, \quad i, j = 1, 2, \tag{D.2}$$

whose block components are given by

$$
\begin{aligned}
T_{11}^w[\varphi] &= (D_2 - D_1)[w_A \varphi], & T_{12}^w[\varphi] &= (S_2 - \nu S_1)[w_A \varphi], \\
T_{21}^w[\varphi] &= (N_2 - N_1)[w_A \varphi], & T_{22}^w[\varphi] &= (K_2 - \nu K_1)[w_A \varphi],
\end{aligned}
\tag{D.3}
$$

the windowed integral equation (D.1) can be equivalently expressed as

$$E\,\boldsymbol{\phi} + T^w[\boldsymbol{\phi}] = \boldsymbol{\psi} \quad \text{on} \quad \Gamma_A. \tag{D.4}$$

Note the integral operators (D.3) can be expressed as:

$$T^w_{11}[\varphi](\boldsymbol{r}) = \frac{i}{4}\int_{\Gamma_A}\left\{k_2 H^{(1)}_1(k_2 R) - k_1 H^{(1)}_1(k_1 R)\right\}\frac{\boldsymbol{R}\cdot n_{\boldsymbol{r}'}}{R}w_A(\boldsymbol{r}')\varphi(\boldsymbol{r}')\,\mathrm{d}s_{\boldsymbol{r}'}, \tag{D.5a}$$

$$\begin{aligned} T^w_{12}[\varphi](\boldsymbol{r}) &= \frac{i}{4}\int_{\Gamma_A}\left\{H^{(1)}_0(k_2 R) - H^{(1)}_0(k_1 R)\right\}w_A(\boldsymbol{r}')\varphi(\boldsymbol{r}')\,\mathrm{d}s_{\boldsymbol{r}'} \\ &\quad + \frac{(1-\nu)i}{4}\int_{\Gamma_A}H^{(1)}_0(k_1 R)w_A(\boldsymbol{r}')\varphi(\boldsymbol{r}')\,\mathrm{d}s_{\boldsymbol{r}'}, \end{aligned} \tag{D.5b}$$

$$\begin{aligned} T^w_{22}[\varphi](\boldsymbol{r}) &= \frac{i}{4}\int_{\Gamma_A}\left\{k_1 H^{(1)}_1(k_1 R) - k_2 H^{(1)}_1(k_2 R)\right\}\frac{\boldsymbol{R}\cdot n_{\boldsymbol{r}'}}{R}w_A(\boldsymbol{r}')\varphi(\boldsymbol{r}')\,\mathrm{d}s_{\boldsymbol{r}'} \\ &\quad + \frac{(\nu-1)i}{4}\int_{\Gamma_A}k_1 H^{(1)}_1(k_1|\boldsymbol{r}-\boldsymbol{r}'|)\frac{\boldsymbol{R}\cdot n_{\boldsymbol{r}}}{R}w_A(\boldsymbol{r}')\varphi(\boldsymbol{r}')\,\mathrm{d}s_{\boldsymbol{r}'} \end{aligned} \tag{D.5c}$$

and

$$\begin{aligned} T^w_{21}[\varphi](\boldsymbol{r}) &= \frac{ik_2^2}{4}\int_{\Gamma_A}\left\{H^{(1)}_0(k_2 R) - H^{(1)}_0(k_1 R)\right\}\frac{(\boldsymbol{R}\cdot n_{\boldsymbol{r}})(\boldsymbol{R}\cdot n_{\boldsymbol{r}'})}{R^2}w_A(\boldsymbol{r}')\varphi(\boldsymbol{r}')\,\mathrm{d}s_{\boldsymbol{r}'} \\ &\quad + \frac{i}{4}\int_{\Gamma_A}\left\{\frac{n_{\boldsymbol{r}}\cdot n_{\boldsymbol{r}'}}{R} - \frac{2(\boldsymbol{R}\cdot n_{\boldsymbol{r}})(\boldsymbol{R}\cdot n_{\boldsymbol{r}'})}{R^3}\right\}\left\{k_2 H^{(1)}_1(k_2 R) - k_1 H^{(1)}_1(k_1 R)\right\}w_A(\boldsymbol{r}')\varphi(\boldsymbol{r}')\,\mathrm{d}s_{\boldsymbol{r}'} \\ &\quad + \frac{i(k_2^2 - k_1^2)}{4}\int_{\Gamma_A}H^{(1)}_0(k_1 r)\frac{(\boldsymbol{R}\cdot n_{\boldsymbol{r}})(\boldsymbol{R}\cdot n_{\boldsymbol{r}'})}{R^2}w_A(\boldsymbol{r}')\varphi(\boldsymbol{r}')\,\mathrm{d}s_{\boldsymbol{r}'}, \end{aligned}$$

$$\tag{D.5d}$$

for $\boldsymbol{r}\in\Gamma_A$, where $\boldsymbol{R} = \boldsymbol{r} - \boldsymbol{r}'$ and $R = |\boldsymbol{R}|$.

Lemma D.0.1. *The integral operator* T^w*, defined in* (D.2)*, is compact on* $C(\overline{\Gamma}_A)^2$*.*

Proof. In view of the estimates $\boldsymbol{R}\cdot n_{\boldsymbol{r}} = \mathcal{O}(R^2)$ and $\boldsymbol{R}\cdot n_{\boldsymbol{r}'} = \mathcal{O}(R^2)$ as $R\to 0$ (cf. [45, Theorem 2.2]) and the asymptotic identities $H^{(1)}_0(k_j R) = \mathcal{O}(\log R)$, $H^{(1)}_1(k_j R) = \mathcal{O}(R^{-1})$ and $k_2 H^{(1)}_1(k_2 R) - k_1 H^{(1)}_1(k_1 R) = \mathcal{O}(R\log R)$ as $R\to 0$ (which follow from the asymptotic expansion of the Hankel functions $H^{(1)}_0$ and $H^{(1)}_1$ for small arguments [76]), we obtain that all integral kernels in the expressions (D.5) are weakly singular. Therefore, from [45, Theorem 1.11] we obtain that T^w_{ij}, $i,j = 1,2$ are compact (and bounded) on $C(\overline{\Gamma}_A)$. Consequently,

T^w is compact on $C(\overline{\Gamma}_A)^2$. The proof is now complete. □

Note that T^w is given in terms of the parameter ν, which equals $(k_1/k_2)^2 = n^{-2}$ in TM-polarization and equals one in TE-polarization, and the operators S_j^w, D_j^w, K_j^w and N_j^w, which depend analytically on k_j for $k_j \in O = \{k \in \mathbb{C} \setminus \{0\} : |\arg k| < \pi\}$, $j = 1, 2$. Hence, for a fixed wavenumber $k_1 > 0$ and setting $k_2 = nk_1$, it follows that $T^w = T^w(n)$ is a compact, operator-valued, analytic function of $n \in O$. From the analytic Fredholm theorem [44, Theorem 8.26] we then obtain the following result:

Lemma D.0.2. *Either:*

1. $(E + T^w(n))^{-1}$ does not exist for any $n \in O = \{k \in \mathbb{C} \setminus \{0\} : |\arg k| < \pi\}$ or,

2. $(E + T^w(n))^{-1}$ exists for all $n \in O \setminus \Lambda$, where Λ is a discrete subset of O.

The following lemma establishes that the first statement in Lemma D.0.2 does not hold.

Lemma D.0.3. *There exists $\delta > 0$ such that $(E + T^w(n))^{-1}$ exists for all $n \in O$ such that $|n - 1| < \delta$.*

Proof. Let $B(n) = E + T^w(n)$ and $n \neq \pm i$. Since E is invertible for all $n \neq \pm i$ we have $E^{-1} B(n) = I_d + E^{-1} T^w(n)$ where I_d denotes the identity operator in $C(\overline{\Gamma}_A)^2$. Clearly, the fact that $T^w(1) = 0$ and the analyticity of $T^w(n)$ at $n = 1$ imply that there exists $\delta > 0$ such that $\| E^{-1} T^w(n) \| < 1$ for all $n \in O$ such that $|n - 1| < \delta$. Hence, the Neumann series $B(n)^{-1} E = \sum_{n=0}^{\infty} (-1)^n \left(E^{-1} T^w(n) \right)^n$ converges (in the operator norm) for all $n \in O$, $|n - 1| < \delta$. Finally, multiplying by E^{-1} from the right on both sides of the identity above we demonstrate the existence of $B(n)^{-1}$ for $|n - 1|$ small enough. The proof is now complete. □

We thus conclude that given $A > 0$ the windowed integral equation (D.4) has a unique continuous solution $\phi \in C(\overline{\Gamma}_A)^2$ for all $k_1 > 0$ and $k_2 \in \{k \in \mathbb{C} \setminus \{0\} : |\arg k| < \pi\} \setminus \Lambda$, where Λ is a discrete set.

Remark D.0.4. *Note that Lemma D.0.1 and Lax's theorem [73, Theorem 4.13] imply that T^w is compact on $L^2(\Gamma_A)^2$. Consequently, Lemmas D.0.2 and D.0.3 are still valid for T^w defined on $L^2(\Gamma_A) \times L^2(\Gamma_A)$. It thus follows that given $A > 0$ and a right-hand side $\psi \in$*

$L^2(\Gamma_A)^2$, *the windowed integral equation* (D.4) *has a unique solution* $\boldsymbol{\phi} \in L^2(\Gamma_A)^2$ *for all* $k_1 > 0$ *and* $k_2 \in \{k \in \mathbb{C} \setminus \{0\} : |\arg k| < \pi\} \setminus \Lambda$, *where* Λ *is a discrete set.*

Bibliography

[1] ABBOUD, T., AND STARLING, F. Scattering of an electromagnetic wave by a screen. In *Boundary value problems and integral equations in nonsmooth domains*. Dekker, New York, 1995, pp. 1–17.

[2] AIRY, G. B. *On the undulatory theory of optics: Designed for the use of students in the university.* Macmillan, 1866.

[3] AKHMETGALIYEV, E. *Fast numerical methods for mixed, singular Helmholtz boundary value problems and Laplace eigenvalue problems-with applications to antenna design, sloshing, electromagnetic scattering and spectral geometry.* PhD thesis, California Institute of Technology, 2016.

[4] AKHMETGALIYEV, E., BRUNO, O. P., AND NIGAM, N. A boundary integral algorithm for the Laplace Dirichlet–Neumann mixed eigenvalue problem. *Journal of Computational Physics 298* (2015), 1–28.

[5] AKSUN, M. I., ALPARSLAN, A., AND MICHALSKI, K. A. *Current status of closed-form Green's functions in layered media composed of natural and artificial materials.* 2009 International Conference on Electromagnetics in Advanced Applications, 2009.

[6] AKSUN, M. I., AND MITTRA, R. Derivation of closed-form green's functions for a general microstrip geometry. *IEEE Transactions on Microwave Theory and Techniques 40*, 11 (1992), 2055–2062.

[7] ALAVIKIA, B., AND RAMAHI, O. M. Finite-element solution of the problem of scattering from cavities in metallic screens using the surface integral equation as a boundary constraint. *Journal of the Optical Society of America A 26*, 9 (2009), 1915–1925.

[8] ALAVIKIA, B., AND RAMAHI, O. M. Hybrid finite element-boundary integral algorithm to solve the problem of scattering from a finite array of cavities with multilayer stratified dielectric coating. *Journal of the Optical Society of America A 28*, 10 (2011), 2192–2199.

[9] AMMARI, H., BAO, G., AND WOOD, A. An integral equation method for the electromagnetic scattering from cavities. *Math. Method. Appl. Sci. 23* (2000), 1057–1072.

[10] ASHEIM, A., AND HUYBRECHS, D. Asymptotic Analysis of Numerical Steepest Descent with Path Approximations. *Foundations of Computational Mathematics. The Journal of the Society for the Foundations of Computational Mathematics 10*, 6 (Dec. 2010), 647–671.

[11] BAO, G., AND SUN, W. A fast algorithm for the electromagnetic scattering from a large cavity. *SIAM Journal on Scientific Computing 27*, 2 (2005), 553–574.

[12] BASHA, M., CHAUDHURI, S., SAFAVI-NAEINI, S., AND EOM, H. Rigorous formulation for electromagnetic plane-wave scattering from a general-shaped groove in a perfectly conducting plane. *Journal of the Optical Society of America A 24*, 6 (2007), 1647–1655.

[13] BEBENDORF, M. *Hierarchical Matrices*. Springer, 2008.

[14] BESPALOV, A., AND HEUER, N. Natural p-BEM for the electric field integral equation on screens. *IMA Journal of Numerical Analysis 30*, 3 (July 2010), 595–628.

[15] BLEISTEIN, N. *Mathematical methods for wave phenomena*. Computer Science and Applied Mathematics. Academic Press, 1984.

[16] BLEISTEIN, N., AND HANDELSMAN, R. A. *Asymptotic expansions of integrals*. Holt, Rinehart and Winston, 1975.

[17] BLESZYNSKI, E., BLESZYNSKI, M., AND JAROSZEWICZ, T. Aim: Adaptive integral method for solving large-scale electromagnetic scattering and radiation problems. *Radio Science 31*, 5 (1996), 1225–1251.

[18] BORN, M., WOLF, E., AND BHATIA, A. *Principles of Optics: Electromagnetic Theory of Propagation, Interference and Diffraction of Light.* Cambridge University Press, 1999.

[19] BRAKHAGE, H., AND WERNER, P. Über das dirichletsche aussenraumproblem für die helmholtzsche schwingungsgleichung. *Archiv der Mathematik 16*, 1 (1965), 325–329.

[20] BREKHOVSKIKH, L. *Waves in Layered Media*, vol. 16. Elsevier, 2012.

[21] BREKHOVSKIKH, L. M., AND GODIN, O. *Acoustics of Layered Media II: Point Sources and Bounded Beams*, vol. 10. Springer, 2013.

[22] BRUNO, O. Integral equations for open surfaces. In *Analysis of boundary element methods (ed. M. Costabel and E. Stephan)* (2008), European Mathematical Society, pp. 1003–1006.

[23] BRUNO, O., ELLING, T., PAFFENROTH, R., AND TURC, C. Electromagnetic integral equations requiring small numbers of krylov-subspace iterations. *Journal of Computational Physics 228*, 17 (2009), 6169–6183.

[24] BRUNO, O., LYON, M., PÉREZ-ARANCIBIA, C., AND TURC, C. Windowed green function method for layered-media scattering. *SIAM Journal on Applied Mathematics (accepted for publication)* (2016).

[25] BRUNO, O. P., AND DELOURME, B. Rapidly convergent two-dimensional quasi-periodic Green function throughout the spectrum—including Wood anomalies. *Journal of Computational Physics 262* (2014), 262–290.

[26] BRUNO, O. P., AND DELOURME, B. Rapidly convergent two-dimensional quasi-periodic Green function throughout the spectrum—including Wood anomalies. *Journal of Computational Physics 262* (2014), 262–290.

[27] BRUNO, O. P., ELLING, T., AND TURC, C. Regularized integral equations and fast high-order solvers for sound-hard acoustic scattering problems. *International Journal for Numerical Methods in Engineering 91*, 10 (June 2012), 1045–1072.

[28] BRUNO, O. P., GEUZAINE, C., MONRO, J., AND REITICH, F. Prescribed error tolerances within fixed computational times for scattering problems of arbitrarily high frequency: the convex case. *Philosophical Transactions of the Royal Society of London. Series A: Mathematical, Physical and Engineering Sciences 362*, 1816 (2004), 629–645.

[29] BRUNO, O. P., AND KUNYANSKY, L. A. A fast, high-order algorithm for the solution of surface scattering problems: basic implementation, tests, and applications. *Journal of Computational Physics* (2001).

[30] BRUNO, O. P., AND LINTNER, S. K. Second-kind integral solvers for TE and TM problems of diffraction by open arcs. *Radio Science 47*, 6 (Dec. 2012), n/a–n/a.

[31] BRUNO, O. P., AND LINTNER, S. K. A high-order integral solver for scalar problems of diffraction by screens and apertures in three-dimensional space. *Journal of Computational Physics 252* (2013), 250–274.

[32] BRUNO, O. P., OVALL, J. S., AND TURC, C. A high-order integral algorithm for highly singular PDE solutions in Lipschitz domains. *Computing 84*, 3-4 (2009), 149–181.

[33] BUCHANAN, J. L., GILBERT, R. P., WIRGIN, A., AND XU, Y. *Marine Acoustics: Direct and Inverse Problems.* SIAM, 2004.

[34] BUCHWALD, J. Z. *The rise of the wave theory of light: Optical theory and experiment in the early nineteenth century.* University of Chicago Press, 1989.

[35] BUFFA, A., AND CHRISTIANSEN, S. H. The electric field integral equation on Lipschitz screens: definitions and numerical approximation. *Numerische Mathematik 94*, 2 (2003), 229–267.

[36] Byun, W. J., Yu, J. W., and Myung, N. H. TM scattering from hollow and dielectric-filled semielliptic channels with arbitrary eccentricity in a perfectly conducting plane. *IEEE Transactions on Microwave Theory and Techniques 46*, 9 (1998), 1336–1339.

[37] Byun, W. J., Yu, J. W., and Myung, N. H. TM scattering from hollow and dielectric-filled semielliptic channels with arbitrary eccentricity in a perfectly conducting plane. *IEEE Transactions on Microwave Theory and Techniques 46*, 9 (1998), 1336–1339.

[38] Cai, W. Algorithmic issues for electromagnetic scattering in layered media: Green's functions, current basis, and fast solver. *Advances in Computational Mathematics 16* (2002), 157–174.

[39] Cai, W., and Yu, T. Fast Calculations of Dyadic Green's Functions for Electromagnetic Scattering in a Multilayered Medium. *Journal of Computational Physics 165* (2000), 1–21.

[40] Chen, Z., Taflove, A., and Backman, V. Photonic nanojet enhancement of backscattering of light by nanoparticles: a potential novel visible-light ultramicroscopy technique. *Optics express 12*, 7 (2004), 1214–1220.

[41] Chew, W. C. *Waves and Fields in Inhomogeneous Media*, vol. 522. IEEE Press, 1995.

[42] Cho, M. H., and Cai, W. A parallel fast algorithm for computing the Helmholtz integral operator in 3-D layered media. *Journal of Computational Physics 231*, 17 (July 2012), 5910–5925.

[43] Chow, Y. L., Yang, J., Fang, D., and Howard, G. A closed-form spatial green's function for the thick microstrip substrate. *IEEE Transactions on Microwave Theory and Techniques 39*, 3 (1991), 588–592.

[44] COLTON, D., AND KRESS, R. *Inverse Acoustic and Electromagnetic Scattering Theory*, third ed., vol. 93. Springer, 2012.

[45] COLTON, D. L., AND KRESS, R. *Integral Equation Methods in Scattering Theory*, first ed. Pure and Applied Mathematics. John Wiley & Sons Inc., 1983.

[46] COSTABEL, M., DAUGE, M., AND DUDUCHAVA, R. Asymptotics without logarithmic terms for crack problems. *Communications in Partial Differential Equations 28*, 5-6 (Jan. 2003), 869–926.

[47] CUI, T. J., AND CHEW, W. C. Efficient evaluation of Sommerfeld integrals for TM wave scattering by buried objects. *Journal of Electromagnetic Waves and Applications 12*, 5 (1998), 607–657.

[48] CUI, T. J., AND CHEW, W. C. Fast evaluation of Sommerfeld integrals for EM scattering and radiation by three-dimensional buried objects. *IEEE Transactions on Geoscience and Remote Sensing 37*, 2 (1999), 887–900.

[49] CUTZACH, P. M., AND HAZARD, C. Existence, uniqueness and analyticity properties for electromagnetic scattering in a two-layered medium. *Mathematical Methods in the Applied Sciences 21*, 5 (1998), 433–461.

[50] DEMANET, L., AND YING, L. Scattering in flatland: efficient representations via wave atoms. *Foundations of Computational Mathematics. The Journal of the Society for the Foundations of Computational Mathematics 10*, 5 (2010), 569–613.

[51] DESANTO, J. A. *Scalar Wave Theory*. Springer, 1992.

[52] DESANTO, J. A., AND MARTIN, P. A. On the derivation of boundary integral equations for scattering by an infinite one-dimensional rough surface. *The Journal of the Acoustical Society of America 102*, 1 (July 1997), 67–77.

[53] DESANTO, J. A., AND MARTIN, P. A. On the derivation of boundary integral equations for scattering by an infinite two-dimensional rough surface. *Journal of Mathematical Physics* (1998).

[54] DU, K. Two transparent boundary conditions for the electromagnetic scattering from two-dimensional overfilled cavities. *Journal of Computational Physics 230*, 15 (2011), 5822–5835.

[55] EOM, H., AND HUR, G. Gaussian beam scattering from a semicircular boss above a conducting plane. *IEEE Transactions on Antennas and Propagation 41*, 1 (1993), 106–108.

[56] EWING, W. M., JARDETZKY, W. S., AND PRESS, F. *Waves in Layered Media.* McGraw-Hill, 1957.

[57] GARG, R. *Microstrip Antenna Design Handbook.* Artech house, 2001.

[58] GIVOLI, D. *Numerical methods for problems in infinite domains*, vol. 33. Elsevier, 2013.

[59] GREENGARD, L., HUANG, J., ROKHLIN, V., AND WANDZURA, S. Accelerating fast multipole methods for the helmholtz equation at low frequencies. *IEEE Computational Science and Engineering 5*, 3 (1998), 32–38.

[60] HINDERS, M. K., AND YAGHJIAN, A. D. Dual-series solution to scattering from a semicircular channel in a ground plane. *IEEE Microwave and Guided Wave Letters 1*, 9 (1991), 239–242.

[61] HOWE, E., AND WOOD, A. TE solutions of an integral equations method for electromagnetic scattering from a 2D cavity. *IEEE Antennas and Wireless Propagation Letters 2* (2003), 93–96.

[62] HUYGENS, C., ARAGO, F., FRESNEL, A. J., AND YOUNG, T. *The Wave Theory of Light: Memoirs by Huygens, Young and Fresnel*, vol. 10. American Book Company, 1900.

[63] ISAACSON, E., AND KELLER, H. *Analysis of numerical methods.* Dover Publications, 1994.

[64] JACKSON, J. D. *Classical Electrodynamics.* John Wiley & Sons: New York, 1998.

[65] JENSEN, F. B., KUPERMAN, W. A., PORTER, M. B., AND SCHMIDT, H. *Computational Ocean Acoustics.* Springer, 2000.

[66] JEREZ-HANCKES, C., AND NÉDÉLEC, J.-C. Asymptotics for Helmholtz and Maxwell Solutions in 3-D Open Waveguides. *Communications in Computational Physics 11*, 2 (Feb. 2012), 629–646.

[67] KATEHI, P., AND ALEXOPOULOS, N. Real axis integration of sommerfeld integrals with applications to printed circuit antennas. *Journal of Mathematical Physics 24*, 3 (1983), 527–533.

[68] KITTAPPA, R., AND KLEINMAN, R. E. Acoustic Scattering by Penetrable Homogeneous Objects. *Journal of Mathematical Physics 16*, 2 (1975), 421–432.

[69] KRESS, R. A Nyström method for boundary integral equations in domains with corners. *Numerische Mathematik 58*, 1 (1990), 145–161.

[70] KRESS, R. A Nystrom method for boundary integral equations in domains with corners. *Numerische Mathematik 58* (1990), 145–161.

[71] KRESS, R. On the numerical solution of a hypersingular integral equation in scattering theory. *Journal of computational and applied mathematics 61*, 3 (Aug. 1995), 345–360.

[72] KRESS, R. Acoustic scattering: Specific theoretical tools. *Scattering (R. Pike, P. Sabatier, eds.), Academic Press, London* (2001), 37–51.

[73] KRESS, R. *Linear Integral Equations*, 3rd ed., vol. 82. Springer, 2014.

[74] KRISTENSSON, G. A uniqueness theorem for Helmholtz' equation: Penetrable Media with an infinite interface. *SIAM Journal on Mathematical Analysis 11*, 6 (1980), 1104–1117.

[75] KUSSMAUL, R. Ein numerisches Verfahren zur Lösung des Neumannschen Aussenraumproblems für die Helmholtzsche Schwingungsgleichung. *Computing (Arch. Elektron. Rechnen) 4* (1969), 246–273.

[76] LEBEDEV, N. N. *Special Functions and their Applications.* Prentice-Hall, 1965.

[77] LEE, S. J., LEE, D. J., LEE, W. S., AND YU, J. W. Electromagnetic scattering from both finite semi-circular channels and bosses in a conducting plane: TM case. *Journal of Electromagnetic Waves and Applications 26* (2012), 2398–2409.

[78] LEIS, R. Zur dirichletschen randwertaufgabe des aussenraumes der schwingungsgleichung. *Mathematische Zeitschrift 90*, 3 (1965), 205–211.

[79] LI, P., AND WOOD, A. A two-dimensional Helmhotlz equation solution for the multiple cavity scattering problem. *Journal of Computational Physics 240* (2013), 100–120.

[80] LINDELL, I. V., AND ALANEN, E. Exact Image Theory for the Sommerfeld Half-Space Problem, Part I: Vertical Magnetic Dipole. *IEEE Transactions on Antennas and Propagation 32*, 2 (1984), 126–133.

[81] LINTNER, S., AND BRUNO, O. P. A generalized calderón formula for open-arc diffraction problems: theoretical considerations. *Proceedings of the Royal Society of Edinburgh: Section A Mathematics 145*, 02 (2015), 331–364.

[82] LUBICH, C. Convolution quadrature and discretized operational calculus. I. *Numerische Mathematik 52*, 2 (1988), 129–145.

[83] MAIER, S. A. *Plasmonics: fundamentals and applications.* Springer Science & Business Media, 2007.

[84] MARTENSEN, E. Über eine methode zum räumlichen Neumannschen problem mit einer anwendung für torusartige berandungen. *Acta Mathematica 109* (1963), 75–135.

[85] MAUE, A. W. Zur Formulierung eines allgemeinen Beugungs-problems durch eine Integralgleichung. *Zeitschrift fr Physik 126*, 7-9 (July 1949), 601–618.

[86] MEIER, A., AND CHANDLER-WILDE, S. N. On the stability and convergence of the finite section method for integral equation formulations of rough surface scattering. *Mathematical Methods in the Applied Sciences 24*, 4 (2001), 209–232.

[87] MEIXNER, J. Strenge theorie der beugung elektromagnetischer wellen an der vollkommen leitenden kreisscheibe. *Zeitschrift für Naturforschung A 3*, 8-11 (1948), 506–518.

[88] MEIXNER, J. The behavior of electromagnetic fields at edges. *IEEE Transactions on Antennas and Propagation 20*, 4 (1972), 442–446.

[89] MICHALSKI, K. A., AND MOSIG, J. R. Efficient computation of Sommerfeld integral tails–methods and algorithms. *Journal of Electromagnetic Waves and Applications* (2016).

[90] MICHALSKI, K. A., AND MOSIG, J. R. The Sommerfeld half-space problem revisited: from radio frequencies and Zenneck waves to visible light and Fano modes. *Journal of Electromagnetic Waves and Applications 30*, 1 (2016), 1–42.

[91] MIE, G. Beiträge zur optik trüber medien, speziell kolloidaler metallösungen. *Annalen der Physik 330*, 3 (1908), 377–445.

[92] MIRET, D., SORIANO, G., AND SAILLARD, M. Rigorous Simulations of Microwave Scattering From Finite Conductivity Two-Dimensional Sea Surfaces at Low Grazing Angles. *IEEE Transactions on Geoscience and Remote Sensing 52*, 6 (2014), 3150–3158.

[93] MONRO JR, J. A. *A Super-Algebraically Convergent, Windowing-Based Approach to the Evaluation of Scattering from Periodic Rough Surfaces*. Ph.D. Thesis, Caltech, 2008.

[94] MOREY, R. M. *Ground penetrating radar for evaluating subsurface conditions for transportation facilities*, vol. 255. Transportation Research Board, 1998.

[95] MOSIG, J. R. Arbitrarily shaped microstrip structures and their analysis with a mixed potential integral equation. *IEEE Transactions on Microwave theory and Techniques 36*, 2 (1988), 314–323.

[96] MOSIG, J. R., AND GARDIOL, F. E. General integral equation formulation for microstrip antennas and scatterers. *IEE Proceedings H - Microwaves, Antennas and Propagation 132*, 7 (1985), 424–432.

[97] NÉDÉLEC, J.-C. *Acoustic and Electromagnetic Equations: Integral Representations for Harmonic Problems. Vol. 144. Springer, 2001.* Vol. 144, Springer, 2001.

[98] O'NEIL, M., GREENGARD, L., AND PATAKI, A. On the efficient representation of the half-space impedance Green's function for the Helmholtz equation. *Wave Motion 51*, 1 (2014), 1–13.

[99] PANICH, I. On the question of the solvability of the exterior boundary-value problems for the wave equation and Maxwell's equations. *Russian Mathematical Surveys 20* (1965), 221–226.

[100] PARK, T., EOM, H., AND YOSHITOMI, K. Analysis of TM scattering from finite rectangular grooves in a conducting plane. *Journal of the Optical Society of America A 10*, 5 (1993), 905–911.

[101] PARK, T. J., EOM, H. J., YAMAGUCHI, Y., AND BOERNER, W. TE-plane wave scattering from a trough in a conducting plane. *Journal of Electromagnetic Waves and Applications 7*, 2 (1993), 235–245.

[102] PARK, T. J., EOM, H. J., YAMAGUCHI, Y., BOERNER, W. M., AND KOZAKI, S. TE-plane wave scattering from a dielectric-loaded semi-circular trough in a conducting plane. *Journal of Electromagnetic Waves and Applications 7*, 2 (1993), 235–245.

[103] PAULUS, M., GAY-BALMAZ, P., AND MARTIN, O. Accurate and efficient computation of the Green's tensor for stratified media. *Physical Review E 62*, 4 (2000), 5797.

[104] PÉREZ-ARANCIBIA, C., AND BRUNO, O. P. High-order integral equation methods for problems of scattering by bumps and cavities on half-planes. *Journal of the Optical Society of America A 31*, 8 (Aug. 2014), 1738–1746.

[105] PÉREZ-ARANCIBIA, C., ZHANG, P., BRUNO, O. P., AND LAU, Y. Electromagnetic power absorption due to bumps and trenches on flat surfaces. *Journal of Applied Physics 116*, 12 (2014), 124904.

[106] PRESS, W. H., TEUKOLSKY, S. A., VETTERLING, W. T., AND FLANNERY, B. P. *Numerical recipes in FORTRAN.* Cambridge University Press, 1992.

[107] RAETHER, H. *Surface Plasmons on Smooth and Rough Surfaces and on Gratings.* Springer, 1988.

[108] RAO, S., WILTON, D., AND GLISSON, A. Electromagnetic scattering by surfaces of arbitrary shape. *IEEE Transactions on antennas and propagation 30*, 3 (1982), 409–418.

[109] RAYLEIGH, L. On the light dispersed from fine lines ruled upon reflecting surfaces or transmitted by very narrow slits. *The London, Edinburgh, and Dublin Philosophical Magazine and Journal of Science 14*, 81 (1907), 350–359.

[110] ROACH, G. F., AND ZHANG, B. A Transmission Problem for the Reduced Wave Equation in Inhomogeneous Media with an Infinite Interface. *Proceedings of the Royal Society of London A: Mathematical, Physical and Engineering Sciences 436*, 1896 (1992), 121–140.

[111] RUPPIN, R. Electric field enhancement near a surface bump. *Solid State Communications 39*, 4 (1981), 903–906.

[112] SACHDEVA, B. K., AND HURD, R. A. Scattering by a dielectricloaded trough in a conducting plane. *Journal of Applied Physics 48*, 4 (1977), 1473–1476.

[113] SAILLARD, M., AND SORIANO, G. Rough surface scattering at low-grazing incidence: A dedicated model. *Radio Science 46*, 5 (Oct. 2011).

[114] SAUTER, S. A., AND SCHWAB, C. *Boundary Element Methods.* Springer, 2010.

[115] SCHWAB, A. J., AND FISCHER, P. Maxwell, Hertz, and German radio-wave history. *Proceedings of the IEEE 86*, 7 (July 1998), 1312–1318.

[116] SENGUPTA, D. L., AND SARKAR, T. K. Maxwell, Hertz, the Maxwellians and the early history of electromagnetic waves. In *Antennas and Propagation Society International Symposium, 2001. IEEE* (2001), IEEE, pp. 14–17 vol.1.

[117] SOMMERFELD, A. Über die Ausbreitung der Wellen in der drahtlosen Telegraphie. *Annalen der Physik 333*, 4 (1909), 665–736.

[118] SPIGA, P., SORIANO, G., AND SAILLARD, M. Scattering of Electromagnetic Waves From Rough Surfaces: A Boundary Integral Method for Low-Grazing Angles. *IEEE Transactions on Antennas and Propagation 56*, 7 (July 2008), 2043–2050.

[119] STEPHAN, E. Boundary integral equations for screen problems in $\mathbb{R}^3$. *Integral Equations and Operator Theory 10*, 2 (1987), 236–257.

[120] STOKES, G. G. On the intensity of the light reflected from or transmitted through a pile of plates. In *Proceedings of the Royal Society of London* (1860).

[121] STRATTON, J. A., AND CHU, L. J. Diffraction theory of electromagnetic waves. *Physical Review 56*, 1 (July 1939), 99–107.

[122] TAFLOVE, A., AND HAGNESS, S. H. *Computational electrodynamics: The finite-difference time-domain method.* Artech House, 2005.

[123] TAYLOR, M. *Partial Differential Equations, Vol. II: Qualitative Studies of Linear Equations*, vol. 117. Springer, 1996.

[124] TUCKERMAN, L. B. On the Intensity of the Light Reflected From or Transmitted Through a Pile of Plates. *Journal of the Optical Society of America A 37*, 10 (1947), 818–825.

[125] Turc, C., Anand, A., Bruno, O. P., and Chaubell, J. Efficient solution of three-dimensional problems of acoustic and electromagnetic scattering by open surfaces. In *Proceedings of WAVES* (2011).

[126] Twersky, V. On the Nonspecular Reflection of Electromagnetic Waves. *Journal of Applied Physics 22*, 6 (1951), 825.

[127] Tyzhnenko, A. Two-dimensional TE-plane wave scattering by a dielectric-loaded semicircular trough in a ground plane. *Electromagnetics 24*, 5 (2004), 357–368.

[128] Tyzhnenko, A. G. A unique solution to the 2-D H-scattering problem for a semicircular trough in a PEC ground plane. *Progress In Electromagnetics Research 54* (2005), 303–319.

[129] Van, T., and Wood, A. Finite element analysis of electromagnetic scattering from a cavity. *IEEE Transactions on Antennas and Propagation 51*, 1 (2003), 130–137.

[130] Van Bladel, J. Field singularities at metal-dielectric wedges. *IEEE Transactions on Antennas and Propagation 33*, 4 (1985), 450–455.

[131] Wait, J. R. The ancient and modern history of EM ground-wave propagation. *IEEE Antennas and Propagation Magazine 40*, 5 (1998), 7–24.

[132] Wang, C.-F., and Gan, Y.-B. 2D cavity modeling using method of moments and iterative solvers. *Prog. Electromagn. Res. 43* (2003), 123–142.

[133] Wang, Y., Du, K., and Sun, W. A second-order method for the electromagnetic scattering from a large cavity. *Numerical Math: Theory, Methods and Applications 1*, 4 (2008), 357–382.

[134] Watson, G. N. *A treatise on the theory of Bessel functions*. Cambridge University Press, 1995.

[135] Wood, A. Analysis of electromagnetic scattering from an overfilled cavity in the ground plane. *Journal of Computational Physics 215*, 2 (2006), 630–641.

[136] WOOD, W. D., AND WOOD, A. W. Development and numerical solution of integral equations for electromagnetic scattering from a trough in a ground plane. *IEEE Transactions on Antennas and Propagation 47*, 8 (1999), 1318–1322.

[137] YU, J.-W., BYUN, W. J., AND MYUNG, N.-H. Multiple scattering from two dielectric-filled semi-circular channels in a conducting plane: TM case. *IEEE Transactions on Antennas and Propagation 50*, 9 (2002), 1250–1253.

[138] ZENNECK, J. Über die fortpflanzung ebener elektromagnetischer wellen längs einer ebenen leiterfläche und ihre beziehung zur drahtlosen telegraphie. *Annalen der Physik 328*, 10 (1907), 846–866.

[139] ZHANG, D., MA, F., AND DONG, H. A finite element method with rectangular perfectly matched layers for the scattering from cavities. *Journal of Computational Mathematics 27*, 6 (2009), 812–834.

[140] ZHANG, P., LAU, Y. Y., AND GILGENBACH, R. M. Analysis of radio-frequency absorption and electric and magnetic field enhancements due to surface roughness. *Journal of Applied Physics 105*, 114908 (2009), 1–9.

[141] ZHAO, Z., LI, L., SMITH, J., AND CARIN, L. Analysis of scattering from very large three-dimensional rough surfaces using MLFMM and ray-based analyses. *IEEE Antennas and Propagation Magazine 47*, 3 (June 2005), 20–30.